PARTITION OF UNITY BOUNDARY ELEMENT AND FINITE ELEMENT METHOD: OVERCOMING NONUNIQUENESS AND COUPLING FOR ACOUSTIC SCATTERING IN HETEROGENEOUS MEDIA

DIWAN, GANESH,CHANDRASHEN

PARTITION OF UNITY BOUNDARY ELEMENT AND FINITE ELEMENT METHOD: OVERCOMING NONUNIQUENESS AND COUPLING FOR ACOUSTIC SCATTERING IN HETEROGENEOUS MEDIA

Ganesh Chandrasen Diwan

Thesis submitted towards the degree of
Doctor of Philosophy

Computational Mechanics Group
School of Engineering and Computing Sciences
Durham University
United Kingdom

June 2014

Partition of Unity Boundary Element and Finite Element Method: Overcoming non-uniqueness and coupling for acoustic scattering in heterogeneous media

Ganesh Chandrasen Diwan

Abstract

The understanding of complex wave phenomenon, such as multiple scattering in heterogeneous media, is often hindered by lack of equations modelling the exact physics. Use of approximate numerical methods, such as Finite Element Method (FEM) and Boundary Element Method (BEM), is therefore needed to understand these complex wave problems. FEM is known for its ability to accurately model the physics of the problem but requires truncating the computational domain. On the other hand, BEM can accurately model waves in unbounded region but is suitable for homogeneous media only. Coupling FEM and BEM therefore is a natural way to solve problems involving a relatively small heterogeneity (to be modelled with FEM) surrounded by an unbounded homogeneous medium (to be modelled with BEM).

The use of a classical FEM-BEM coupling can become computationally demanding due to high mesh density requirement at high frequencies. Secondly, BEM is an integral equation based technique and suffers from the problem of non-uniqueness. To overcome the requirement of high mesh density for high frequencies, a technique known as the 'Partition of Unity' (PU) method has been developed by previous researchers. The work presented in this thesis extends the concept of PU to BEM (PUBEM) while effectively treating the problem of non-uniqueness. Two of the well-known methods, namely CHIEF and Burton-Miller approaches, to overcome the non-uniqueness problem, are compared for PUBEM. It is shown that the CHIEF method is relatively easy to implement and results in at least one order of magnitude of improvement in the accuracy. A modified 'PU' concept is presented to solve the heterogeneous problems with the PU based FEM (PUFEM). It is shown that use of PUFEM results in close to two orders of magnitude improvement over FEM despite using a much coarser mesh. The two methods, namely PUBEM and PUFEM, are then coupled to solve the heterogeneous wave problems in unbounded media. Compared to PUFEM, the coupled PUFEM-PUBEM apporach is shown to result between 30-40% savings in the total degress of freedom required to achieve similar accuracy.

Declaration

The work in this thesis is based on research carried out in the Computational Mechanics Group, School of Engineering and Computing Sciences, Durham University. No part of this report has been submitted elsewhere for any other degree or qualification and it is all my own work unless referenced to the contrary in the text.

Parts of this work have been published in the following:

Journals

- G.C. Diwan, J. Trevelyan and G. Coates
  A comparison of techniques for overcoming non-uniqueness of boundary integral equations for the collocation partition of unity method in two-dimensional acoustic scattering
  International Journal for Numerical Methods in Engineering, **96**(10): 645-664, 2013

- G.C. Diwan, M.S. Mohamed, M. Seaid, J. Trevelyan and O. Laghrouche
  Mixed enrichment for the finite element method in heterogeneous media
  International Journal for Numerical Methods in Engineering, 2014, Submitted.

- G.C. Diwan, J. Trevelyan, G. Coates and O. Laghrouche
  A Partition of Unity Coupled FEM-Collocation BEM for acoustic scattering in heterogeneous media in 2D
  In preparation.

Acknowledgements

I express sincere gratitude towards my supervisors Prof. Jon Trevelyan and Dr. Graham Coates, who patiently supervised me during my doctoral studies at Durham University. I am grateful to both Jon and Graham for carrying out a painstaking task of proofreading this thesis. Also, I take this opportunity to acknowledge Jon for several discussions we had that helped me to gain a better understanding of boundary integral equations.

I am also thankful for the inspiration and learning experience I gained from working with my colleagues, including Dr. M Shadi Mohamed, Dr. Mohammed Seaid and Dr. Robert Simpson. Thanks are also due to Prof. Omar Laghrouche of Heriot-Watt University who has always been very helpful during the development of PUFEM code.

I gratefully acknowledge the generous financial support from Durham University through the Durham Doctoral Fellowship.

Deep thanks to all my friends at Durham - Baseer, Zahur (now postdoc at Glasgow University), Ibrahim and Michael for making my stay in Durham memorable.

I would like to thank my family- father (Dr. Chadrasen Diwan), mother (Vaishali), sister (Vishakha), brother (Yogesh) and my in-laws for their endless support, love and encouragement during my studies at Durham.

Last and not the least, I would like to thank my wife Preeti for sticking with me through thick and thin.

Ganesh C. Diwan
Durham, June 2014

Contents

List of Figures

List of Tables

Nomenclature & Abbreviations

BEM	Boundary Element Method
BGT	Bayliss-Gunzburger-Turkel
BIE	Boundary Integral Equation
CBIE	Conventional Boundary Integral Equation
CHBIE	Combined Hypersingular Boundary Integral Equation
EM	Engquist-Majda
FEM	Finite Element Method
FMM	Fast Multipole Method
HBIE	Hypersingular Boundary Integral Equation
NRBC	Non reflecting boundary condition
PUBEM	Partition of Unity Boundary Element Method
PUFEM	Partition of Unity Finite Element Method
$\mathbf{A}$	coefficient matrix for the FEM linear system
$\mathbf{A}_c$	coefficient matrix for the coupled PUFEM-PUBEM linear system
$\bar{\mathbf{A}}$	coefficient matrix for the PUFEM linear system
$\boldsymbol{\mathcal{A}}^e$	column vector containing the plane wave amplitudes for approximating the pressure for an element e for the 'homogeneous basis'
$\hat{\boldsymbol{\mathcal{A}}}^e$	column vector containing the plane wave amplitudes for approximating the pressure for an element e for the 'mixed basis'
a_{jm}	amplitude of the m^{th} plane wave at j^{th} node
B	boundary damper operator for an NRBC
$\mathfrak{B}$	adiabatic bulk modulus
$\boldsymbol{\mathcal{B}}^e$	column vector containing the plane wave amplitudes for approximating normal derivative of pressure for an element e for the 'homogeneous basis'
$\hat{\boldsymbol{\mathcal{B}}}^e$	column vector containing the plane wave amplitudes for approximating the normal derivative of pressure for an element e for the 'mixed basis'
$[\mathbf{C}^e]$	element radiation damping matrix for FEM
$[\bar{\mathbf{C}}^e]$	enriched element radiation damping matrix for PUFEM
$c(\mathbf{x})$	jump term at point $\mathbf{x}$ on boundary Γ_s
d_{jm}	direction vector at node j for m^{th} plane wave
$E^2(\Gamma_r)$	relative L^2 error in the total pressure on radiation boundary Γ_r
$E^2(\Gamma_s)$	relative L^2 error in the total pressure on scatterer surface Γ_s
$E^2(\Omega_f)$	relative L^2 error in the total pressure for computational domain Ω_f
$\{\bar{\mathbf{f}}^e\}$	enriched element load vector for PUFEM
$\{\mathbf{f}^e\}$	element load vector for FEM
$\bar{\mathbf{f}}$	global load vector either for PUFEM or PUBEM
$\mathbf{f}$	global load vector either for FEM or BEM
$\mathbf{f}_c$	load vector for the coupled PUFEM-PUBEM linear system
G	Green's function for Helmholtz equation

G_0	Green's function for Laplace equation
$H_0^{(1)}(\cdot)$	Hankel function of order zero and of first kind
$\bar{\mathbf{H}}$	coefficient matrix for the PUBEM linear system for sound hard Γ_s
J	jacobian matrix
$J_n^{(1)}(\cdot)$	Bessel function of order n and of first kind
$[\mathbf{K}^e]$	element stiffness matrix for FEM
$[\bar{\mathbf{K}}^e]$	enriched element stiffness matrix for PUFEM
k	wavenumber
k_0	wavenumber of the homogeneous exterior medium Ω_0
M_j	number of plane waves associated with node j
$[\mathbf{M}^e]$	element mass matrix for FEM
$[\bar{\mathbf{M}}^e]$	enriched element mass matrix for PUFEM
N_j	shape function at node j
$n_{\mathbf{x}}$	normal vector at point $\mathbf{x}$
$n_{\mathbf{y}}$	normal vector at point $\mathbf{y}$
n_{FB}	number of nodes on the FE-BE coupling boundary
n_{tot}	total number of nodes in the FE mesh
nDof	total degrees of freedom in the system
nnz	number of non-zero entries in the matrix
$\hat{p}$	complex acoustic pressure
p	amplitude of the complex acoustic pressure
p^{inc}	incident wave acoustic pressure
p^{sct}	Scattered acoustic pressure
$\mathbf{Q}^e$	row vector containing the product of FE shape functions and plane waves for a finite element e for the 'homogeneous basis'
$\hat{\mathbf{Q}}^e$	row vector containing the product of FE shape functions and plane waves for a finite element e for the 'mixed basis'
$\mathbf{\mathcal{R}}^e$	row vector containing product of BE shape functions and plane waves for a boundary element e for 'homogeneous basis'
$\hat{\mathbf{\mathcal{R}}}^e$	row vector containing product of BE shape functions and plane waves for a boundary element e for the 'mixed basis'
$\mathbf{u}_c$	solution vector of the coupled PUFEM-PUBEM linear system
$Y_n^{(1)}(\cdot)$	Bessel function of order n and of second kind
λ	wavelength
τ	degrees of freedom per wavelength
α	coupling constant for Burton-Miller formualtion
Γ_i	interface between two media
Γ_r	radiation boundary or FE-BE interface
Γ_s	boundary of scatterer Ω_s
κ	condition number of the matrix
Ω_0	homogeneous exterior domain with wavenumber k_0
Ω_∞	unbounded acoustic domain
Ω_f	Computational domain
Ω_s	region occupied by scatterer
ω	circular frequency of acoustic wave
ρ	mass density of the acoustic medium
∇	gradient operator
0	zero matrix

Chapter 1

Motivation and Objective

The mathematics of the full treatment may be altogether beyond human power in a reasonable time; nevertheless... (Heaviside,[76])

1.1 Long range propagation, short waves and heterogeneous media

The study of wave propagation and scattering is important in fields such as acoustics, seismic analysis, non-destructive testing, electromagnetics to name a few. One of the reasons why the phenomenon of wave propagation is important to scientists and engineers is that waves can travel a long distance compared to their wavelength. Consider for example the case of underwater sound propagation. The oceans are transparent to low frequency sound and the acoustic waves are known to travel great distances of several thousand kilometers in a particular waveguide region known as SOund Frequency and Ranging (SOFAR) channel [46]. The second example is that of high frequency (HF) radar signals. It is known that radar signals can travel with little attenuation in the line of sight (ground wave propagation) as the absorption in the atmosphere is negligible for electromagnetic waves. HF radars are increasingly used in several remote sensing applications such as ocean current measurements, early warning systems for Tsunamis and oil spills, remote surveillance [4, 12, 177]. Earthquakes are another important wave phenomenon which can be felt over great distances. The Koyna dam earthquake that killed close to 200 people in Western India was felt over a distance up to 700 km from its epicenter, the Koyna Dam [134]. Typical frequencies in the long range propagation used in underwater acoustics are

from 20 Hz to 500 Hz. The wavelength, say λ, can be given by the relation

$$\lambda = \frac{2\pi}{k} = \frac{c}{f} \tag{1.1}$$

where k is the wavenumber, c is the speed of the propagating wave and f is the frequency of the wave. This indicates that the wavelengths under consideration range from 75 m (for $f = 20$ Hz) to 3 m (for $f = 500$ Hz) with $c = 1500$ m/s. Note that as the frequency increases, the wavelength decreases. Consequently, the long range propagation could mean detecting acoustic pulses at a distance of 5-10 km from the source. In case of remote sensing application such as HF radar, the wavelength ranges from 40 m to 5 m whereas the waves are used for remote sensing in a region that is at a distance up to 200 km. It can therefore be understood that for the purpose of numerically simulating these wave problems, one needs to model a domain that spans thousands of wavelengths and this can be identified as the first challenge in numerical modelling.

The second problem when numerically solving the wave problems is the increasing frequency. Applications such as medical imaging which rely on the use of ultrasonic waves involve acoustic pulses with frequencies ranging from 1 MHz to 15 MHz. This results in a wavelength of 1.5 mm (for $f = 1$ MHz) to 100 microns (for $f = 15$ MHz) for $c = 1500$ m/s. Modelling such short wavelength problems with the classical Finite Element Method (FEM) or Boundary Element Method (BEM) would be a highly computationally intensive task. For example a numerical study of ultrasonic wave propagation in human bones using a 3D FE model was carried out by Protopappas *et al* [150]. The computational model was taken as a hollow cylinder with outer and inner radii as 8.61 and 4.53 mm respectively, while the length of the cylinder was 50 mm. This cylinder is equivalent in volume to a solid cube of side approximately 20 mm. The authors used a FE model with 4 million degrees of freedom (with eight-node linear hexahedral continuum elements, element type C3D8R in ABAQUS version 6.4) and the problem was solved using a 64-CPU, Origin 2000 supercomputer with 32 Gbytes shared memory. The typical computational time was 40 min and the frequencies tested ranged from 0.1-1.5 MHz.

Another example is of a short wave problem in seismic wave scattering. Consider an earth model using a cube domain of side 3 km and let the acoustic wave speeds range from 1500 to 4500 km/s (and thus a heterogeneous problem). Now consider an acoustic source with frequency

25 Hz, thus the shortest wavelength would be $\lambda = 1500/25 = 60$ m. Thus the problem size in terms of wavelengths is $50 \times 50 \times 50$. If the wave propagation is simulated only for 1 sec in this domain, using the explicit Finite Difference Method (FDM) and if 10 grid points per wavelength are taken, one would need a stencil of $500 \times 500 \times 500$ grid points. The total number of grid point evaluations is therefore $5000 \times 500^3 = 6.25 \times 10^{11}$ [178].

It is therefore clear that numerically solving wave problems can become computationally demanding either due to

1. a very large computational domain relative to the wavelength, or,
2. highly heterogeneous media with either a low (seismic waves in geophysical exploration) or a high frequency (ultrasonic waves in human tissue) wave.

At this point, it will be useful to define a parameter τ that specifies the number of degrees of freedom per wavelength, i.e.,

$$\tau = \lambda \left(\frac{\text{nDof}}{A} \right)^{1/2} \quad \text{for 2D FEM} \tag{1.2a}$$

$$\tau = \lambda \left(\frac{\text{nDof}}{P} \right) \quad \text{for 2D BEM} \tag{1.2b}$$

where nDof is the total degrees of freedom in the problem, A is the area under consideration when solving the problem with FEM ($A = \int dA$) and P is the length of the boundary ($P = \int d\Gamma$) when solving the problem with BEM. We have considered the definition of the parameter τ for a two dimensional case alone as it is the focus of this thesis. It is well known that both FEM and BEM require $\tau \approx 6$ to 10 to model the wave scattering problems and obtain results with engineering accuracy ($\approx 1\%$). Clearly the nDof needed (see (1.2)) grows linearly for BEM and quadratically for FEM with the wavenumber k. This is a major problem when modelling short waves with FEM or BEM as a FE or BE mesh satisfying $\tau \approx 6$ to 10 will lead to large computer memory requirements especially at high frequencies (see Figure 1.1). Consider the practical problem of the seismic waves mentioned earlier. If a time harmonic case was to be solved with FEM, with source frequency of 100 Hz ($\lambda = 1500/100 = 15$ m), the problem size in terms of wavelength is $200 \times 200 \times 200$. The 'rule of thumb' of $\tau \approx 10$ requires a FE mesh with $(200 \times 10)^3 = 8 \times 10^9$ nodes. Even if such a large model could be constructed and run using parallel processors, a major problem with polynomial based FEM or BEM remains which

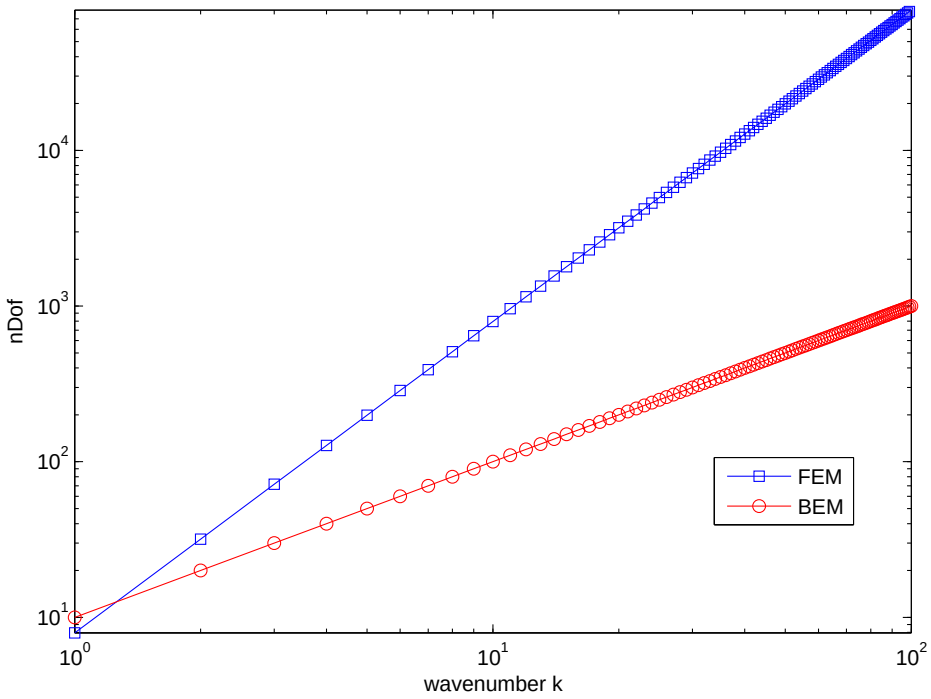

Figure 1.1: nDof vs k at $\tau = 10$ for FEM and BEM

is known as the pollution error. As the frequency of the wave increases, the error in the solution grows even if the criteria of $\tau \approx 10$ is followed [9]. This is a major concern for engineers as many imaging problems involve very short waves.

1.2 Unbounded domain problem

The FEM has long established itself as an attractive choice for numerical modelling wave scattering problems [73], [71], [175]. The most important feature of FEM is that it is a general numerical method that can be applied to complex geometries and heterogeneous materials. Consider the wave scattering problem encountered in ocean acoustics or in ultrasound imaging. The acoustic medium in these cases is highly heterogeneous (such as temperature and density dependent sound speed in oceans or soft and attenuating tissues in the brain) and often with intricate features (nonplanar bathymetry and complex tissue structures). FEM therefore appears to be an ideal choice in such applications. FEM however can become computationally intensive when modelling unbounded media. Consider a wave being scattered from an object and propagating in an unbounded medium such as sound scattering from underwater ship hull or electromagnetic scattering from an aeroplane. Since the real life media (oceans, atmosphere)

are practically infinite to be modelled on a finite computer, the computational domain needs to be truncated to a finite size for the purpose of numerical modelling. A suitable 'non reflecting boundary condition' (NRBC) then needs to be used on the truncated domain if FEM is used. Since these boundary conditions are not exact, spurious reflections occur at these boundaries which pollute the solution obtained with FEM. The larger the computational domain, the better the results obtained with a NRBC. Clearly, for long range propagation problems, FEM will become expensive. There is abundant literature on this topic and NRBCs will be discussed in Chapter 3 in detail (§3.3). At this point, it should suffice to say that the development of an optimal NRBC is still an ongoing research topic.

BEM on the other hand is known to be best suited for wave problems in unbounded, linear, homogeneous media [36], [186],[95]. The major advantage of BEM is that the dimension of the problem is reduced by one. This drastically reduces the total number of degrees of freedom ($ndof$) needed to solve a particular scattering problem. Coupling of FEM with BEM therefore appears to be a natural way of solving wave problems in unbounded media. A coupled algorithm would ideally use FEM in the region where geometry is complex and/or the medium is heterogeneous. The BEM would be used for treating waves in the unbounded and homogeneous medium. As will be discussed later in the thesis, the limitation of a coupled FEM-BEM approach remains the unsymmetric structure of the linear system of equations formed as a result of direct coupling.

1.3 Non-uniqueness of the boundary integral equations in acoustics

BEM in acoustics is based on use of boundary integral equations (BIE) which are known to result in non-unique solutions at certain characteristic frequencies (or wavenumbers) for an unbounded domain problem [36]. BEM either used on its own or in a coupled FEM-BEM algorithm for solving acoustic scattering problems, will result in a non-unique solution at the characteristic wavenumbers. While it is possible to predict these characteristic wavenumbers for simple shaped scatterers (sphere, cylinder), for practical problems might involve wave scattering from arbitrary shaped obstacles, for which these wavenumbers cannot be known in advance. Additionally, the characteristic wavenumbers become densely packed for increasing frequencies. Several methods

are available to alleviate the problem of non-uniqueness each with its own advantages and disadvantages.

1.4 Objective and organisation of the thesis

With this background in mind, a question such as the following can be phrased. Can we devise an algorithm to solve the wave scattering problem efficiently such that

1. FEM can be used for modelling the heterogeneous domain,
2. BEM can be used to model the homogeneous unbounded domain,
3. The algorithm provides a unique solution at all wavenumbers no matter what the shape of the scatterer, and,
4. the requirement on τ can somehow be reduced.

Whereas, the requirements mentioned in 1, 2 and 3 above can be met with the use of a coupled FEM-BEM approach along with some arrangement for BEM to handle the non-uniqueness problem, the reduction in the parameter τ can be achieved using the 'Partition of Unity' (PU) concept. The PU method was introduced by Melenk and Babuška [124, 125]. The idea used was to inject the knowledge of the problem under consideration into the FE approximation space, namely the particular solution of the partial differential equation governing the physics. For example time harmonic wave problems are governed by the Helmholtz equation and plane waves or Bessel functions, which are the particular solutions of the Helmholtz equation, can be effectively used as the 'enrichment' along with the classical polynomial shape functions. This was shown in many works to be effective in reducing the τ requirement besides alleviating the problem of pollution error; see [25, 48, 54, 81, 142, 156]. The objective of the thesis therefore can be stated as

> 'to develop an algorithm for coupling PU based FEM and BEM for solving wave scattering in heterogeneous media while effectively handling the problem of non-uniqueness'

The remainder of this thesis is arranged as follows. Chapter 2 gives background theory of acoustic wave scattering and a discussion on Sommerfeld's radiation condition. Chapter 3 mainly reviews the weak formulation required for FEM and the boundary integral equation for acoustic wave scattering problems but also provides a brief discussion on other numerical methods in

use for wave problems. Some of the NRBCs used for FEM in this thesis are also introduced. Chapter 4 discusses the concept of element based discretization along with the idea of 'Partition of Unity'*. The discretization of the weak form and the BIE using the PU concept are discussed. Chapter 5 compares the Partition of Unity BEM implementations of Combined Helmholtz Integral Equation Formulation (CHIEF) and Burton-Miller approaches which are used to treat the non-uniqueness problem of the integral equations. Chapter 6 first introduces the idea of mixed basis and then provides results for PUFEM for heterogeneous wave problems. Next in Chapter 7, the method described in Chapter 5, namely PUBEM is coupled with the PUFEM method described in Chapter 6. Finally Chapter 8 gives conclusions and directions for future work. In general, the main contribution of this thesis is in Chapters 5 to 7 where the objectives discussed above will be incorporated.

*'Partition of unity' and 'plane wave basis' are often used synonymously.

Chapter 2

Acoustic scattering: background theory and numerical methods

This chapter gives the background theory for the Helmholtz equation followed by various numerical methods presently in use in the acoustics community for its solution. The basic theory of acoustic wave propagation and derivation of the wave equation can be found in many acoustics textbooks [133], [94]. §2.1 gives the PDE governing time harmonic propagation of acoustic waves, namely the Helmholtz equation.

2.1 The Helmholtz equation

Consider a linear acoustic problem in a domain in $\mathbb{R}^d$ denoted by Ω_∞. The wave equation in Ω_∞ is then given as [94]

$$\rho(\mathbf{x})\nabla\cdot\left(\frac{1}{\rho(\mathbf{x})}\nabla\hat{p}(\mathbf{x},t)\right)+\frac{1}{c^2(\mathbf{x})}\frac{\partial^2\hat{p}(\mathbf{x},t)}{\partial t^2}=0 \tag{2.1}$$

where $\hat{p}$ is the acoustic pressure, c is the thermodynamic speed of sound, t is the time, ρ is the mass density of the considered medium, ∇ is the gradient operator and $\mathbf{x}$ is a considered point in the domain Ω_∞. The sound speed c can be given by the relation,

$$c=\frac{\mathfrak{B}}{\rho} \tag{2.2}$$

where, $\mathfrak{B}$ is the adiabatic bulk modulus of the medium. Some basic assumptions in deriving the wave equation (2.1) are enumerated to follow.

1. The medium Ω_∞ is inviscid thus the phenomenon of wave propagation will be lossless.

2. The amplitude of the acoustic wave under consideration will be assumed to be relatively small and therefore the change in the density of the medium is small.

The classical choice of the time dependence in acoustics is $e^{-i\omega t}$ where ω is the circular frequency of the propagating wave and $i = \sqrt{-1}$*. The acoustic pressure $\hat{p}(\mathbf{x}, t)$ can therefore be expressed as,

$$\hat{p}(\mathbf{x}, t) = p(\mathbf{x})e^{-i\omega t} \tag{2.3}$$

where $p(\mathbf{x})$ is the amplitude of the complex pressure. Many practical applications involve modelling the response of a physical system due to periodic forces and more often than not these forces are time harmonic in nature. The circular frequencies of such forces can be different and so interpreted as harmonic components. The acoustic response of the system therefore can be considered as a linear combination of these harmonic components and usually only a finite number of such harmonic components are important. For example the sound power radiated from an engine cover (such as oil pan, cam cover) shows peaks at certain frequencies which turn out to be the natural vibration modes of the covers [77], see Figure 2.1. It is therefore clear

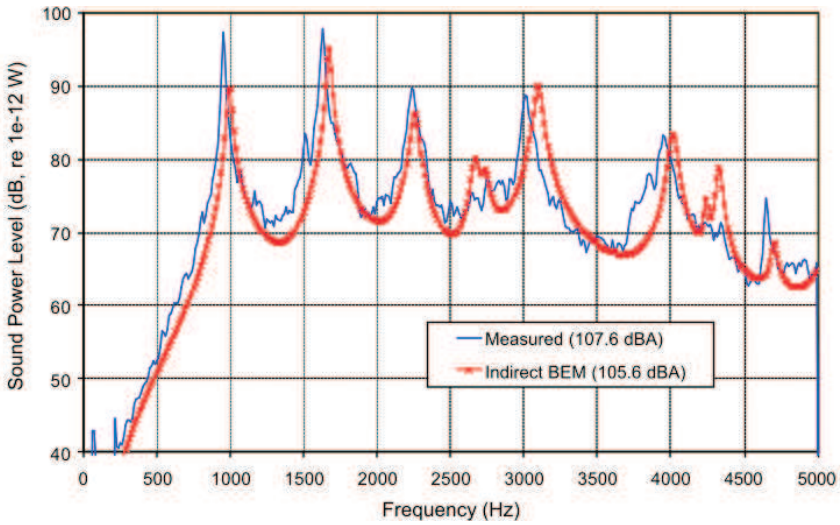

Figure 2.1: Sound power radiation from engine cover (ref. Herrin *et el*[77])

that for practical purposes where the response of the physical system only for certain harmonics is required, expressing the pressure in a form given by (2.3) is more convenient. The physical quantity of interest then becomes the spatial part, i.e., $p(\mathbf{x})$ of the dynamic quantity $\hat{p}(\mathbf{x}, t)$ for

*It is clear that since the time factor is discarded, for a time dependence of the form $e^{-i\omega t}$ one recovers a traveling wave with positive exponent i.e., $e^{ik\mathbf{r}}$, $\mathbf{r}$ being the position vector.

a given frequency ω. If one is interested in building a dynamic pressure field, the inverse Fourier transform can be used. In this thesis, however, only monofrequency time harmonic waves are considered. Thus for a progressive wave with circular frequency ω, a reduced wave equation or the Helmholtz equation[†] can be obtain by using (2.3) in (2.1), i.e.,

$$\rho(\mathbf{x})\nabla\cdot\left(\frac{1}{\rho(\mathbf{x})}\nabla p(\mathbf{x})\right)+k^2p(\mathbf{x})=0, \qquad \mathbf{x}\in\Omega_\infty\subset\mathbb{R}^d \tag{2.4}$$

where $k=\omega/c$ is the wavenumber. It may be noted that in view of (2.2), the wavenumber k is allowed to change in the domain Ω_∞.

2.2 Wave scattering: the boundary value problem and boundary conditions

A basic wave propagation problem, such as a plane wave propagating in an unbounded medium, can be solved relatively easily with either (2.1) or (2.4). However, as discussed in §1.1, in practice engineers are more interested in situations where waves encounter obstacles or the acoustic medium undergoes a change in the properties resulting in interesting phenomena such as multiple scattering and/or reflections at the interface between two media. In this section, the boundary value problem (BVP) for wave scattering is described for a time harmonic case (i.e. using the Helmholtz equation (2.4)).

The total acoustic pressure $p(\mathbf{x})$ due to a time harmonic wave with wavenumber k propagating in the infinite medium Ω_∞ satisfies (2.4). Consider such a wave, p^{inc}, scattering off an obstacle Ω_s bounded by a surface Γ_s in $\mathbb{R}^2$ and let n denote the normal vector to Γ_s which points away from the acoustic medium. Let p^{sct} denote the scattered acoustic pressure. Thus,

$$p(\mathbf{x})=p^{\text{inc}}(\mathbf{x})+p^{\text{sct}}(\mathbf{x}) \tag{2.5}$$

Though no surface can be considered as perfectly reflecting or perfectly absorbing, for practical purposes, it can be assumed that a given surface is either sound hard or sound soft. The obstacles considered in this thesis are assumed to be perfectly sound hard meaning there is total reflection of the waves from the obstacle surfaces. In other words, the normal component of fluid particle

[†]Hermann Ludwig Ferdinand von Helmholtz (1821-1894)-German physicist, carried out fundamental research in the fields of acoustics, optics and electromagnetism.

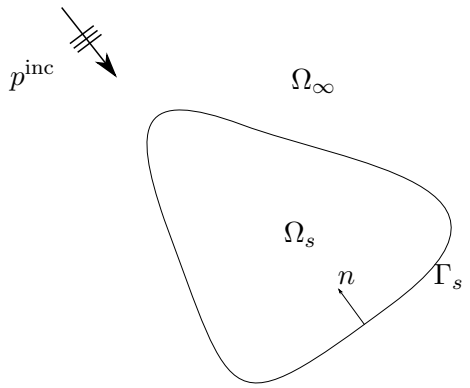

Figure 2.2: Definition of an acoustic scattering problem

velocity is zero on these surfaces, i.e.,

$$\frac{1}{i\rho\omega}\frac{\partial p(\mathbf{x})}{\partial n(\mathbf{x})} = 0 \qquad \mathbf{x} \in \Gamma_s \tag{2.6}$$

Apart from having to satisfy (2.4) and a boundary condition such as in (2.6), the total acoustic field also needs to satisfy the 'radiation condition' at infinity attributed to Sommerfeld [‡]. For a wave problem either in acoustics, electromagnetics or optics, Sommerfeld states '... *the sources must be sources, not sinks, of energy. The energy which is radiated from the sources must scatter to infinity; no energy may be radiated from infinity into the prescribed singularities of the field*' in his classical book on partial differential equations [168]. Established over a hundred years ago in 1912, Sommerfeld's radiation condition is essential in ensuring a unique solution to a wave scattering problem. Firstly, as per Sommerfeld's radiation condition, the scattered wave satisfies

$$p^{\text{sct}}(\mathbf{x}) = \mathcal{O}\left(\frac{1}{|\mathbf{x}|}\right), \quad |\mathbf{x}| \to \infty \tag{2.7}$$

uniformly in all directions and this condition is generally regarded as a *regularity condition* at infinity. Secondly, at infinity the field p^{sct} must be representable as a sum of (alternatively an integral of) only divergent waves. Thus there cannot be any wave of incoming type at infinity. This second condition can be established with the use of Green's theorem applied to (2.4); see §9.1 in [170]. For this purpose consider a region bounded internally by Γ_s and externally by Σ,

[‡]Arnold Johannes Wilhelm Sommerfeld (1868-1951)- German theoretical physicist who pioneered developments in atomic and quantum physics.

then, Green's theorem for (2.4) for a point $\mathbf{x}$ that lies outside Γ_s but interior to Σ gives

$$p^{\text{sct}}(\mathbf{x}) = \int_{\Gamma_s} \left(\frac{\partial p^{\text{sct}}(\mathbf{x})}{\partial n(\mathbf{x})} G - p^{\text{sct}}(\mathbf{x}) \frac{\partial G}{\partial n} \right) d\Gamma_s + \int_{\Sigma} \left(\frac{\partial p^{\text{sct}}(\mathbf{x})}{\partial n(\mathbf{x})} G - p^{\text{sct}}(\mathbf{x}) \frac{\partial G}{\partial n} \right) d\Sigma \tag{2.8}$$

where G is the Green's function for the Helmholtz equation (2.4). To clarify matters, let us consider a 3D case as the Green's function is simpler and therefore differentiation of G in (2.8) is relatively easy. The Green's function G in 3D is given as

$$G = \frac{e^{ikR}}{4\pi R} \tag{2.9}$$

where R is the distance of point $\mathbf{x}$ from Σ. Using (2.9) in (2.8) and simplifying, we obtain

$$\begin{aligned} p^{\text{sct}}(\mathbf{x}) = \frac{1}{4\pi} \int_{\Gamma_s} \frac{e^{ikR}}{R} \frac{\partial p^{\text{sct}}(\mathbf{x})}{\partial n(\mathbf{x})} d\Gamma_s - \frac{1}{4\pi} \int_{\Gamma_s} \frac{\partial}{\partial n} \left[\frac{e^{ikR}}{4\pi R} \right] p^{\text{sct}}(\mathbf{x}) d\Gamma_s + \\ + \frac{1}{4\pi} \int_{\Sigma} p^{\text{sct}}(\mathbf{x}) \frac{e^{ikR}}{R^2} d\Sigma - \frac{1}{4\pi} \int_{\Sigma} R \left(\frac{\partial p^{\text{sct}}(\mathbf{x})}{\partial n(\mathbf{x})} - ikp^{\text{sct}}(\mathbf{x}) \right) \frac{e^{ikR}}{R^2} d\Sigma \end{aligned} \tag{2.10}$$

The first two integrals in (2.10) represent diverging or outgoing waves from the source. The third integral in (2.10) vanishes on account of the condition in (2.7), and the last integral in (2.7) represents the incoming waves from the points on surface Σ and must be carefully accounted for. Unless a condition on the last integral in (2.10) is specified, the solution interior to the surface Σ will also contain incoming waves which is an unphysical situation as we know for a scattering problem with no sources at infinity the waves must only be outgoing. Therefore, to ensure a unique solution, we must have,

$$\lim_{r \to \infty} r \left(\frac{\partial p^{\text{sct}}(\mathbf{x})}{\partial r} - ikp^{\text{sct}}(\mathbf{x}) \right) = 0 \tag{2.11}$$

Equation (2.11) is known as Sommerfeld's *radiation condition* and the limit in (2.11) must be approached uniformly and through all angles. As mentioned earlier, we consider only 2D problems in this thesis for which the term r in (2.11) needs to be replaced by $r^{1/2}$. Thus the general form of the radiation condition can be given by

$$\lim_{r \to \infty} r^{\frac{d-1}{2}} \left(\frac{\partial}{\partial r} - ik \right) p^{\text{sct}}(\mathbf{x}) = 0 \tag{2.12}$$

where d is the dimension of the space. The BVP in 2D ($d = 2$) therefore can be summarized as: Find the total acoustic pressure $p(\mathbf{x})$ such that,

$$\rho(\mathbf{x})\nabla \cdot \left(\frac{1}{\rho(\mathbf{x})}\nabla p(\mathbf{x})\right) + k^2 p(\mathbf{x}) = 0, \qquad \mathbf{x} \in \Omega_\infty \subset \mathbb{R}^2, \tag{2.13a}$$

$$\frac{1}{i\rho\omega}\frac{\partial p(\mathbf{x})}{\partial n(\mathbf{x})} = 0 \qquad \mathbf{x} \in \Gamma_s, \tag{2.13b}$$

$$\lim_{r\to\infty} p^{\text{sct}}(\mathbf{x}) = 0, \tag{2.13c}$$

$$\lim_{r\to\infty} r^{\frac{1}{2}}\left(\frac{\partial}{\partial r} - ik\right) p^{\text{sct}}(\mathbf{x}) = 0. \tag{2.13d}$$

2.3 Numerical methods for time harmonic acoustics

Numerical modelling of wave scattering problems is indispensable unless the geometry under consideration is simple such as a sphere or a cylinder so that the analytical solutions can be constructed. In real life however such simple shapes are not always possible. Consider for example the noise radiation from an internal combustion engine where the numerical modelling either with FEM or BEM is essential. Another case is that of scattering of ultrasound in a heterogeneous medium such as human tissue where it is impossible to construct an analytical solution. In this section, an overview of some of the methods in use for numerical modelling of acoustic scattering for high frequency problems is presented. The methods briefly reviewed here are i) PUFEM, ii) PUBEM, iii) ultraweak variational formulation (UVWF) and iv) the discontinuous Galerkin method (DG). There are numerous other methods being used for modelling the wave problems such as ray tracing and statistical energy analysis.

2.3.1 Partition of Unity Finite Element Method (PUFEM)

The development of the FEM goes more than five decades back where it originated as a numerical tool for analysing civil engineering structures [35]. Since then, with the advent of technology in computer science, FEM like several other fields has undergone many developments. The basic essence of the FEM however can be described in two steps [78]:

1. Writing a variational statement of the problem under consideration; and
2. approximating the solution of the equations in the variational statement using the finite element basis.

As will become apparent later in the thesis (see §3.1), the variational form contains derivatives of first order as opposed to the original second order derivatives present in the PDE (strong form). This means the constraints on the solution variable of the PDE are less stringent or are 'weak' in the variational form. An exhaustive review of the FEM would be beyond the scope of this thesis but there are numerous textbooks on FEM covering a wide variety of engineering applications; see [42] (flow problems), [131] (electromagnetic waves), [190] (solid mechanics), [152] (heat problems). A brief review of FEM applied to wave problems along with the boundary conditions for unbounded problems is given by Bettess [16]. Thompson has given a review of FEM for time harmonic acoustic problems in [175]. Here we briefly review some contributions in the FEM/PUFEM specifically applied to wave problems. The FEM has been used extensively for acoustic-structure interaction for the past four to five decades and the majority of the studies were focussed on interior problems. Young and Crocker used FEM for the transmission loss analysis of a muffler [39]. Craggs used tetrahedral and cuboid finite elements for determining the mode shapes of the interior of a passenger car [38]. Gladwell studied vibration problems using adjoint pressure and displacement models [60]. There are many other studies conducted for interior problems; see [7, 92, 135, 172]. As discussed at the end of §1.1, the primary difficulty with the classical FEM (polynomial shape function based) remains the high resolution needed and the pollution error at high frequencies. Ihlenburg [83] gives the following equation for the relative error bound ($\tilde{e}_1$) for a finite element solution of an oscillatory problem such as the Helmholtz equation,

$$\tilde{e}_1 \leq C_1 hk + C_2 k^3 h^2, \qquad hk < 1, \tag{2.14}$$

where h is the element size, k is the wavenumber and C_1 and C_2 are constants that are independent of the wavelength. It can be noted that though the product kh is kept constant, the second term k^3h^2 in (2.14) will result in an error that will grow with the wavenumber k. In order to control the error therefore, one would need to keep refining the mesh (or add more dof in the system) such that the product k^3h^2 is kept constant as the wavenumber k increases. This clearly is a highly computationally intensive task for high wavenumbers. Ihlenburg gives a second error bound if the order (p) of the polynomial is varied along with the size of the element (h).

$$\tilde{e}_1 \leq C_1 \left(\frac{hk}{2p}\right)^p + C_2 k \left(\frac{hk}{2p}\right)^{2p}, \qquad hk < 1, \tag{2.15}$$

The first term in (2.15) gives the approximation error whereas the second term gives the pollution error in the solution. Clearly, the errors can be significantly reduced by increasing the order of the approximation p instead of simply refining the FE mesh (i.e. reducing h). An alternative to the h and p refinement is to use a modified FE basis such as in PUFEM. The concept used in PUFEM is to use the plane waves along with the classical polynomial basis functions. Thus the basis function at a node on a finite element will be of the form $N_j e^{ik\mathbf{d}\cdot\mathbf{x}}$, where $\mathbf{d}$ is the unit vector, $\mathbf{x}$ is the spatial location of the node and N_j is the polynomial shape function at node j[§]. It has been shown that if many plane waves are used at each node, the requirement on τ is significantly reduced. For example, as demonstrated through several papers on PUFEM for wave scattering problems the value of the parameter τ needed for high frequency problems is close to 2 as against 10 as needed by classical FEM; see [17, 106–108, 129, 142]. As discussed earlier (see §1.4), though the concept of the Generalised FEM such as PUFEM was originally introduced by Melenk and Babuška [124, 125], the full potential of this method was greatly exploited by Bettess and coworkers to solve short wave diffraction problems [100–102, 104, 105]. The major problems with PUFEM however are:

1. ill-conditioning of the linear system of equations with increasing wavenumber, and,

2. the requirement to evaluate highly oscillatory integrals.

Mohamed [128] studied PUFEM for wave diffraction problems for homogeneous media using various convergence studies viz. h, p and q [¶]. Mohamed reports a linear rise in the condition number of the system matrix with the addition of plane waves (q-convergence) and/or mesh refinement (h-convergence). It is observed through the results presented in [128] that errors from PUFEM do not improve despite either the h or q refinement because of severely ill-conditioned systems (condition no. $\approx 10^{19}$). The second problem is that of highly oscillatory integrals. To this effect, numerous authors have devised special quadrature schemes that efficiently evaluate the oscillatory integrals. For example, Sugimoto *et al* [171] use a semi-analytical approach to integrate the oscillatory functions in a straight edged quadrilateral finite element. Ortiz and Sanchez [138] use triangular elements and perform a coordinate transformation (rotation in a local coordinate system) such that the oscillatory kernel varies only in a single direction.

[§]The concept of shape functions will be discussed in Chapter 4.

[¶]q convergence is achieved by successively adding plane waves at a finite element node while keeping the mesh resolution h and order of the polynomial p constant.

Significant savings in the number of operations were demonstrated. Both the issues of ill-conditioning and oscillatory integrals will be further discussed in the thesis, however, at this point, a general conclusion from the previous work can be mentioned. PUFEM can result in a reduction in the parameter of τ by at least a quarter, thus the gain in solving a 2D problem is $4^2 = 16$ over the classical FEM.

2.3.2 Partition of Unity Boundary Element Method (PUBEM)

The advantage of using BEM over FEM is well known which is that of working in one dimension less than that for FEM. Despite this significant advantage, BEM does not enjoy the popularity that FEM has primarily because of the following reasons:

1. dense and unsymmetric linear system,

2. singular integrals, and,

3. inability to model heterogeneous material.

FEM on the other hand results in sparse symmetric linear systems for which efficient solvers are widely available. Harari and Hughes [73] compare FEM and BEM for Helmholtz problems and give a clear cut verdict in favour of FEM. Obviously, when solving 3D problems, the mesh generation is very easy for BEM and therefore for sound radiation or scattering problems, BEM appears to be a natural choice. Recent developments in BEM such as fast multipole [32, 40, 136] or hierarchical matrix methods [21] indicate fast solutions can be retrieved using efficient algorithms. In general, since the Sommerfeld's radiation condition is automatically satisfied by the Green's functions, BEM has been very popular in numerically solving the wave problems for unbounded homogeneous media, see [6, 11, 26, 30, 34, 109, 111, 185]. After its use in FEM, the concept of plane wave basis was further extended to BEM (PUBEM) by Perrey-Debain and co-workers; see [144, 146, 147]. It can be observed from the work of Perrey Debain and co-workers on PUBEM that close to 4 orders of magnitude improvement can be achieved over classical BEM despite using 4 times less degrees of freedom per wavelength. Recently Peake *et al* [140] have used the Non-uniform rational B-spline (NURBS) basis functions to extend the capability of plane wave based BEM (XIBEM). These authors report a significant reduction in the degrees of freedom required for a given problem. For an accuracy of 1%, three-times fewer degrees of freedom are required for XIBEM simulations than for conventional BEM. In summary, similar

to PUFEM, PUBEM also outperforms the classical BEM in the τ requirement. This, however, comes at having to solve a dense unsymmetric and an ill-conditioned linear system. Apart from having to deal with singular integrals, some of the problems encountered when solving exterior acoustic scattering problems with PUBEM are

1. ill-conditioned system of equations,
2. highly oscillatory integrals,
3. non-uniqueness of integral equations, and,
4. exact geometry requirement.

The last aspect of exact geometry is important because when solving short wavelength problems, any inaccuracies in representing the actual geometry of the scatterer can accentuate the errors in the solution. This is especially true for PUBEM because the condition numbers encountered are significantly high (greater than 10^{10}). At such high condition numbers, it becomes imperative to compute the PUBEM integrals with at least double precision. The accurate representation of the geometry is therefore important for PUBEM computations. There are few more reasons for the requirement of exact geometry and these will be discussed in Chapter 5 as well (see §5.2).

The problem of unsymmetric matrices mentioned earlier can be alleviated if Galerkin BEM is used [11, 26, 26, 27]. Though mathematically more robust, the method involves time consuming double integrals. It is important to note here that both PUFEM and the PUBEM [‖] studied in this thesis require the number of degrees of freedom to grow as the product ka increases, where a is the significant dimension of the scatterer. Whereas for the PUFEM work mentioned earlier, the dof needed for a fixed accuracy grows as $(ka)^N$, PUBEM requires the dof to grow $(ka)^{N-1}$, N being the dimension of the problem. Chandler-Wilde *et al* [28] have shown that for high wavenumbers this requirement for plane wave enriched Galerkin BEM grows only logarithmically. It should however be noted that, both PUBEM and Galerkin BEM suffer from the problem of non-uniqueness. To the author's knowledge, no comparison between these two methods has been published to date. However, collocation based BEM appears to be more popular among engineers as it is easy to implement and integration time required is less.

[‖] i.e. plane wave based direct collocation BEM

2.4 Methods with discontinuous basis functions

Often we encounter situations where the medium is not homogeneous. It is convenient to assume piecewise constant properties within each element and then use discontinuous basis functions for each individual finite element. These discontinuous basis functions then need to be tied in some manner. There are primarily three numerical methods which are classified according to the way the continuity on the basis function across each element is enforced viz. i) Ultra Weak Variational Formulation (UVWF) ii) discontinuous enrichment method (DEM) and iii) the method of least squares.

2.4.1 Ultra weak variational formulation (UWVF)

In UWVF, as the name suggests, the continuity is enforced on the discontinuous basis functions weakly through the variational formulation. Cessenat and Despres presented this method by solving the Helmholtz equation in 2D and showed that the order of convergence for UVWF is lower bounded by a linear function of the number of basis functions per element [25]. The method is efficient as the unknown variable is defined on the interface between elements and a plane wave basis is used for the approximation. Naturally after the matrix equations are solved and if the solution inside the element is required, the method requires to solve additional equations to compute the solution within a finite element. In order to be able to get the solution at all the points in the domain, all the equations on the interface of elements will have to be solved thus increasing the complexity of the method. Although the method was derived by Cessenat in his PhD thesis [24] for Helmholtz and Maxwell equations, it was later extended to solve problems in linear elasticity [80] and fluid-structure interaction [79]. Compared to PUFEM, UWVF can result in a better conditioned linear system by changing the number of enrichment functions on each element [81].

2.4.2 Discontinuous enrichment method (DEM)

The DEM is similar to UWVF as it uses discontinuous basis for each element but the continuity is enforced via use of Lagrange multipliers [48–50, 121, 174]. It may be noted that, Farhat *et al*, after their first paper on DEM [48], dropped the polynomial shape functions, thus retaining only the plane wave as a basis. This approach was termed as 'discontinuous Galerkin' (DG) method; see [49]. Gabard used the DG method to solve the Helmholtz equation with a focus on studying the locking phenomenon [52]. Farhat *et al* show the convergence of DG for mid-frequency

Helmholtz problem using higher order (Q_2, Q_4) elements. Amara *et al* show a convergence analysis for low order elements for the DG method for the Helmholtz problems. See [121] for an application of DG to wave propagation in multi-fluid media, [189] for elastic wave propagation problems, [122] for vibration problems.

2.4.3 Least square method (LSM)

In the LSM approach, a functional containing penalty terms involving the jumps across the element interfaces is minimized. The method can be attributed to Jirousek and Wrblewski [87] who showed that the convergence can be achieved without refining or increasing the polynomial order in the mesh but by simply adding more enrichment functions. The least square method, like any other wave based method (DG, UVWF) is a Trefftz based method where the differential equation is needed to satisfy inside the element and the continuity conditions can be enforced later on the inter element boundaries. Stojek [169] used Bessel and Hankel functions as the T-complete set to solve Helmholtz problem using LSM. It was shown that special techniques such as infinite elements are not needed if a Bessel basis is used. The concept of LSM was further studied by Monk and Wang [132] for the Helmholtz equation where they compared the performance of the plane wave and the Bessel functions basis. The authors observed that the plane waves are preferable as the oscillatory integrals can be evaluated rapidly. Gamallo and Astley compared UWVF and LSM for wave problems in a soft-duct and in an L-shaped domain with a sharp corner[53]. They conclude UWVF to be superior to LSM as the former provides a better accuracy for a given number of degrees of freedom and with a low condition number. The ill-conditioning of the wave based methods such as DG or LSM has been widely reported. Gamallo and Astley also report the problem with conditioning in one of their results where they could not achieve the convergence by simply adding more enrichment functions.

Chapter 3

Weak formulation and the Boundary Integral Equation

The weak form needed for the FEM and the boundary integral equation for acoustics are the concern of this chapter. Although the weak form for FEM when solving wave problems is well known, it is discussed here to underline some differences when solving a heterogeneous wave problem. Additionally, some of the well known NRBCs will also be introduced in this chapter.

3.1 Weak form for FEM

Recall the Helmholtz equation in Chapter 2 (2.4) which is reproduced here for convenience.

$$\rho(\mathbf{x})\nabla\cdot\left(\frac{1}{\rho(\mathbf{x})}\nabla p(\mathbf{x})\right)+k^2p(\mathbf{x})=0, \qquad \mathbf{x}\in\Omega_\infty\subset\mathbb{R}^d \tag{3.1}$$

As is well known, the PDE such as in (3.1) is a *strong form* of the governing equation for waves, meaning, (3.1) requires a strong continuity of the variable p. Thus any solution that satisfies (3.1) has to be differentiable up to and including the order of the PDE in (3.1) (i.e. they have to be second order differentiable). A *weak form* on the other hand requires the variable p to be weakly continuous. Clearly for complex geometries and where an exact solution cannot be found, use of the weak form is justified as we hope a function that satisfies the weak form gives us results with acceptable engineering accuracy. The finite element formulations based on the weak form are known to result in a well-behaved system of equations apart from being able to handle complex boundary conditions and geometries [151, 190]. The weak form for a given PDE

can be obtained either by using i) energy principles ii) or by the weighted residual method. We will follow the method of weighted residuals in this thesis.

Before we proceed with the weak formulation for the BVP defined in (2.13), we need to redefine the infinite domain Ω_∞ for the following reason. Recall that the 2D domain of interest is unbounded in (3.1) (also see Figure 2.2). In order to be able to model the problem on a finite computer, we need to truncate the domain by introducing an artificial boundary Γ_r (see Figure 3.1). Of course this artificial boundary needs to have certain boundary condition for the BVP in (2.13) to be meaningful and these boundary conditions will be discussed subsequently.

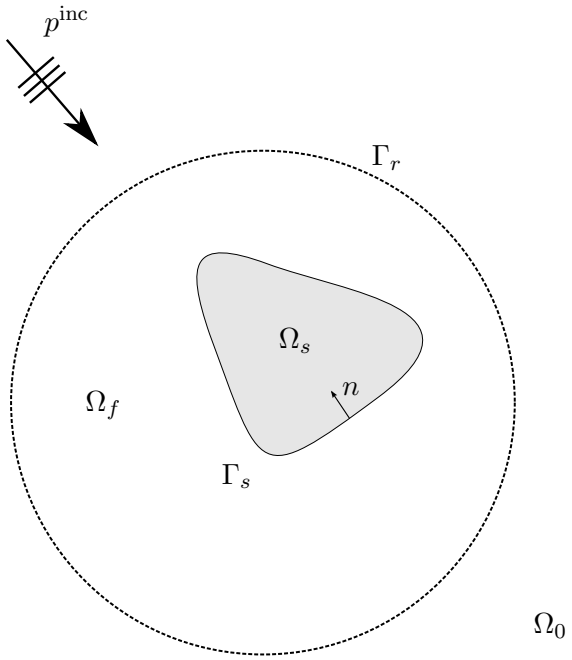

Figure 3.1: Definition of an acoustic scattering problem with artificial boundary Γ_r.

It can be observed that $\Gamma_r = \Omega_0 \cap \Omega_f$ where Ω_0 is the homogeneous exterior medium and Ω_f is the computational domain. Let v be a weighting function and multiplying (3.1) with v then integrating gives

$$\int_{\Omega_f} v \left(\nabla \cdot \left(\frac{1}{\rho(\mathbf{x})} \nabla p(\mathbf{x}) \right) + \frac{1}{\rho(\mathbf{x})} k^2 p(\mathbf{x}) \right) d\Omega = 0 \tag{3.2}$$

Using Green's theorem for (3.2) gives,

$$\int_{\Omega_f} \frac{1}{\rho(\mathbf{x})} \left(\nabla p \cdot \nabla v - k^2 v p \right) d\Omega - \int_{\Gamma_r} v \frac{1}{\rho(\mathbf{x})} \frac{\partial p}{\partial n} d\Gamma_r = - \int_{\Gamma_s} v \frac{1}{\rho(\mathbf{x})} \frac{\partial p}{\partial n} d\Gamma_s, \tag{3.3}$$

It should be noted here that any form of heterogeneity that may arise in the computational domain Ω_f is purely because of the change in the density ($\rho = \rho(\mathbf{x})$) in the present case.

Secondly, the weak form in (3.3) is in terms of the total acoustic pressure. It is not uncommon to use the scattered part p^{sct} of the field to write the weak form. The reason for using the total acoustic field p as the variable in the weak form is the following. Consider a case where the computational domain Ω_f contains heterogeneities which might exhibit different wavenumbers and assume that the weak form is in terms of scattered pressure, i.e.,

$$\int_{\Omega_f} \frac{1}{\rho(\mathbf{x})} \left(\nabla p^{\text{sct}} \cdot \nabla v - k^2 v p^{\text{sct}} \right) d\Omega - \int_{\Gamma_r} v \frac{1}{\rho(\mathbf{x})} \frac{\partial p^{\text{sct}}}{\partial n} d\Gamma_r = - \int_{\Gamma_s} v \frac{1}{\rho(\mathbf{x})} \frac{\partial p^{\text{sct}}}{\partial n} d\Gamma_s, \tag{3.4}$$

While, we could make some approximation for p^{sct} or its normal derivative $\frac{\partial p^{\text{sct}}}{\partial n}$ on the exterior artificial boundary Γ_r, we cannot make such an approximation about $\frac{\partial p^{\text{sct}}}{\partial n}$ on Γ_s. Consider the case of the sound hard scatterer where it is known that the normal particle velocity v_n (see (2.13)) is zero on Γ_s and that v_n is a function of total acoustic pressure p and not the scattered pressure p^{sct}. Therefore for such a case, the weak form must be written in terms of total acoustic pressure. In another situation, where two different media are present, compatibility conditions need to be used. One of the conditions is that the total acoustic pressure must be continuous across the interface which is another reason why the weak form used in this thesis is in terms of total acoustic pressure.

3.2 Non-reflecting boundary conditions

It is known that using a boundary condition on Γ_r in a naive or oversimplified manner can result in large spurious reflections. Givoli in his review paper [55] describes what exactly these spurious reflections are. He solved the Helmholtz equation with a Sommerfeld-like boundary condition on Γ_r and demonstrated that results are seriously polluted because of the reflections from the boundary. However, for this particular example, no error analysis was provided. As described earlier we need to have a boundary condition on the boundary Γ_r such that the boundary appears truly transparent to the outgoing waves. Deriving an accurate non-reflecting boundary condition, the numerical analysis of the associated FEM and its use in various wave problem situations (heterogeneous, layered, multiple scattering), is a continuing field of research. In this section, we will briefly review, some important contributions made towards the development of effective NRBCs followed by introducing some NRBCs which are popular among engineers for solving wave problems with FEM. The boundary conditions reviewed here are those used in time-harmonic acoustic problems. Of course, NRBCs do exist for time-dependent wave equation

with non-constant coefficients but to review all the NRBCs for wave problems in general will be beyond the scope of this thesis.

Based on the way p^{sct} and $\frac{\partial p^{\text{sct}}}{\partial n}$ are related, the NRBCs can be broadly classified into two main categories i) local and ii) non-local. A local NRBC relates p^{sct} and $\frac{\partial p^{\text{sct}}}{\partial n}$ using differentials whereas a non-local NRBC uses an integral equation for the same. In general non-local conditions are more accurate than local conditions but difficult to implement at the same time [55].

3.2.1 Non-local NRBCs

Non-local NRBCs are sometimes referred to as *exact* conditions on the truncation boundary Γ_r. Consider for instance the following equation,

$$\frac{\partial p^{\text{sct}}}{\partial n} = B p^{\text{sct}}, \qquad \text{on } \Gamma_r \tag{3.5}$$

For a non-local NRBC, the operator B is an integral operator. If it is possible to find an operator B such that the solution p^{sct} is an exact solution to the original unbounded problem of wave scattering, then we can say that the condition given in (3.5) is an exact NRBC. It is not always possible to find such an operator, for example when the truncation boundary is not a circle or a sphere. One of the early attempts in devising a non-local condition is by Gustafsson and Kreiss for a hyperbolic wave equation in waveguide geometry [66]. They derived a non-local condition using a Fourier expansion and implemented it for a finite difference scheme. Hagstrom and Keller studied a non-linear parabolic problem (a reaction-diffusion equation) and derived the non-local boundary condition [68]. Hagstrom and Keller [67] derived exact boundary conditions for to solve nonlinear elliptic and parabolic problems. Ting and Miksis use the Kirchhoff integral equation on the truncation boundary to replace an approximate NRBC but do not give a numerical analysis [176]. When solving time-dependent problems in unbounded domains with non-local NRBC, the requirement on the boundary condition to be able to *remember* the information from previous time steps is important; see for example [179]. Choosing an appropriate time integration scheme is therefore crucial when using non-local NRBC in time. Many authors therefore use local NRBC for time and non-local NRBC for space; see [57, 63]. Following the work of Ting and Miksis in [176], Givoli and Cohen extended their approach of using Kirchhoff integral for 3D acoustic and elastic waves. They investigated the temporal instabilities associated with the introduction of the Kirchhoff integral using a one dimensional problem. Givoli and Keller derived an exact

non-local condition for the Laplace equation (an elliptic problem) to analyse linear electrostatic problems [59]. They chose a sphere in 3D and a circle in 2D as their artificial boundary and coined the term Dirichlet-to-Neumann or the DtN map. Earlier, Givoli and Keller used the DtN condition for the reduced wave equation where they have also examined the convergence of FEM when the DtN map is used for unbounded problems [93]. Other closely related works (i.e. specifically for wave problems) are that of Fix and Marin [51], Marin [118], Goldstein [61]. Marin [118] solved acoustic scattering in 2D from infinite cylinders and used an integral operator as the non-local boundary condition. Fix and Marin presented a non-local outflow condition for waveguide problems in [51]. The concept involved decomposing the far field into a normal mode representation and using that in a variational Galerkin scheme. Goldstein [61] derived a nonreflecting boundary condition using the eigenvalues and eigenfunctions of the Laplacian for the waveguide problem. Bayliss *et al* used Goldstein's NRBC [61] for waveguides, employing a finite element scheme with a preconditioned conjugate gradient linear equation solver. There are several other PDEs for which non-local NRBCs have been developed; see a review in [74]. Following the review of the work on non-local NRBCs, certain key points must be mentioned when using a non-local NRBC:

1. The non-local NRBC needs an analytical shape for the truncation boundary Γ_r, i.e., a sphere in 3D or a circle in 2D,

2. computational effort is increased as the condition imposed is not local, and,

3. for a finite element framework, the bandwidth of the coefficient matrix is increased by the number of degrees of freedom on Γ_r.

Givoli and Keller [93] have shown that with the marginal increase in the number of degrees of freedom due to use of the DtN condition, the bandedness of the coefficient matrix for FEM can still be maintained provided the finite element nodes are carefully numbered. The nonlocal nature of the DtN condition, at the first sight, gives an impression that the sparseness of the matrix is affected, but, a renumbering method used by Givoli and Keller has been shown not to degrade the sparsity of coefficient matrix; see for more details on the implementation of DtN using a renumbering approach Chapter 8 of reference [56].

3.3 Local NRBCs

One of the most cited work on local NRBC is by Engquist and Majda (EM) [44] (also see [45]). They developed a series of local NRBCs using the theory of pseudodifferential operators for acoustics and linearized shallow water equations. Another well known local NRBC is due to Bayliss and Turkel [15] and Bayliss, Gunzburger and Turkel [14] commonly known as the BGT conditions. EM and BGT are the most widely used local NRBCs in the acoustics community. Both EM and BGT conditions were originally derived for the time-dependent wave equation but of course their time-harmonic counterparts can be obtained by following the same procedure as for the Helmholtz equation. A review of high order local NRBCs is given by Givoli in [58]. As the author notes, a high order NRBC, where the order stands for the level of accuracy, is not always a good choice. For example an arbitrarily high order NRBC in [15], although it can result in highly accurate solution, is in practicality very difficult to implement in a finite element code. Since we will be studying EM, BGT and Feng NRBCs in this thesis, it will be appropriate to review the background for these conditions in more detail.

3.3.1 Engquist-Majda NRBC

Consider the Helmholtz equation for scattered wave alone but for simplicity let us omit the reference to density terms, i.e.,

$$\frac{\partial^2 p^{\text{sct}}}{\partial^2 x} + \frac{\partial^2 p^{\text{sct}}}{\partial^2 y} + k^2 p^{\text{sct}} = 0 \tag{3.6}$$

If we were to look for a nontrivial solution of (3.6) of the form

$$p^{\text{sct}} = X(x)Y(y), \tag{3.7}$$

we should have,

$$X''/X + Y''/Y + k^2 = 0, \quad \text{or,} \tag{3.8a}$$

$$-X''/X = Y''/Y + k^2. \tag{3.8b}$$

Since, the left hand side of (3.8b) is a function of x alone and the right hand side is a function of y alone, both sides must be equal to a constant, say η. Thus,

$$X^{''} + \eta X = 0, \tag{3.9a}$$

$$Y^{''} + (k^2 - \eta)Y = 0. \tag{3.9b}$$

Of course, the equations in (3.9) need to hold simultaneously. Let $\eta = \xi_1^2$ and $k^2 - \eta = k^2 - \xi_1^2 = \xi_2^2$, thus the system in (3.9) becomes,

$$X^{''} + \xi_1^2 X = 0, \tag{3.10a}$$

$$Y^{''} + \xi_2^2 Y = 0. \tag{3.10b}$$

Clearly, the solution for (3.6) will be of the form

$$p^{\text{sct}}(x, y) = e^{\mathrm{i}(\xi_1 x + \xi_2 y)} \tag{3.11}$$

which is simply a plane wave *. It can be observed that,

$$\xi_1 = \pm\sqrt{k^2 - \xi_2^2} \tag{3.12}$$

and the equation (3.12) is known as the *dispersion relation* [94]. Consider a straight line segment of Γ_r and define $s = \xi_2/k$, we have,

$$\xi_1 = \pm k\sqrt{1 - s^2} \tag{3.13}$$

It may be noted that $\xi_1 = +k\sqrt{1 - s^2}$ indicates a plane wave travelling in the positive x direction whereas $\xi_1 = -k\sqrt{1 - s^2}$ indicates a plane wave travelling in the negative x direction. The non-reflecting condition then can be chosen such that Γ_r allows only outgoing waves, i.e., choosing the equation with the positive sign. Thus,

$$\frac{\partial p^{\text{sct}}}{\partial x} = B p^{\text{sct}}, \quad \text{on} \quad \Gamma_r \tag{3.14}$$

*If we were to take the wave equation as the starting point in place of the Helmholtz equation, we would have, $p(x, y, t) = e^{\mathrm{i}(-\omega t + \xi_1 x + \xi_2 y)}$.

Two important observations about (3.14) are:

1. because (3.13) involves an irrational function of s, B is a pseudodifferential operator therefore not easy for computer implementation, and,

2. when implementing (3.14), an inverse Fourier transform of B will be needed (for example to solve the wave equation) and this makes the operator B non-local both in space and time.

Engquist and Majda [44] used a rational approximation based on Padé's approximations of increasing accuracy for the irrational function in (3.13). Each higher order of approximation of increasing accuracy therefore corresponds to a local NRBC of the corresponding order. Originally Padé's approximations were derived for solving the one-way equations in ocean acoustics and were found to be useful in deriving local NRBCs. The boundary operator B for 1st and 2nd order due to Engquist and Majda are given by

$$Bp^{\text{sct}} = \left(\frac{\partial}{\partial r} - ik + \frac{1}{2R}\right) p^{\text{sct}} = 0, \cdots \text{(1st order)} \tag{3.15a}$$

$$Bp^{\text{sct}} = \left[\frac{\partial}{\partial r} - \left(ik - \frac{1}{2R}\right) p^{\text{sct}} - \left(\frac{i}{2kR^2} + \frac{1}{2k^2R^3}\right) \frac{\partial^2}{\partial \theta^2}\right] p^{\text{sct}} = 0 \cdots \text{(2nd order)} \tag{3.15b}$$

where R is the distance from origin. Importantly, the authors [44] have also shown that the boundary operators in (3.15) are most accurate if the incident wave is at normal incidence to the boundary Γ_r (rarely a case in multiple scattering problems). The reflection coefficient, which is a measure of the amount of energy reflected back from the a surface, can be given for EM operators as [44, 83],

$$|R_n| = \left|\frac{\cos\theta - 1}{\cos\theta + 1}\right|^{n+1}, \tag{3.16}$$

where R_n is the reflection coefficient, θ is the angle of incidence and n is the order of the boundary operator B in (3.14). Clearly, for higher order conditions we would expect negligible energy reflected in to the computational domain (see Figure 3.2), however this comes at the cost of having to implement higher order derivative terms in the finite element code. It may be noted that although the EM conditions are based on the Padé's approximation, there are many other possibilities for approximating the irrational function in (3.13). For example, Halpern and Trefethen use a different approximation for each different incident wave angle; see [69].

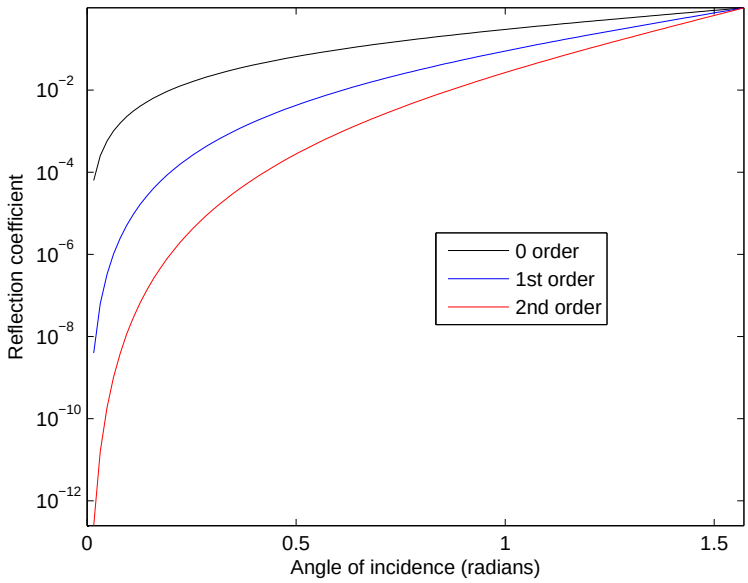

Figure 3.2: Reflection coefficient as a function of angle of incidence and order of NRBC, [44].

3.3.2 Bayliss-Gunzburger-Turkel (BGT) NRBC

The technique of Bayliss *et al* [14, 15] is based on expanding the solution in the far field in terms of an infinite series. These series expansions were originally derived by Atkinson [8] and Wilcox [182]. Consider, for example, the expansion for the solution of the Helmholtz equation in 2D,

$$p^{\text{sct}} = \sqrt{\frac{2}{\pi kr}} e^{\mathrm{i}(kr-\frac{\pi}{2})} \sum_{j=0}^{\infty} \frac{F_j(\theta)}{r^j} \tag{3.17}$$

where F_j denotes the eigenfunctions of the Laplacian and θ the polar angle. Bayliss *et al* [14] show that a differential operator of the following form exactly absorbs the first m modes in the expansion,

$$P_m = \prod_{j=1}^{m} \left[\frac{\partial}{\partial r} - \mathrm{i}k + \frac{2j-\frac{3}{2}}{r} \right] \tag{3.18}$$

Thus, P_m can be termed as an m^{th} order BGT damper. Bayliss *et al* [15] prove that the distance between the original solution and the one with BGT condition of m^{th} order is $\mathcal{O}(R^{-m-\frac{1}{2}})$, where R is the radius of the truncation boundary as before. Following the paper of Bayliss and co-workers, several authors have extended the use of the BGT condition to other problems. Pinsky and Abboud used the BGT condition for solving a time-dependent fluid-structure interaction (FSI) problem with FEM [148] . The authors [149] later extended this work for a viscoelastic

structure and attempted to resolve some of the difficulties associated with radial partial derivatives appearing in the BGT expressions. Manoj and Bhattacharyya [115] studied a 2nd and 3rd order BGT damper for transient FSI problem with an out-of-core solver for FEM. The first order BGT and EM operators are identical and so only the 2nd order BGT operator is given below,

$$(\mathrm{i}k - \frac{1}{R})\frac{\partial p^{\mathrm{sct}}}{\partial r} + \frac{1}{2}\left(2k^2 + \frac{3\mathrm{i}k}{R} - \frac{3}{4R^2} + \frac{1}{R^2}\frac{\partial^2}{\partial\theta^2}\right)p^{\mathrm{sct}} = 0. \tag{3.19}$$

3.3.3 Feng NRBC

Finally, we mention the last NRBC of interest in this thesis which is due to Feng [91]. Feng derived his NRBC by first finding a DtN-like condition on the boundary Γ_r and then localizing this equation on Γ_r. The localization is achieved by using an asymptotic approximation that is valid at a large distance from the scatterer. It may be noted that this approach is similar to that followed by Bayliss *et al* [14]. Again, the first order NRBC of Feng is identical to first order BGT and EM NRBCs and we list only the 2nd and 3rd order Feng NRBCs below.

$$-\frac{\partial p^{\mathrm{sct}}}{\partial r} - \left(-\mathrm{i}k + \frac{1}{2R} - \frac{\mathrm{i}}{8kR^2}\right)p^{\mathrm{sct}} + \frac{\mathrm{i}}{2kR^2}\frac{\partial^2 p^{\mathrm{sct}}}{\partial\theta^2} = 0, \quad \text{2nd order} \tag{3.20}$$

$$-\frac{\partial p^{\mathrm{sct}}}{\partial r} - \left(-\mathrm{i}k + \frac{1}{2R} - \frac{\mathrm{i}}{8kR^2} - \frac{1}{8k^2R^3}\right)p^{\mathrm{sct}} + \left(\frac{\mathrm{i}}{2kR^2} + \frac{1}{2k^2R^3}\right)\frac{\partial^2 p^{\mathrm{sct}}}{\partial\theta^2} = 0, \quad \text{3rd order} \tag{3.21}$$

3.4 Some observations about NRBCs

The non-local and local boundary conditions mentioned here have been compared by numerous authors for their accuracy for solving exterior acoustic problems. Shirron compared various NRBCs in his PhD thesis [160]. Shirron studied the scattering problem when a circular cylinder is insonified with only a certain incident mode. Of course, the scattered wave will have only that particular mode which needs to be absorbed by the NRBC on Γ_r. From the results in Shirron's thesis it can be observed that the BGT conditions of 2nd order are the most accurate. Shirron and Babuška [161] compared the performance of BGT, EM and Feng conditions with the infinite element method for exterior acoustic problems in 2D (scattering from a circular cylinder) and in 3D (scattering from a sphere). The authors demonstrate that the conjugated infinite element approach is superior to any of the NRBCs mentioned and for high wavenumbers the results from all the NRBCs are close to each other. Laghrouche *et al* [107] have performed a comparison of

these NRBCs on similar lines but in a plane wave enriched FEM scheme. From their results, it can be seen that with increasing wavenumbers, the difference between the errors from various NRBCs is diminished. In summary, based on the results in [83, 107, 160], it can be observed that:

1. For sufficiently large radius R of the truncation boundary Γ_r, BGT, EM and Feng's NRBCs are equivalent, †

2. As the wavenumber increases, the difference between the 1st and 2nd order BGT condition diminishes, and,

3. Most importantly, as observed by Ihlenburg in his benchmark book [83], simply increasing the order of the damping operator B does not improve the accuracy. In fact, for higher wavenumbers, the accuracy of the solution is bound to decrease as the wavenumber k is in the denominator.

3.5 Weak form for scattering problem

It may be noted that, we have studied only the local NRBCs in this thesis. Therefore, in this section, we will first include the local NRBC in the weak form and then obtain the discrete FE equations. It is important to note here that the NRBCs discussed in previous sections apply to an outgoing scattered wave. (3.14) is reproduced below for convenience,

$$\frac{\partial p^{\text{sct}}}{\partial r} = B p^{\text{sct}}, \quad \text{on} \quad \Gamma_r \tag{3.22}$$

Using (2.5) in (3.22),

$$\frac{\partial p}{\partial r} - \frac{\partial p^{\text{inc}}}{\partial r} = B\left(p - p^{\text{inc}}\right) \quad \text{on} \quad \Gamma_r. \tag{3.23}$$

Or,

$$\frac{\partial p}{\partial r} = B\left(p - p^{\text{inc}}\right) + \frac{\partial p^{\text{inc}}}{\partial r} \quad \text{on} \quad \Gamma_r. \tag{3.24}$$

As mentioned earlier, all of the obstacles considered here are sound hard, thus any term containing normal derivative of the total acoustic pressure on a surface ($\frac{\partial p}{\partial n}$) must vanish. Thus

†This observation will be tested in this thesis in the context of plane wave enriched FEM.

with the use of (3.24), (3.3) reduces to,

$$\int_{\Omega_f} \frac{1}{\rho(\mathbf{x})} \left(\nabla p \cdot \nabla v - k^2 vp\right) d\Omega - \int_{\Gamma_r} \frac{1}{\rho(\mathbf{x})} vBpd\Gamma = \int_{\Gamma_r} \frac{1}{\rho(\mathbf{x})} v \left(\frac{\partial p^{\text{inc}}}{\partial r} - Bp^{\text{inc}}\right) d\Gamma \qquad (3.25)$$

This is the final weak form for the scattering problem considered in this thesis and will be used for solving the wave scattering problems using either the polynomial FEM or PUFEM. It should be noted here that the weak form in (3.25):

1. has only total acoustic pressure p as the unknown, and,

2. the field on the radiation boundary Γ_r is approximate and governed by the operator B.

Of course, the weak form in (3.25) can be used for a homogeneous computational domain Ω_f, i.e. when $\rho = \rho(\mathbf{x}) = const.$ The FE discretization process for this weak form will be discussed in Chapter 4 (§4.3).

3.6 The boundary integral equation

The Boundary Integral Equation method (BIEM) or the Boundary Element Method (BEM) are used synonymously for the discrete form of the method based on boundary integral equations. In this thesis, we will adapt the latter name, the BEM.

As stated before, the BEM is suited for problems where the medium under consideration is homogeneous, isotropic and linear. This is not to say that BEM cannot be used for a heterogeneous medium problem. Consider for example the problem depicted in Figure 3.3. If the acoustic media viz. medium 1 and 2 are assumed themselves to be homogeneous, it is possible to use a pair of integral equations on the interface between the two media to solve for the scattering problem. This approach was used by Costabel and Stephan to solve a transmission problem [37] using Galerkin BEM. Kittappa and Kleinman used a coupled integral equations to solve a 3D transmission problem [96]. They used a Neumann series for approximating the solution on the interface and then used an iterative procedure to solve the coupled system. Kleinman and Martin have derived a single integral equation to solve the transmission problem [97]. The idea used by Kleinman and Martin is to combine the equations from direct and indirect BIE to obtain a single 'hybrid' equation for the transmission problem.

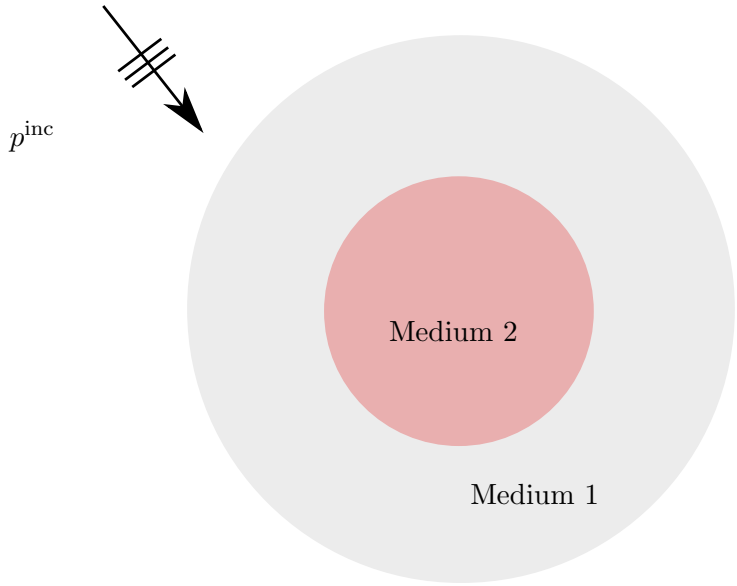

Figure 3.3: Heterogeneous wave scattering problem for BEM-BEM coupling

However, even the idea of coupled or single integral equation would work only if the Green's function for individual regions are known. For a problem with multiple or spatially dependent wavenumbers, it would be difficult to use the boundary integral equation approach. Interestingly, there have been some attempts to obtain the Green's function for such cases, but only very simple cases can be considered. See for experimental studies on 'retrieval' of the Green's function in ultrasonics [181], underwater acoustics [153] or in seismic waves [157] and for theoretical studies, see [116, 154, 158, 166, 180]. One must however keep in mind that the experimental techniques and the quality of the results obtained depends heavily on the complexity of the media involved. Many attempts, therefore, in deriving the Green's functions for heterogeneous media remain restricted to simple geometries or configurations. For example, Michalski and Mosig derive Green's functions to solve electromagnetic wave problem in a multilayerd medium [127]. Jensen and Freeze [85] obtain the Green's function recursively for an electromagnetic problem and use a domain decomposition approach. In a parallel work, Jensen [86] derived the Green's function for acoustic scattering by cylindrical and spherical inclusions similar to [85] and the computational complexity of this recursive algorithm is shown as $\mathcal{O}(N^2)$ in 2D and $\mathcal{O}(N^{7/3})$ in 3D. Presenting a complete and up-to-date account of the research focused on Green's functions and integral equation techniques is beyond the scope of this research, because, as mentioned earlier (§1.4), the motivation of this thesis is to use BEM for treating wave propagation in homogeneous unbounded domain.

3.7 Boundary integral equation (BIE) for exterior acoustics

The procedure for obtaining an integral equation from a given PDE is well established [34]. There are basically two ways to obtain an integral equation:

1. by the indirect integral equation method, or,

2. by the direct integral equation method.

The indirect method is older than the direct method and involves use of 'single' and 'double' layer potentials. The direct method, on the other hand, uses Green's theorem applied to the differential equation and is the method used in this thesis. Before we proceed to obtain the direct BIE for the Helmholtz equation, it is useful to describe the concept of Green's functions which are also known as 'fundamental solutions'. The Green's function for the Helmholtz equation (2.4) in 2D (assuming constant density ρ) is given as

$$G(\mathbf{x}, \mathbf{y}) = \frac{\mathrm{i}}{4} H_0^{(1)}(kr), \tag{3.26}$$

where $\mathbf{x}, \mathbf{y} \in \mathbb{R}^2$, $H_0^{(1)}(\cdot)$ is the Hankel function of order zero and of the first kind, k is the wavenumber of homogeneous medium and $r = |\mathbf{y} - \mathbf{x}|$. In general, the Hankel function of order n can be given as

$$H_n^{(1)}(kr) = J_n^{(1)}(kr) + \mathrm{i} Y_n^{(1)}(kr), \tag{3.27}$$

where $J_n^{(1)}(\cdot)$ and $Y_n^{(1)}(\cdot)$ are Bessel functions of order n and kind 1 and 2 respectively. At this point, we make a note that only the Bessel function of the second kind i.e., $Y_n^{(1)}(\cdot)$ is singular at $r = 0$ (see Figure 3.4) and this creates considerable difficulties in implementing the BIE that we will be using. It is easy to see that $G(\mathbf{x}, \mathbf{y})$ satisfies the Helmholtz equation (2.4) with an appropriate right hand side. More precisely, the Green's function satisfies the inhomogeneous Helmholtz equation where the right hand side is a point source term given by a Dirac Delta function, i.e.,

$$\nabla^2 G(\mathbf{x}, \mathbf{y}) + k^2 G(\mathbf{x}, \mathbf{y}) = -\delta(\mathbf{x}, \mathbf{y}) \tag{3.28}$$

where $\mathbf{x}$ is the source point and $\mathbf{y}$ is the field point. Green's function therefore can also be interpreted as the 'effect' experienced at point $\mathbf{y}$ due to a point source at $\mathbf{x}$.

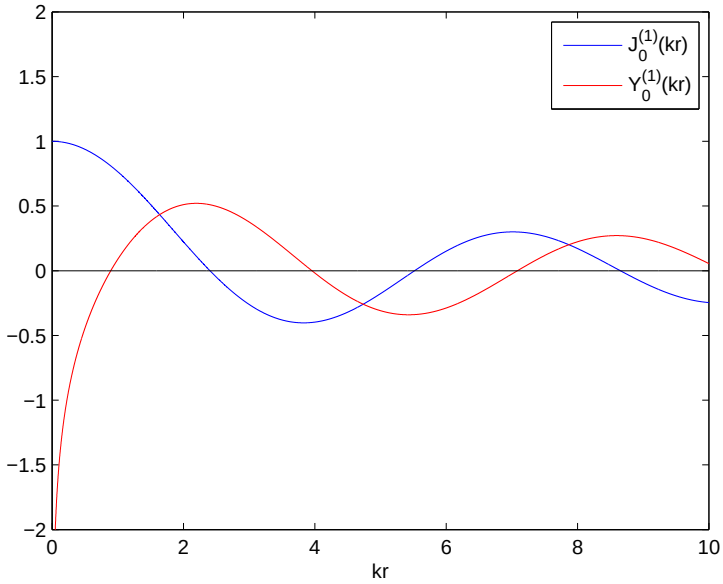

Figure 3.4: $J_0^{(1)}(kr)$ and $Y_0^{(1)}(kr)$.

The procedure for deriving the BIE for an exterior acoustic problem now follows. We reproduce Figure 3.1 for this purpose with some modifications.

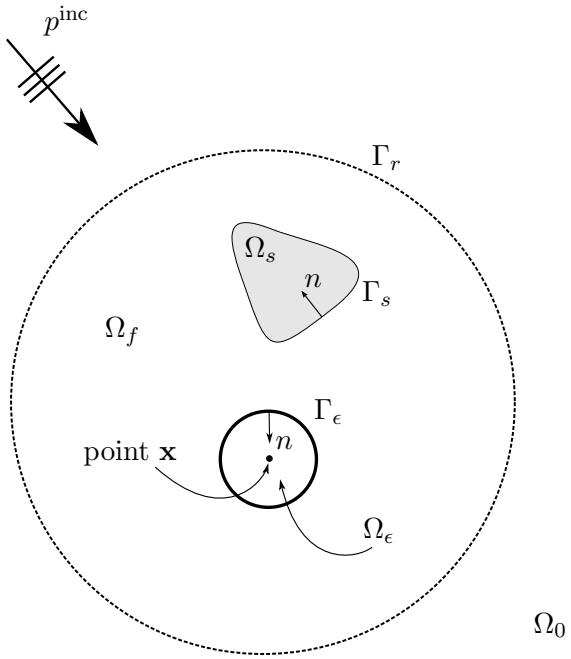

Figure 3.5: Exterior acoustic problem

The objective is to solve Helmholtz equation using BIE for a homogeneous medium. It is therefore convenient to rewrite (2.4) by eliminating the density term ρ, thus,

$$\nabla^2 p(\mathbf{x}) + k^2 p(\mathbf{x}) = 0, \qquad \mathbf{x} \in \Omega_f \subset \mathbb{R}^2 \tag{3.29}$$

Note that we have added a small circular area Ω_ϵ surrounding the singular point $\mathbf{x}$ bounded by Γ_ϵ. Let ϵ be the radius of circular boundary Γ_ϵ. We have also retained the boundary Γ_r that we used for the FEM. It will soon be clear that the integrals over the boundary Γ_r vanish due to the Sommerfeld radiation condition.

Green's second theorem is well known and can be written for the geometry shown in Figure 3.5 as,

$$\int_{\Gamma_s+\Gamma_\epsilon+\Gamma_r} \left(G\frac{\partial p}{\partial n} - p\frac{\partial G}{\partial n} \right) d\Gamma = \int_{\Omega_f-\Omega_\epsilon} \left(G\nabla^2 p - p\nabla^2 G \right) d\Omega \tag{3.30}$$

where G is the same two point Green's function defined in (3.26) but we have dropped $\mathbf{x}$ and $\mathbf{y}$ only for convenience. For the precise requirements on the functions p and G in order to satisfy (3.30), see discussion in [36]. Of course, one obvious requirement is that both p and G must be at least twice differentiable.

Now, since we have excluded the singular point $\mathbf{x}$ from the domain under consideration, i.e. $\Omega_f - \Omega_\epsilon$ (see Figure 3.5), we must have, from (3.29),

$$\nabla^2 p = -k^2 p \tag{3.31a}$$

$$\nabla^2 G = -k^2 G \tag{3.31b}$$

Thus,

$$G\nabla^2 p - p\nabla^2 G = G(-k^2 p) - p(-k^2 G) = -k^2 pG + k^2 pG = 0 \tag{3.32}$$

Therefore the integral on the right hand side in (3.30) vanishes. Let us split the boundary integral on the left hand side in (3.30) for convenience and also use (3.32), thus, (3.30) reduces to,

$$\begin{aligned} &\int_{\Gamma_s} \left(G\frac{\partial p}{\partial n} - p\frac{\partial G}{\partial n} \right) d\Gamma + \int_{\Gamma_\epsilon} \left(G\frac{\partial p}{\partial n} - p\frac{\partial G}{\partial n} \right) d\Gamma \\ &+ \int_{\Gamma_r} \left(G\frac{\partial p}{\partial n} - p\frac{\partial G}{\partial n} \right) d\Gamma = 0, \quad \mathbf{x} \subset \Omega_f \end{aligned} \tag{3.33}$$

We now analyse each of the integrals in (3.33) separately. Let us denote the second integral in (3.33) as I_2, thus,

$$\begin{aligned} I_2 &= \int_{\Gamma_\epsilon} \left(G\frac{\partial p}{\partial n} - p\frac{\partial G}{\partial n} \right) d\Gamma \\ &= \int_{\Gamma_\epsilon} G\frac{\partial p}{\partial n} d\Gamma - \int_{\Gamma_\epsilon} p\frac{\partial G}{\partial n} d\Gamma \end{aligned} \tag{3.34}$$

Consider the first integral in (3.34) and let us take the limit as $\epsilon \to 0$,

$$\lim_{\epsilon \to 0} \int_{\Gamma_\epsilon} G\frac{\partial p}{\partial n} d\Gamma \tag{3.35}$$

Note that G is a two point function where the source point is $\mathbf{x}$ and the integration point $\mathbf{y}$ is located on Γ_ϵ (see Figure 3.6). Thus, $|\mathbf{y} - \mathbf{x}| = \epsilon$, or,

$$G = \frac{i}{4} H_0^{(1)}(k\epsilon) = \frac{i}{4} \Big(J_0(k\epsilon) + \mathrm{i} Y_0(k\epsilon) \Big) \tag{3.36}$$

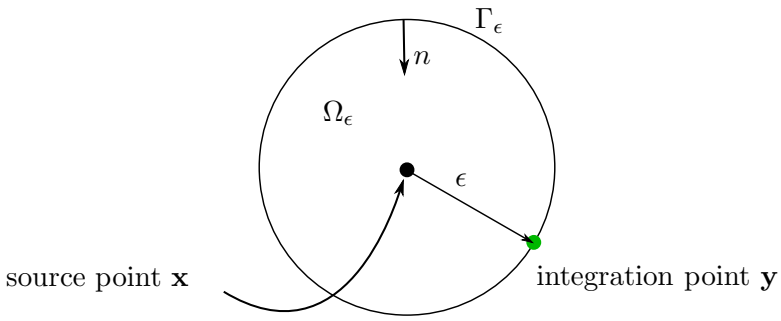

Figure 3.6: Excluded region for $\epsilon \to 0$

Also, the asymptotic behaviour of Bessel functions J_0 and Y_0, for a given argument x can be given as [1, 137],

$$\lim_{x \to 0} J_0(x) = 1 \tag{3.37a}$$

$$\lim_{x \to 0} Y_0(x) = \frac{2}{\pi} \ln(x) \tag{3.37b}$$

Clearly, $Y_0(\cdot)$ (and hence the Green's function) becomes singular in view of (3.37b), however, it can be observed that the integration length $d\Gamma$ goes to zero much faster (linearly) than the function $Y_0(\cdot)$ goes to zero (logarithmically) when the limit $\epsilon \to 0$ is taken. Therefore, we can

write,

$$\lim_{\epsilon \to 0} \int_{\Gamma_\epsilon} G \frac{\partial p}{\partial n} d\Gamma = 0 \tag{3.38}$$

Let us now consider the second integral in (3.34) and let us subtract and then add the value of pressure p at point $\mathbf{x}$ from the second integral in in (3.34), i.e.,

$$\int_{\Gamma_\epsilon} p \frac{\partial G}{\partial n} d\Gamma \tag{3.39a}$$

$$= \int_{\Gamma_\epsilon} \Big(p(\mathbf{y}) - p(\mathbf{x}) \Big) \frac{\partial G}{\partial n} d\Gamma + p(\mathbf{x}) \int_{\Gamma_\epsilon} \frac{\partial G}{\partial n} d\Gamma \tag{3.39b}$$

Now, the last integral in (3.39b) is considered below when limit $\epsilon \to 0$, i.e.,

$$\lim_{\epsilon \to 0} p(\mathbf{x}) \int_{\Gamma_\epsilon} \frac{\partial G}{\partial n} d\Gamma \tag{3.40}$$

Using polar coordinates, $d\Gamma = \epsilon d\theta$ and using the limits of integration for circle as $\theta \in [0, 2\pi]$, (3.40) reduces to,

$$\begin{aligned} &\lim_{\epsilon \to 0} p(\mathbf{x}) \int_{\Gamma_\epsilon} \frac{\partial G}{\partial n} d\Gamma \\ &= \lim_{\epsilon \to 0} p(\mathbf{x}) \int_0^{2\pi} \frac{\partial G}{\partial n} \epsilon d\theta \\ &= p(\mathbf{x}) \end{aligned} \tag{3.41}$$

It is evident that as $\epsilon \to 0$, the pressure at integration point and the singular point becomes the same and therefore the first integral in (3.39b) vanishes, i.e.,

$$\lim_{\epsilon \to 0} \int_{\Gamma_\epsilon} \Big(p(\mathbf{y}) - p(\mathbf{x}) \Big) \frac{\partial G}{\partial n} d\Gamma = 0 \tag{3.42}$$

We therefore have,

$$I_2 = -p(\mathbf{x}) \tag{3.43}$$

Now, let us denote the last integral in (3.33) as I_3,

$$I_3 = \int_{\Gamma_r} \left(G \frac{\partial p}{\partial n} - p \frac{\partial G}{\partial n} \right) d\Gamma \tag{3.44}$$

Sommefeld's regularity condition requires that the physical solution p (or its derivative) behaves similar to the fundamental solution (or its derivative) as the radius of Γ_r (say R) increases. Thus if the function p and G have the same form at infinity, we have,

$$I_3 = \lim_{R\to 0} \int_{\Gamma_r} \left(G\frac{\partial p}{\partial n} - p\frac{\partial G}{\partial n} \right) d\Gamma = 0 \tag{3.45}$$

Therefore, using (3.43) and (3.45) in (3.33), we can write,

$$-p(\mathbf{x}) + \int_{\Gamma_s} \left(G\frac{\partial p}{\partial n} - p\frac{\partial G}{\partial n} \right) d\Gamma = 0, \quad \mathbf{x} \subset \Omega_f \tag{3.46}$$

Note that in (3.46), point $\mathbf{x}$ is still in the domain and not on the boundary Γ_s. If we know the pressure p and its normal derivative $\frac{\partial p}{\partial n}$ on the boundary, we can compute the pressure field in the entire domain using (3.46). This is a useful boundary integral equation as only the boundary values of p and $\frac{\partial p}{\partial n}$ are needed and more importantly (3.46) will not contain singular terms as point $\mathbf{x}$ is not taken on Γ_s. However, such an equation will be of limited use as both the boundary pressure and its normal derivative need to be specified. For a well-posed problem therefore, we need to place the source point $\mathbf{x}$ on the boundary Γ_s, and in doing so, as before, we exclude a small domain Ω_ϵ from the boundary Γ_s. If Γ_s is taken as a smooth surface, Ω_ϵ can be conveniently taken as a semicircle for 2D problems (see Figure 3.7).

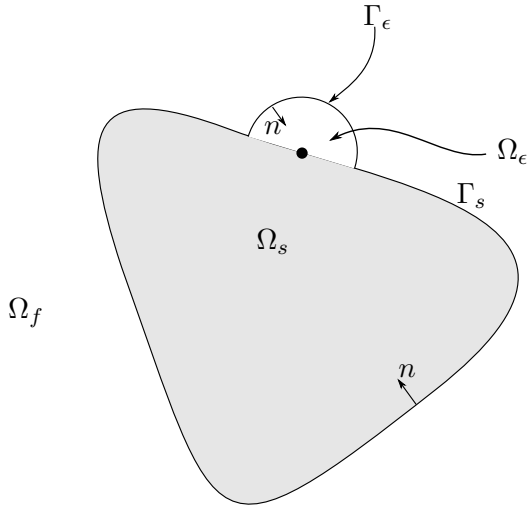

Figure 3.7: Exclusion of domain for evaluation of the jump term

The steps followed in arriving at (3.43) (i.e. through (3.43) and (3.45)) can be repeated to obtain,

$$\begin{aligned}
&\lim_{\epsilon\to 0}\int_{\Gamma_\epsilon}\left(G\frac{\partial p}{\partial n}-p\frac{\partial G}{\partial n}\right)d\Gamma\\
&=-\lim_{\epsilon\to 0}\int_{\Gamma_\epsilon}p\frac{\partial G}{\partial n}d\Gamma\\
&=-\lim_{\epsilon\to 0}\int_{0}^{\pi}p\frac{\partial G}{\partial n}\epsilon d\theta\\
&=-\frac{1}{2}p(\mathbf{x})
\end{aligned}\tag{3.47}$$

Using (3.47) when $\mathbf{x}\subset\Gamma_s$ therefore gives,

$$-\frac{1}{2}p(\mathbf{x})+\int_{\Gamma_s}\left(G\frac{\partial p}{\partial n}-p\frac{\partial G}{\partial n}\right)d\Gamma=0,\quad \mathbf{x}\subset\Gamma_s \tag{3.48}$$

It can be noted that for (3.48) the integral is evaluated only over the semicircular region ($\theta\in[0,\pi]$) and this is the reason we obtain a factor of $1/2$ commonly called as the *jump term*. In a general case however, when Γ_s is not smooth, the solid angle subtended at $\mathbf{x}$ needs to be computed and the free term, say $c(\mathbf{x})$, is then given as

$$c(\mathbf{x})=\frac{\alpha}{2\pi} \tag{3.49}$$

The BIE for the exterior problem therefore can be written as,

$$c(\mathbf{x})p(\mathbf{x})+\int_{\Gamma_s}p\frac{\partial G}{\partial n}d\Gamma=\int_{\Gamma_s}G\frac{\partial p}{\partial n}d\Gamma,\quad \mathbf{x}\subset\Gamma_s \tag{3.50}$$

When solving the exterior acoustic scattering problem due to a known incident wave, (3.50) needs to include the incident wave as follows,

$$c(\mathbf{x})p(\mathbf{x})+\int_{\Gamma_s}p\frac{\partial G}{\partial n}d\Gamma=\int_{\Gamma_s}G\frac{\partial p}{\partial n}d\Gamma+p^{\text{inc}}(\mathbf{x}),\quad \mathbf{x}\subset\Gamma_s \tag{3.51}$$

Note that when solving exterior acoustic problems using (3.51), the density term ρ is not considered as (3.51) applies to homogeneous domain. However, as will become clear later in the thesis (see §7.1), the term $1/\rho$ needs to be retained in the BIE when this equation is to be coupled with the weak form (3.25).

Chapter 4

Discretization and plane wave enrichment

This chapter gives the discrete equations obtained from the weak form and BIE discussed in the previous chapter. Explicit expressions for the element matrix integral will be given in this chapter. First, the concept of shape functions is introduced in the finite element context. This will be followed by a discussion on the idea of plane wave enrichment.

4.1 Galerkin method

We know that the PDE in (2.4) is satisfied at each continuum point in Ω_f. Consider such S continuum points in the domain Ω_f and let us write the weak form in (3.25) using a compact operator notation, i.e.,

$$\int_{\Omega_f} \boldsymbol{\mathcal{T}}^{\mathrm{T}} \boldsymbol{\mathcal{X}}(\mathbf{p}) d\Omega + \int_{\Omega_f} \boldsymbol{\mathcal{U}}^{\mathrm{T}} \boldsymbol{\mathcal{Y}}(\mathbf{p}) d\Omega + \int_{\Gamma} \boldsymbol{\mathcal{U}}^{\mathrm{T}} \boldsymbol{\mathcal{Z}}(\mathbf{p}) d\Gamma = \int_{\Gamma} \boldsymbol{\mathcal{U}}^{\mathrm{T}} \boldsymbol{\mathcal{F}}(\mathbf{p}^{\mathrm{inc}}) d\Gamma \tag{4.1}$$

where $\mathbf{p}$ is the vector of unknown field variable i.e., pressure p in the computational domain Ω and $\mathbf{p}^{\mathrm{inc}}$ is the vector of known incident wave (p^{inc}) evaluated on Γ_r, and,

$$\boldsymbol{\mathcal{T}} = [\mathcal{T}_1, \mathcal{T}_2, \cdots, \mathcal{T}_S], \quad \text{and,} \quad \boldsymbol{\mathcal{U}} = [\mathcal{U}_1, \mathcal{U}_2, \cdots, \mathcal{U}_S] \tag{4.2}$$

are the arbitrary functions evaluated at n points viz. $\mathbf{x}_1, \mathbf{x}_1, \cdots, \mathbf{x}_S$, in the domain Ω_f. In view of (3.25), we should have,

$$\mathcal{X}_i(p) = \frac{1}{\rho(\mathbf{x})}\nabla p(\mathbf{x})\bigg|_{\mathbf{x}=\mathbf{x}_i}, \quad \mathcal{Y}_i(p) = -\frac{1}{\rho(\mathbf{x})}k^2 p(\mathbf{x})\bigg|_{\mathbf{x}=\mathbf{x}_i}, \tag{4.3a}$$

$$\mathcal{Z}_i(p) = -\frac{1}{\rho(\mathbf{x})}Bp(\mathbf{x})\bigg|_{\mathbf{x}=\mathbf{x}_i}, \quad \mathcal{F}_i(p^{\text{inc}}) = \frac{1}{\rho(\mathbf{x})}\left(\frac{\partial p^{\text{inc}}(\mathbf{x})}{\partial r} - Bp^{\text{inc}}(\mathbf{x})\right)\bigg|_{\mathbf{x}=\mathbf{x}_i} \tag{4.3b}$$

Alternatively we can write,

$$\int_{\Omega_f}\sum_{i=1}^{S}\mathcal{T}_i\mathcal{X}_i(p)d\Omega + \int_{\Omega_f}\sum_{i=1}^{S}\mathcal{U}_i\mathcal{Y}_i(p)d\Omega + \int_{\Gamma_r}\sum_{i=1}^{S}\mathcal{U}_i\mathcal{Z}_i(p)d\Gamma \quad = \int_{\Gamma_r}\sum_{i=1}^{S}\mathcal{U}_i\mathcal{F}_i(p^{\text{inc}})d\Gamma \tag{4.4}$$

We have used this operator notation here only for compactly writing the weak form and to explain the concept of the Galerkin formulation in a concise manner. Clearly, if we are able to find the non-zero functions $\boldsymbol{\mathcal{T}}$ and $\boldsymbol{\mathcal{U}}$, then this automatically means that the PDE in (3.25) will be satisfied (even though in a weak manner), via the original weak form in (3.25) (or the notation form in (4.4)). It is important to mention that the functions $\boldsymbol{\mathcal{T}}$ and $\boldsymbol{\mathcal{U}}$ need to satisfy certain conditions. We note that the weak form in (3.25) has the derivatives of the pressure field that are of first order whereas the original PDE, namely the Helmholtz equation in (2.4), has derivatives of the second order. Clearly, we will need functions $\boldsymbol{\mathcal{T}}$ and $\boldsymbol{\mathcal{U}}$ such that their first derivative exists. In general, if the weak form involves derivatives of order m then the trial functions $\boldsymbol{\mathcal{T}}$ and $\boldsymbol{\mathcal{U}}$ need to be chosen such that their $(m-1)^{\text{th}}$ derivative is continuous. Moreover, the choice of the trial functions $\boldsymbol{\mathcal{T}}$ and $\boldsymbol{\mathcal{U}}$ will depend on the quality of the results they provide or how efficiently they approximate the field variable in the computational domain. By quality, we mean the accuracy of the results which in turn means the 'convergence' of the method. A common choice in the finite element community is to chose $\boldsymbol{\mathcal{T}}$ and $\boldsymbol{\mathcal{U}}$ to be polynomials although there are several other options possible. Let the pressure field in the computational domain be approximated by

$$\mathbf{p} \approx \bar{\mathbf{p}} = \sum_{j=1}^{n} N_j a_j, \tag{4.5}$$

where N_j is the function of the independent variable (the spatial coordinates) and a_j represent the degrees of freedom for the discrete approximation. Equation (4.5) can be compactly written in vector notation as

$$\mathbf{p} \approx \bar{\mathbf{p}} = \mathbf{N}\mathbf{a} \tag{4.6}$$

Let the vector $\mathfrak{U}$ be approximated by

$$\mathfrak{U} = \sum_{j=1}^{n} w_j a_j \tag{4.7}$$

It is immediately clear that the approximation for the vector $\mathfrak{T}$ is

$$\mathfrak{T} = \sum_{j=1}^{n} \nabla w_j a_j \tag{4.8}$$

where w_j are the weighting functions and a_j are the unknown multipliers that we need to determine. Using (4.7) and (4.8) in (4.1), we obtain,

$$\mathbf{a_j}^{\mathrm{T}} \left[\int_{\Omega_f} \nabla \mathbf{w}_j^{\mathrm{T}} \mathfrak{X}\left(\mathbf{Na}\right) d\Omega + \int_{\Omega_f} \mathbf{w}_j^{\mathrm{T}} \mathfrak{Y}\left(\mathbf{Na}\right) d\Omega + \int_{\Gamma_r} \mathbf{w}_j^{\mathrm{T}} \mathfrak{Z}\left(\mathbf{Na}\right) d\Gamma - \int_{\Gamma_r} \mathbf{w}_j^{\mathrm{T}} \mathfrak{F} d\Gamma \right] = 0 \tag{4.9}$$

It is interesting to note here that the term $\mathfrak{X}\left(\mathbf{Na}\right)$ (or $\mathfrak{Y}\left(\mathbf{Na}\right)$) is the 'residual' resulting from the approximation that we make in (4.5). The similar residual term for the boundary integral term is $\mathfrak{Z}\left(\mathbf{Na}\right)$. Note that since the terms $\mathfrak{X}\left(\mathbf{Na}\right)$ and $\mathfrak{Y}\left(\mathbf{Na}\right)$ are weighted and integrated over the domain Ω_f (or the term $\mathfrak{Z}\left(\mathbf{Na}\right)$ over the boundary Γ_r), the method is also called the 'weighted residual method'. There are various choices available for choosing the weighting functions w_j such as i) subdomain collocation, ii) point collocation and iii) the Bubnov-Galerkin method. Here, we use the Bubnov-Galerkin method more commonly known as *Galerkin method*[*] where the weighting functions w_j are chosen to be same as the basis functions N_j. This choice is arguably the most popular in the finite element community for the following reasons

1. The choice $w_j = N_j$ generally leads to a symmetric linear system of equations.

2. The Galerkin method results in a positive-definite coefficient matrix. It is known that a positive definite matrix has a unique inverse and therefore the linear system resulting from the Galerkin method has a unique solution[†].

[*]Boris G. Galerkin (1871-1945). Galerkin was a Russian engineer who published his first technical paper on the buckling of bars while imprisoned in 1906 by the Tzar in pre-revolutionary Russia.

[†]An $n \times n$ complex matrix $\mathbf{A}$ is said to be positive definite if, $c^{\mathrm{T}}\mathbf{A}c > 0, c \in \mathbb{C}^n$.

In practical terms, a symmetric, positive-definite linear system enables use of highly efficient solvers. Recall the weak form (3.25) from Chapter 3 which is reproduced below,

$$\int_{\Omega_f} \frac{1}{\rho(\mathbf{x})} \left(\nabla p \cdot \nabla v - k^2 v p\right) d\Omega - \int_{\Gamma_r} \frac{1}{\rho(\mathbf{x})} v B p d\Gamma = \int_{\Gamma_r} \frac{1}{\rho(\mathbf{x})} v \left(\frac{\partial p^{\text{inc}}}{\partial r} - B p^{\text{inc}}\right) d\Gamma \tag{4.10}$$

Substitute (4.5) in (4.10) and noting that we use the Bubnov-Galerkin formulation, we obtain,

$$\begin{aligned} &\sum_{j=1}^{n} \left[\int_{\Omega_f} \frac{1}{\rho(\mathbf{x})} \left(\nabla N_i^{\mathrm{T}} \cdot \nabla N_j - k^2 N_i^{\mathrm{T}} N_j\right) d\Omega - \int_{\Gamma_r} \frac{1}{\rho(\mathbf{x})} B N_i^{\mathrm{T}} N_j d\Gamma\right] a_j \\ &= \sum_{j=1}^{n} \left[\int_{\Gamma_r} \frac{1}{\rho(\mathbf{x})} N_i^{\mathrm{T}} \left(\frac{\partial p^{\text{inc}}}{\partial r} - B p^{\text{inc}}\right) d\Gamma\right] \end{aligned} \tag{4.11}$$

Consequently, a discrete system of equations can be formed from (4.11), i.e.,

$$\Big[[\mathbf{K}] - [\mathbf{M}] + B\,[\mathbf{C}]\Big]\{\mathbf{a}\} = \{\mathbf{f}\} \tag{4.12}$$

where

$$\begin{aligned} [\mathbf{K}] &= \int_{\Omega_f} \frac{1}{\rho(\mathbf{x})} \nabla N_i \nabla N_j \; d\Omega \;, \quad [\mathbf{M}] = \int_{\Omega_f} \frac{1}{\rho(\mathbf{x})} k^2 N_i N_j \; d\Omega \;, \\ [\mathbf{C}] &= -\int_{\Gamma_r} \frac{1}{\rho(\mathbf{x})} B N_i N_j \; d\Gamma \;, \quad \{\mathbf{f}\} = \int_{\Gamma_r} \frac{1}{\rho(\mathbf{x})} \left(N_i \frac{\partial p^{inc}}{\partial r} - B N_i p^{inc}\right) \; d\Gamma \end{aligned} \tag{4.13}$$

where $i, j = 1, 2, , \cdots n$ and thus the dimension of the matrices $[\mathbf{K}]$, $[\mathbf{M}]$ and $[\mathbf{C}]$ will be $n \times n$, and that for the vector $\{\mathbf{f}\}$ will be $n \times 1$. The assembly of (4.12) leads to a global system of equations

$$\mathbf{A}\mathbf{x} = \mathbf{f} \tag{4.14}$$

where the vector $\mathbf{x}$ contains the unknown multipliers a_{js}. We call $[\mathbf{K}]$, $[\mathbf{M}]$, $[\mathbf{C}]$ and $\{\mathbf{f}\}$ the stiffness, mass, damping matrices and the load vector respectively.

4.2 Selection of the trial functions

We have only stipulated that N_j are chosen as functions of the independent variables, namely, the spatial coordinates. Before we proceed further, we need to briefly discuss specifically this spatial dependence of the trial functions N_j. Consider a case where we have a computational domain

wherein the geometry is very simple and let the medium properties vary smoothly over the domain and on the boundary. It is known that for such cases, a global trial function can be used and such methods which are based on global functions are known as *pseudo-spectral methods* [16, 151]. For example, when solving a wave propagation problem in a layered medium, the trial functions can be chosen as the eigenfunctions of the underlying differential equation. It is known that, for example in a homogeneous layered medium, the eigenfunctions for the Helmholtz equation are sinusoidal functions and therefore can be conveniently used as trial functions. However, it is also known that if the layered medium is not homogeneous (i.e. either non-smooth variation or multiple discontinuities in the density), then obtaining eigenfunctions analytically is not possible. It should not be forgotten that analytical expressions for eigenfunctions can be obtained for very simple geometries. Now, as outlined in Chapter 1, we are interested in this thesis in solving a problem where internal discontinuities are encountered in Ω_f. Also, we would like to pose no restriction on the shape of the domain Ω_f. In such a case, since global trial functions are impractical, we use the so called *local* trial functions. Here, each trial function is non-vanishing in a small subdomain where the coefficients are smooth functions of spatial coordinates. This forms the basis of the 'finite element method' where an *element* is a small subdomain where we assume a smooth variation in the medium properties. We therefore divide our computational domain, into a finite number of subdomains or elements which are connected and the joining points of the adjacent elements are termed as *nodes*.

The concept of local trial functions can be compactly explained via a simple 1D example as shown in Figure 4.1. Consider a 1D domain of length L divided into $n-1$ elements (and thus n

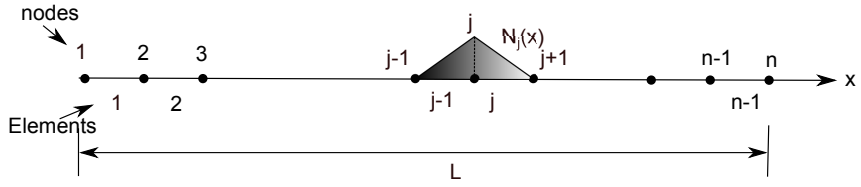

Figure 4.1: Concept of local trial functions

nodes) with each element having two nodes. We let the medium properties be discontinuous at the nodes. As seen from Figure 4.1, the *local* trial functions for a given node j (i.e. N_j) can be constructed using a linear combination of spatial coordinates of the nodes corresponding to the element containing the node j. This idea can be given by the well known Lagrange expansion

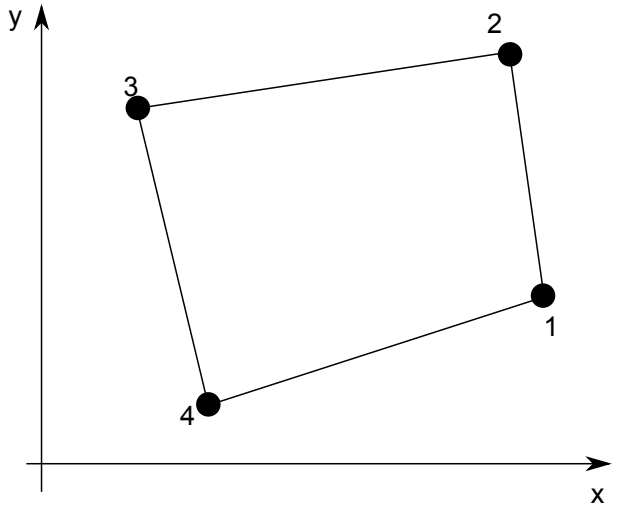

Figure 4.2: 4-noded quadrilateral element

as

$$N_j(x) = \prod_{i=1}^{n} \frac{x - x_i}{x_j - x_i}, \quad i \neq j, \tag{4.15a}$$

$$N_j(x) = 0, \quad x \leq x_{j-1}, x \geq x_{j+1} \tag{4.15b}$$

Since the j^{th} nodal trial function N_j can be computed independently of the other elements that do not contain node j, the concept of using a local trial function is usually termed as *local support* in FEM. In other words, the trial functions N_j are non-zero only locally. It is clear that if we divide the computational domain Ω_f, we will be able to treat the change in the density by assuming a piecewise constant variation, and complicated geometries can be modelled by choosing appropriate elements. If the change in medium property is not smooth, obviously, we will have to take a very small element size, such that, within each element, we can safely assume a constant density value. However, as mentioned before (see §3.1), though we will consider density as a function of space ($\rho = \rho(\mathbf{x})$), the variation considered here is only a step discontinuity and not a continuous variation.

4.3 FE discretization

It will now be appropriate to introduce the finite element 'type' that we will use in this thesis. For the problems studied here, we have considered only the 4-noded quadrilateral finite element (see Figure 4.2). It is clear that the pressure field is a scalar quantity and thus the element in Figure 4.2 has only 4 degrees of freedom. If we assume a bilinear interpolation, the pressure

$p(\mathbf{x})$ at a point $\mathbf{x}$ inside the finite element can be given as a function of the pressure values at the finite element nodes, i.e.,

$$p(\mathbf{x}) = N_1(\mathbf{x})p_1 + N_2(\mathbf{x})p_2 + N_3(\mathbf{x})p_3 + N_4(\mathbf{x})p_4 \tag{4.16}$$

where p_j $(j = 1, 2, 3, 4)$ is the pressure value at the j^{th} finite element node and N_j are the linear interpolation functions. Alternatively, we can write (4.16) in a compact form as,

$$p(\mathbf{x}) = \mathbf{N}^e\mathbf{p}^e \tag{4.17}$$

where

$$\mathbf{N}^e = [N_1, N_2, N_3, N_4] \quad \text{and} \tag{4.18}$$

$$\mathbf{p}^e = [p_1, p_2, p_3, p_4]^{\mathrm{T}} \tag{4.19}$$

The local matrices or commonly called element matrices and can be given as

$$\begin{aligned}
[\mathbf{K}^e] &= \int_{\Omega_f^e} \frac{1}{\rho(\mathbf{x})} \nabla(\mathbf{N}^e)^{\mathrm{T}} \nabla(\mathbf{N}^e)\, d\Omega\ , \quad [\mathbf{M}^e] = \int_{\Omega_f^e} \frac{1}{\rho(\mathbf{x})} k^2 (\mathbf{N}^e)^{\mathrm{T}} (\mathbf{N}^e)\, d\Omega\ , \\
[\mathbf{C}^e] &= -\int_{\Gamma_r^e} \frac{1}{\rho(\mathbf{x})} B(\mathbf{N}^e)^{\mathrm{T}} (\mathbf{N}^e)\, d\Gamma\ , \quad \{\mathbf{f}^e\} = \int_{\Gamma_r^e} \frac{1}{\rho(\mathbf{x})} \left((\mathbf{N}^e) \frac{\partial p^{inc}}{\partial r} - B(\mathbf{N}^e) p^{inc} \right) d\Gamma
\end{aligned} \tag{4.20}$$

where Ω_f^e represents the element area (as $\Omega_f \subset \mathbb{R}^2$) and Γ_r^e represents the element boundary. The global coefficient matrix $\mathbf{A}$ in (4.14) can then be obtained by first evaluating the element matrices in (4.20) and following the assembly process as per element connectivity. This is a standard procedure in FEM and for details see Chapter 12 in [13]. As N_j is chosen as the linear function of nodal coordinates (say (x_j, y_j)), we can write,

$$N_j^e(x, y) = \gamma_{j1} + \gamma_{j2}x + \gamma_{j3}y, \quad j = 1, \cdots, 4, \tag{4.21}$$

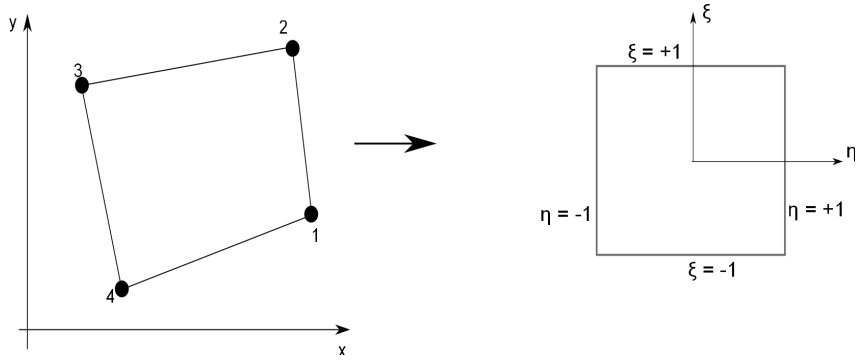

Figure 4.3: Coordinate transformation

and therefore,

$$\begin{bmatrix} \gamma_{11} & \gamma_{12} & \gamma_{13} \\ \gamma_{21} & \gamma_{22} & \gamma_{23} \\ \gamma_{31} & \gamma_{32} & \gamma_{33} \\ \gamma_{41} & \gamma_{42} & \gamma_{43} \end{bmatrix} = \begin{bmatrix} 1 & 1 & 1 & 1 \\ \mathrm{x}_1 & \mathrm{x}_2 & \mathrm{x}_3 & \mathrm{x}_4 \\ \mathrm{y}_1 & \mathrm{y}_2 & \mathrm{y}_3 & \mathrm{y}_4 \end{bmatrix}^{-1} \tag{4.22}$$

It can be noted that (4.22) will be dependent upon the spatial coordinates and it is highly inconvenient to perform matrix inversions such as in (4.22) for each element[‡]. Also, as can be noted from any of the equations from (4.20) or (4.13), if we assume that the density or the medium properties in general, are constant within a finite element, the element matrices such as $[\mathbf{K}^e]$ or $[\mathbf{M}^e]$ will depend only on the element geometry. It is for these reasons, it is desirable that N_j be made functions of coordinates over some *master* element. The transformation of a physical element such as the one shown in Figure 4.2 into a master element is shown in Figure 4.3. As can be seen, the physical element is mapped from (x, y) to (ξ, η) coordinates and these new coordinates are commonly called intrinsic coordinates. Any point in the finite element can be given as a linear function of ξ and η, i.e.,

$$x = \frac{1}{4}\mathrm{x}_1(1-\xi)(1-\eta) + \frac{1}{4}\mathrm{x}_2(1+\xi)(1-\eta) + \frac{1}{4}\mathrm{x}_3(1+\xi)(1+\eta) + \frac{1}{4}\mathrm{x}_4(1-\xi)(1+\eta) \tag{4.23}$$

and

$$y = \frac{1}{4}\mathrm{y}_1(1-\xi)(1-\eta) + \frac{1}{4}\mathrm{y}_2(1+\xi)(1-\eta) + \frac{1}{4}\mathrm{y}_3(1+\xi)(1+\eta) + \frac{1}{4}\mathrm{y}_4(1-\xi)(1+\eta) \tag{4.24}$$

[‡]Of course, inverting a rectangular matrix will require pseudo-inverse method, however, for a triangular element a square matrix can be obtained and the inverse can be computed in a straightforward manner.

where $(\mathrm{x}_j, \mathrm{y}_j)$ $(j = 1, \cdots, 4)$ are the nodal coordinates of the element under consideration in the physical (x, y) space and $\xi, \eta \in [-1, 1]^2$. Consider the stiffness matrix integral, say I^e, for an element that covers the subdomain Ω_f^e and rewrite the equation for $[\mathbf{K}^e]$ in (4.20), i.e.,

$$I^e = \int\limits_{\Omega_f^e} \frac{1}{\rho(\mathbf{x})} \nabla(\mathbf{N}^e)^{\mathrm{T}} \nabla(\mathbf{N}^e)\, d\Omega \tag{4.25}$$

The (x, y) to (ξ, η) coordinate mapping necessitates that we include a parameter called *Jacobian* (denoted as J) when performing above integration in (ξ, η) space, i.e.,

$$I^e = \int_{-1}^{1} \int_{-1}^{1} \frac{1}{\rho(\mathbf{x})} \nabla(\mathbf{N}^e)^{\mathrm{T}} \nabla(\mathbf{N}^e)\, |J| d\xi d\eta \tag{4.26}$$

where $|J|$ is the determinant of the Jacobian of transformation matrix J which is given as

$$J = \begin{bmatrix} \frac{\partial x}{\partial \xi} & \frac{\partial x}{\partial \eta} \\ \frac{\partial y}{\partial \xi} & \frac{\partial y}{\partial \eta} \end{bmatrix} \tag{4.27}$$

Clearly $|J|$ is a scaling factor between an elemental area $dxdy$ to the area $d\xi d\eta$ in the intrinsic coordinates, i.e.,

$$dxdy = |J| d\xi d\eta \tag{4.28}$$

For simple element shapes, such as triangles or rectangles, the Jacobian can be computed analytically. For a four noded linear element as shown in Figure 4.2, it is clear that the element matrices ($[\mathbf{K}^e]$, $[\mathbf{M}^e]$, $[\mathbf{C}^e]$) will be of size 4×4 and the global matrix formed after assembly (see (4.14)) will be of size $n \times n$ if there are n finite element nodes in the FE mesh of the computational domain Ω_f.

4.4 BE discretization

Implementing the BIE introduced in the previous chapter (see §3.7) for numerical computations extends the concept of finite elements (not the Galerkin formulation) to the integral equations. The underlying principle of using the discretization remains the same. The most significant difference is the appearance of Green's functions in the BEM and the singular nature of the kernels associated with them along with the reduced dimensionality. In this section we will briefly review the BE discretization. Since the BEM is essentially extending the concept of

finite elements to BIE, following the discussion in §4.2, it transpires that the concept of global and local trial spaces applies equally to BIE. The T-matrix method uses the global trial functions whereas the BEM, like FEM, uses local trial spaces [190]. In this thesis, we will discretize the BIE discussed in §3.7 using the local trial spaces arriving at a method commonly known as the BEM. Recall the BIE in (3.51) in the previous chapter for acoustic scattering problem (see Figure 4.4) which is reproduced below for convenience.

$$\frac{1}{\rho}c(\mathbf{x})p(\mathbf{x}) + \int_{\Gamma_s}\frac{1}{\rho}p(\mathbf{x})\frac{\partial G(\mathbf{x},\mathbf{y})}{\partial n}d\Gamma(\mathbf{y}) = \int_{\Gamma_s}\frac{1}{\rho}\frac{\partial p}{\partial n}G(\mathbf{x},\mathbf{y})d\Gamma(\mathbf{y}) + \frac{1}{\rho}p^{\text{inc}} \tag{4.29}$$

Following the concepts discussed in §4.2, the acoustic pressure at a point $\mathbf{y} \in \Gamma_s$ can be given

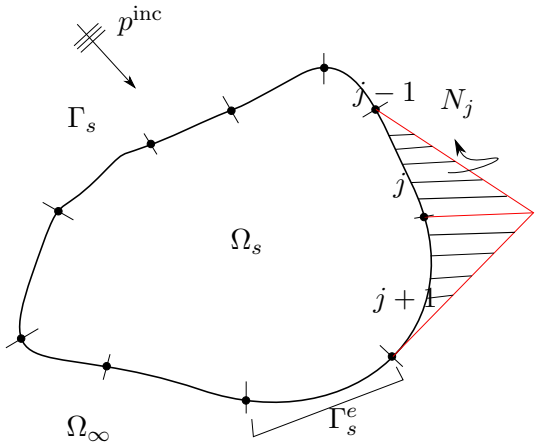

Figure 4.4: Boundary Element discretization and local trial space

as

$$p(\mathbf{y}) = \sum_{j=1}^{n} N_j(\mathbf{y})p_j, \quad \mathbf{y} \in \Gamma_s \tag{4.30}$$

and similarly,

$$\frac{\partial p(\mathbf{y})}{\partial n} = \sum_{j=1}^{n} N_j(\mathbf{y})\frac{\partial p_j}{\partial n}, \quad \mathbf{y} \in \Gamma_s \tag{4.31}$$

Clearly, we have $2n$ unknowns as per (4.30)-(4.31). If we now use (4.30)-(4.31) in (4.29) and choose the points $\mathbf{x}_j$ $(j = 1, \cdots, n)$ such that we have n equations or an equivalent matrix system given by

$$\mathbf{Ha} - \mathbf{Gb} = \mathbf{f} \tag{4.32}$$

where

$$H_{ij} = \frac{1}{\rho(\mathbf{x})}c(\mathbf{x})N_i(\mathbf{x}) + \int_{\Gamma_s}\frac{1}{\rho(\mathbf{y})}\frac{\partial G}{\partial n}N_j(\mathbf{y})d\Gamma \tag{4.33}$$

$$G_{ij} = \int_{\Gamma_s} \frac{1}{\rho(\mathbf{y})} G N_j(\mathbf{y}) d\Gamma \tag{4.34}$$

and

$$f_i = \frac{1}{\rho(\mathbf{x})} p^{\text{inc}}. \tag{4.35}$$

The vectors **a** and **b** respectively contain the point values for pressure and the normal derivative. Clearly, since both are unknowns, in order to be able to solve (4.32), we will need boundary conditions to be provided at n points. Often, it is assumed that the scatterer boundary Γ_s is sound hard ($\frac{\partial p}{\partial n} = 0$), leading to

$$\mathbf{Ha} = \mathbf{f} \tag{4.36}$$

Assuming a local support for the shape functions N_j, we can discretize the scatterer surface $\Gamma_s = \bigcup_{i=1}^{n_e} \Gamma_s^e$ and thus, equations (4.33)-(4.34) can be recast as

$$H_{ij} = \frac{1}{\rho(\mathbf{x})} c(\mathbf{x}) N_i(\mathbf{x}) + \sum_{i=1}^{n_e} \int_{\Gamma_s^e} \frac{1}{\rho(\mathbf{y})} \frac{\partial G}{\partial n} N_j^e(\mathbf{y}) d\Gamma \tag{4.37}$$

$$G_{ij} = \sum_{i=1}^{n_e} \int_{\Gamma_s^e} \frac{1}{\rho(\mathbf{y})} G N_j^e(\mathbf{y}) d\Gamma. \tag{4.38}$$

It should be noted that in the approach in obtaining a system of linear equations, such as in (4.36) or in (4.32), we follow a *collocation* approach. As noted before, we place the point **x** on the boundary Γ_s and obtain a discrete equation valid at that point. Conventionally, the collocation points **x** are chosen as the element nodes (see Figure 4.4), thus when (4.36) is solved, we recover the acoustic pressures on the surface of the scatterer given an incident wave and the boundary condition for $\frac{\partial p}{\partial n}$. Of course, there will be approximations introduced when using (4.30) or (4.31). As for FEM, the BIE in (4.29) can also be solved in a *weak* manner a procedure commonly known as *Galerkin BEM*.

4.5 Plane wave enrichment

We discussed in §2.3.1 the pollution error in the context of FEM. There have been both theoretical [84] and numerical [72] studies that prove that it is impossible to avoid the pollution error for Galerkin based FEM. However, the generalised Galerkin FEM has been shown to *reduce* these errors substantially but it is known that is not possible to completely remove the pollution errors, see the theoretical analysis by Babuška and Sauter in [10]. The BEM, like FEM, is also

an element based method and as mentioned previously, it requires the thumb rule of $\tau \approx 10$ to be followed in order to obtain results with engineering accuracy, i.e. 1% error. In this section, we discuss the concept of plane wave enrichment for the Galerkin FEM (§4.3) and for the BEM (§4.4). The idea of using a plane wave basis is identical for FEM and BEM. However, it will be convenient to separately write the equations with plane wave enrichment for FEM and BEM to assess their individual numerical performance.

4.5.1 Galerkin FEM with plane wave enrichment

Recall (4.16) that expands the acoustic pressure in terms of the corresponding nodal values using a bilinear interpolation, i.e.,

$$p(\mathbf{x}) = N_1(\mathbf{x})p_1 + N_2(\mathbf{x})p_2 + N_3(\mathbf{x})p_3 + N_4(\mathbf{x})p_4 \tag{4.39}$$

Figure 4.5 shows a plane wave enriched finite element. Each of the finite element nodes (1 through 4) is shown along with three red arrows that represent plane waves associated with that particular node. We therefore say, in Figure 4.5, the local approximation made at each of the finite element nodes is *enriched* with three plane waves. Equation (4.40) gives a corresponding expansion for the acoustic pressure.

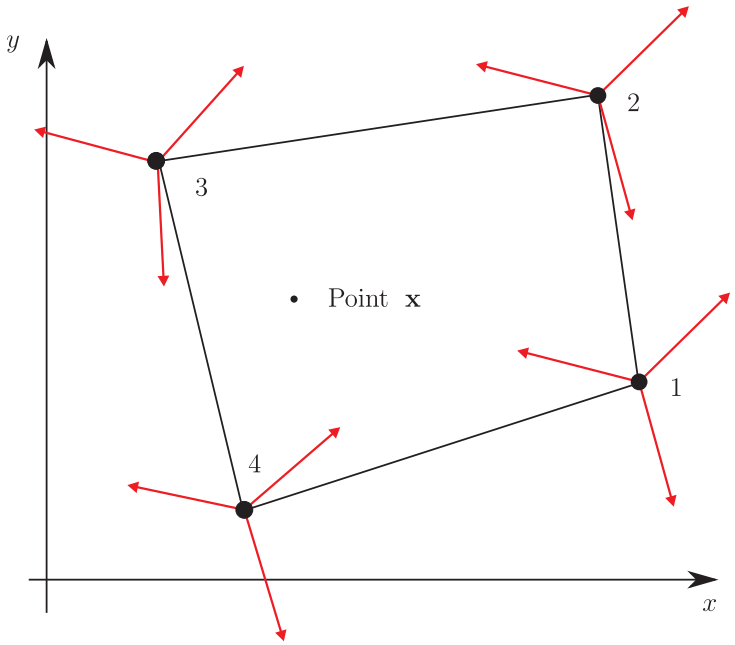

Figure 4.5: Plane wave enriched finite element

$$p(\mathbf{x}) = N_1(\mathbf{x}) \sum_{m=1}^{3} e^{\mathrm{i}kd_{1m}\cdot\mathbf{x}} a_{1m} + N_2(\mathbf{x}) \sum_{m=1}^{3} e^{\mathrm{i}kd_{2m}\cdot\mathbf{x}} a_{2m} + N_3(\mathbf{x}) \sum_{m=1}^{3} e^{\mathrm{i}kd_{3m}\cdot\mathbf{x}} a_{3m} + N_4(\mathbf{x}) \sum_{m=1}^{3} e^{\mathrm{i}kd_{4m}\cdot\mathbf{x}} a_{4m} \tag{4.40}$$

In (4.40), d_{1m} gives the direction of the m^{th} plane wave associated with node 1 with amplitude a_{1m}, d_{2m} gives the direction of the m^{th} plane wave associated with node 2 with amplitude a_{2m} and so on. Also note that the direction vector d_{jm} at node j is of unit length. In compact notation therefore, we can write, in general for a finite element with n nodes,

$$p(\mathbf{x}) = \sum_{j=1}^{n} N_j(\mathbf{x}) \left(\sum_{m=1}^{M_j} e^{\mathrm{i}kd_{jm}\cdot\mathbf{x}} a_{jm} \right) \tag{4.41}$$

We thus have a plane wave expansion of the pressure field where the unknowns at each node are the plane wave amplitudes a_{jm}. The number of plane waves at node j is M_j and distribution of the directions at each node is assumed uniform. For example, if we take three plane waves at each node, then they are at 120° from each other. In compact form, this can be given as,

$$\theta_m^l = l\frac{2\pi}{M_j} \tag{4.42}$$

where $l = 1, 2, \cdots, M_j$. We thus have the possibility of choosing a variable number of directions for each of the finite element nodes. It is possible that, in certain cases, the direction of the incident wave p^{inc} is not known beforehand, and in such a case, it may be convenient to set the directions of the plane waves uniformly or equally distributed as per (4.42). It is clear from the comparison of Figures 4.2 and 4.5 (and also from (4.39) and (4.41)) that the number of unknowns per element has increased due to the use of the plane wave enrichment from four nodal values to 4×3 (plane waves) $= 12$. Now, let us define a 'modified' shape function, say χ_{jm}, which is a product of the m^{th} plane wave at node j ($e^{\mathrm{i}kd_{jm}\cdot\mathbf{x}}$) and the polynomial shape function N_j, i.e.,

$$\chi_{jm}(\mathbf{x}) = N_j(\mathbf{x}) e^{\mathrm{i}kd_{jm}\cdot\mathbf{x}} \tag{4.43}$$

Thus, the acoustic pressure in (4.41) can be expressed in a further compact form,

$$p(\mathbf{x}) = \sum_{j=1}^{n} \sum_{m=1}^{M_j} \chi_{jm}(\mathbf{x}) a_{jm} \tag{4.44}$$

Alternatively, following the idea used in writing (4.17), we can express the pressure $p(\mathbf{x})$ using a matrix notation,

$$p(\mathbf{x}) = \boldsymbol{\mathfrak{Q}}^e \boldsymbol{\mathcal{A}}^e \tag{4.45}$$

where $\boldsymbol{\mathfrak{Q}}^e$ is a row vector given by,

$$\boldsymbol{\mathfrak{Q}}^e = [\mathcal{Q}_1, \cdots, \mathcal{Q}_n] \tag{4.46}$$

and $\boldsymbol{\mathcal{A}}^e$ is a column vector given by,

$$\boldsymbol{\mathcal{A}}^e = [\mathcal{A}_1, \cdots, \mathcal{A}_n]^{\mathrm{T}} \tag{4.47}$$

The elements of the vectors $\boldsymbol{\mathfrak{Q}}^e$ and $\boldsymbol{\mathcal{A}}^e$ are further given by

$$\mathcal{Q}_j = \left[\chi_{j1}, \chi_{j2}, \chi_{j3}, \cdots, \chi_{jM_j}\right] \tag{4.48}$$

and

$$\mathcal{A}_j = \left[a_{j1}, a_{j2}, a_{j3}, \cdots, a_{jM_j}\right]^{\mathrm{T}}. \tag{4.49}$$

The *enriched* element matrices in view of (4.45) can therefore be given as

$$\begin{aligned}
[\bar{\mathbf{K}}^e] &= \int_{\Omega_f^e} \frac{1}{\rho} \nabla(\boldsymbol{\mathfrak{Q}}^e)^{\mathrm{T}} \nabla(\boldsymbol{\mathfrak{Q}}^e)\, d\Omega\,, \quad [\bar{\mathbf{M}}^e] = \int_{\Omega_f^e} \frac{1}{\rho} k^2 (\boldsymbol{\mathfrak{Q}}^e)^{\mathrm{T}} (\boldsymbol{\mathfrak{Q}}^e)\, d\Omega\,, \\
[\bar{\mathbf{C}}^e] &= -\int_{\Gamma_r^e} \frac{1}{\rho} B(\boldsymbol{\mathfrak{Q}}^e)^{\mathrm{T}} (\boldsymbol{\mathfrak{Q}}^e)\, d\Gamma\,, \quad \{\bar{\mathbf{f}}^e\} = \int_{\Gamma_r^e} \frac{1}{\rho} \left((\boldsymbol{\mathfrak{Q}}^e) \frac{\partial p^{\mathrm{inc}}}{\partial r} - B(\boldsymbol{\mathfrak{Q}}^e) p^{\mathrm{inc}} \right) d\Gamma
\end{aligned} \tag{4.50}$$

It should be noted that, the element matrices in (4.50) for the plane wave enriched approach are denoted with an overbar and thus they should be distinguished from their polynomial based counterparts in (4.20). Assembling the enriched element matrices in (4.50), and keeping in mind element connectivity, we obtain a global linear system of equations for the plane wave enriched FEM or PUFEM,

$$\bar{\mathbf{A}}\bar{\mathbf{x}} = \bar{\mathbf{f}} \tag{4.51}$$

Note again that we distinguish the linear system for PUFEM in (4.51) and that for the polynomial based FEM in (4.14) by using an overbar for the global matrices of the former. The unknown vector $\bar{\mathbf{x}}$ contains the amplitudes of the plane waves associated with each node in the

finite element mesh. If the FE mesh for the entire computational domain contains n_{tot} nodes and each node is enriched with M plane waves (a uniform enrichment) then we would have total number of unknowns as $n_{tot}M$ and the dimension of the system matrix $\bar{\mathbf{A}}$ in (4.51) would be $n_{tot}M \times n_{tot}M$. Once the system of equations in (4.51) is solved, we can reuse (4.41) to recombine the plane wave amplitudes to obtain the acoustic pressure at a desired point in the computation domain.

4.5.2 A remark on the plane wave basis in (4.41)

Before proceeding further, we make a note of the difference between the element matrices for the FEM (see (4.20)) and for the PUFEM (see (4.50)). Note that for element matrices for PUFEM, we have considered the density ρ to be a constant value. The density term in (4.50) is not a function of the spatial coordinates ($\rho \neq \rho(\mathbf{x})$) whereas the weak form we originally used (see (3.25)) allows for the variable density (and hence variable wavenumber). This would potentially mean that with the polynomial FEM system (4.14) we are able to solve a truly heterogeneous problem whereas it will not be possible with the PUFEM system in (4.51) as the density is assumed to be constant for the latter. This conflict can be explained by considering at equation (4.41). Note that (4.41) gives a plane wave expansion of the pressure field $p(\mathbf{x})$, $\mathbf{x}$ being the point in the computational domain. Observe that the plane wave basis in (4.41) has only one wave number, namely k. It is important here to note that we use only those basis functions in PUFEM that satisfy the Helmholtz equation. For example, plane waves of the form $e^{\mathrm{i}k\mathbf{x}}$ or Bessel functions of the first kind $J(k\mathbf{x})$, which form a complete T set are to be used in PUFEM. However, it is known that for a domain Ω_f where the variation of the medium properties results in the Helmholtz equation with non-constant coefficients, it is not possible to obtain the particular solution in closed form. It is for this reason we use a constant density term in the equations appearing in enriched element matrices in (4.50). The question would then naturally arise "how do we solve a heterogeneous problem using the PUFEM?". We discuss this aspect in more detail in Chapter 6 where we will need to modify our basis in (4.41) so that heterogeneity can be modelled without having to look for particular solutions that satisfy the heterogeneous Helmholtz equation globally. At this point, it should be kept in mind that if the basis such as in (4.41) is used, we can solve only a homogeneous wave scattering problem with PUFEM i.e. we need to have the density and hence wavenumber as a constant.

4.5.3 BEM with plane wave enrichment

We discussed how the concept of local trial functions in the FEM is extended to BEM in §4.4. In a similar manner, the concept of plane wave enrichment is extended to BEM. Figure 4.4 is reproduced below but with each boundary element node now enriched with three plane waves. Let the acoustic pressure at a point $\mathbf{y}$ on the boundary Γ_s be expressed using plane wave basis

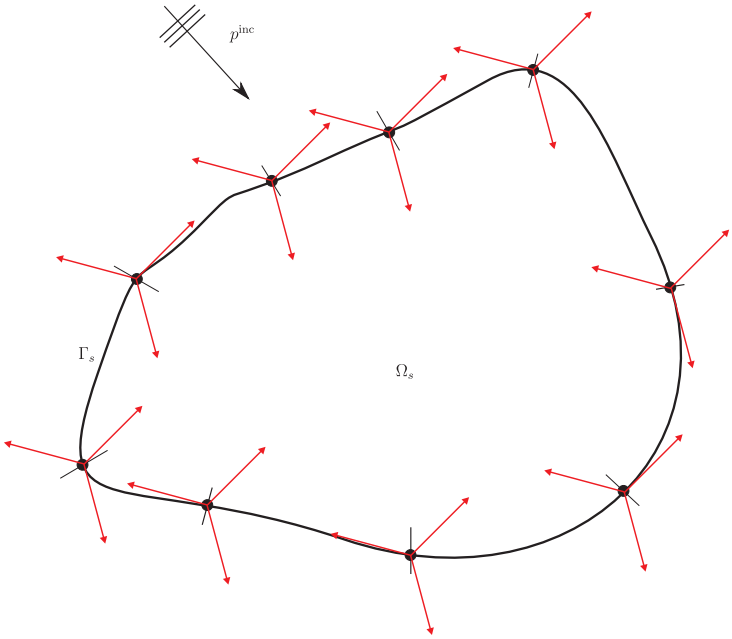

Figure 4.6: Plane wave enriched boundary elements

as,

$$p(\mathbf{y}) = \sum_{j=1}^{n} N_j(\mathbf{y}) \sum_{m=1}^{M_j} e^{\mathrm{i}kd_{jm}\cdot\mathbf{y}} a_{jm}, \quad \mathbf{y} \in \Gamma_s \tag{4.52}$$

and the normal derivative $\frac{\partial p}{\partial n}$ expressed as,

$$\frac{\partial p(\mathbf{y})}{\partial n} = \sum_{j=1}^{n} N_j(\mathbf{y}) \sum_{m=1}^{M_j} e^{\mathrm{i}kd_{jm}\cdot\mathbf{y}} b_{jm}, \quad \mathbf{y} \in \Gamma_s \tag{4.53}$$

Following the concept we used in writing (4.45), (4.52) and (4.53) can be written using compact vector notations,

$$p(\mathbf{y}) = \boldsymbol{\mathcal{R}}^e \boldsymbol{\mathcal{A}}^e, \qquad \mathbf{y} \in \Gamma_s \tag{4.54a}$$

$$\frac{\partial p(\mathbf{y})}{\partial n} = \boldsymbol{\mathcal{R}}^e \boldsymbol{\mathcal{B}}^e, \qquad \mathbf{y} \in \Gamma_s. \tag{4.54b}$$

where, $\boldsymbol{\mathfrak{R}}^e$ is the row vector given by

$$\boldsymbol{\mathfrak{R}}^e = [\mathcal{R}_1, \cdots, \mathcal{R}_n] \tag{4.55}$$

and $\boldsymbol{\mathcal{A}}^e$ and $\boldsymbol{\mathcal{B}}^e$ are column vectors given by,

$$\boldsymbol{\mathcal{A}}^e = [\mathcal{A}_1, \cdots, \mathcal{A}_n]^{\mathrm{T}} \tag{4.56a}$$

$$\boldsymbol{\mathcal{B}}^e = [\mathcal{B}_1, \cdots, \mathcal{B}_n]^{\mathrm{T}}. \tag{4.56b}$$

Note that, whereas the row vector $\boldsymbol{\mathfrak{R}}^e$ is obtained from the multiplication of the boundary element shape functions with the plane waves, the row vector $\boldsymbol{\mathfrak{Q}}^e$ in (4.46) is obtained with the multiplication of finite element shape functions with the plane waves. The elements of the vector $\boldsymbol{\mathfrak{R}}^e$ are further given by

$$\mathcal{R}_j = \left[\chi_{j1}, \chi_{j2}, \chi_{j3}, \cdots, \chi_{jM_j}\right] \tag{4.57}$$

The *enriched* boundary element matrices therefore can be written as

$$[\bar{H}] = \frac{1}{\rho(\mathbf{x})} c(\mathbf{x}) \boldsymbol{\mathfrak{R}}^e(\mathbf{x}) + \sum_{i=1}^{n_e} \int_{\Gamma_s^e} \frac{1}{\rho(\mathbf{y})} \frac{\partial G}{\partial n} \boldsymbol{\mathfrak{R}}^e(\mathbf{y}) d\Gamma \tag{4.58}$$

$$[\bar{G}] = \sum_{i=1}^{n_e} \int_{\Gamma_s^e} \frac{1}{\rho(\mathbf{y})} G \boldsymbol{\mathfrak{R}}^e(\mathbf{y}) d\Gamma. \tag{4.59}$$

which leads to a global PUBEM system given by

$$\bar{\mathbf{H}}\bar{\mathbf{a}} - \bar{\mathbf{G}}\bar{\mathbf{b}} = \bar{\mathbf{f}} \tag{4.60}$$

As mentioned previously, note that, the global PUBEM system matrices in (4.60) are denoted with an overbar to distinguish them from the global polynomial BEM matrices in (4.32). The vector $\bar{\mathbf{a}}$ contains the amplitudes (a_{jm}) of the plane waves associated with the pressure data on the scatterer boundary Γ_s (or the Dirichlet data) and the vector $\bar{\mathbf{b}}$ contains the amplitudes (b_{jm}) of the plane waves associated with the normal derivative of the pressure data on the scatterer boundary Γ_s (or the Neumann data). We will need to specify a boundary condition on Γ_s in

order to be able to solve (4.60). For a sound hard boundary Γ_s, (4.60) reduces to

$$\bar{\mathbf{H}}\bar{\mathbf{a}} = \bar{\mathbf{f}} \tag{4.61}$$

Consider the geometry shown previously in Figure 4.6 where the boundary Γ_s is discretized using linear two noded elements. If there are n_e such elements in total on Γ_s, there will be in total n_e nodes[§]. If each of the boundary element nodes is enriched with M plane waves (uniform enrichment), the size of the system matrix $\bar{\mathbf{H}}$ in (4.61) will be $n_eM \times n_eM$. Once the linear system in (4.61) is solved and the plane wave amplitudes associated with the Dirichlet data computed, (4.52) can be used to recombine the plane wave amplitudes to obtain the pressure field at all the points on the boundary of the scatterer. We should remark here that in most PUBEM formulations published to date, a Neumann or Robin condition is used to avoid having to approximate the Neumann data using a separate plane wave basis (or polynomial basis in case of the conventional BEM), thereby avoiding the computation of vector $\bar{\mathbf{b}}$. This specific aspect will be discussed again in Chapter 7 in §7.2.

4.6 Overview

In this chapter, we have reviewed the basic FE and BE discretization process for the weak form and the boundary integral equation respectively. Following the arguments presented in Chapter 1 for the pollution error, a plane wave based FE and BE formulation was presented. One can note from the plane wave based approximations, both for PUFEM and PUBEM (see equations (4.41) and (4.52)), that the associated element matrix integrals involve oscillatory terms, i.e. the integrals involved in the plane wave based methods are of the form

$$I(k,x) = \int f(x)e^{ikg(x)}dx \tag{4.62}$$

With increasing wavenumbers, these integrals need to be evaluated carefully so that their convergence is ensured. We mentioned briefly, in the first chapter (see §1.3) the problem of non-uniqueness of the BIE. In the next chapter, we focus on this particular aspect of the BIE and two prominent methods used to handle this characteristic. Several other associated aspects, such

[§]For linear two noded elements, the total number of boundary elements on Γ_s = total number of boundary element nodes.

as various orders of singularities and the methods to accurately evaluate the integrals involving the singularities, are also discussed.

Chapter 5

Overcoming non-uniqueness: comparison of CHIEF and Burton-Miller formulations

5.1 Introduction

As mentioned earlier in §1.3, the Boundary Integral Equation (BIE) in (3.51) for an exterior acoustic problem suffers from non-uniqueness of the solution. The BIE in (3.51), hereafter called the 'Conventional BIE' (CBIE), results in a non-unique solution at certain irregular frequencies for the corresponding interior problem and it is known that this is a purely mathematical phenomenon [36]. Two of the available approaches to overcome the non-uniqueness are the Combined Helmholtz Integral Equation Formulation (CHIEF) method [155] and the Burton-Miller method [22]. The primary motivation of this chapter is to compare these two methods for the PUBEM formulation and choose the best for coupling with PUFEM formulation. The two methods are compared for their accuracy, solution efficiency and conditioning of the coefficient matrix. Next, we review previous work carried out on the CHIEF and Burton and Miller formulations.

5.2 Background material

The CHIEF method due to Schenck [155] uses some additional Helmholtz integral equations evaluated at points interior to the scatterer (and exterior to the acoustic domain) which are

appended in the original system matrix. Although this results in an over-determined system, CHIEF ensures a unique solution at an irregular frequency provided the chosen interior points do not lie on the nodal lines of the eigenmodes of the interior Helmholtz problem. This, however, can introduce uncertainties at high wavenumbers as the nodal lines become densely packed in the interior which makes it difficult to find suitable locations for the placement of interior points. Apart from stating the problem with the interior collocation points when they lie on the nodal lines of the interior modes, Schenck has not provided any criteria as to what number of CHIEF points be chosen to ensure a unique solution. To this effect, some work has been done by Wu and Seybert [187], Juhl [90] to further enhance the CHIEF method to obtain a unique solution. Wu and Seybert propose a weighted residual form of the CHIEF method which can ensure a unique solution using the concept of a 'CHIEF block'. A CHIEF block is a volume considered inside the scatterer where the CHIEF equation (or the interior Helmholtz problem) is solved in a weighted residual sense. Juhl's approach on the other hand uses the Singular Value Decomposition (SVD) technique to identify the rank deficiency of the coefficient matrix and with this assess the quality of the CHIEF points. An important observation of Juhl relates to the accuracy with which the scatterer geometry is modelled and the associated possibility to circumvent the non-uniqueness problem. It is known that the CBIE can result in a non-unique solution at wavenumbers near the eigenvalues of the interior problem for a coarse mesh. This 'band' of spurious wavenumbers is the major concern when solving exterior acoustic problems as one is less likely to solve exactly at a spurious wavenumber. As observed by Juhl, the non-uniqueness in this particular spurious 'band' may be avoided if one uses a fine mesh. Note that a fine mesh would essentially mean modelling the geometry more accurately, though, this comes at the cost of excessive computation. One of the motivations for using Partition of Unity methods (apart from obtaining a very high accuracy), is to be able to use a coarse mesh. It is therefore crucial that the geometric modelling of the scatterer be accurate for exterior acoustic problems in view of the problem with non-uniqueness in the spurious band. A rigorous analytical and numerical investigation of the CHIEF method has been presented by Chen *et al* [29] for the spurious eigensolution in a multiply connected domain. There are several other variations of the CHIEF method and for a good discussion on the non-uniqueness problem and on the several enhancements of the CHIEF method, see Chapter 15 by Marburg and Wu in [117]).

Another method to avoid the non-uniqueness problem is due to Burton and Miller [22]. They showed that the integral equation resulting from linear combination of the CBIE and its normal derivative at the collocation point always results in a unique solution. The major problem with this method is the evaluation of a hypersingular integral* which arises as a result of the differentiation of the CBIE at the collocation point. There are various techniques available to handle the hypersingular integral in the Burton-Miller formulation. One such technique is the 'regularisation' procedure which is a subtraction of singularity technique (SST) combined with identities from potential theory [109]. Various methods of regularisation for use with the BEM technique for acoustic and elastic scattering problems can be found in [113],[82],[33],[114],[110]. Another technique is due to Guiggiani [65] which is based again on the subtraction of singularity but it does not use the identities from potential theory. Rather, the technique is based on expanding the singular kernel in a Taylor series using polynomial shape functions. Although mathematically elegant and widely applied for practical problems [126],[163] (Dual BEM for fracture mechanics), [162](Stokes flow in duct), it can become difficult to obtain complicated expansions for the fundamental solutions (the Green's functions). Often an exact geometry is essential in the PUBEM technique [145] and Guiggiani's method can become highly involved when performing the analytical integration on the exact boundary. Also, since the PUBEM is specifically aimed at solving short wavelength problems, the use of an approximate model of the scatterer geometry can introduce numerical dispersion in the solution. It is for this reason that we use the regularisation procedure [109] where the singularity subtraction is analytical.

The BEM system of equations, formed using either the CHIEF or Burton-Miller formulation, is dense and often ill-conditioned (in the case of plane wave based methods). This may be become a problem for high frequency problems when using conventional direct solvers as the cost of solving the system scales with $\mathcal{O}(N^3)$ where N is the total number of equations in the BEM system. One of the many techniques to accelerate the BEM solution is the Fast Multipole Method (FMM). An adaptive version of the FMM [159],[184] has been used to solve several 3D acoustic scattering problems using the Burton and Miller formulation. The authors show that significant savings in CPU time can be achieved compared to the conventional BEM or non-adaptive FMM. Load balancing is known to be a problem for parallel implementation of FMM.

*The precise definitions for the terms such as *hypersingular, strongly singular and weakly singular* will be given in §5.3. At this point, it is suffice to say that these terms indicate the 'severity' of the singular nature of the integrand in the BIE.

Hariharan *et al* [75] present an algorithm that avoids the load balancing steps and demonstrate considerable speed-up for the parallel FMM for electromagnetic scattering problems.

5.3 Orders of singularity

An important observation of the integral equation based methods that use the Green's function (such as BEM) is that these methods inherently suffer from singularities. This is because the fundamental solution is a two point ($\mathbf{x}$ and $\mathbf{y}$) function and as these two points are brought close to each other ($|\mathbf{y}-\mathbf{x}| \to 0$), a singularity appears in the solution process[†]. More importantly, the singularity appearing in the solution process is unrelated to the physical problem that we intend to solve. For example, the exterior acoustic problem considered here, namely the Helmholtz BVP (2.13), should be free from singularities provided the scatterers are perfectly smooth. The integral formulations that we will use (viz. CHIEF and Burton and Miller) involve either weak, strong or hypersingular integrals and we will be discussing some special techniques designed to handle these integrals (see §5.4.1 for the regularisation to handle the hypersingular integral and §5.7 for the weakly singular integrals). Therefore, before we proceed with the integral formulations for handling the non-uniqueness, it is essential that we precisely define what we mean by various orders (weak, strong and hyper) of singularities.

Consider a real function $f(\mathbf{x}, \mathbf{y})$ and let this function be bounded everywhere in the domain of interest, say $V \subset \mathbb{R}^d$ where d is the dimension of the space. In the context of BEM, $\mathbf{x}$ will be the collocation or source point and $\mathbf{y}$ will be the field or integration point. Let the distance between the collocation point and field point be denoted as r. We are now interested in the behaviour of the following integral

$$I = \int_V \frac{f(\mathbf{x}, \mathbf{y})}{r^\nu} dV(\mathbf{y}) \tag{5.1}$$

where ν is a real number. In general, it can be said that, if the integrand in (5.1) becomes infinite at some point(s) in the integration interval, the integral in I is (5.1) singular. However, the order of singularity of the integral I in (5.1) is determined through the values that the parameter ν assumes and this is summarised in Table 5.1. It is clear that for $\nu = 0$, the integrand in (5.1) will be regular and the integration can be performed using well known quadrature schemes such as Gauss-Legendre (GL) or the trapezium rule. Weakly singular integrals ($0 < \nu < d$) on the

[†]Recall that the Green's function for the Helmholtz equation is $G = \frac{\mathrm{i}}{4} H_0^{(1)}(kr)$ and $r = |\mathbf{y} - \mathbf{x}|$

ν	Order of singularity
0	Regular
$0 < \nu < d$	weakly singular
$\nu = d$	strongly singular
$\nu = d + 1$	hypersingular
$\nu = d + 2$	supersingular

Table 5.1: Orders of singularity

other hand, if treated in the same manner as the regular integrals, i.e. without any regard to the singularity, may not converge at all. For this purpose one either needs to use special quadrature scheme such as the logarithmic GL as the conventional GL scheme is not useful. In the boundary element computations, especially those involving oscillatory terms (such as in PUBEM), we need to have integrals that converge rapidly. Many techniques have been developed in the past to efficiently evaluate the weakly singular integrals and we will compare some of these techniques in §5.7. The strongly and hypersingular integrals however need some special attention and the techniques that will be discussed in §5.7 are not suitable for strongly and hypersingular integrals. We can show through examples that a weakly singular integral can exist. But, the strongly singular integrals of some functions simply may not exist and we need to consider their existence by following an approach called *Cauchy principal value* (CPV) sense. Of course, the strongly singular and hypersingular integrals that arise in the integral equations of the physical problems, such as the acoustic scattering considered in this thesis, must exist. The CPV approach is a limiting process where the singularity is excluded by encircling it with a small volume and the behaviour of the integral is examined as this volume is reduced. The CPV approach used for strongly singular integrals however does not work for hypersingular integral and we need to use what is called *Hadamard finite part* approach for the hypersingular integral. The concepts of CPV and Hadamard finite part are well documented [165], but we briefly discuss the limiting process here for completeness.

5.3.1 Weakly singular integral

Consider again the integral in (5.1). For simplicity we assume the domain V in (5.1) to be a smooth curve Γ with length L as shown in Figure 5.1. Consider now the interval $[a, b]$ on the curve Γ. We are interested in the integral in (5.1) that is evaluated over the domain $\Gamma - \Gamma_\epsilon$ as

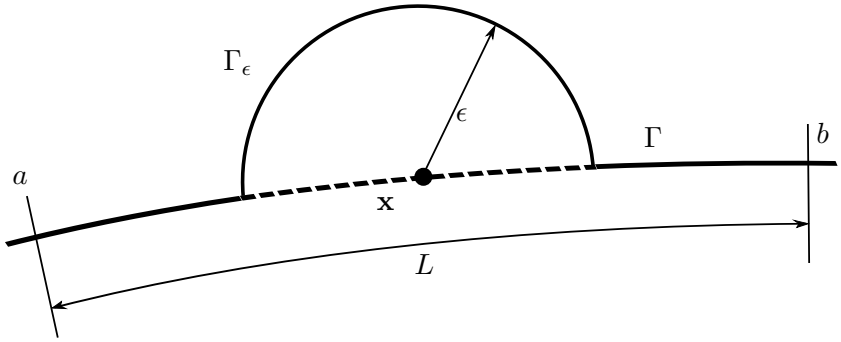

Figure 5.1: Limit process for defining a singular integral

we shrink the semicircular region Γ_ϵ, or more precisely,

$$I = \lim_{\epsilon \to 0} \int_{\Gamma - \Gamma_\epsilon} \frac{f(\mathbf{x}, \mathbf{y})}{r^\nu} d\Gamma(\mathbf{y}) \tag{5.2}$$

The integral I in (5.2) is called a weakly singular integral if the limit exists independent of the shape of Γ_ϵ. Consider a function $f(\mathbf{x}, \mathbf{y}) = \ln |\mathbf{y} - \mathbf{x}|$ and let $\nu = 0$. It is clear from Figure 5.2

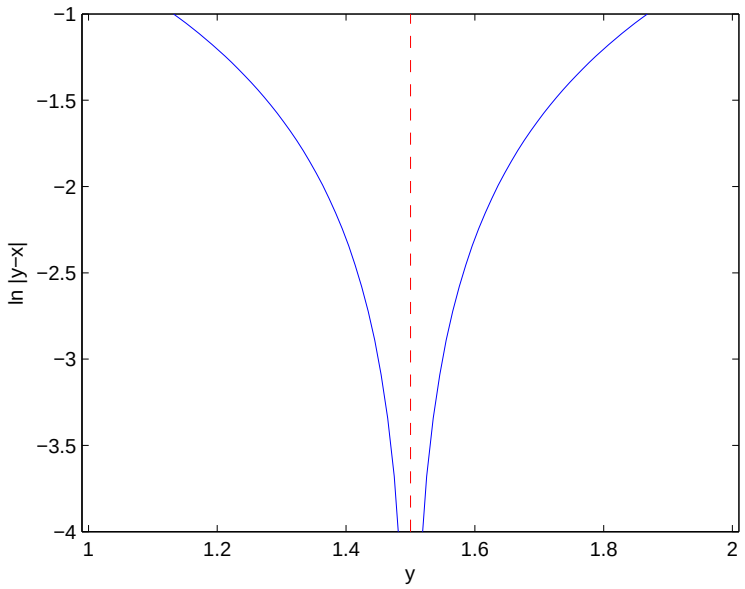

Figure 5.2: Logarithmically singular function $\ln(\mathbf{y} - \mathbf{x})$

that the function $\ln(\mathbf{y} - \mathbf{x})$ becomes singular when $\mathbf{y} = \mathbf{x}$ (the singular point is $\mathbf{x} = 1.5$) in the

interval $[1, 2]$. By approaching the singularity from left and right, we can verify this as follows.

$$I_{\text{weak}} = \lim_{\epsilon_1 \to 0} \int_a^{\mathbf{x}-\epsilon_1} \ln|\mathbf{y}-\mathbf{x}| d\Gamma + \lim_{\epsilon_2 \to 0} \int_{\mathbf{x}+\epsilon_2}^{b} \ln|\mathbf{y}-\mathbf{x}| d\Gamma \tag{5.3}$$
$$= (\mathbf{x}-a)\ln(\mathbf{x}-a) + (b-\mathbf{x})\ln(b-\mathbf{x}) + (a-b)$$

It can therefore be observed that though the function $\ln|\mathbf{y}-\mathbf{x}|$ is singular at $\mathbf{x} = \mathbf{y}$, its integral can be evaluated.

5.3.2 Strongly singular integral

Consider now an integral with $f(\mathbf{x}, \mathbf{y}) = 1$ and $\nu = 1$, thus,

$$I_{\text{strong}} = \int_a^b \frac{1}{|\mathbf{y}-\mathbf{x}|} d\Gamma, \quad \mathbf{x} \in (a, b) \tag{5.4}$$

The integrand in (5.4) has a strong singularity at $\mathbf{x} = \mathbf{y}$ (see Figure 5.3, $\mathbf{x} = 1.5$) Following the

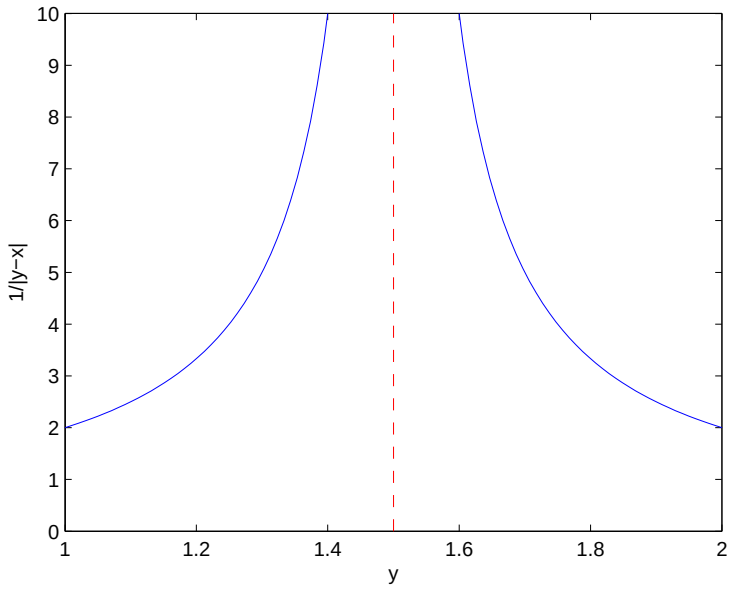

Figure 5.3: Strongly singular function $1/|\mathbf{y}-\mathbf{x}|$

same limiting approach used for weakly singular integrals, we obtain,

$$I_{\text{strong}} = \lim_{\epsilon_1 \to 0} \int_a^{\mathbf{x}-\epsilon_1} \frac{1}{|\mathbf{y}-\mathbf{x}|} d\Gamma + \lim_{\epsilon_2 \to 0} \int_{\mathbf{x}+\epsilon_2}^{b} \frac{1}{|\mathbf{y}-\mathbf{x}|} d\Gamma \tag{5.5}$$
$$= \ln|\mathbf{y}-\mathbf{x}|\Big|_a^{\mathbf{x}-\epsilon_1} + \ln|\mathbf{y}-\mathbf{x}|\Big|_{\mathbf{x}+\epsilon_2}^{b}$$

If the singularity at $\mathbf{x}$ is approached from both sides *symmetrically*, i.e. by setting, $\epsilon_1 = \epsilon_2$, we obtain,

$$I_{\text{strong}} = \ln \frac{b - \mathbf{x}}{\mathbf{x} - a} \tag{5.6}$$

Note that the result in (5.6) is possible *if and only if* the exclusion zone Γ_ϵ is made symmetric by setting $\epsilon_1 = \epsilon_2$. It can therefore be said that, the integral I_{strong} exists in a CPV sense if the exclusion zone Γ_ϵ is symmetric and integral I_{strong} should strictly be denoted as

$$I_{\text{strong}} = \text{p.v.} \int_a^b \frac{1}{|\mathbf{y} - \mathbf{x}|} d\Gamma = \ln \frac{b - \mathbf{x}}{\mathbf{x} - a} \tag{5.7}$$

5.3.3 Hypersingular integral

Finally, consider an integral with $f(\mathbf{x}, \mathbf{y}) = 1$ and $\nu = 2$, thus,

$$I_{\text{hyper}} = \int_a^b \frac{1}{|\mathbf{y} - \mathbf{x}|^2} d\Gamma, \quad \mathbf{x} \in (a, b) \tag{5.8}$$

The integrand in (5.8) is hypersingular at $\mathbf{x} = \mathbf{y}$ (see Figure 5.4, $\mathbf{x} = 1.5$) The integral I_{hyper} is

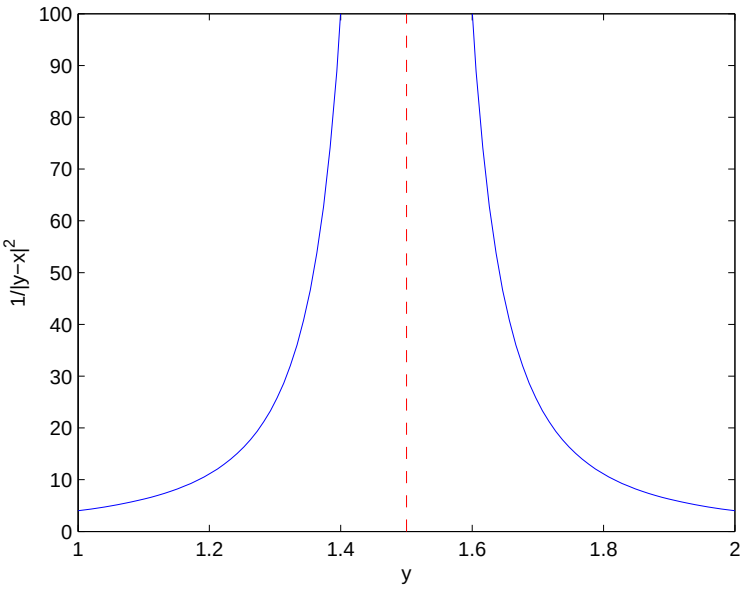

Figure 5.4: Hypersingular function $1/|\mathbf{y} - \mathbf{x}|^2$

divergent and its interpretation in the sense of Hadamard is necessary. The justification of doing so is given by Krishnasamy *et al* in [99]. The Hadamard principal value (HPV) (alternatively

called Hadamard finite part) of the integral I_{hyper} is given as

$$HPV \int_a^b \frac{1}{|\mathbf{y}-\mathbf{x}|^2} d\Gamma = \lim_{\epsilon \to 0} \left(\int_a^{\mathbf{x}-\epsilon} \frac{1}{|\mathbf{y}-\mathbf{x}|^2} d\Gamma + \int_{\mathbf{x}+\epsilon}^b \frac{1}{|\mathbf{y}-\mathbf{x}|^2} d\Gamma - \frac{2f(\mathbf{y})}{\epsilon} \right) \tag{5.9}$$

Again, as can be noted from (5.9), the exclusion zone is symmetric with radius ϵ.

Now that we have discussed the various orders of singularity, we can introduce the integral formulations to treat the non-uniqueness and various singular integrals encountered therein.

5.4 Integral equation formulations for handling non-uniqueness

Recall the CBIE given in Chapter 3 (see §3.7) for an acoustic scattering problem governed by the Helmholtz differential equation. The CBIE is reproduced here for convenience.

$$c(\mathbf{x})p(\mathbf{x}) + \int_{\Gamma_s} \frac{\partial G}{\partial n_{\mathbf{y}}} p(\mathbf{y}) d\Gamma = \int_{\Gamma_s} G \frac{\partial p(\mathbf{y})}{\partial n_{\mathbf{y}}} d\Gamma + p^{\text{inc}}(\mathbf{x}), \quad \mathbf{x}, \mathbf{y} \in \Gamma_s \tag{5.10}$$

where $\mathbf{x}$ is the collocation or source point (see Figure 5.5), $\mathbf{y}$ the field point, $r = |\mathbf{y} - \mathbf{x}|$, G the

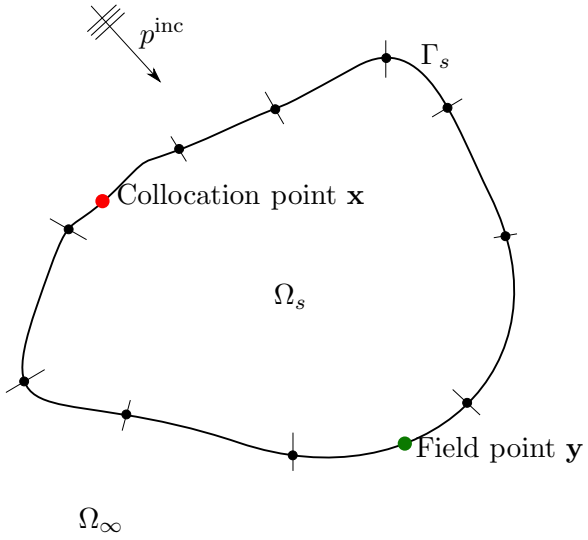

Figure 5.5: Definition: Collocation and field point

free space Green's function for the Helmholtz problem, $n_{\mathbf{y}}$ the outward normal at point $\mathbf{y}$ on the boundary Γ_s, $p(\mathbf{y})$ the unknown acoustic pressure and $p^{\text{inc}}(\mathbf{x})$ the known incident acoustic wave. The term $c(\mathbf{x})$ is the free coefficient which depends on the local geometry of Γ_s at $\mathbf{x}$. As mentioned before, in this thesis we assume Γ_s is smooth and take $c(\mathbf{x}) = \frac{1}{2}$. Thus when the normal derivative of the acoustic pressure is prescribed on the boundary, (5.10) can be used

to compute the acoustic pressure. Note that we have removed the density term $\rho(\mathbf{x})$ from the integral equation. This is because

1. we want to investigate the performance of the two methods (viz. CHIEF vs Burton-Miller) to overcome the non-uniqueness problem and,

2. we will be solving an acoustic problem in a homogeneous medium only and therefore it is convenient to take the density to be constant.

The Green's function for the Helmholtz equation in two-dimensions is given by

$$G = \frac{\mathrm{i}}{4} H_0(kr) \tag{5.11}$$

where $H_0(\cdot)$ is the first kind Hankel function of order zero.

5.4.1 Burton-Miller formulation

The Burton-Miller equation is obtained by combining the CBIE and its normal derivative using a coupling constant. The normal derivative of (5.10) at the collocation point $\mathbf{x}$ with respect to the direction of the normal at $\mathbf{x}$ is given by

$$c(\mathbf{x})\frac{\partial p(\mathbf{x})}{\partial n_{\mathbf{x}}} + \int_{\Gamma_s} \frac{\partial^2 G}{\partial n_{\mathbf{x}} \partial n_{\mathbf{y}}} p(\mathbf{y}) d\Gamma = \int_{\Gamma_s} \frac{\partial G}{\partial n_{\mathbf{x}}} \frac{\partial p(\mathbf{y})}{\partial n_{\mathbf{y}}} d\Gamma + \frac{\partial p^{\mathrm{inc}}(\mathbf{x})}{\partial n_{\mathbf{x}}} \tag{5.12}$$

and the Combined Hypersingular BIE (CHBIE) due to Burton and Miller [22] is

$$\begin{aligned} c(\mathbf{x})p(\mathbf{x}) + \alpha c(\mathbf{x})\frac{\partial p(\mathbf{x})}{\partial n_{\mathbf{x}}} + \int_{\Gamma_s} \frac{\partial G}{\partial n_{\mathbf{y}}} p(\mathbf{y}) d\Gamma + \alpha \int_{\Gamma_s} \frac{\partial^2 G}{\partial n_{\mathbf{x}} \partial n_{\mathbf{y}}} p(\mathbf{y}) d\Gamma = \\ \int_{\Gamma_s} G \frac{\partial p(\mathbf{y})}{\partial n_{\mathbf{y}}} d\Gamma + \alpha \int_{\Gamma_s} \frac{\partial G}{\partial n_{\mathbf{x}}} \frac{\partial p(\mathbf{y})}{\partial n_{\mathbf{y}}} d\Gamma + p^{\mathrm{inc}}(\mathbf{x}) + \alpha \frac{\partial p^{\mathrm{inc}}(\mathbf{x})}{\partial n_{\mathbf{x}}} \end{aligned} \tag{5.13}$$

where α is a coupling constant most commonly taken as i/k. In the present study, we analyse the acoustic scattering from a sound hard surface for which the normal derivative of the total acoustic pressure vanishes. Therefore, all the terms in (5.13) involving the term $\frac{\partial p}{\partial n}$ vanish. Although (5.13) results in a unique solution, its main drawback remains the numerical treatment of the hypersingular integral, i.e. the last integral on the left hand side. Chen *et al* [30] and more recently Li and Huang [109] presented the following weakly singular form of the hypersingular

integral

$$\int_{\Gamma_s} \frac{\partial^2 G}{\partial n_{\mathbf{x}} \partial n_{\mathbf{y}}} p(\mathbf{y}) d\Gamma = \int_{\Gamma_s} \left[\frac{\partial^2 G}{\partial n_{\mathbf{x}} \partial n_{\mathbf{y}}} - \frac{\partial^2 G_0}{\partial n_{\mathbf{x}} \partial n_{\mathbf{y}}} \right] p(\mathbf{y}) \Gamma \tag{5.14}$$
$$+ \int_{\Gamma_s} \left[p(\mathbf{y}) - p(\mathbf{x}) - \nabla p(\mathbf{x}) \cdot (\mathbf{y} - \mathbf{x}) \right] \frac{\partial^2 G_0}{\partial n_{\mathbf{x}} \partial n_{\mathbf{y}}} d\Gamma$$
$$+ \int_{\Gamma_s} \nabla p(\mathbf{x}) \cdot n_{\mathbf{y}} \frac{\partial G_0}{\partial n_{\mathbf{x}}} d\Gamma - \frac{1}{2} \nabla p(\mathbf{x}) \cdot n_{\mathbf{x}}$$

where G_0 is the free space Green's function for the Laplace equation and is given as

$$G_0 = \frac{1}{2\pi} \ln \left(\frac{1}{r} \right). \tag{5.15}$$

Again, for the present case of a hard boundary, the last term on the right hand side of (5.14) vanishes. Consequently, the final equation for this case of a hard boundary can be expanded as

$$c(\mathbf{x}) p(\mathbf{x}) + \int_{\Gamma_s} \frac{\partial G}{\partial n_{\mathbf{y}}} p(\mathbf{y}) d\Gamma + \alpha \int_{\Gamma_s} \left[\frac{\partial^2 G}{\partial n_{\mathbf{x}} \partial n_{\mathbf{y}}} - \frac{\partial^2 G_0}{\partial n_{\mathbf{x}} \partial n_{\mathbf{y}}} \right] p(\mathbf{y}) d\Gamma \tag{5.16}$$
$$+ \alpha \int_{\Gamma_s} \left[p(\mathbf{y}) - p(\mathbf{x}) - \nabla p(\mathbf{x}) \cdot (\mathbf{y} - \mathbf{x}) \right] \frac{\partial^2 G_0}{\partial n_{\mathbf{x}} \partial n_{\mathbf{y}}} d\Gamma +$$
$$\alpha \int_{\Gamma_s} \nabla p(\mathbf{x}) \cdot n_{\mathbf{y}} \frac{\partial G_0}{\partial n_{\mathbf{x}}} d\Gamma = p^{\text{inc}}(\mathbf{x}) + \alpha \frac{\partial p^{\text{inc}}(\mathbf{x})}{\partial n_{\mathbf{x}}}.$$

The explicit expressions for various derivatives of the Green's function involved in (5.16) are given Appendix A. The second approach to handle the non-uniqueness problem, namely the CHIEF formulation, relies on adding some extra collocation points in the interior of the scatterer and then solving the resulting system of equations. This essentially is appending the discretized form of the CBIE with some additional equations evaluated in the interior of the scatterer. Since the discretization process is the same either for CHBIE used previously or CHIEF and since both will contain the CBIE, we first discuss the discretized form of CHBIE and this will then be followed by the implementation of the CHIEF method.

5.4.1.1 Plane wave basis and and discretization of CHBIE

Recall the equation in compact form for the plane wave basis for the approximation of pressure. We have reproduced (4.54a) for convenience,

$$p(\mathbf{y}) = \boldsymbol{\mathcal{R}}^e(\mathbf{y}) \boldsymbol{\mathcal{A}}^e(\mathbf{y}), \qquad \mathbf{y} \in \Gamma_s \tag{5.17}$$

The $\boldsymbol{\mathcal{R}}^e(\mathbf{y})$ term indicates that the vector corresponds to the boundary element containing the point $\mathbf{y}$ and $\boldsymbol{\mathcal{A}}^e(\mathbf{y})$ is the vector of unknown plane wave amplitudes of the boundary element nodes containing the point $\mathbf{y}$. Using (5.17), we can write the following discretized form of (5.16)

$$C_1 + \sum_{s=1}^{s=4} \sum_{e=1}^{n_e} I_s^e = C_2 + C_3 \tag{5.18}$$

where

$$C_1 = c(\mathbf{x}) \boldsymbol{\mathcal{R}}^e(\mathbf{x}) \boldsymbol{\mathcal{A}}^e(\mathbf{x}) \tag{5.19}$$

$$I_1^e = \int_{\Gamma_s^e} \left(\frac{\partial G}{\partial n_{\mathbf{y}}} \right) \boldsymbol{\mathcal{R}}^e(\mathbf{y}) \boldsymbol{\mathcal{A}}^e(\mathbf{y}) d\Gamma^e \tag{5.20}$$

$$I_2^e = \alpha \int_{\Gamma_s^e} \frac{\partial^2 G}{\partial n_{\mathbf{x}} \partial n_{\mathbf{y}}} \left(\boldsymbol{\mathcal{R}}^e(\mathbf{y}) \boldsymbol{\mathcal{A}}^e(\mathbf{y}) - \boldsymbol{\mathcal{R}}^e(\mathbf{x}) \boldsymbol{\mathcal{A}}^e(\mathbf{x}) \right) d\Gamma^e \tag{5.21}$$

$$I_3^e = \alpha \int_{\Gamma_s^e} \frac{\partial^2 G_0}{\partial n_{\mathbf{x}} \partial n_{\mathbf{y}}} \left(\boldsymbol{\mathcal{R}}^e(\mathbf{y}) \boldsymbol{\mathcal{A}}^e(\mathbf{y}) - \boldsymbol{\mathcal{R}}^e(\mathbf{x}) \boldsymbol{\mathcal{A}}^e(\mathbf{x}) \right) - \left(\frac{\partial \boldsymbol{\mathcal{R}}^e(\mathbf{x})}{\partial x} \boldsymbol{\mathcal{A}}^e(\mathbf{x}) r_x + \frac{\partial \boldsymbol{\mathcal{R}}^e(\mathbf{x})}{\partial y} \boldsymbol{\mathcal{A}}^e(\mathbf{x}) r_y \right) d\Gamma^e \tag{5.22}$$

$$I_4^e = \alpha \int_{\Gamma_s^e} \frac{\partial \boldsymbol{\mathcal{R}}^e(\mathbf{x})}{\partial x} \boldsymbol{\mathcal{A}}^e(\mathbf{x}) n_x(\mathbf{x}) + \frac{\partial \boldsymbol{\mathcal{R}}^e(\mathbf{x})}{\partial y} \boldsymbol{\mathcal{A}}^e(\mathbf{x}) n_y(\mathbf{y}) d\Gamma^e(q) \tag{5.23}$$

and

$$C_2 = p^{\text{inc}}(\mathbf{x}) \ ; \ C_3 = \alpha \frac{\partial p^{\text{inc}}(\mathbf{x})}{\partial n_{\mathbf{x}}} \tag{5.24}$$

where n_e is the total number of boundary elements dividing the boundary Γ_s, and Γ^e is the division of Γ_s corresponding to the e^{th} boundary element, $a_{jm}(\mathbf{x})$ ($a_{jm}(\mathbf{y})$) is the amplitude of m^{th} plane wave associated with j^{th} node on the element that contains the collocation point $\mathbf{x}$ (field point $\mathbf{y}$), $N_j(\mathbf{x})$ ($N_j(\mathbf{y})$) are the polynomial shape functions for node j of the element containing the collocation point $\mathbf{x}$ (field point $\mathbf{y}$), $n_x(\mathbf{y})$ and $n_y(\mathbf{y})$ are the x and y components of the unit outward normal at the field point $\mathbf{y}$ on the boundary Γ_s. Also, $r_x = x(\mathbf{y}) - x(\mathbf{x})$ and $r_y = y(\mathbf{y}) - y(\mathbf{x})$ where x and y are the Cartesian coordinates. Choosing appropriate locations on the boundary Γ_s as collocation points $\mathbf{x}$ yields the following set of linear equations

$$[\bar{\mathbf{H}}]\{\bar{\mathbf{a}}\} = \{\bar{\mathbf{F}}\} \tag{5.25}$$

where the vector $\bar{\mathbf{a}}$ contains the amplitudes of plane waves. The load vector $\bar{\mathbf{F}}$ is obtained as

$$\{\bar{\mathbf{F}}\} = \{\mathbf{C_2} + \mathbf{C_3}\} \tag{5.26}$$

where $\{\mathbf{C_2}\}$ and $\{\mathbf{C_3}\}$ are the vectors formed using (5.24). The matrix $\bar{\mathbf{H}}$ is obtained by evaluating the boundary integrals. The solution of the linear system (5.25) yields the amplitudes of the plane waves, $\boldsymbol{\mathcal{A}}^e$ which can be used to recover the acoustic pressures on the boundary Γ_s using (5.17).

5.4.2 CHIEF formulation

For the CHIEF formulation, we need some additional equations formed using the collocation points in the interior of the scatterer (i.e. $\mathbf{x} \in \Omega_s$). If the collocation point $\mathbf{x}$ is moved in the interior, the CBIE in the interior becomes

$$\int_{\Gamma_s} \frac{\partial G}{\partial n_{\mathbf{y}}} p(\mathbf{y}) d\Gamma = p^{\text{inc}}(\mathbf{x}), \quad \mathbf{y} \in \Gamma_s, \mathbf{x} \in \Omega_s \tag{5.27}$$

Note that we have omitted the term containing $\frac{\partial p}{\partial n_{\mathbf{y}}}$ as the scatterer is assumed to be sound hard[‡]. Secondly, the jump term $c(\mathbf{x}) = 0$ by definition as for any interior collocation point, the term $c(\mathbf{x})$ vanishes. Following the similar discretization process as described in §5.4.1.1, we can write (5.27) in the following discretized form,

$$\sum_{e=1}^{n_e} I^e_{\text{int}} = f_{\text{int}} \tag{5.28}$$

where

$$I^e_{\text{int}} = \int_{\Gamma^e_s} \frac{\partial G}{\partial n_{\mathbf{y}}} \boldsymbol{\mathfrak{R}}^e(\mathbf{y}) \boldsymbol{\mathcal{A}}^e(\mathbf{y}) d\Gamma^e, \quad \mathbf{y} \in \Gamma_s, \mathbf{x} \in \Omega_s \tag{5.29}$$

and

$$f_{\text{int}} = p^{\text{inc}}(\mathbf{x}), \quad \mathbf{x} \in \Omega_s. \tag{5.30}$$

Choosing the interior collocation locations $\mathbf{x}$, we can form a set of linear equations

$$[\bar{\mathbf{H}}_{\text{int}}]\{\bar{\mathbf{a}}_{\text{int}}\} = \{\bar{\mathbf{F}}_{\text{int}}\} \tag{5.31}$$

[‡]This is because $\mathbf{y} \in \Gamma_s$ and Γ_s is sound hard.

Additionally, we can form another system of equations by using the terms I_1, C_1 and C_2 alone as they correspond to the discretized form of the CBIE.

$$[\bar{\mathbf{H}}_{\text{CBIE}}]\{\bar{\mathbf{a}}_{\text{CBIE}}\} = \{\bar{\mathbf{F}}_{\text{CBIE}}\} \tag{5.32}$$

It can be seen that the matrix $[\bar{\mathbf{H}}_{\text{CBIE}}]$ is obtained by evaluating the boundary integrals corresponding to the CBIE only (i.e. (5.10) minus the integral containing the $\frac{\partial p}{\partial n}$ term). The final system of equations for the CHIEF formulation is then given as

$$\begin{bmatrix} \bar{\mathbf{H}}_{\text{CBIE}} \\ \bar{\mathbf{H}}_{\text{int}} \end{bmatrix} \begin{Bmatrix} \bar{\mathbf{a}}_{\text{CBIE}} \\ \bar{\mathbf{a}}_{\text{int}} \end{Bmatrix} = \begin{Bmatrix} \bar{\mathbf{F}}_{\text{CBIE}} \\ \bar{\mathbf{F}}_{\text{int}} \end{Bmatrix} \tag{5.33}$$

Now, in order to ensure a unique solution using the CHIEF formulation, the questions that naturally arise are,

1. where do we place the interior ($\mathbf{x} \in \Omega_s$) collocation points?

2. how many such points are sufficient to ensure that the non-uniqueness problem is solved?

We will answer these questions through the numerical examples presented in §5.8.

5.5 Collocation

We discussed earlier in §2.3.2 the requirement for an exact geometry for PUBEM in order to obtain accurate results. We therefore use the exact geometry of the scatterer so that Γ_s^e becomes analytical and is given as

$$\Gamma_s^e = \{\gamma_s^e(\xi) : -1 \leq \xi \leq 1\}. \tag{5.34}$$

It is a common practice in the conventional BEM to use the boundary element nodes as the collocation points. However, since the number of unknowns is increased due to the introduction of the plane wave basis, we require additional collocation points as the total number of unknowns has now increased to $2n_eM$ as compared to $2n_e$ for conventional collocation BEM, for the case of a 3-noded continuous element. It is therefore convenient to write,

$$\mathcal{P}_s = \left\{\gamma_s^e(\xi) : \xi = a - 2 + \frac{m-1}{M},\ a = 1, 2,\ m = 1, 2, ..M.\right\} \tag{5.35}$$

where $s = 1, 2, ..., 2M$, with $2M$ being the total number of degrees of freedom for the element Γ_s^e. It follows immediately that (5.35) generates the collocation points p_s that are regularly spaced in $\{\xi : -1 \leq \xi \leq 1\}$. A theoretical restriction on the continuity of the acoustic pressure requires further attention to the placement of point $\mathcal{P}$ in the case where two adjacent elements are concerned. A frequently mentioned problem with continuous elements for the use with hypersingular integrals is the Hölder continuity requirement on the density function (or the acoustic pressure in the present case). The Hölder continuity requirement needs the density functions to be $C^{1,\alpha}$ continuous whereas the continuous elements are only $C^{0,\alpha}$ continuous at the inter-element edges. Although satisfactory results have been presented by violating this condition [113], we will follow a collocation strategy where the collocation points always lie entirely inside an element which automatically satisfies the $C^{1,\alpha}$ condition [98].

5.6 Numerical integration

It can be observed that the boundary integrals in (5.16) become oscillatory in nature due to the introduction of the plane wave basis apart from the inherent oscillatory nature of the fundamental solution present in the kernel of the integral equation, i.e. the Green's function. A complicating factor for the integration is that the PUBEM formulation encourages the use of elements spanning many wavelengths, so there is the requirement to evaluate accurately highly oscillatory integrals. Apart from the requirement of using an analytical geometry where possible, accuracy of the PUBEM solution heavily depends on how accurately these oscillatory integrals are evaluated. Also it should not be forgotten that the PUBEM system is highly ill-conditioned and the errors in modelling the geometry can result in erroneous solution particularly at high frequencies. We use a subdivision of the $-1 \leq \xi \leq 1$ interval into C cells of equal size to evaluate the oscillatory integrals using Gauss quadrature. In the present work, we use 10 Gauss points per cell. There are other more sophisticated integration schemes but this scheme is adopted, namely, element subdivision in C equal length cells, for its robustness. To make this concept clear, let us rewrite one of the boundary integrals, say I_1^e (see (5.20)),

$$I_1^e = \int_{\Gamma^e} \left(\frac{\partial G}{\partial n_{\mathbf{y}}} \right) \sum_{j=1}^{3} N_j(\mathbf{y}) \sum_{m=1}^{M_j} a_{jm}(\mathbf{y}) e^{ikd_{jm}\cdot\mathbf{y}} d\Gamma^e \tag{5.36}$$

Using the first parametric mapping (5.34), I_1^e can be written as

$$I_1^e = \int_{\xi=-1}^{\xi=1} \left(\frac{\partial G}{\partial n_{\mathbf{y}}} \right) \sum_{j=1}^{3} N_j(\mathbf{y}) \sum_{m=1}^{M_j} a_{jm}(\mathbf{y}) e^{ikd_{jm}\cdot\mathbf{y}} J(\xi) d\xi \tag{5.37}$$

where $J(\xi)$ is the Jacobian of transformation $\Gamma^e \to \xi$. Now, using the division of the ξ interval in C cells, we can write (5.37) as

$$I_1^e = \sum^{C} \int_{\eta=-1}^{\eta=1} \left(\frac{\partial G}{\partial n_{\mathbf{y}}} \right) \sum_{j=1}^{3} N_j(\mathbf{y}) \sum_{m=1}^{M_j} a_{jm}(\mathbf{y}) e^{ikd_{jm}\cdot\mathbf{y}} J(\eta) d\eta. \tag{5.38}$$

Now η is the local coordinate in each individual cell and $J(\eta)$ is the Jacobian of transformation $\Gamma^e \to \eta$. Note that $\xi \to \eta$ is a simple linear mapping.

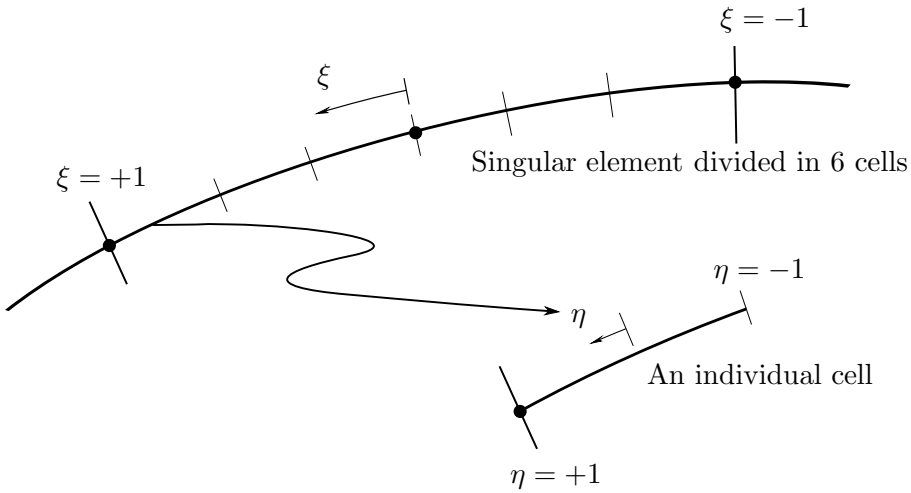

Figure 5.6: Cell subdivision for oscillatory integrals in PUBEM

5.7 Coordinate transformation techniques for weakly singular integrals

It was briefly mentioned in Chapter 3 (see §3.7, also see Figure 3.4) that the Green's function for the Helmholtz equation in 2D exhibits singular nature due to the Bessel function of the second kind $Y_n(\cdot)$. We also reviewed the definitions of various orders of singularities in §5.3. As was mentioned in §5.6, the integrals obtained after regularisation of the hypersingular integral following the approach of Chen *et al* [30] are still weakly singular. This requires a suitable coordinate transformation to be applied so that the integrals are evaluated correctly. From the several coordinate transformation methods available, we compare the performance of four

different techniques for evaluating the weakly singular integrals in (5.16). The coordinate transformation methods investigated here are i) Telles [173], ii) Monegato - Sloan (MS [130]), iii) bicubic [23] and iv) Wu's transformation [186]. The Telles and MS transformations are applied in the entire local interval $\eta \in (-1, 1)$ if it contains the singular point, $\mathbf{x}$. Bicubic and Wu's scheme, on the other hand, split this local interval (η) towards the left and right of the singularity (i.e. the point $\mathbf{x}$) and then apply the transformation in each individual interval. It may be noted that all of these techniques are aimed only at handling weakly singular integrals.

The various coordinate transformations discussed here rely on mapping the original local coordinate η in to a different coordinate, say γ. Naturally, while performing the mapping from η to γ, we will need to compute the Jacobian of transformation, say $J(\gamma)$. It is this Jacobian, in most cases, that handles the weak singularity. The underlying principle being, the coordinate transformation $\eta \to \gamma$ is written such that, at the singular point, the Jacobian of transformation $J(\gamma)$ has a minimum value (ideally zero for a truly singular function). Thus, at the singularity, we multiply a high value of the integrand[§] by a very low value of Jacobian $J(\gamma)$ and thus we have a regular function. In the following sections, we briefly review the coordinate transformation techniques.

5.7.1 Telles transformation

The Telles transformation uses the following nonlinear coordinate mapping

$$\eta(\gamma) = a\gamma^3 + b\gamma^2 + c\gamma + d \tag{5.39}$$

Equation (5.39) thus gives a third degree relation between η and γ. Let us denote the intrinsic coordinate at the singular point $\mathbf{x}$ as $\bar{\eta}$. Then, the constants a, b, c and d can be found by using following conditions

$$\eta|_{\gamma=1} = 1 \tag{5.40a}$$

$$\eta|_{\gamma=-1} = -1 \tag{5.40b}$$

$$\frac{d\eta}{d\gamma}|_{\bar{\eta}} = 0 \tag{5.40c}$$

$$\frac{d^2\eta}{d\gamma^2}|_{\bar{\eta}} = 0 \tag{5.40d}$$

[§]Because the integrand is singular at $\mathbf{x} = \mathbf{y}$

The conditions in (5.40a) and (5.40b) are trivial. The condition in (5.40c) indicates that the Jacobian $J(\gamma)$ should decrease the order of singularity at the singular point $\bar{\eta}$. The fourth condition in (5.40d) specifies that the gradient of the singularity is smooth at the singular point after the coordinate transformation. The constants in (5.39) are then given as,

$$a = 1/Q \tag{5.41a}$$

$$b = -d = -3\bar{\gamma}/Q \tag{5.41b}$$

$$c = 3\bar{\gamma}^2/Q \tag{5.41c}$$

$$Q = 1 + 3\bar{\gamma}^2 \tag{5.41d}$$

where

$$\bar{\gamma} = (\bar{\eta}\eta^* + |\eta^*|)^{\frac{1}{3}} + (\bar{\eta}\eta^* - |\eta^*|)^{\frac{1}{3}} + \bar{\eta} \tag{5.42a}$$

$$\eta^* = \bar{\eta}^2 - 1 \tag{5.42b}$$

Let $f(\eta)$ be a weakly singular function at $\eta = \bar{\eta}$ where $\eta \in [-1, 1]$. Then,

$$I = \int_{\eta=-1}^{\eta=1} f(\eta) d\eta \tag{5.43}$$

is a weakly singular integral. The coordinate mapping $\eta \to \gamma$ gives the following regular integral,

$$I = \int_{\gamma=-1}^{\gamma=1} f(\eta(\gamma)) J(\gamma) d\gamma, \tag{5.44}$$

where

$$J(\gamma) = \frac{3(\gamma - \bar{\gamma})^2}{1 + 3\bar{\gamma}^2} \tag{5.45}$$

Equation (5.44) can be implemented with the usual Gauss quadrature. An important feature of Telles transformation is that the Gauss integration points get clustered near the singular point. Since we have a higher density of the integration points near the singular point, the integrand is now smooth and accurate evaluation of the integral becomes possible.

5.7.2 Bicubic transformation

The concept used in bicubic transformation is similar to the Telles transformation. As the name suggests, the singular interval (in the present case $\eta \in [-1, 1]$) is divided in to two parts viz. towards the left and the right of the singular point $\bar{\eta}$, and a cubic transformation is then applied separately in both parts. The bicubic transformation is originally attributed to Cerrolaza and Alarcon [23]. Consider the weakly singular integral in (5.43 and let the interval $\eta \in [-1, 1]$ be divided in to two parts i) $\eta_1 \in [-1, \bar{\eta}]$ (left of singularity) and ii) $\eta_2 \in [\bar{\eta}, 1]$ (right of singularity). Thus, (5.43) can be rewritten as

$$\begin{aligned} I &= \int_{\eta=-1}^{\eta=1} f(\eta) d\eta \\ &= \int_{\eta_1=-1}^{\eta_1=\bar{\eta}} f(\eta_1) d\eta_1 + \int_{\eta_2=\bar{\eta}}^{\eta_2=1} f(\eta_2) d\eta_2 \end{aligned} \tag{5.46}$$

Note that, the left interval is given by $\eta_1 \in [-1, \bar{\eta}]$ and the right interval by $\eta_2 \in [\bar{\eta}, 1]$ and these coordinates are given as

$$\eta_1 = \bar{\eta} + A(\zeta_1 - 1)^2 + B(\zeta_1 - 1)^3 \tag{5.47a}$$

$$\eta_2 = \bar{\eta} + C(\zeta_2 - 1)^2 + D(\zeta_2 - 1)^3 \tag{5.47b}$$

Following the transformations given in (5.47) the coordinates η_1 and η_2 will be replaced by ζ_1 and ζ_2 respectively. Thus, similar to the conditions mentioned in (5.40), we can write for ζ_1,

$$\eta_1|_{\zeta_1=-1} = -1 \tag{5.48a}$$

$$\eta_1|_{\zeta_1=1} = \bar{\eta} \tag{5.48b}$$

$$\eta_1|_{\mu_n} = \bar{\eta} - \epsilon \tag{5.48c}$$

and

$$\eta_1|_{\zeta_2=-1} = \bar{\eta} \tag{5.49a}$$

$$\eta_1|_{\zeta_2=1} = 1 \tag{5.49b}$$

$$\eta_1|_{-\mu_n} = \bar{\eta} + \epsilon \tag{5.49c}$$

where μ_n is the largest Gaussian point abscissa of the Gauss quadrature rule being used. The constants A, B, C and D are given as

$$A = \frac{-8\epsilon - (1+\bar{\eta})(\mu_n - 1)^3}{8(\mu_n - 1)^2 + 4(\mu_n - 1)^3}, \qquad B = -\frac{4\epsilon - (1+\bar{\eta})(\mu_n - 1)^2}{8(\mu_n - 1)^2 + 4(\mu_n - 1)^3} \tag{5.50a}$$

$$C = \frac{8\epsilon + (1-\bar{\eta})(\mu_n - 1)^3}{8(\mu_n - 1)^2 + 4(\mu_n - 1)^3}, \qquad D = \frac{-4\epsilon + (1-\bar{\eta})(\mu_n - 1)^2}{8(\mu_n - 1)^2 + 4(\mu_n - 1)^3} \tag{5.50b}$$

Thus, after the coordinate mappings, (5.46) can be rewritten as

$$I = \int_{\zeta_1=1}^{\zeta_1=1} f(\eta_1(\zeta_1))J(\zeta_1)d\zeta_1 + \int_{\zeta_2=1}^{\zeta_2=1} f(\eta_2(\zeta_2))J(\zeta_2)d\zeta_2 \tag{5.51}$$

where the Jacobians of transformation are given as

$$J(\zeta_1) = 2A(\zeta_1 - 1) + 3B(\zeta_1 - 1)^2 \tag{5.52a}$$

$$J(\zeta_2) = 2C(\zeta_2 + 1) + 3D(\zeta_2 + 1)^2 \tag{5.52b}$$

As seen from (5.48c) and (5.49c), the bicubic mapping depends on a parameter ϵ and Chen [31] derived an expression for optimal value of ϵ given by the following inequality,

$$\epsilon > \frac{1 + \bar{\eta}(1 - \mu_n)^2}{4} \tag{5.53}$$

5.7.3 Wu's transformation

This technique relies again on interval splitting. Wu's [186] transformation ($\eta \to \gamma$) is given as

$$\eta = \bar{\eta} - \gamma^2, \qquad \eta < \bar{\eta} \tag{5.54a}$$

$$\eta = \bar{\eta} + \gamma^2, \qquad \eta > \bar{\eta} \tag{5.54b}$$

Thus,

$$\gamma = \sqrt{1 + \bar{\eta}}\Big|_{\eta=-1} \tag{5.55a}$$

$$\gamma = \sqrt{1 - \bar{\eta}}\Big|_{\eta=1} \tag{5.55b}$$

$$\gamma = 0|_{\eta=\bar{\eta}} \tag{5.55c}$$

The weakly singular integral therefore is divided as follows,

$$I = \int_{\gamma=\sqrt{1+\bar{\eta}}}^{\gamma=0} f(\eta(\gamma))J(\gamma)d\gamma + \int_{\gamma=0}^{\gamma=\sqrt{1-\bar{\eta}}} f(\eta(\gamma))J(\gamma)d\gamma \tag{5.56}$$

It should be noted that, from (5.54), differentiation gives,

$$d\eta = -2\zeta d\gamma, \qquad \eta < \bar{\eta} \tag{5.57a}$$

$$d\eta = 2\zeta d\gamma, \qquad \eta > \bar{\eta} \tag{5.57b}$$

Clearly, when working in the transformed coordinate γ, the Jacobian of transformation will involve a factor of 2γ. Since 2γ tends to zero much faster than $2\ln(\gamma)$, any logarithmic singularity will be effectively cancelled. Note that (5.56) does not have the usual [-1,1] limits to be able to implement the usual Gauss quadrature and therefore needs a further transformation.

5.7.4 Monegato-Sloan transformation

The Monegato-Sloan transformation (MST) can be considered as a generalised polynomial transformation. The Telles transformation mentioned previously is a special case of the MST. Although Monegato and Sloan used their scheme for the solution of integral equations for an airfoil problem, the use of MST for singular integrals was first investigated by Johnston and Elliot [89]. A MST of order q can be given as

$$\gamma = \bar{\eta} + \delta(\bar{\eta}, m)(\eta - \eta_0)^m \tag{5.58}$$

where

$$\delta(\bar{\eta}, m) = 2^{-m}\left([1+\bar{\eta}]^{\frac{1}{m}} + [1-\bar{\eta}]^{\frac{1}{m}}\right)^m \tag{5.59}$$

and

$$\eta_0 = \frac{[1+\bar{\eta}]^{\frac{1}{m}} - [1-\bar{\eta}]^{\frac{1}{m}}}{[1+\bar{\eta}]^{\frac{1}{m}} + [1-\bar{\eta}]^{\frac{1}{m}}} \tag{5.60}$$

and the parameter m must be an odd integer. Thus the weakly singular integral when MST is used can be given as follows,

$$I = \int_{\gamma=-1}^{\gamma=1} f(\eta(\gamma))J(\gamma)d\gamma \tag{5.61}$$

where

$$J(\gamma) = m2^{-m}\left([1+\bar{\eta}]^{\frac{1}{m}} + [1-\bar{\eta}]^{\frac{1}{m}}\right)(\eta-\eta_0)^{m-1} \tag{5.62}$$

5.7.5 Split Telles transformation

It has been demonstrated by Singh and Tanaka that the cubic transformations, such as Telles, are not very effective when the singularity is at the end of the singular element [164]. This can be a case when a continuous element (2 or 3 noded) is used and nodal collocation is performed. In such cases, Singh and Tanaka suggest that the singular element be partitioned and the Telles scheme is then applied separately in each part and therefore called 'Split Telles transformation'. Though this is similar to the bicubic approach, it may be noted that the split Telles approach does not need a criterion as required by the bicubic method (see (5.53)). The weakly singular integral following a split Telles approach can be given as [164]

$$I = I_1 + I_2 \tag{5.63}$$

where

$$I_1 = \frac{3}{8}(1+\bar{\eta})\int_{-1}^{1} f(\eta(\eta_1(\gamma),\gamma_s)(\gamma-1)^2 d\gamma \tag{5.64a}$$

$$I_2 = \frac{3}{8}(1-\bar{\eta})\int_{-1}^{1} f(\eta(\eta_2(\gamma),\gamma_s)(\gamma+1)^2 d\gamma \tag{5.64b}$$

and the non-linear transformations in each interval are given as

$$\eta_1(\gamma) = \frac{1}{4}\left(\gamma^3 - 3\gamma^2 + 3\gamma + 3\right), \qquad \bar{\eta} = 1 \tag{5.65a}$$

$$\eta_1(\gamma) = \frac{1}{4}\left(\gamma^3 - 3\gamma^2 + 3\gamma - 3\right), \qquad \bar{\eta} = -1 \tag{5.65b}$$

5.8 Scattering from sound hard cylinder(s)

Recall the definition used for parameter τ for BEM in Chapter 1 (see (1.2b)). We rewrite (1.2b) and remembering wavelength $\lambda = 2\pi/k$,

$$\begin{aligned}\tau &= \lambda\left(\frac{nDof}{Length}\right)\\ &= \left(\frac{2\pi}{k}\right)\frac{T}{2\pi a}\\ &= \frac{T}{ka}\end{aligned} \tag{5.66}$$

where T is the total number of degrees of freedom in the system for one cylinder and a is the radius of the cylinder. Thus, for the problem of scattering from a single cylinder with unit radius, $\tau = T/k$ where T will be the product of the total number of nodes on the scatterer boundary and number of plane waves per node. It should be noted that we use one integration cell per collocation point and thus the total number of degrees of freedom T (in 5.66) is equal to the total number of integration cells used on the boundary of one cylinder, i.e.

$$T = n_e C \tag{5.67}$$

The parameter C is the number of integration cells per element (see 5.38). For all the results presented in this chapter the parameter $\tau \approx 3.0$ unless otherwise mentioned. This value has been found to be sufficient to recover solutions with acceptable engineering accuracy with L^2 errors close to 1% and moderate condition numbers which can be efficiently handled with the SVD algorithm, see [145]. For smooth scatterers, this accuracy will be shown to be much better ($\approx 10^{-4}$). Also all the results are obtained with 30 integration (Gauss) points per wavelength unless otherwise mentioned. Note that the focus of present thesis is to develop an algorithm for coupling PUFEM with PUBEM. Therefore, a rigorous numerical study of the number of integration points per wavelength needed for PUBEM, for a given range of k and geometry is not presented here. For both the single cylinder and four cylinder examples, we use two 3-noded continuous elements per cylinder along with the trigonometric shape functions presented by Peake *et al* [141]. The trigonometric shape functions have been shown to improve the accuracy over the conventional polynomial shape functions because of their smoothness and

C^∞ continuity; see [141]. Thus the single cylinder case has only two continuous elements and the four cylinder case uses 8 continuous elements. For all computations the integration points are placed analytically on the scatterer boundary. We now define the relative L^2 error for the total acoustic pressure p on the boundary Γ, $E^2(\Gamma_s)$ as

$$E^2(\Gamma_s) = \frac{\|p - \tilde{p}\|}{\|\tilde{p}\|} \tag{5.68}$$

where p is the numerically computed solution and $\tilde{p}$ is the analytical solution computed using the infinite or approximate series for a given scattering problem [20]. Note that the norms in (5.68) are taken in L^2 sense over the boundary Γ_s. The coefficient matrix $\bar{\mathbf{H}}$ generated using the plane wave basis is always highly ill-conditioned. A typical condition number for the coefficient matrix $\bar{\mathbf{H}}$ for a moderately high value of $k > 100$ is approximately 10^{15}. The problem of poorly conditioned systems due to the use of the plane waves has been widely reported; see the discussion in [103] and the references therein. In general, the condition number for a plane wave enriched BEM increases as the wavenumber increases. Clearly, in order to obtain accurate and reliable results from such highly ill-conditioned systems one must ensure that sufficient arithmetic precision is maintained in the computation of the matrix terms. We use double precision arithmetic for all the computations in this study. A natural choice for obtaining accurate solution from the ill-conditioned system (5.25) is therefore the SVD technique. The applicability of SVD for obtaining accurate solutions from ill-conditioned systems is well established and the readers may be referred to the benchmark paper by Golub and Kahan [62] for the underlying theory. In the present study, we obtain the solution vector $\bar{\mathbf{a}}$ in (5.25) by solving the following complex linear least squares problem:

$$\min \|\bar{\mathbf{F}} - \bar{\mathbf{H}}\bar{\mathbf{a}}\|^2 \tag{5.69}$$

using the SVD of $\bar{\mathbf{H}}$.

The 2-norm condition number for the matrix $\bar{\mathbf{H}}$, $\kappa(\bar{\mathbf{H}})$ may be defined as

$$\kappa(\bar{\mathbf{H}}) = \frac{\sigma_{\max}(\bar{\mathbf{H}})}{\sigma_{\min}(\bar{\mathbf{H}})} \tag{5.70}$$

where $\sigma_{\max}(\bar{\mathbf{H}})$ and $\sigma_{\min}(\bar{\mathbf{H}})$ are the maximum and minimum singular values of the matrix $\bar{\mathbf{H}}$ respectively computed using the SVD. Relevant routines from the LAPACK library are used to solve (5.69) [3]. As discussed in §5.1, the placement of interior collocation points for the CHIEF method can become an issue. For the numerical examples presented here, the interior points are placed randomly in the interior of the cylinder(s). This randomness can practically guarantee that there will always be enough CHIEF points to provide the linear independence needed to obtain a unique solution. The number of interior points (or the number of CHIEF equations) used here is 20% of the total number of equations in (5.25) since this has been found to give stable results for the CHIEF method. Also the CHIEF points in the interior of the cylinder(s) are placed such that the integrals in the CHIEF integral equation (5.27) do not become near-singular. For this, the interior collocation points are placed in a circle of radius $0.9a$ (a being the radius of the cylinder), and within this circle the interior collocation points are placed randomly.

5.8.1 Scattering from a single sound hard cylinder

We first investigate the performance of CHIEF and Burton-Miller methods for the classical problem of plane wave scattering from an acoustically hard cylinder of infinite extent. The analytical solution for the scattered pressure on the surface of a hard cylinder centred at origin $(0, 0)$ due to an incident acoustic plane wave with direction $(-1, 0)$ is given by an infinite series [20],

$$p^s(\mathbf{x}) = -\frac{\mathrm{J}_0'(ka)}{\mathrm{H}_0'(ka)}\mathrm{H}_0(kr) - 2\sum_{\nu=1}^{\infty} i^\nu \frac{\mathrm{J}_\nu'(ka)}{\mathrm{H}_\nu'(ka)}\mathrm{H}_\nu(kr)\cos(\nu\theta), \tag{5.71}$$

where $\mathbf{x} = r(\cos(\theta), \sin(\theta))$, $\mathrm{H}_\nu(\cdot)$ is the Hankel function of the first kind and order ν, $\mathrm{J}_\nu(\cdot)$ is the Bessel function of the first kind and order ν. The prime sign denotes a derivative with respect to kr. The total acoustic pressure p can be computed by performing a complex addition of incident wave to the scattered pressure given by (5.71), i.e., $p = p^{\mathrm{inc}} + p^{\mathrm{sct}}$. The relative L^2 error for the total acoustic pressure is then computed using (5.68).

5.8.1.1 Truncated SVD

Before proceeding to the error analyses for the scattering problems with different coordinate transformation schemes for singular integrals, we first present results that demonstrate the ability of SVD to produce stable and accurate results via the single cylinder scattering problem. Since the coefficient matrix $\bar{\mathbf{H}}$ is ill-conditioned (or rank deficient), this makes the problem stated in (5.69) ill-posed because a small perturbation in the right hand side vector $\bar{\mathbf{b}}$ can result

in a significantly large perturbation in the solution vector $\bar{\mathbf{a}}$. It is therefore important to be able to solve (5.69) reliably when $\kappa(\bar{\mathbf{H}})$ is significantly high to obtain stable and accurate solution. In the present study, we use the truncated SVD routine ZGELSS from LAPACK to solve (5.69). The principle used in ZGELSS is to obtain a minimum $||\bar{a}||$ solution from the set of least squares solutions that minimize $\|\bar{\mathbf{b}} - \bar{\mathbf{H}}\bar{\mathbf{a}}\|^2$ over a solution space that is spanned by the singular vectors with singular values greater than ϵ_0, where ϵ_0 is the user input for the truncation threshold of singular values. This essentially means filtering out those singular values from the SVD of $\bar{\mathbf{H}}$ that are below ϵ_0 and solving (5.69) with a modified $\bar{\mathbf{H}}$, possibly with an improved rank. A well known method to estimate the suitable value for the parameter ϵ_0 is the so called L-curve method [70]. Figure 5.7 shows the L-curves for (5.25) for the problem of plane wave scattering from a single cylinder for three different wavenumbers, namely, $k = 32$, $k = 100$ and $k = 152$. The singular values (σ_c) computed using SVD for each wavenumber case corresponding to the respective L-curve corner points are also shown in Figure 5.7. For example, the corner value for $k = 32$ is $\sigma_c(k = 32) = 1.82 \times 10^{-4}$, indicating that it is possible to obtain accurate solution by truncating the singular values that are below $\sigma_c(k = 32)$, i.e. by setting $\epsilon_0 = 1.82 \times 10^{-4}$ for the $k = 32$ case. Although the threshold value ϵ_0 is dependent on the wavenumber of the problem being solved, in this study, we take the threshold $\epsilon_0 = 1.0 \times 10^{-10}$, as this was found to give satisfactory results for all the examples considered. This is demonstrated through numerical results for various values of ϵ_0 as shown in Figure 5.8. The results shown in Figure 5.8 are only for the CHIEF method, however, similar behaviour is observed in the results for the Burton-Miller method as well. As seen from Figure 5.8, it is clear that the SVD algorithm with $\epsilon_0 = 1.0 \times 10^{-10}$ produces stable results with very good accuracy (relative L^2 errors better than 10^{-4}).

5.8.1.2 Comparison of CHIEF and Burton-Miller methods with singular integration schemes

We now present the comparison between the CHIEF and the Burton-Miller methods with various singular integration schemes. Figure 5.9 shows the relative L^2 error, $E^2(\Gamma_s)$ for CHIEF and Burton-Miller methods and Figure 5.10 gives the comparison for the condition number defined in (5.70). The multiple lines for the Burton-Miller method in Figures 5.9-5.10 correspond to various coordinate transformation schemes used to handle the weakly singular integrals.

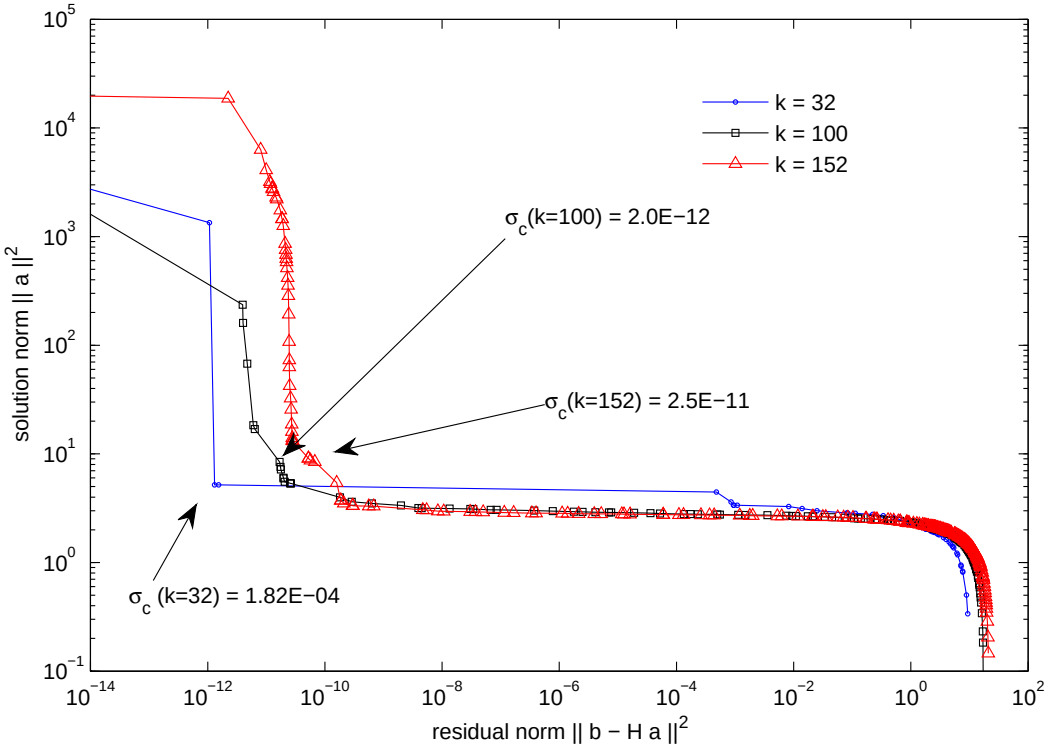

Figure 5.7: L-curve for (5.69) for scattering from single cylinder.

As seen from Figure 5.9, CHIEF provides better accuracy compared to Burton-Miller results obtained with various singular integration schemes at 30 integration points per wavelength. Note that when the weak singularity in (5.16) is handled with the Telles scheme without splitting the interval containing the singularity ($\eta \in (-1, 1)$), the Burton-Miller formulation needs at least 300 integration points per wavelength to achieve a comparable accuracy to that of CHIEF with 30 integration points per wavelength. It should be mentioned here that although the regularised form of the Burton-Miller formulation used here is only weakly singular, the third integral on the left hand side of (5.16) converges extremely slowly. Consequently, Burton-Miller needs a very high number of integration points in order to achieve an accuracy comparable to that from the CHIEF method, if it uses the Telles transformation without interval splitting. The efficacy of the Telles scheme for handling the weakly singular integrals has been investigated by many researchers,[23],[164],[88]. It is clear from these studies that the Telles transformation when used without partitioning gives poor results. Singh and Tanaka[164] report at least 3 orders of magnitude improvement for a logarithmic singularity when the Telles transformation is used with the partition of the interval for 10 Gauss points. We see from Figure 5.9 that splitting the

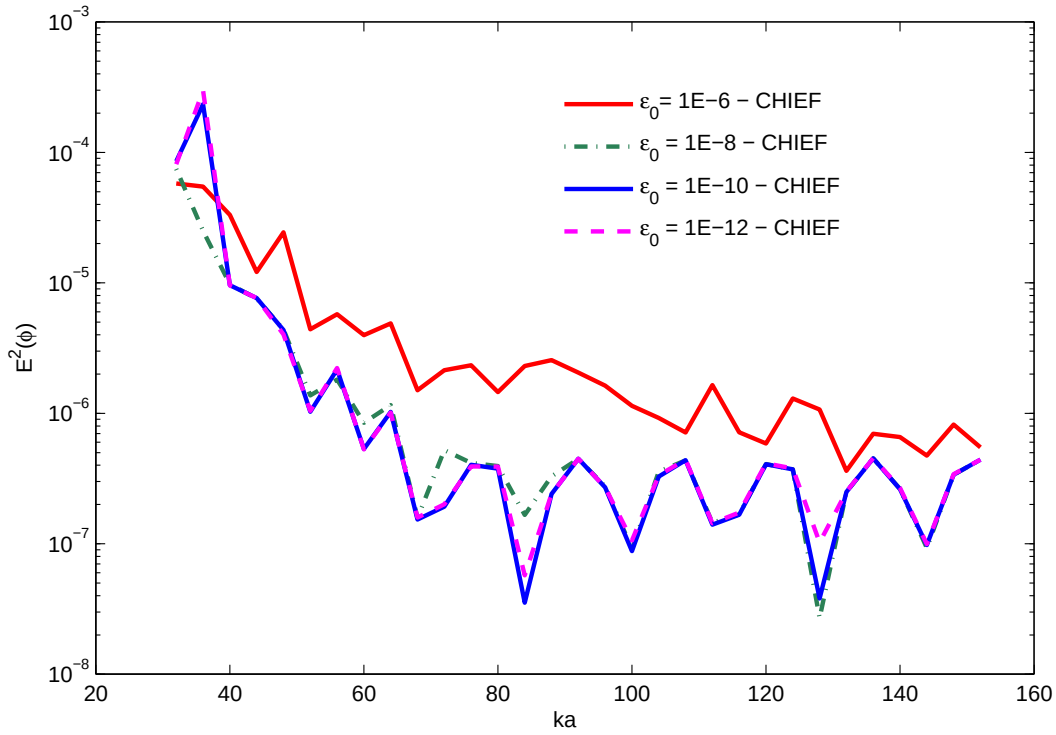

Figure 5.8: PUBEM results for various values of ϵ_0 for single cylinder problem.

local interval $\eta \in (-1, 1)$ indeed improves the Burton-Miller result in comparison with the result obtained without splitting the interval. Similar numerical experiments carried out with conventional polynomial BEM show that the L_2 errors with the various singular integration schemes discussed do not vary significantly. For instance, the L_2 errors for the single cylinder problem using the quadratic discontinuous elements are of the $\mathcal{O}(10^{-3})$ for all the singular integration schemes discussed and for $\tau = 20$. The collocation points used are the nodal locations of the discontinuous element which is a common practice followed in conventional polynomial BEM. We use discontinuous elements for polynomial BEM in order to satisfy the Hölder continuity requirement on the hypersingular integral. It is found that when the element nodes are used as the collocation points, the convergence of the slowly converging integral in (5.16) is possible with a relatively low number (10 to 12) of Gauss points irrespective of the singular integration scheme used. Therefore, the results obtained with various singular integration schemes remain within the same order of magnitude for polynomial BEM. This disparity in the results with various singular integration schemes for PUBEM and polynomial BEM can be attributed to the

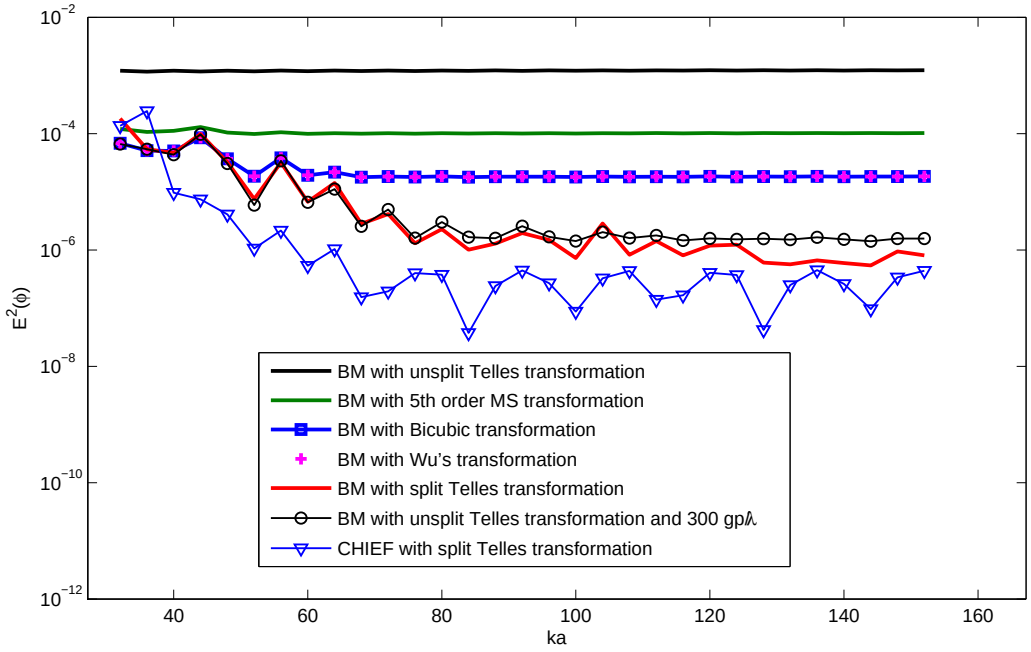

Figure 5.9: $E^2(\Gamma_s)$ for the single cylinder problem.

fact that the collocation points used in PUBEM are not element nodes causing the integrals for PUBEM to converge slowly.

The condition numbers for CHIEF for $k < 64$ are better in comparison with Burton-Miller but degrade with increasing k (see Figure 5.10). Interestingly an accurately computed Burton-Miller solution provides a better conditioning of the system matrix. Amini and Harris [2] studied the dependence of the condition number on the wavenumber k. The numerical examples they presented are with conventional BEM and with $k < 20$ for a 3D problem. It follows from their work that the condition number for a regularised Burton-Miller formulation increases steadily with growing k and the coupling parameter α. In a PUBEM context, as shown in Figure 5.10, the ill-conditioning arising from the plane wave basis is the dominant effect and the steady increase noticed by Amini and Harris is no longer evident. However, despite the high condition numbers encountered, the SVD algorithm is able to find a unique solution. It is evident from Figure 5.9 that the PUBEM implementations of both CHIEF and Burton-Miller are accurate and stable over the range of wavenumbers considered here.

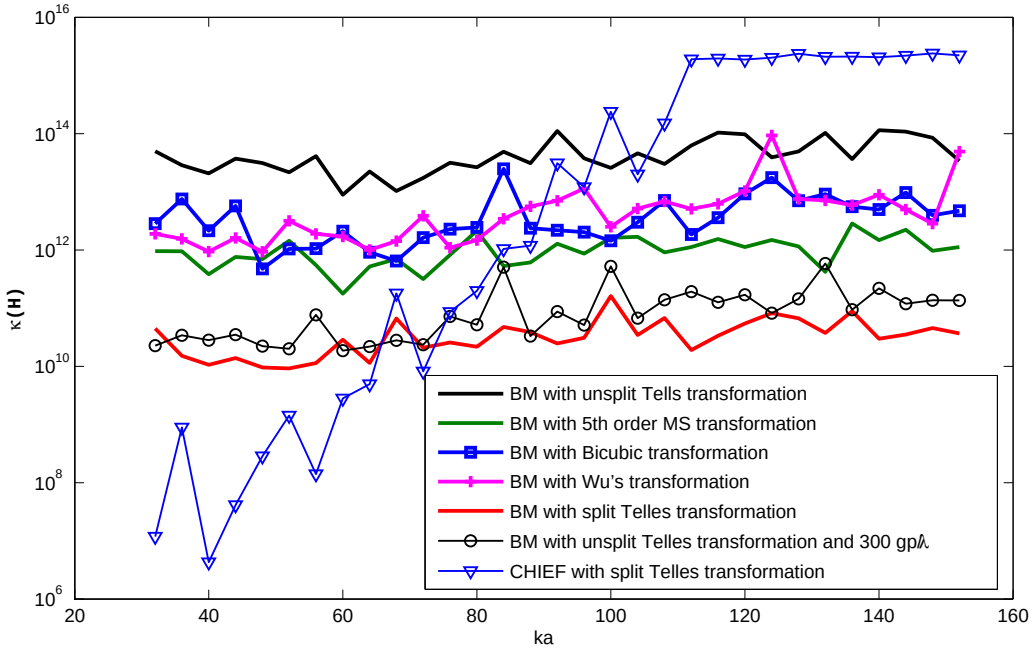

Figure 5.10: $\kappa(\bar{\mathbf{H}})$ for the single cylinder problem.

5.8.2 Scattering from an array of four cylinders

The scattering from a multi-cylinder array presents a more challenging case as it involves multiple reflections from individual cylinders which ultimately forms the total acoustic field. The recursive multiple reflections make this problem an ideal candidate to test the efficacy of PUBEM to obtain an accurate solution. We consider a setting of four unit radius sound hard cylinders of infinite extent with their centres placed at (-2,-2), (2,-2), (2,2) and (-2,2) in a two dimensional homogeneous unbounded acoustic medium (air). A unit amplitude plane wave with wavenumber k is taken to be incident on this cylinder array at an angle of $\theta^I = 45^\circ$ with the horizontal. There are various methods to solve a multiple scattering boundary value problem such as that described and a good review of these methods can be found in [120]. We use the formula proposed by Linton and Evans [112] (eq. 2.15) to compare our PUBEM solution for the total acoustic pressure on the surface of each cylinder. The formula proposed by Linton and Evans is based on the addition theorem that combines the separable solutions of Helmholtz equation, see [120] for details. The addition theorem can be efficiently used to compute the solution but the infinite series has to be truncated in practice. Theoretically of course, an infinite sum should result in a converged solution. However, when solving even the truncated system of linear equations, the addition of

extra terms in the series can make the system matrix highly ill-conditioned. Figure 5.11 shows the dependence of the condition number of the system matrix formed from (2.15) in [112] on the number of terms included in the series. Note that $k = 2.4048$ is an irregular wavenumber (first zero of the first kind Bessel function, J_0). Clearly the reason for such significantly high condition numbers is the wide spread of eigenvalues with the growing number of terms in the series. In light of the result shown in Figure 5.11 it becomes imperative to find the number of

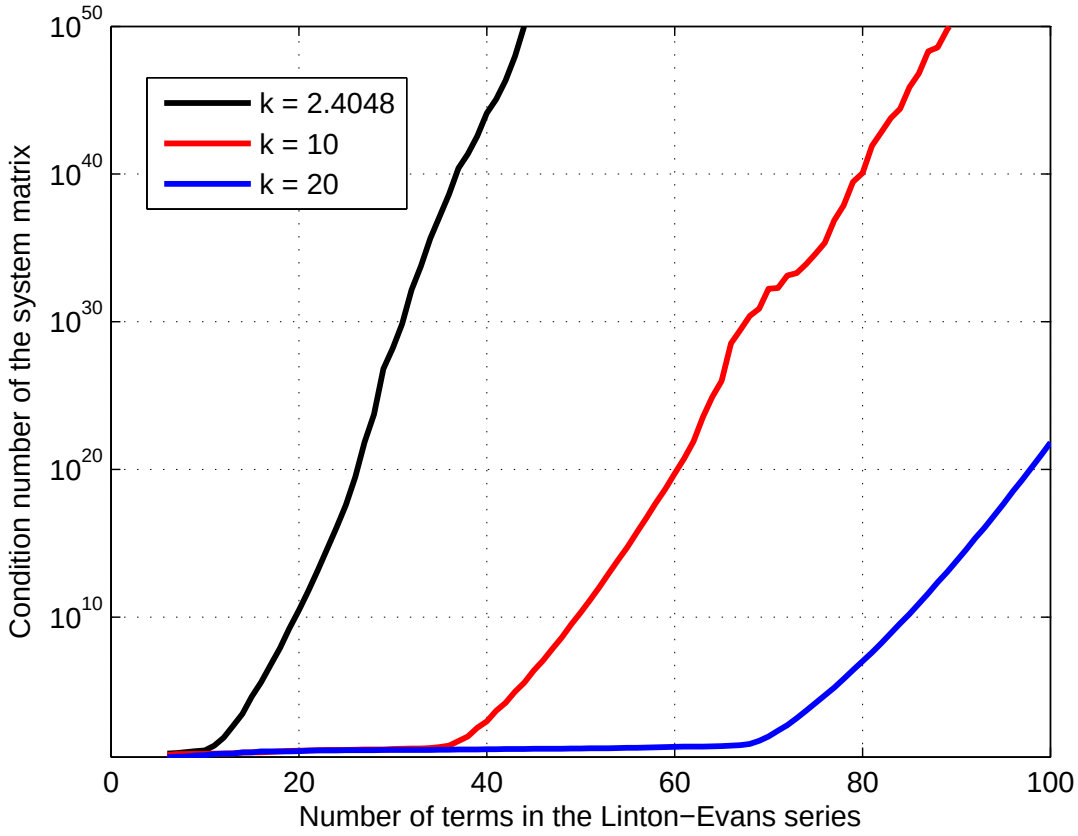

Figure 5.11: Stability of Linton-Evans series, eq. (2.15) in [112].

terms needed to include in the series in order to obtain a correct solution from the truncated series. This is because the relative L^2 errors will depend heavily on how accurately the series in [112] is computed. A good discussion on the upper and lower bounds on the number of terms to be included in the series can be found in [139]. More related works from the acoustics domain [188], [41] give an empirical relation for a two cylinder problem, for the number of terms that need to be included for a given value of ka where a is the radius of the cylinder. Recently, Antoine *et al* [5] have presented an empirical relationship for the number of terms to be used in

	Cyl. 1		Cyl. 2		Cyl. 3		Cyl. 4	
	CHIEF	BM	CHIEF	BM	CHIEF	BM	CHIEF	BM
$\tau \approx 3.0$	5.98E-04	1.03	2.15E-04	2.71	2.78E-04	6.26	1.67E-04	2.01
$\tau \approx 3.5$	8.67E-06	4.06E-05	1.28E-05	9.39E-05	7.6E-06	3.29E-05	516E-06	3.82E-05
$\tau \approx 3.9$	2.01E-07	4.07E-06	1.87E-07	4.01E-06	3.46E-07	6.32E-06	1.92E-07	5.17E-06

Table 5.2: PUBEM results - $E^2(\Gamma_s)$ for scattering from four cylinder array for $k = 36.9171$ and $\theta^I = 45°$, 100 terms in Linton-Evans series.

the infinite series for scattering from multiple circular cylinders

$$M_u = \left[ka_u + \left(\frac{1}{2\sqrt{2}} \ln \left(2\sqrt{2}\pi k a_u \epsilon^{-1} \right) \right)^{\frac{2}{3}} (ka_u)^{\frac{1}{3}} + 1 \right], \tag{5.72}$$

where M_u is the minimum number of terms that need to be included in the infinite series for the u^{th} cylinder with radius a_u, and ϵ is the desired error bound on the Fourier coefficients that need to be computed in the infinite series. The value of error bound on the Fourier coefficients used by Antoine *et al* was 10^{-8}. For our case of scattering from identical circular cylinders (all cylinders are unit radius), the number of terms M_u obtained from (5.72) for each cylinder is the same (say M). We use (5.72) only as a guideline to find the number of terms (M) needed in the Linton-Evans series (2.15 in [112]) with $\epsilon = 10^{-8}$ in (5.72). A system of linear equations of size $N_c(2M + 1)$ is then formed where N_c is the number of cylinders (4 in the present case). We use a linear least squares solver with QR factorisation to solve this system of linear equations using suitable routines from the LAPACK library and obtain the total acoustic pressure on each cylinder surface. This solution is considered as the reference solution and used to compute the relative L^2 error (see (5.68)) for our PUBEM solution with the CHIEF and Burton-Miller methods. For the error analysis of the four cylinder problem, we consider three cases of the wavenumber, namely, $k = 36.9171$, $k = 100$ and $k = 150$. It may be noted that from the three cases mentioned, $k = 36.9171$ and $k = 150$ are irregular wavenumbers. The regularised Burton-Miller results included for comparison here are obtained with the Telles scheme for the weakly singular integrals in conjunction with splitting the interval $\eta \in (-1, 1)$. The L^2 error results shown in Tables 5.2-5.4 are obtained using two continuous elements per cylinder with trigonometric shape functions as indicated previously. All the results are obtained with 30 integration points per wavelength. The condition numbers for the first case of $k = 36.9171$ are given in Table 5.5 and for the latter two cases of $k = 100, 150$ in Table 5.6. We have used $M =$ 100 for $k = 36.9171$, $M =$150 for $k = 100$, and $M =$200 for $k = 150$, in the Linton-Evans series.

	Cyl. 1		Cyl. 2		Cyl. 3		Cyl. 4	
	CHIEF	BM	CHIEF	BM	CHIEF	BM	CHIEF	BM
$\tau \approx 2.2$	43.80	39.34	24.83	16.80	30.95	20.84	24.52	28.28
$\tau \approx 2.6$	7.66E-05	2.30E-03	1.27E-04	4.72E-03	3.52E-04	3.10E-02	8.88E-05	5.17E-03
$\tau \approx 3.0$	3.77E-07	8.18E-06	5.65E-07	1.09E-05	5.08E-07	9.83E-06	5.78E-07	2.04E-05

Table 5.3: PUBEM results - $E^2(\Gamma_s)$ for scattering from four cylinder array for $k = 100$ and $\theta^I = 45°$, 150 terms in Linton-Evans series.

	Cyl. 1		Cyl. 2		Cyl. 3		Cyl. 4	
	CHIEF	BM	CHIEF	BM	CHIEF	BM	CHIEF	BM
$\tau \approx 2.2$	8.26	15.26	12.53	27.67	42.43	98.36	15.68	37.90
$\tau \approx 2.6$	6.73E-05	3.0E-03	7.30E-05	2.6E-03	7.23E-05	4.8E-03	7.98E-05	7.0E-03
$\tau \approx 3.0$	6.48E-05	6.47E-05	6.40E-05	6.39E-05	6.68E-05	6.70E-05	6.40E-05	6.46E-05

Table 5.4: PUBEM results - $E^2(\Gamma_s)$ for scattering from four cylinder array for $k = 150$ and $\theta^I = 45°$, 200 terms in Linton-Evans series.

It may be noted that the number of terms used for the cases studied here (M) is higher than those prescribed by (5.72) and this is done in order to obtain the maximum possible accuracy for the solution obtained from the Linton-Evans series. We reiterate the fact that the errors listed in Tables 5.2-5.4 are for the particular number of terms used in the Linton-Evans series. The condition number of the coefficient matrix for the Linton-Evans series for $k = 36.9171$ with 100 terms was 14.28, for $k = 100$ with 150 terms was 12.28 and that for $k = 150$ with 200 terms was 16.29. It can be noted from the Tables 5.2-5.4 that the accuracy of both CHIEF and regularised Burton-Miller methods improves with more plane waves per node i.e. by increasing the value of the parameter τ. Finally we present a polar plot for the total acoustic pressure, p, on the surface of the first cylinder with centre at (-2,-2) for the case of $k = 150$ (Figure 5.12). The case of $k = 150$ is chosen as at such a high wavenumber, the recursive reflections give rise to an interesting scattering pattern. An additional plot is shown in Figure 5.13 for the same case but only for the region $\theta \in [0, \frac{\pi}{4}]$ on the first cylinder where θ is measured anticlockwise. This is the region where the effect of recursive reflections is the most prominent. The plots shown correspond to the result presented in Table 5.4 with $\tau = 3.0$. From Figures 5.12-5.13, it is evident that the PUBEM solution is able to capture efficiently a complex pattern of the scattered wave at a reasonably high wavenumber. It is not possible to distinguish the CHIEF and Burton-Miller results from Linton-Evans series solution as all three of them visually lie on top of each other.

$k = 36.9171$		
	CHIEF	BM
$\tau \approx 3.0$	3.78E+08	1.01E+10
$\tau \approx 3.5$	3.67E+09	1.39E+10
$\tau \approx 3.9$	1.31E+12	1.24E+11

Table 5.5: PUBEM conditioning - $\kappa(\bar{\mathbf{H}})$ for CHIEF and regularised Burton-Miller method for four cylinder problem, $k = 36.9171$.

	$k = 100$		$k = 150$	
	CHIEF	BM	CHIEF	BM
$\tau \approx 2.2$	1.35E+06	6.54E+05	2.88E+07	4.46E+07
$\tau \approx 2.6$	1.32E+08	9.41E+09	2.07E+11	2.13E+10
$\tau \approx 3.0$	3.0E+14	2.89E+10	9.96E+14	5.11E+10

Table 5.6: PUBEM conditioning - $\kappa(\bar{\mathbf{H}})$ for CHIEF and regularised Burton-Miller method for four cylinder problem at $k = 100$ and $k = 150$.

5.9 Scattering from a long capsule

It is known that the density of characteristic wavenumbers for a given scatterer geometry increases as the wavenumber increases. This is a major concern for the CHIEF method when choosing the interior collocation points. For an elongated object the problem may be exacerbated as the characteristic wavenumbers become very closely spaced. For this purpose, we will investigate PUBEM implementation of only the CHIEF method for an elongated body. In order to study this problem, we consider the geometry that of a long capsule (Figure 5.14). The overall length of the capsule is $(b + 2R)$ where b is the length of the straight edge and R is the radius of the semicircular end of the capsule. A total of four cases are presented for two values of the ratio b/a, where a is the perimeter of the semicircular end. For all the cases, three noded continuous elements with trigonometric shape functions are used. The integration points are placed analytically on the geometry. As before, the value of parameter τ is taken as 3.0. Since we intend to investigate the performance of the CHIEF method at high wavenumbers, it will be convenient to define the relative L_2 error in total acoustic pressure on the boundary of capsule as

$$E^2(\Gamma_s) = \frac{\|p_j - p_1\|}{\|p_1\|} \tag{5.73}$$

where p_j is the solution obtained from the j^{th} instance of CHIEF method and p_1 is the solution from the first instance of CHIEF method at a given wavenumber. Note that for each instance of the CHIEF method, the location of the interior collocation points will be different as they

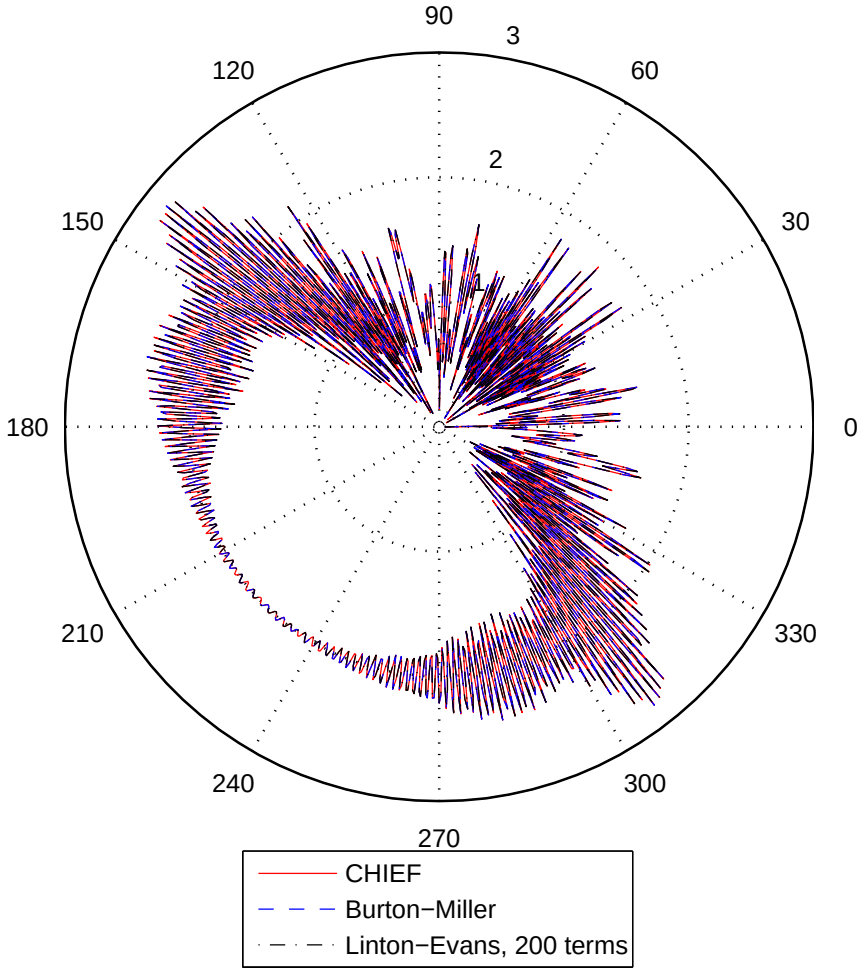

Figure 5.12: $|p|$ for cylinder 1, $k = 150$.

are positioned completely randomly each time. Therefore, the solution at every instance from the CHIEF method will differ from each other. This potentially forms the basis for testing the stability of the method for an elongated geometry where the characteristic wavenumbers are very closely spaced. A total of one hundred instances are tried for each case to examine the stability of the CHIEF method. For this problem, both of the semicircular ends of the capsule are modelled with one element. The parameters used for this problem are summarized in Table 5.7. As is evident from Figure 5.15, the CHIEF method is stable even for a considerably elongated geometry at $b/a = 10$ and 20. For such a geometry, one would expect the eigenvalues for the interior Dirichlet problem to be extremely close to each other making CHIEF method susceptible to errors in finding the correct solution. However as seen from Figure 5.15, the strategy described earlier (see the discussion preceding §5.8.1) to position the CHIEF points

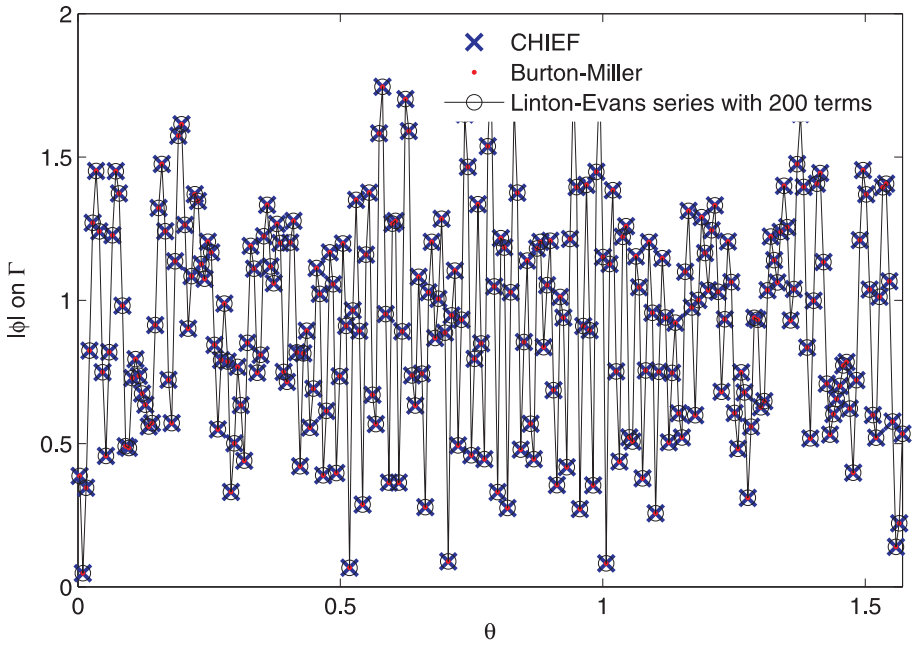

Figure 5.13: $|p|$ for cylinder 1 for $\theta \in [0, \frac{\pi}{4}]$, $k = 150$.

b/a	k	P/λ	n_e	T
10	48	528	22	1548
10	100	1100	22	3300
20	32	672	42	2016
20	64	1344	42	4032

Table 5.7: Parameters for capsule problem, $P = 2a + 2b$, T: total degrees of freedom for capsule problem.

completely randomly with sufficient offset from the boundary gives good results ($\mathcal{O}(10^{-4})$). Interestingly, the CHIEF results become increasingly stable as the wavenumber increases. Note that two of the cases solved here have more than 1000 wavelengths around the scatterer which makes them particularly attractive problems to be solved with PUBEM.

5.10 Conclusions

As was mentioned at the beginning of this chapter (§5.1), the motivation of comparing CHIEF and Burton-Miller methods was to find out which method is more suitable for coupling with PUFEM. The findings in this chapter are summarised as follows.

1. The error analyses presented for the classical single and the multiple scattering problems show that the CHIEF method outperforms Burton-Miller method by at least one order of magnitude for the range of wavenumbers considered. The Burton-Miller method can

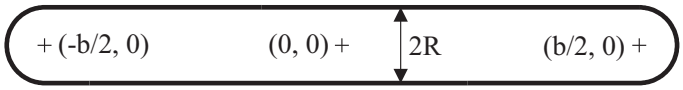

Figure 5.14: Capsule geometry.

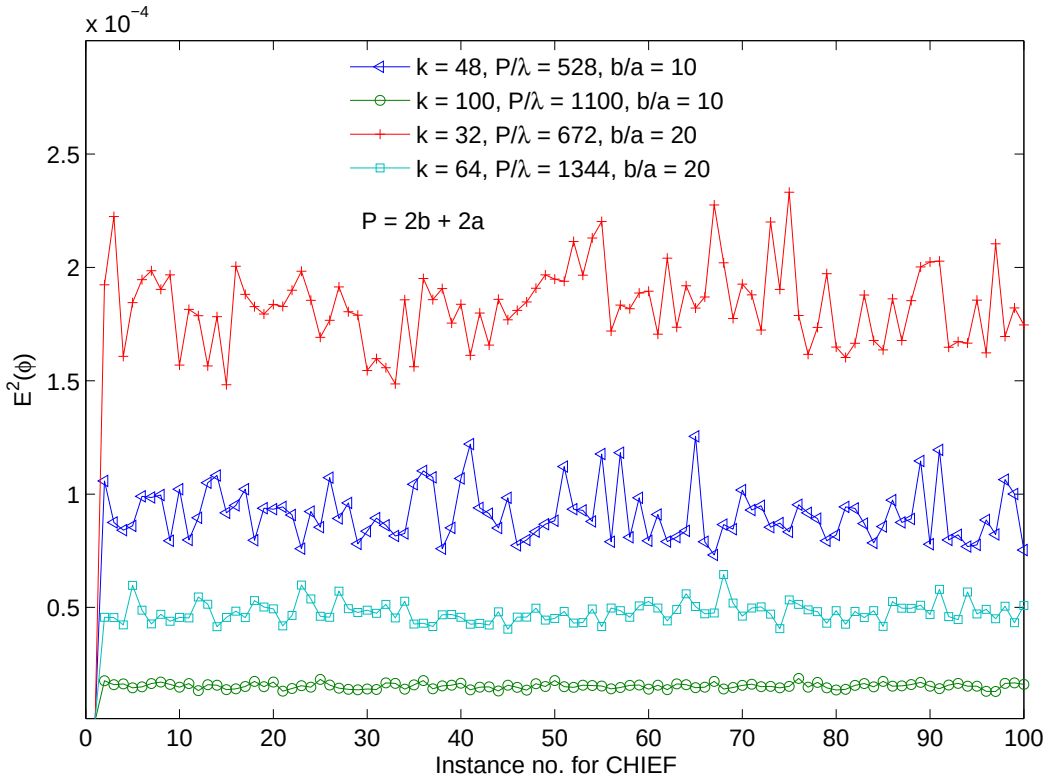

Figure 5.15: $E^2(\Gamma_s)$ for the capsule problem.

prove competitive despite the difficult and slowly converging integrals if suitable coordinate transformations are implemented. Investigation of several coordinate transformation techniques for the weakly singular integrals in the regularised Burton-Miller formulation shows that the Telles transformation with interval splitting is the most accurate method. For both single and multiple scattering problems, the enriched form of the regularised Burton-Miller formulation has smaller condition numbers when compared to the CHIEF method.

2. The final example shows that the CHIEF results are stable even for an elongated capsule problem for the medium range of wavenumbers. This indicates that the CHIEF method may be preferred over the Burton-Miller formulation, at least for simpler geometries and

moderate wavenumbers ($k < 200$), as the former does not have the problem of hypersingular integrals. Of course, we need to have a sufficient number of interior collocation points so that the linear independence of the coefficient matrix $\bar{\mathbf{H}}$ is ensured. The stability and accuracy of the PUBEM scheme have both been clearly demonstrated in previous works [141–143, 145] and here further evidence is provided. In Figure 5.15, the stability of the CHIEF method through repeated instances is shown, and highly accurate solutions are demonstrated in Figures 5.9, 5.13 and Tables 5.2-5.4.

In the next chapter, the PUFEM approach is investigated for solving heterogeneous wave scattering problems.

Chapter 6

PUFEM for heterogeneous media

6.1 Introduction

This chapter focuses on solving wave scattering problems in heterogeneous media. The primary goal of this chapter is to discuss the concept of mixed basis for the problem with multiple heterogeneities. Additionally, some of the well known NRBCs that were discussed in Chapter 3 (see §3.3) will also be compared for the PUFEM.

6.2 Wave scattering in heterogeneous media

Recall the equation (3.25) for the weak form for the Helmholtz equation which is reproduced below for convenience,

$$\int_{\Omega_f} \frac{1}{\rho(\mathbf{x})} \left(\nabla p \cdot \nabla v - k^2 v p\right) d\Omega - \int_{\Gamma_r} \frac{1}{\rho(\mathbf{x})} v B p d\Gamma = \int_{\Gamma_r} \frac{1}{\rho(\mathbf{x})} v \left(\frac{\partial p^{\text{inc}}}{\partial r} - B p^{\text{inc}}\right) d\Gamma \qquad (6.1)$$

It is generally not possible to solve the Helmholtz equation for a heterogeneous problem in closed form. Since in this chapter, we intend to study the convergence of the PUFEM approach, it is imperative that

1. we solve a problem which is heterogeneous in nature, and,

2. at the same time, an analytical solution be available for that problem.

One such problem which is heterogeneous and for which a truncated series solution can be found is defined in Figure 6.1. We consider here the problem of a plane wave scattering in a medium with a jump in the wavenumber where the jump arises on account of a discontinuity in the

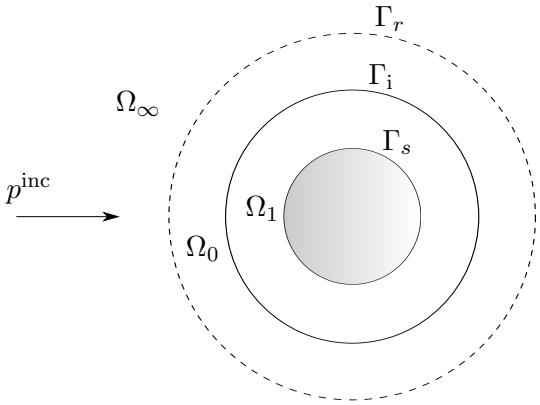

Figure 6.1: Wave scattering in medium with a jump in wavenumber.

density ρ of the medium. Let ρ_1 and ρ_0 respectively be the densities of the fluids contained in the annular regions Ω_1 and Ω_0. Note that the domains of interest are canonical annular circular rings for which a truncated series solution can be constructed. We seek the total acoustic pressure in the computational domain defined as $\Omega_f = \Omega_1 \cup \Omega_0$. Let the circular scatterer boundary be denoted with Γ_s with radius r_1. Let Γ_i with radius r_2 be the interface between the regions Ω_1 and Ω_0 and let Γ_r with radius r_3 be the artificial circular truncation boundary. We denote k_1 and k_0 as the wavenumbers in the regions Ω_1 and Ω_0 respectively. Thus, the plane wave $p^{\mathrm{inc}}(\mathbf{x}) = e^{ik_0\mathbf{d}\cdot\mathbf{x}}$ travelling in the direction $\mathbf{d}$ will be scattered from a circular scatterer in a media with a jump in the wavenumber. In Figure 6.1, Ω_∞ is the homogeneous and unbounded domain with wavenumber k_0, thus, $k_\infty = k_0$.

6.3 Boundary conditions

Let p_1 and p_0 denote the total acoustic pressures in the domains Ω_1 and Ω_0 respectively. The scatterer is assumed to be fully rigid, and so, on Γ_s we have

$$\frac{\partial p_1(\mathbf{x})}{\partial n} = 0, \qquad \mathbf{x} \in \Gamma_s, \tag{6.2}$$

In view of (6.2), we have a total reflection of the incident plane wave off the cylinder surface Γ_s. The normal particle velocity across the interface, Γ_i, between the two domains must be continuous i.e.,

$$\frac{1}{\rho_1}\frac{\partial p_1(\mathbf{x})}{\partial n} = \frac{1}{\rho_0}\frac{\partial p_0(\mathbf{x})}{\partial n}, \qquad \mathbf{x} \in \Gamma_i, \tag{6.3}$$

The third boundary condition is for the scattered waves that travel away from the scatterer into the unbounded domain Ω_∞. We truncate the infinite domain by introducing an approximate

condition over an artificial boundary (denoted by Γ_r) (this boundary condition has been already discussed in §3.5, see (3.24)),

$$\frac{\partial p}{\partial r} = B\left(p - p^{\text{inc}}\right) + \frac{\partial p^{\text{inc}}}{\partial r} \quad \text{on} \quad \Gamma_r. \tag{6.4}$$

where the B is the local radiation boundary damper operator for any of the NRBCs discussed in §3.3. It may be noted that the weak form in (6.1) is similar to the one used in [106] except for the inclusion of a additional boundary integral in [106] that takes into account the continuity of normal particle velocity across the interface Γ_i which does not appear in (6.1).

6.4 Mixed basis for heterogeneous wave problem

Recall the discussion in Chapter 4 (see §4.5.2) on the difficulty in the use of the plane wave basis expansion (4.41) for a heterogeneous problem. It was remarked that in order to solve a heterogeneous problem, we need to have a modified basis which includes the information of the underlying heterogeneous problem. In this section, an idea of modified basis, hereafter called *mixed basis* is discussed.

The problem considered in Figure 6.1 has only a single jump in the density and thus has two distinct wavenumbers, namely k_1 and k_0. It should be noted that with the FEM there is no need to consider interface conditions because the boundary integral contributions from either sides of the interface cancel each other. However, if the problem is solved with enriching the FEM space with plane waves (i.e. PUFEM) of different wavenumbers on each side of the interface (see Figure 6.2), a constraint equation needs to be provided in order to ensure the continuity. Consider for example, the pressure field approximation in a given region that uses the plane wave basis with the corresponding medium wavenumber, i.e.,

$$p(\mathbf{x}) = \sum_{j=1}^{4} N_j \sum_{m=1}^{M_j} e^{ik_1 d_{jm}\cdot\mathbf{x}}\, a^1_{jm}, \quad \mathbf{x} \in \Omega_1, \tag{6.5a}$$

$$p(\mathbf{x}) = \sum_{j=1}^{4} N_j \sum_{m=1}^{M_j} e^{ik_0 d_{jm}\cdot\mathbf{x}}\, a^0_{jm}, \quad \mathbf{x} \in \Omega_0, \tag{6.5b}$$

If the basis equations (6.5a)-(6.5b), are used in the PUFEM, then continuity across the interface needs to be enforced using the Lagrange multipliers, see for example [106]. Applying such

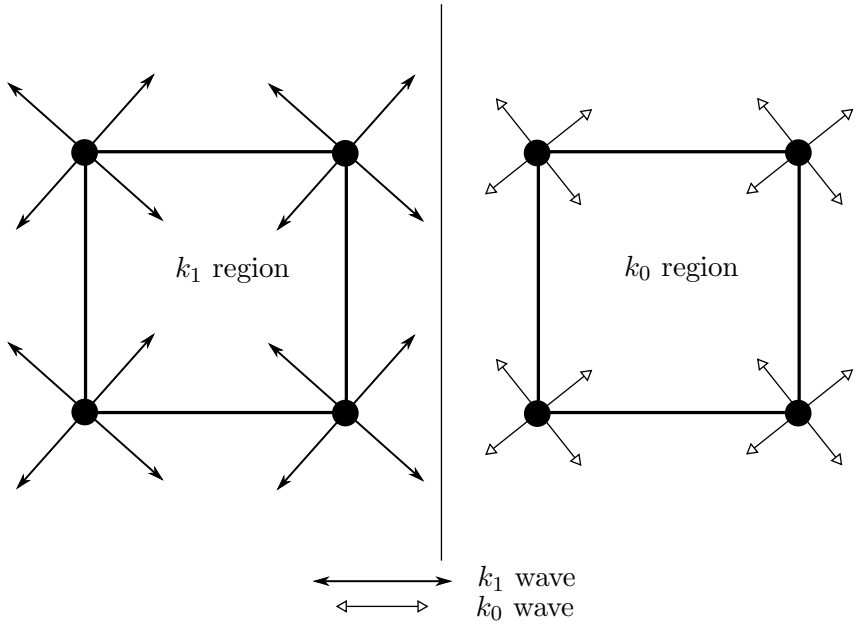

Figure 6.2: Plane wave basis for heterogeneous problem, Laghrouche *et al* [106]

constraints may become computationally demanding particularly when multiple discontinuities are present.

In the mixed basis considered here the plane wave basis associated with each wave number is continuous across the interface, hence, there is no need for Lagrange multipliers. The mixed basis uses two sets of plane waves each with a different wavenumber, and to blend these two sets together the plane waves are applied globally over the entire domain. Mathematically, the concept of mixed basis can be described as follows. The heterogeneity arising on account of variation in the density in Ω_f results in a corresponding change in the wavenumber k. Let the computational domain Ω_f contain heterogeneities with L distinct densities (and hence L distinct wavenumbers), i.e.,

$$\Omega_f = \Omega_{k_1} \cup \Omega_{k_2} \cup \cdots \cup \Omega_{k_L}, \tag{6.6a}$$

$$\Omega_{k_i} \cap \Omega_{k_j} = \emptyset, \quad \text{when} \quad i \neq j, i, j = 1, \cdots L. \tag{6.6b}$$

The pressure field at a point $\mathbf{x} \in \Omega_f$ using the 'mixed' basis for a n-noded finite element is then given as,

$$p(\mathbf{x}) = \sum_{j=1}^{n} N_j \sum_{l=1}^{L} \sum_{m=1}^{M_l} a^l_{jm_l} e^{ik_l d_{jm_l} \cdot \mathbf{x}}, \qquad \mathbf{x} \in \Omega_f, \tag{6.7}$$

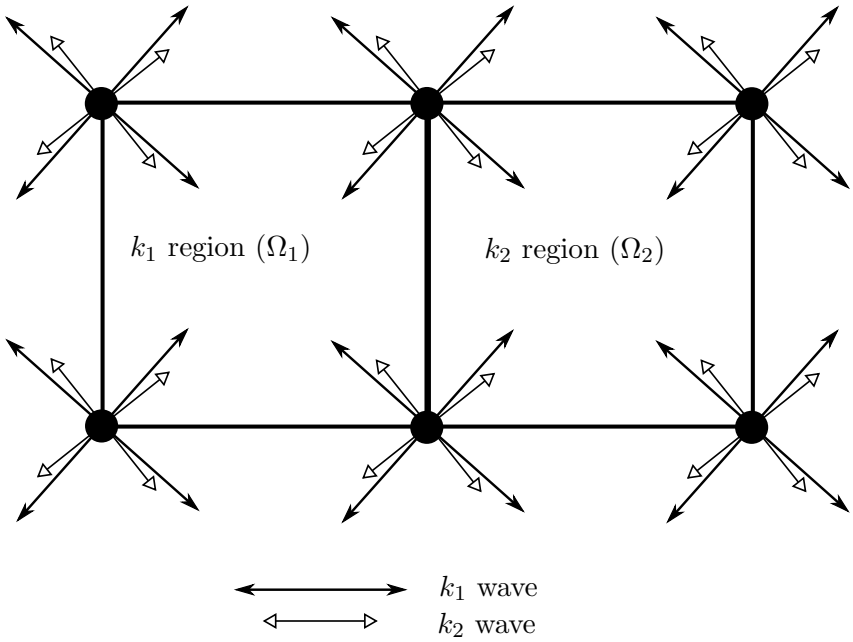

Figure 6.3: Mixed basis for heterogeneous problem

where, $a^l_{jm_l}$ denotes the amplitude of the m^{th} plane wave at the j^{th} node with wavenumber k_l, and $l = 1, \cdots, L$. It will be useful to rewrite (6.7) in a compact notation* similar to (4.45) (see §4.5),

$$p(\mathbf{x}) = \hat{\boldsymbol{\mathcal{Q}}}^e \hat{\boldsymbol{\mathcal{A}}}^e, \quad \mathbf{x} \in \Omega_f, \tag{6.8}$$

where $\hat{\boldsymbol{\mathcal{Q}}}^e$ is a row vector given by,

$$\hat{\boldsymbol{\mathcal{Q}}}^e = \left[\hat{\mathcal{Q}}_1, \cdots, \hat{\mathcal{Q}}_n\right] \tag{6.9}$$

and $\hat{\boldsymbol{\mathcal{A}}}^e$ is a column vector given by,

$$\boldsymbol{\mathcal{A}}^e = \left[\hat{\mathcal{A}}_1, \cdots, \hat{\mathcal{A}}_n\right]^{\mathrm{T}} \tag{6.10}$$

The elements of the vectors $\hat{\boldsymbol{\mathcal{Q}}}^e$ and $\hat{\boldsymbol{\mathcal{A}}}^e$ are further given by

$$\hat{\mathcal{Q}}_j = [\Psi_{j1}, \Psi_{j2}, \cdots, \Psi_{jL}] \tag{6.11a}$$

$$\Psi_{jl} = \left[\psi^l_{j1}, \psi^l_{j2}, \cdots, \psi^l_{M_l}\right] \tag{6.11b}$$

$$\psi^l_{jm_l}(\mathbf{x}) = N_j(\mathbf{x}) e^{\mathrm{i}k_l d_{jm_l} \cdot \mathbf{x}} \tag{6.11c}$$

*These notations will be useful when forming a coupled PUFEM-PUBEM system in Chapter 7.

and

$$\hat{\mathcal{A}}_j = [\Phi_{j1}, \Phi_{j2}, \cdots, \Phi_{jL}] \tag{6.12a}$$

$$\Phi_{jl} = \left[a^l_{j1}, a^l_{j2}, \cdots, a^l_{jm_l}\right] \tag{6.12b}$$

It is important here to note that the element matrices in (4.50) and the resulting linear system of equations in (4.51) corresponds to the PUFEM with the homogeneous basis (4.41) or (4.45). The element matrices needed for the PUFEM system using the mixed basis in (6.7) (or its compact form in (6.8)), can be formed by simply replacing $\mathfrak{Q}^e$ in (4.50) with $\hat{\mathfrak{Q}}^e$. A linear system of equations similar to (4.51) can then readily be formed to solve the heterogeneous problems. It is clear that if we set $L = 1$, it will become a homogeneous problem and we have

$$\hat{\mathfrak{Q}}^e = \mathfrak{Q}^e \tag{6.13}$$

Compared to the approach of Laghrouche *et al* [106] (Figure 6.2), the concept of mixed basis in (6.7) (Figure 6.3) will result in an increased number of unknowns at every node. However, since the mixed basis now contains the plane waves representing each of the individual heterogeneities, the continuity requirement on the solution and normal derivative across the interface separating the two media is naturally satisfied. Of course, if there are many heterogeneities, each with a different wavenumber, the mixed basis will result in a large linear system. For example, in a problem involving L distinct heterogeneities, the total degrees of freedom in the PUFEM linear system will be $n_{tot}ML$, where n_{tot} is the total number of nodes in the FE mesh, $M = \sum_{l=1}^{L} M_l$ is the total number of plane waves at each node, and M_l is the total number of plane waves corresponding to an individual heterogeneity. Clearly, the size of the system grows linearly with L if M is constant at each node. However, the use of the mixed basis is justified in cases when the number of distinct density jumps L is small but Ω_f is allowed to have many such heterogeneities. For instance consider the configuration shown in Figure 6.4. A problem such as that in Figure 6.4, would become computationally intensive when solved using polynomial FEM (or with PUFEM and with the basis defined in (6.5)) as even if L is kept small, a high number of heterogeneities would require a very refined mesh leading to a large linear system.

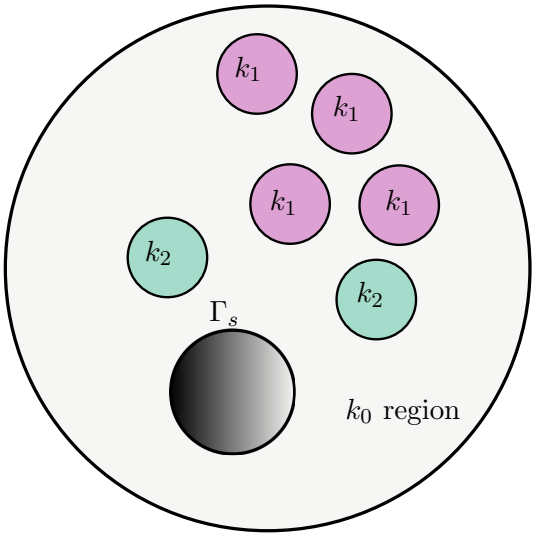

Figure 6.4: Medium with multiple heterogeneities and with three density jumps ($L = 3$).

6.5 Numerical examples

In this section, several numerical examples are presented to illustrate the effectiveness of the PUFEM with the mixed basis for solving problems in heterogeneous media. In order to establish the convergence, the problem defined in §6.2 is solved. For a problem where an analytical solution is difficult to find, a fine FEM mesh is used to recover a converged reference solution. The efficiency of the PUFEM is demonstrated here by achieving a similar accuracy to the FEM but with a much lower number of degrees of freedom which will be quantified in each case.

6.5.1 Acoustic wave scattering with a single jump

Let us consider the problem of wave scattering in heterogeneous media as depicted in Figure 6.1. For this example a series solution can be derived as discussed in Appendix B . We can therefore demonstrate the h-convergence through mesh refinement and q-convergence through addition of enrichment functions or the plane waves. For the examples presented in this section, the BGT-2 damper condition is used on Γ_r (see (3.19)). Since the wavelength changes across the interface Γ_i, it is convenient to define parameters τ_1 and τ_0 as dof/λ for domains Ω_1 and Ω_0 ($\Omega_f = \Omega_1 \cup \Omega_0$) respectively, i.e.,

$$\tau_1 = \lambda_1 \sqrt{\frac{n_1 M}{A_{\Omega_1}}}, \tag{6.14a}$$

$$\tau_0 = \lambda_0 \sqrt{\frac{n_0 M}{A_{\Omega_0}}}. \tag{6.14b}$$

where, n_1 and n_0 are the total number of nodes respectively in Ω_1 and Ω_0, M is the total number of plane waves at each node, $n_i M$ thus gives the total dof in Ω_i, $(i = 0, 1)$ and A_{Ω_i} gives the area of the computational domain Ω_i. We use the following convention when setting up the problem data,

$$\rho_0/\rho_1 = 1.2 \quad \text{when} \quad k_0 > k_1 \tag{6.15a}$$

$$\rho_0/\rho_1 = \frac{1}{1.2} \quad \text{when} \quad k_0 < k_1 \tag{6.15b}$$

6.5.1.1 h-convergence

We consider the various radii for the geometry shown in Figure 6.1 as $r_1 = 1$, $r_2 = 2$ and $r_3 = 3$. For numerical integration inside a given finite element, we use a $n_{\text{gauss}} \times n_{\text{gauss}}$ rule where n_{gauss} is the number of integration of points per wavelength and set $n_{\text{gauss}} = 10$, which is a common practice when solving wave problems. For instance, if an element spans four wavelengths then the integration rule leads to 40×40 integration points. Note that for PUBEM computations in Chapter 5, we used 30 integration points per wavelength due to the presence of Green's functions which are oscillatory in nature. For PUFEM, however, only the plane wave basis appears in the integration and therefore 10 integration points per wavelength were found to give satisfactory results. This was also observed by Mohamed; see [128]. In all simulations, the integration points are placed analytically on the geometry. The accuracy of PUFEM is investigated using a relative L_2-norm as the measure given by,

$$E_2(\Gamma_s) = \frac{\|p - \tilde{p}\|_{L_2(\Gamma_s)}}{\|\tilde{p}\|_{L_2(\Gamma_s)}}, \tag{6.16}$$

$$E_2(\Omega_f) = \frac{\|p - \tilde{p}\|_{L_2(\Omega_f)}}{\|\tilde{p}\|_{L_2(\Omega_f)}}, \tag{6.17}$$

where, $\tilde{p}$ is the total acoustic pressure obtained using the series solution given in Appendix B. For h convergence, two FE meshes, as shown in Figure 6.5, are considered for the PUFEM.

The h-refinement in the PUFEM is discussed using the considered meshes in Figure 6.5. To this end we summarize in Table 6.1 the errors $E^2(\Gamma_s)$ and $E^2(\Omega_f)$, and the condition number κ (actually $\log_{10}(\kappa)$). Here, M_1 and M_0 refer to the number of plane waves used for enrichment

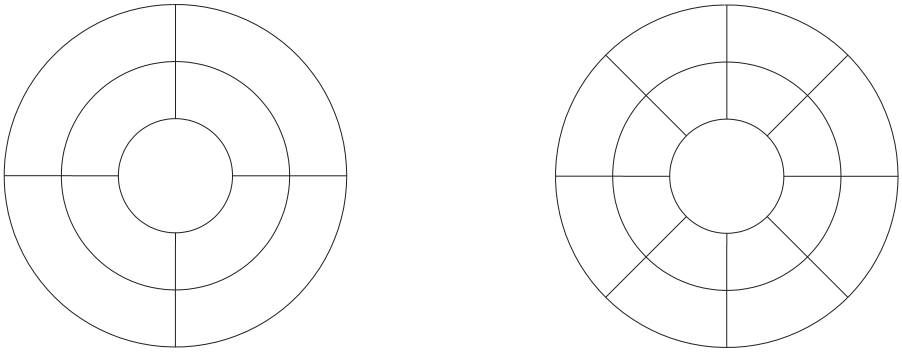

(a) Mesh 1 (b) Mesh 2

Figure 6.5: Mesh configurations for h-convergence

	Case	k_1	k_0	M_1	nDof	$E^2(\Gamma_s)$	$E^2(\Omega_f)$	$\log_{10}(\kappa)$
	1	π	2π	8	192	2.37E-01	3.18E-01	4.5
Mesh 1	2	π	2π	16	384	1.14E-02	1.09E-02	8.6
	3	π	2π	32	768	8.61E-04	5.63E-03	18.9
	4	π	2π	8	640	2.95E-03	1.10E-02	7.6
Mesh 2	5	π	2π	16	1280	1.04E-04	5.57E-03	14.1
	6	π	2π	32	2560	1.24E-04	5.56E-03	20.2

Table 6.1: Results for h-refinement in PUFEM for wave scattering in a medium with single jump.

with wavenumbers k_1 and k_0 respectively. In this test example we have used the same enrichment for wavenumbers k_1 and k_0, i.e. $M_1 = M_0$. It is clear that, in most cases, PUFEM exhibits close to an order of magnitude better accuracy near the scatterer when compared with the errors in the entire domain ($E^2(\Gamma_s)$ is generally smaller compared to $E^2(\Omega_f)$ except for case 1 and 2). This can be explained by the fact that near the scatterer, the elements are smaller in size and as we move away from the scatterer the elements increase in size. Thus, near the scatterer, in general, the FE space is more enriched compared to the elements near the radiation boundary Γ_r because the enrichment functions used are uniform. As expected, smaller errors are obtained on the finer mesh 2 than the mesh 1 for the considered cases which confirm the h-convergence of the PUFEM. The large values of the condition number should also be noticed in the presented results. It is worth mentioning that solving the wave scattering problem discussed here with conventional FEM is computationally very demanding. For example, solving the considered wave scattering in a medium with single jump (i.e. with $k_0 = 2\pi, k_1 = \pi$) using FEM with linear quadrilateral elements with 3108 degrees of freedom results in an $E^2(\Omega_f) \approx 12\%$. We will provide results with polynomial FEM for this problem in §6.5.1.3 to get a perspective on the quality of FEM results when using a comparable nDof and τ to that for PUFEM. In Figure 6.6 we present the PUFEM results obtained on Mesh 2 using $k_1 = 2\pi$ and $k_0 = 4\pi$. In this figure,

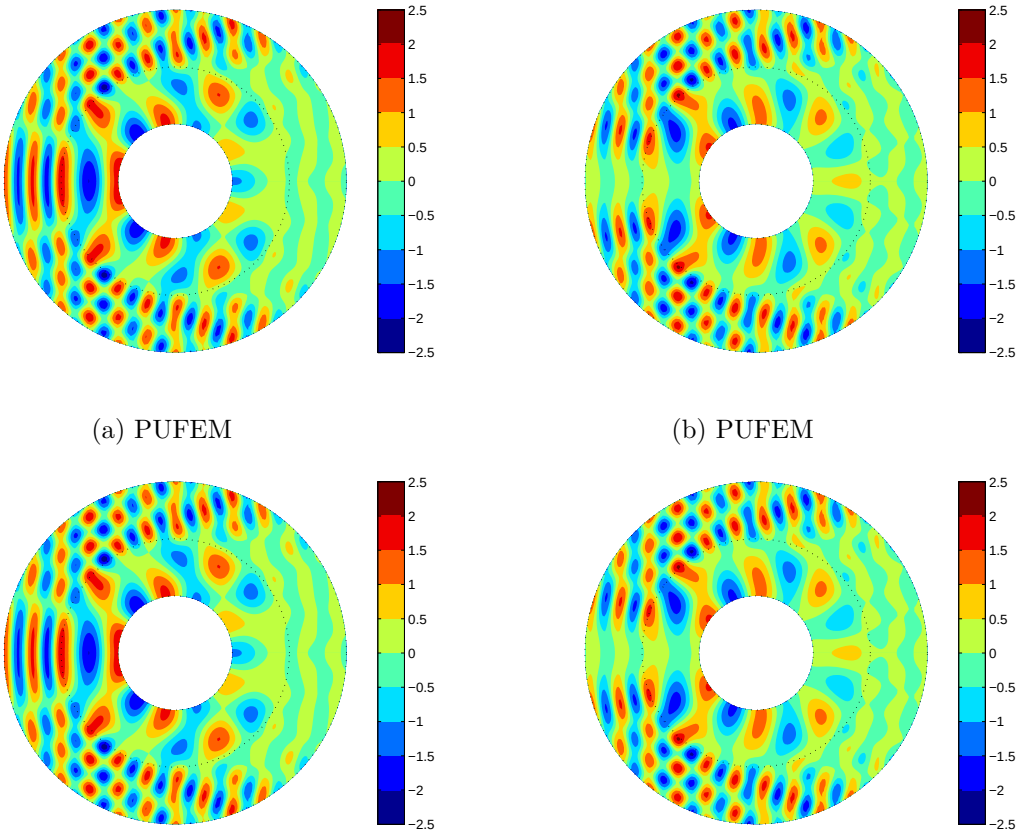

(a) PUFEM (b) PUFEM

(c) Series solution (d) Series solution

Figure 6.6: Real part (Figures 6.6a and 6.6c) and imaginary part (Figures 6.6b and 6.6d) of total pressure for wave scattering in a medium with single jump using $k_1 = 2\pi$ and $k_0 = 2k_1$.

the real and imaginary parts of the total pressure and the series solution are displayed. As can be seen from the results presented for the considered values of k_1 and k_0, there is no visual difference between the PUFEM solution and the analytical solution. The PUFEM accurately resolves this test problem on a reasonably coarse mesh and without any special treatment of the interface between the two media such as Lagrange multipliers discussed in [49, 106] for acoustics and in [47] for electromagnetics.

6.5.1.2 q-convergence

The next concern is to study the q-refinement in the PUFEM for this test example using different values of the ratio k_0/k_1. In Table 6.2 we list the obtained PUFEM results on the Mesh 2 shown in Figure 6.5 and the wavenumber $k_1 = \pi$. It is evident that the PUFEM can predict accurate solutions even for higher values of the ratio k_0/k_1. It should be noted that for results in Table 6.2, the number of plane waves M_1 is not the same as the number of plane waves M_0, unlike in Table 6.1 where we used $M_1 = M_0$, indicating that the proposed PUFEM can work with unequal enrichment functions. In these simulations, increasing the value of the ratio k_0/k_1 or the number of enrichments M_1 or M_0 results in an increase in the condition number associated with the PUFEM. As can be noted from Table 6.2, the number of plane waves associated with the

k_0/k_1	Case	M_1	M_0	nDof	$E^2(\Gamma_s)$	$E^2(\Omega_f)$	$\log_{10}(\kappa)$	τ_1	τ_0
	1	4	16	800	1.11E-03	5.79E-03	8.34	14.2	5.5
2	2	8	16	960	5.02E-04	5.61E-03	9.23	15.6	6.0
	3	12	16	1120	1.81E-04	5.58E-03	12.07	16.9	6.5
	4	16	16	1280	1.10E-04	5.57E-03	14.13	18.05	6.9
	5	16	32	1920	2.68E-04	1.11E-02	16.15	22.1	5.7
3	6	20	32	2080	1.84E-04	1.11E-02	18.56	23.0	5.9
	7	24	32	2240	3.78E-04	1.11E-02	19.43	23.8	6.1
	8	32	32	2560	3.06E-04	1.11E-02	20.48	25.5	6.6
	9	32	48	3200	2.50E-03	4.85E-02	20.42	28.5	5.5
4	10	36	48	3360	1.79E-03	4.85E-02	20.81	29.2	5.6
	11	40	48	3520	3.45E-03	4.85E-02	20.83	29.9	5.8
	12	48	48	3840	1.53E-03	4.85E-02	21.25	31.2	6.0

Table 6.2: Results for q-refinement in PUFEM for wave scattering in a medium with single jump.

higher wavenumber k_0 are kept constant whereas those associated with k_1 are increased steadily. Interestingly, we do not see much improvement in the accuracy both on the scatterer and in the entire domain (i.e. the errors remain within the same order of magnitude for each case). Apart from this, the condition number of the PUFEM system increases drastically. It is observed that for the first case, when $k_0/k_1 = 2$, there is only one order of magnitude improvement due to

q-refinement. Note that for this case, the $\log_{10}$ value of the condition number increases from 8.34 to 14.13. However, for the cases $k_0/k_1 = 3$ and $k_0/k_1 = 4$ we see that the errors remain stagnant within the same order of magnitude despite the addition of more plane waves. The possible cause appears at first sight to be the condition number of the PUFEM system which is of the order 10^{20} for k_0/k_1 ratios of 3 and 4.

6.5.1.3 Comparison with FEM

Before proceeding further, a comparison with classical FEM is in order. The results presented in previous sections demonstrated the h and q convergence of the PUFEM algorithm. We now investigate the results obtained with the FEM for the similar range of nDof and the parameter τ_1 and τ_0 used for PUFEM. For this purpose, consider again the two layer problem defined in §6.2. We set $k_1 = \pi$ and $k_0 = 2\pi$ and the density ratios are chosen following (6.15). The FE mesh for the FEM results is chosen such that the parameters τ_1 and τ_0 are in the similar range as used for the first case in Table 6.2 (i.e. for case $k_0/k_1 = 2$). The parameter nDof is increased by successively refining the mesh and the BGT-2 damper condition is used on Γ_r. Table 6.3 lists the L^2 errors computed in the entire computational domain along with the parameters τ_1 and τ_0 used. It can be observed that despite using higher values of τ_1 and τ_0 (third column onwards

$k_0 = 2\pi, k_1 = \pi$								
nDof	1008	1512	3108	3612	4200	5040	6300	8400
τ_1	14.9	18.34	26.30	28.35	30.57	33.49	37.44	43.24
τ_0	5.8	7.10	10.19	10.98	11.84	12.97	14.50	16.75
$E^2(\Omega_f)$	5.70E-01	3.30E-01	1.22E-01	1.07E-01	9.64E-02	8.88E-02	8.38E-02	8.0E-02

Table 6.3: FEM results for two layer problem

in Table 6.3), the FEM results in Table 6.3 show a very slow convergence as compared to the PUFEM results in Table 6.2. Note again that, the degrees of freedom per wavelength required by the FEM, in the region with higher wavenumber, is significantly high ($\tau_1 > 40$) to achieve an error of $\mathcal{O}(10^{-2})$. In contrast, better level of accuracy ($\mathcal{O}(10^{-3})$) can be achieved with PUFEM with a significantly less degrees of freedom in the region with higher wavenumber ($\tau_1 \approx 18$). This clearly shows the advantage of using the plane wave enrichment and indicates that a significant improvement in the results can be obtained despite using less degrees of freedom per wavelength with PUFEM. It is important to note here that the NRBC used here for the FEM results in Table 6.3 is the same as that used for the PUFEM results in Table 6.2 (i.e. the BGT-2 damper condition). This indicates that the slow convergence associated with the FEM in Table 6.3 is

not due to the approximate NRBC but rather due to the inability of the FEM to efficiently model the heterogeneous wave scattering problem.

6.5.1.4 Reversal of wavenumbers and effect of radiation boundary

As seen from Table 6.2, it appears that the results from PUFEM stagnate due to poor conditioning of the system matrix. In order to verify this, we repeat the numerical experiment in Table 6.2 for the first two ratios ($k_0/k_1 = 2$ and $k_0/k_1 = 3$), except, the wavenumber in the inner and outer layers are reversed. Note that with this we also reverse the number of plane waves used in the interior and exterior. The results are noted in Table 6.4. Some observations

k_1/k_0	Case	M_1	M_0	nDof	$E^2(\Gamma_s)$	$E^2(\Omega_f)$	$\log_{10}(\kappa)$	τ_1	τ_0
	1	16	4	800	1.50E-02	1.66E-02	8.46	7.14	11.06
2	2	16	8	960	1.51E-02	1.65E-02	9.16	7.82	12.11
	3	16	12	1120	1.50E-02	1.65E-02	12.09	8.44	13.08
	4	16	16	1280	1.50E-02	1.64E-02	14.07	9.03	13.98
	5	32	16	1920	2.16E-02	1.82E-02	16.21	7.37	17.13
3	6	32	20	2080	2.16E-02	1.82E-02	19.19	7.67	17.83
	7	32	24	2240	2.16E-02	1.82E-02	19.61	7.96	18.50
	8	32	32	2560	2.16E-02	1.82E-02	20.05	8.51	19.78

Table 6.4: q-convergence with reversal of wavenumbers and $r(\Gamma_i) = 3$.

summarizing Tables 6.2 and 6.4 follow.

1. Observe that the range of the condition numbers shown in Tables 6.2 and 6.4 for the k_0/k_1 ratios of 2 and 3 is approximately the same. Observe that $\log_{10}(\kappa)$ varies between 8.5 to 14 for a k_0/k_1 ratio of 2 and 16 to 20 for the ratio of 3. However, the parameters τ_1 and τ_0 vary significantly in Tables 6.2 and 6.4. This is expected as the wavenumbers are reversed (see the formulae in (6.14)).

2. The accuracy of PUFEM deteriorates when the lower wavenumber region is placed in the exterior for the same number of enrichment functions. For example, observe that the L^2 error on the scatterer for the first case ($k_1 = \pi, k_0 = 2\pi$) in Table 6.2 is $\mathcal{O}(10^{-3})$ with $M_1 = 4$ and $M_0 = 16$. This case when reversed ($k_1 = 2\pi, k_0 = \pi$) in the first case in Table 6.4 with $M_1 = 16$ and $M_0 = 4$, we see that the L^2 error on the scatterer is $\mathcal{O}(10^{-2})$. Similar behaviour can be observed for other cases as well. This can be explained by the reduction in the parameter τ_1 for the results shown in Table 6.4. Note that for k_0/k_1 ratios of 2 and 3, the parameter τ_1 in Table 6.2 is greater than that for the results shown in Table 6.4. Clearly therefore we would expect better accuracy on the scatterer in Table 6.2.

3. Most importantly, note the condition numbers listed in Tables 6.2 and 6.4. For both sets, we observe that the PUFEM system is severely ill-conditioned and would expect this to affect the accuracy of the results. A second numerical experiment is therefore carried out, where we use the same data as in Table 6.4, but we place the radiation boundary Γ_r farther from the scatterer by taking $r(\Gamma_i) = 4$. These results are presented in Table 6.5.

4. As seen from Table 6.5 (where $r(\Gamma_i) = 3$), we see that the condition numbers are again in the same range as in Table 6.4 (where $r(\Gamma_i) = 3$). However, we observe that despite the same range of condition numbers encountered, the accuracy of the results is improved by placing the radiation boundary further away. Note that the parameter τ_1 is the same for the cases in Tables 6.4 and 6.5, whereas, the parameter τ_0 is always small in Table 6.5 compared to Table 6.4. Thus, despite having a smaller τ_0 in Table 6.5 compared to that in Table 6.4, Table 6.5 exhibits better accuracy not only on the scatterer but also globally.

k_0/k_1	Case	M_1	M_0	nDof	$E^2(\Gamma_s)$	$E^2(\Omega_f)$	$\log_{10}(\kappa)$	τ_1	τ_0
	1	16	4	1120	1.33E-02	1.41E-02	8.49	7.14	9.21
2	2	16	8	1344	4.47E-03	3.67E-03	8.84	7.82	10.09
	3	16	12	1568	4.12E-03	3.53E-03	11.91	8.44	10.90
	4	16	16	1792	3.85E-03	3.48E-03	13.83	9.03	11.65
	5	32	16	2688	3.78E-03	3.55E-03	15.99	7.37	14.27
3	6	32	20	2912	3.80E-03	3.54E-03	18.21	7.67	14.86
	7	32	24	3136	3.80E-03	3.53E-03	18.29	7.96	15.42
	8	32	32	3584	3.82E-03	3.54E-03	19.91	8.51	16.48

Table 6.5: q-convergence with reversal of wavenumbers and $r(\Gamma_i) = 4$.

6.5.2 Plane wave scattering in a medium with multiple jumps.

In this example, the problem of wave scattering in a medium with multiple jumps in the density is solved. Consider a sound hard cylinder surrounded by four concentric fluid layers as shown in Figure 6.7 with wavenumbers $k_1 = k_3$ and $k_2 = k_4 = k_0$. As in the previous example, we use linear quadrilateral finite elements for the spatial discretization, see Figure 6.7. The analytical solution for this problem can be found using the approach used for a two layer problem as discussed in Appendix B. However, the expressions for interface coefficients will be highly involved. Therefore, a FEM solution obtained using a fine mesh with 705920 degrees of freedom is used as the reference to obtain a converged solution. The motivation in solving this problem is to demonstrate the idea illustrated in Figure 6.4. Although individual fluid pockets as depicted in Figure 6.4 are not considered here, the problem in Figure 6.7 demonstrates that if there

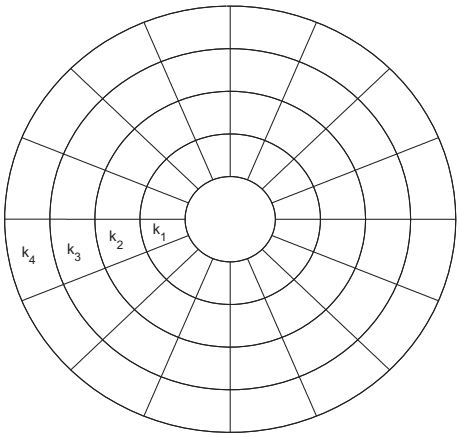

Figure 6.7: Mesh used for wave scattering in a medium with multiple jumps.

are multiple jumps in the density but the number of distinct densities involved is small, the mixed basis is an attractive alternative to the Lagrange multipliers. Figure 6.8 presents the PUFEM results obtained using $k_1 = k_3 = 2\pi$ and $k_2 = k_4 = 2k_1$ whereas, those obtained using $k_1 = k_3 = \pi/2$ and $k_2 = k_4 = 4k_1$ are presented in Figure 6.9. It is clear that the PUFEM accurately captures the small wave features in this problem and produces similar scattering patterns as those obtained using FEM on a very fine mesh. To further compare the PUFEM to the standard FEM we present in Figure 6.11 the modulus of the total pressure on the scatterer surface obtained using PUFEM and FEM using three different meshes. It is clear that for the considered three FEM results included in Figures 6.10 and 6.11, only the FEM solution on the finest mesh (705920 dof) matches well with the solution from PUFEM. The significant savings in degrees of freedom with PUFEM is evident. Although, for the present study, the entire FE domain is enriched with both k_1 and k_0 plane waves, it is indeed possible to use this enrichment in a more optimal way. For example, when the k_0/k_1 ratio is very high, using a combined basis will result in an excessive enrichment in the region of the lower wavenumber. It is therefore essential to optimize the present approach such that the combined basis is applied only on the interface of regions with different wavenumbers. The FE nodes close to (and on) the scatterer can be enriched with k_1 plane waves alone whereas those near the radiation boundary can be enriched with k_0 plane waves alone. Use of Lagrange multipliers is inevitable when solving wave scattering problems with plane wave based methods in a domain that has jumps in the medium properties. Laghrouche *et al.* [106] and Farhat *et al.* [49] (for acoustics) and more recently Facco *et al.* [47] (for electromagnetics) have used the Lagrange multiplier to solve the wave problem with jump in wave speed. While continuity conditions can be correctly enforced using

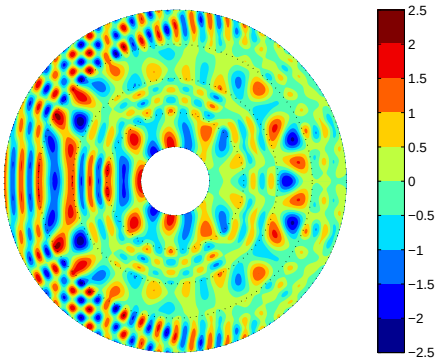

(a) PUFEM: nDof = 3840

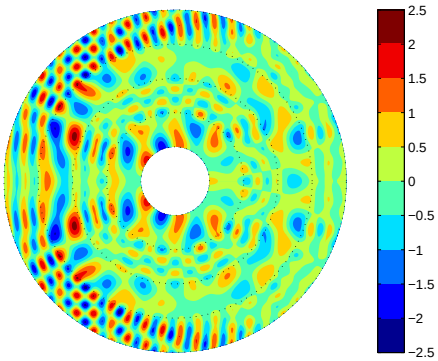

(b) PUFEM: nDof = 3840

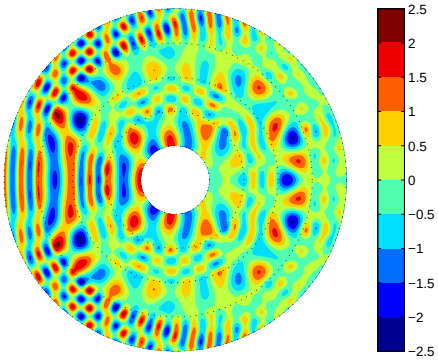

(c) Polynomial FEM: nDof = 705920

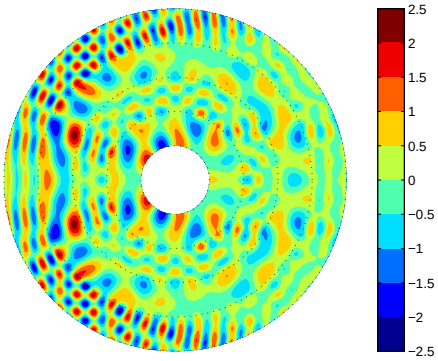

(d) Polynomial FEM: nDof = 705920

Figure 6.8: Real part (first column) and imaginary part (second column) of total pressure for wave scattering in a medium with multiple jumps using $k_1 = k_3 = 2\pi$ and $k_2 = k_4 = 2k_1$.

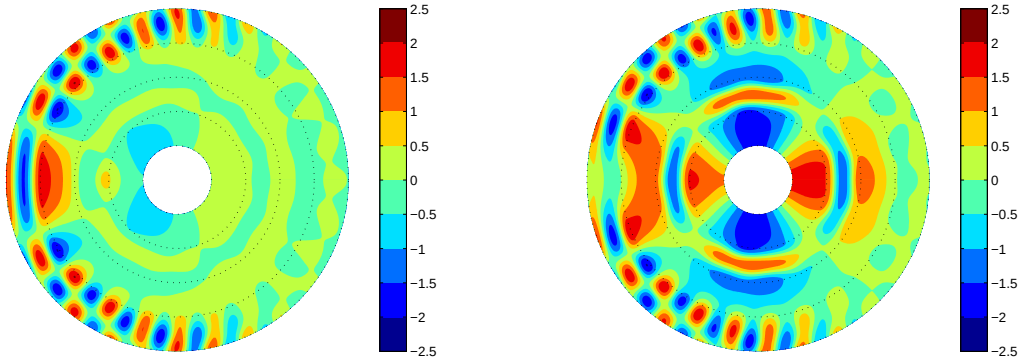

(a) PUFEM: nDof = 3840

(b) PUFEM: nDof = 3840

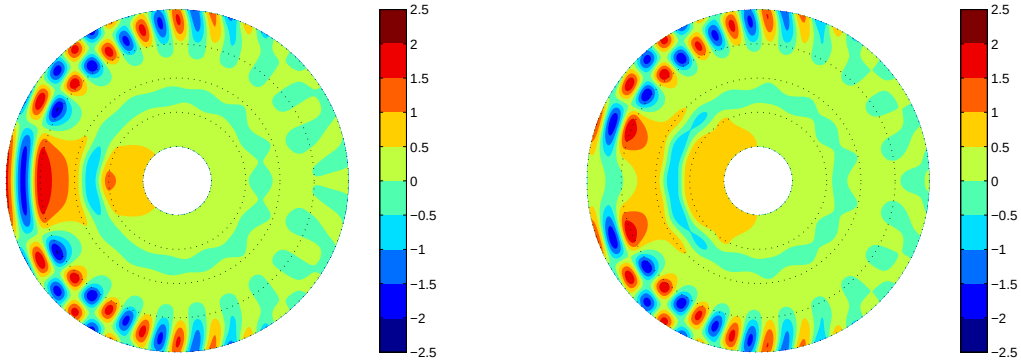

(c) Polynomial FEM: nDof = 705920

(d) Polynomial FEM: nDof = 705920

Figure 6.9: Real part (first column) and imaginary part (second column) of total pressure for wave scattering in a medium with multiple jumps using $k_1 = k_3 = \pi/2$ and $k_2 = k_4 = 4k_1$.

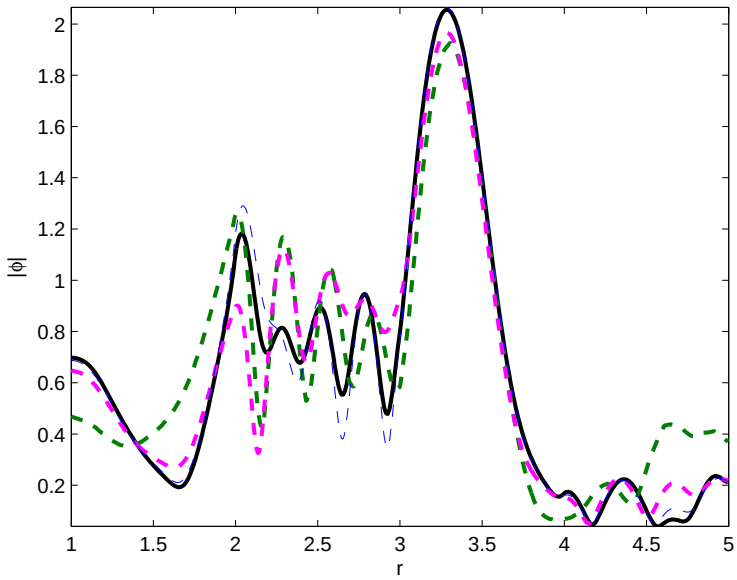

Figure 6.10: Radial cross section of the modulus $|p|$ at $\theta = 0$ with $k_1 = k_3 = 2\pi$ and $k_2 = k_4 = 2k_1$.

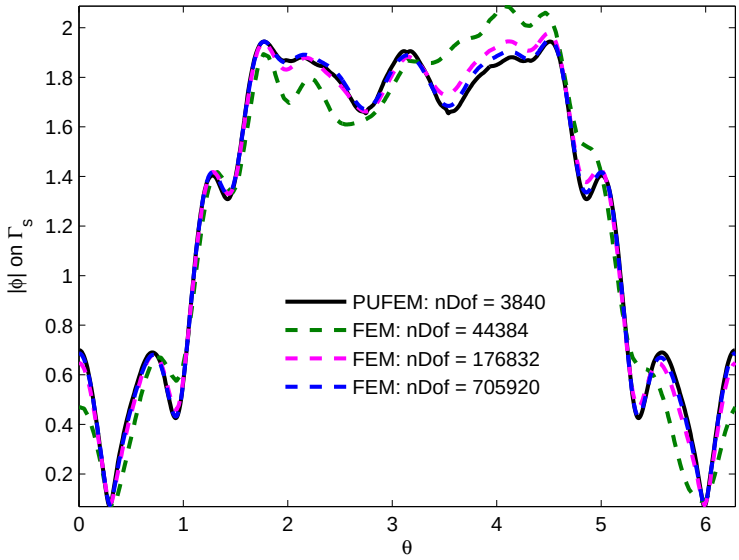

Figure 6.11: $\left|p\right|$ on Γ_s with $k_1 = k_3 = 2\pi$ and $k_2 = k_4 = 2k_1$.

the Lagrange multipliers, the problem such as illustrated in Figure 6.7 can bring significant challenges during the implementation.

6.5.3 Comparison of NRBCs

It is imperative that the different NRBCs discussed in §3.3 be compared for their accuracy so that the best among them can be chosen for a further comparison with the coupled PUFEM-PUBEM (in Chapter 7). For this purpose, we again consider the two layer problem and carry out numerical experiment by setting first i) $k_1 = \pi, k_0 = 2\pi$ and then ii) $k_1 = 2\pi, k_0 = \pi$. This reversal of wavenumbers is needed to understand the effect it has on the accuracy of the PUFEM solution. Figure 6.12 shows a comparison between various NRBCs when $k_1 = \pi, k_0 = 2\pi$ (higher wavenumber in exterior case). As expected, the first order BGT condition (BGT-1) performs poorly and the associated errors remain more than 10%. In contrast, BGT-2 and EM-2 boundary conditions result in errors of $\mathcal{O}(10^{-3})$. When the wavenumbers are reversed, it can be seen that the accuracy of PUFEM is diminished by close to two orders of magnitude as shown in Figure 6.13. Note that when the region with a lower wavenumber is placed in the exterior, the radiation boundary damper has to deal with waves which have longer wavelength. On the other hand, if the region with higher wavenumber is in the exterior, the boundary damper is more effective as the wavelength is shorter. In general, the PUFEM solution with BGT-2, EM-2 and Feng-3 boundary dampers appears to be within the same range of accuracy. Laghrouche *et al* [107]

have studied various NRBCs for PUFEM but for a homogeneous wave scattering problem. They conclude that as the wavenumber increases, BGT-2, EM-2 and Feng-3 boundary dampers result in the same level of accuracy. We will consider only the BGT-2 boundary damper for the comparison with coupled PUFEM-PUBEM approach.

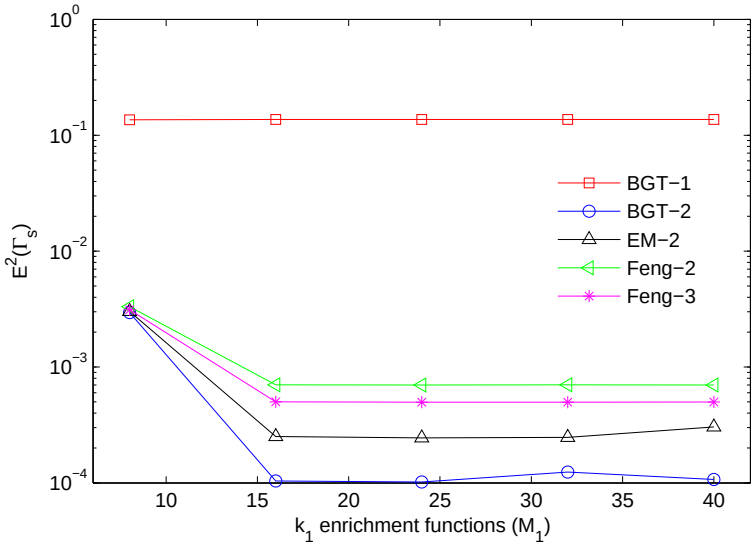

Figure 6.12: Comparison of local NRBCs for PUFEM, $k_1 = \pi, k_0 = 2\pi$

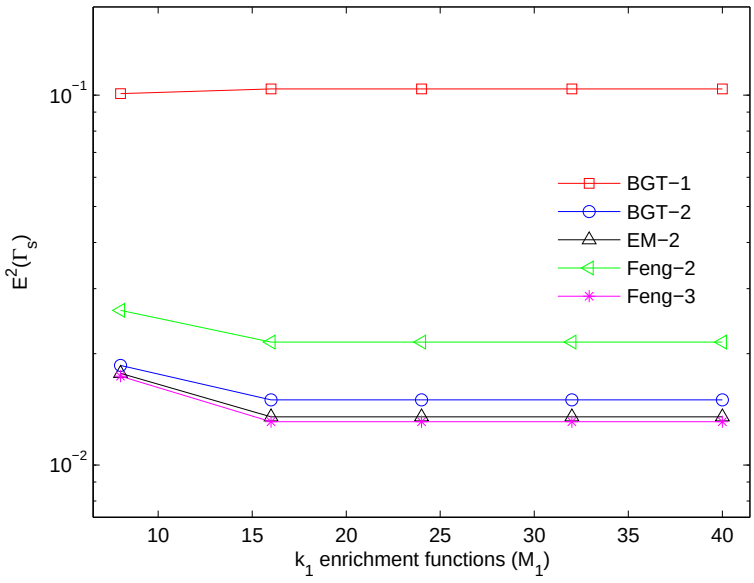

Figure 6.13: Comparison of local NRBCs for PUFEM, $k_1 = 2\pi, k_0 = \pi$

6.6 Conclusions

The PUFEM is extended here for a wave scattering problem in heterogeneous media by blending the enrichment functions of each material/subdomain into a global enrichment which is then applied over the entire domain. The enrichment continuity is naturally ensured without having to enforce it between the subdomains as in previous approaches. On the other hand, the weak discontinuities of the material's interface are approximated by the finite elements polynomial shape functions [†]. The extension has a wide range of applications especially in problems of multiple scales of interest. Some of the applications where the concept of mixed basis can be really beneficial is discussed in Chapter 8 (§8.2.1). We introduce the PUFEM-PUBEM coupling in the next chapter.

[†]We always have an interface between two media lying on element boundaries and it never passes through the element.

Chapter 7

The partition of unity coupled FE-BE method

Before presenting the coupled PUFEM-PUBEM algorithm, let us recall the weak form for PUFEM that we used in the last chapter,

$$\int_{\Omega_f} \frac{1}{\rho(\mathbf{x})} \left(\nabla p \cdot \nabla v - k^2 v p\right) d\Omega - \int_{\Gamma_r} \frac{1}{\rho(\mathbf{x})} v B p d\Gamma = \int_{\Gamma_r} \frac{1}{\rho(\mathbf{x})} v \left(\frac{\partial p^{\text{inc}}}{\partial r} - B p^{\text{inc}}\right) d\Gamma \tag{7.1}$$

The weak form for PUFEM is reproduced here only to bring out the difference between (7.1) and the weak form that we will use for the coupled PUFEM-PUBEM approach.

7.1 Weak form for coupled PUFEM-PUBEM formulation

The weak form for PUFEM that is suitable for coupling with PUBEM is obtained in the same way as in §3.1 except we make no approximation on Γ_r for the scattered waves*.

Following the steps in §3.1, the Helmholtz equation in (2.4) when multiplied with a test function v gives,

$$\int_{\Omega_f} \left(\rho^{-1} \nabla v \cdot \nabla p - \rho^{-1} k^2 v p\right) d\Omega - \int_{\Gamma_r} \rho^{-1} v \frac{\partial p}{\partial n} d\Gamma = 0. \tag{7.2}$$

It should be noted that the normal derivative of pressure, i.e., $\frac{\partial p}{\partial n}$ that appears in the line integral in (7.2) is an unknown and as such (7.2) cannot be solved on its own. The driving term, viz. the incident wave, is introduced after coupling (7.2) with the BIE for pressure p on Γ_r. The BIE

*see (7.1) where the boundary damper operator B is an approximation for the scattered waves.

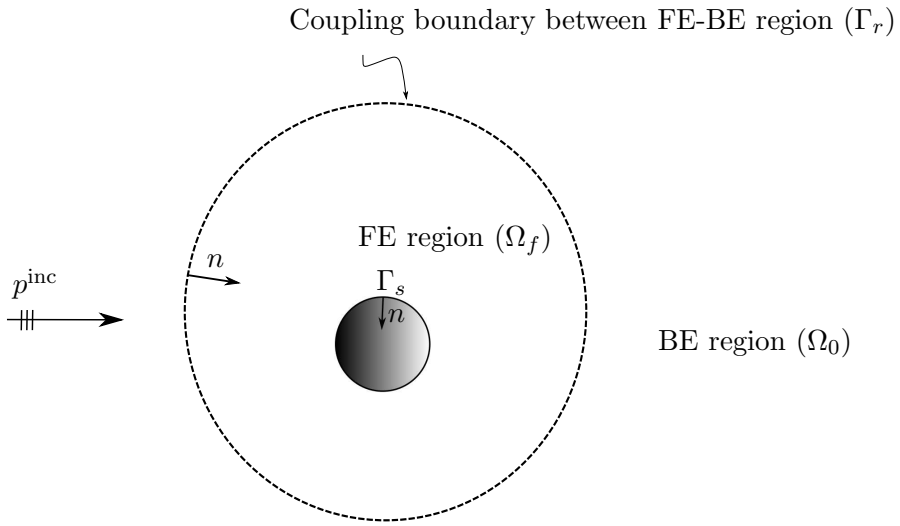

Figure 7.1: Coupled FEM-BEM problem

for total acoustic pressure on Γ_r is

$$\rho(\mathbf{x})^{-1}c(\mathbf{x})p(\mathbf{x}) + \int_{\Gamma_r} \rho(\mathbf{x})^{-1}\frac{\partial G(\mathbf{x},\mathbf{y})}{\partial n_y}p(\mathbf{y})d\Gamma - \int_{\Gamma_r} \rho(\mathbf{x})^{-1}G(\mathbf{x},\mathbf{y})\frac{\partial p}{\partial n}d\Gamma$$
$$= \rho(\mathbf{x})^{-1}p^{inc}(\mathbf{x}), \quad \mathbf{x},\mathbf{y} \in \Gamma_r, \tag{7.3}$$

It is important to note here that,

1. the BIE in (7.3) is the conventional BIE,

2. (7.3) is normalised with the density term in order to be coupled with the weak form in (7.2), and,

3. Γ_r needs to be a transparent surface for the waves that scatter from the boundary Γ_s and propagate into Ω_0. The integral involving the term $\frac{\partial p}{\partial n}$ in (7.3), therefore, does not vanish on Γ_r[†]. We will thus have an additional boundary integral in the BIE for the coupled PUFEM-PUBEM compared to the CBIE we used in Chapter 5 for solving scattering from hard cylinders.

The CBIE in (7.3) describes an outgoing wave through Γ_r exactly (at least the continuous equations) but, as was discussed in Chapter 5, it suffers from the problem of non-uniqueness. The CBIE in (7.3) even when coupled with the weak form in (7.2) will result in the non-uniqueness

[†]Note that the BIE or the hypersingular form of the CHBIE we used in Chapter 5 was solved on Γ_s and not on Γ_r. The integrals involving the terms $\frac{\partial p}{\partial n}$ either in the CBIE or CHBIE vanish as we only needed to solve the scattering problem on the scatterer Γ_s.

problem. The CHIEF method discussed in Chapter 5 will be used here to overcome the non-uniqueness problem in the coupled PUFEM-PUBEM approach. The integral equation for the CHIEF is reproduced below,

$$\rho(\mathbf{x})^{-1}c(\mathbf{x})p(\mathbf{x}) + \int_{\Gamma_r} \rho(\mathbf{x})^{-1}\frac{\partial G(\mathbf{x},\mathbf{y})}{\partial n_y}p(\mathbf{y})d\Gamma - \int_{\Gamma_r} \rho(\mathbf{x})^{-1}G(\mathbf{x},\mathbf{y})\frac{\partial p}{\partial n}d\Gamma$$
$$= \rho(\mathbf{x})^{-1}p^{inc}(\mathbf{x}), \qquad \mathbf{y} \in \Gamma_r, \mathbf{x} \in \Omega_f \cup \Omega_s \tag{7.4}$$

Note that the CHIEF points that we used in Chapter 5 were located inside the scatterer (i.e. interior to Γ_s). Since (7.4) will now be applied on the coupling boundary between the FE and BE regions, i.e. Γ_r, the CHIEF point locations can be taken such that $\mathbf{y} \in \Gamma_r$ and $\mathbf{x} \in \Omega_f \cup \Omega_s$. Note that $\mathbf{x}$ is the interior collocation point and $\mathbf{y}$ is the integration point for CHIEF. Also, recall from the discussion in Chapter 5 that CHIEF equations can become redundant if the CHIEF points lie on the nodal lines of the interior Dirichlet problem. However, following the procedure in Chapter 5, we choose the CHIEF points randomly, so that the CHIEF method gives stable and accurate results. The PUFEM-PUBEM coupling is achieved by arranging the matrix equations resulting from the discretization of equations (7.2), (7.3) and (7.4). Before forming the coupled system, however, we need to consider the plane wave basis that we will use for (7.2), (7.3) and (7.4). Only after introducing the plane wave basis for a coupled approach, will we be able to discuss the matrix manipulation that will give a coupled system.

7.2 Plane wave basis for the coupled PUFEM-PUBEM

Let us reproduce the compact notation (6.8) we introduced in Chapter 6 for the pressure field at a point $\mathbf{x} \in \Omega_f$ using the mixed basis,

$$p(\mathbf{x}) = \hat{\mathbf{\Omega}}^e \hat{\boldsymbol{\mathcal{A}}}^e \tag{7.5}$$

Recall that in (7.5), the row vector $\hat{\mathbf{\Omega}}^e$ is computed using the product of finite element shape functions and a combination of plane waves with the constituent wavenumbers in the domain Ω_f. The basis in (7.5) can be readily used for approximating the pressure variable $p(\mathbf{x})$ appearing in the integral over Ω_f in (7.2). However, the same plane wave amplitudes in the basis in (7.5) can not be used to approximate the normal derivative of the pressure appearing in the boundary integral over Γ_r. This is because $\frac{\partial p}{\partial n}$ on the FE-BE coupling boundary Γ_r, either in (7.2) or

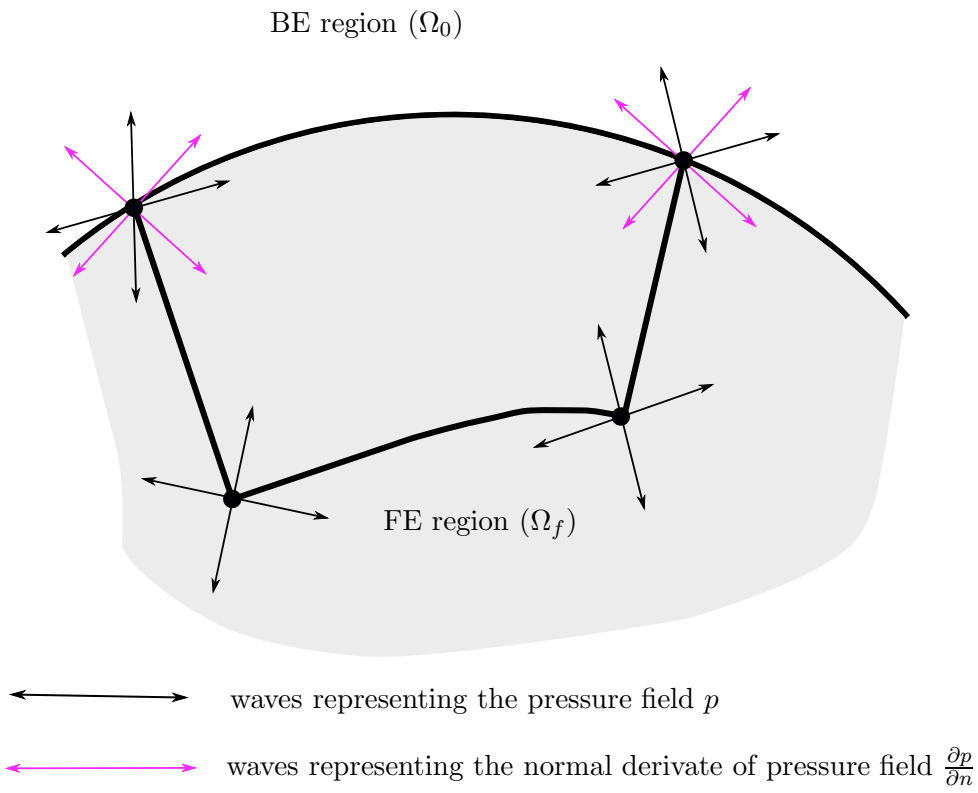

Figure 7.2: Plane wave basis for pressure and its normal derivative for coupled PUFEM-PUBEM

in (7.3), is also an unknown. This requires that the quantity $\frac{\partial p}{\partial n}$ on Γ_r also to be expressed using the plane wave basis approximation similar to (7.5). Clearly, we need to have different amplitudes for the plane waves that approximate the quantity $\frac{\partial p}{\partial n}$ on Γ_r, than those in (7.5) (i.e. the elements of vector $\hat{\boldsymbol{\mathcal{A}}}^e$) . Let these new plane wave amplitudes that correspond to the Neumann data be denoted as $b^l_{jm_l}$, i.e., the amplitude of the m^{th} plane wave at the j^{th} node with wavenumber k_l, $l = 1, \cdots, L$. We can therefore write,

$$\frac{\partial p(\mathbf{x})}{\partial n} = \sum_{j=1}^{n} N_j \sum_{l=1}^{L} \sum_{m_l=1}^{M_l} b^{k_l}_{jm_l} e^{ik_l \mathbf{d}_{jm_l} \cdot \mathbf{x}}, \qquad \mathbf{x} \in \Gamma_r. \tag{7.6}$$

Following the convention we used for writing (7.5), (7.6) can be further written in the compact form as,

$$\frac{\partial p(\mathbf{x})}{\partial n} = \hat{\mathbf{\Omega}}^e \hat{\boldsymbol{\mathcal{B}}}^e \tag{7.7}$$

The plane wave basis given in (7.5) and (7.7) are depicted in Figure 7.2. It is important to note here that the differentiation of (7.5) does not lead to (7.7) so that these two expansions for pressure and its normal derivative are not explicitly mutually consistent. However, this is

standard in BEM[‡], and the consistency is derived from their roles in the boundary integral equation which also contains the Green's function and its normal derivative. Following this, two important points need to be underlined here:

1. For a coupled PUFEM-PUBEM approach, both (7.5) and (7.6) are needed for the weak form (7.2), and,

2. Note that both (7.5) and (7.6) are mixed basis expansions, but, the plane wave basis defined for a PUBEM system in Chapter 4, i.e., (4.54a) and (4.54b), uses only a single wavenumber, namely k. Therefore, we need to modify the basis (4.54a) and (4.54b) so that the plane wave amplitudes for the basis to be used in a PUBEM system are shared with those used in the PUFEM system. In other words, we also need to write a mixed basis for the PUBEM system.

In view of point 2, we can write following matrix notations that will be used for a PUBEM system,

$$p(\mathbf{y}) = \hat{\boldsymbol{\mathfrak{R}}}^e \hat{\boldsymbol{\mathcal{A}}}^e, \qquad \mathbf{y} \in \Gamma_r \tag{7.8a}$$

$$\frac{\partial p(\mathbf{y})}{\partial n} = \hat{\boldsymbol{\mathfrak{R}}}^e \hat{\boldsymbol{\mathcal{B}}}^e, \qquad \mathbf{y} \in \Gamma_r \tag{7.8b}$$

where, $\hat{\boldsymbol{\mathfrak{R}}}^e$ is the row vector given by

$$\hat{\boldsymbol{\mathfrak{R}}}^e = \left[\hat{\mathcal{R}}_1, \cdots, \hat{\mathcal{R}}_n\right] \tag{7.9}$$

The elements of the vectors $\hat{\boldsymbol{\mathfrak{R}}}^e$ are further given as,

$$\hat{\mathcal{R}}_j = [\Psi_{j1}, \Psi_{j2}, \cdots, \Psi_{jL}] \tag{7.10a}$$

$$\Psi_{jl} = \left[\psi^l_{j1}, \psi^l_{j2}, \cdots, \psi^l_{M_l}\right] \tag{7.10b}$$

$$\psi^l_{jm_l}(\mathbf{x}) = N_j(\mathbf{x}) e^{\mathrm{i}k_l d_{jm_l}\cdot\mathbf{x}}, \qquad \mathbf{x} \in \Gamma_r \tag{7.10c}$$

The coupling is realised in the process as the plane wave amplitudes corresponding to a Dirichlet or Neumann value on the FE-BE interface Γ_r are common for PUFEM and PUBEM. Use of a

[‡]Recall that we defined two separate basis for pressure and its normal derivative for a PUBEM framework; see (4.54a) and (4.54b) for details. However, we did not use the basis in (4.54b) because $\partial p/\partial n = 0$ on Γ_s is assumed.

separate basis, such as in (7.5) and (7.7), is not needed when the iterative FE-BE coupling algorithms are used; see [167],[43]. The process of PUFEM-PUBEM coupling is now demonstrated through the matrix equations in the following section.

7.3 Linear system of equations for coupled PUFEM-PUBEM

Let the linear system of equations for the coupled PUFEM-PUBEM approach be given as

$$[\mathbf{A}_c]\{\mathbf{u}_c\} = \{\mathbf{f}_c\} \tag{7.11}$$

where $[\mathbf{A}_c]$ is the coupled PUFEM-PUBEM system matrix, $\{\mathbf{u}_c\}$ is the vector that contains unknown plane wave amplitudes associated with pressure and its normal derivative and $\{\mathbf{f}_c\}$ is the right hand side vector computed using collocation of the known incident wave on Γ_r. The coupled matrix $[\mathbf{A}_c]$ is composed of seven distinct block matrices viz. $\mathbf{A}_1, \mathbf{A}_2, \mathbf{A}_3, \mathbf{A}_4, \mathbf{A}_5, \mathbf{A}_6$, and $\mathbf{A}_7$. The coupled linear system in (7.11) can be written using the block matrix form as,

$$\left[\begin{array}{c|c|c} & & 0 \\ & & \\ \mathbf{A}_1 & \mathbf{A}_2 & \\ & & \mathbf{A}_3 \\ \hline & & \\ 0 & \mathbf{A}_4 & \mathbf{A}_5 \\ \hline & \mathbf{A}_6 & \mathbf{A}_7 \end{array}\right] \left\{\begin{array}{c} \\ \hat{\boldsymbol{\mathcal{A}}}_{\Omega_f \setminus \Gamma_r} \\ \hline \\ \hat{\boldsymbol{\mathcal{A}}}_{\Omega_f \cap \Gamma_r} \\ \hline \\ \hat{\mathfrak{B}}_{\Gamma_r} \\ \\ \end{array}\right\} = \left\{\begin{array}{c} \\ 0 \\ \\ \hline \\ \mathbf{b}_1 \\ \hline \mathbf{b}_2 \end{array}\right\} \tag{7.12}$$

The individual element matrices for the block matrices in (7.12) are given as

$$[\mathbf{A}_1^e] = \int_{\Omega_f^e \setminus \Gamma_r^e} \frac{1}{\rho(\mathbf{x})} \left(\nabla(\hat{\mathbf{\Omega}}^e)^{\mathrm{T}} \nabla(\hat{\mathbf{\Omega}}^e) - k^2 (\mathbf{\Omega}^e)^{\mathrm{T}} (\mathbf{\Omega}^e) \right) \, d\Omega \, , \tag{7.13a}$$

$$[\mathbf{A}_2^e] = \int_{\Omega_f^e \cap \Gamma_r^e} \frac{1}{\rho(\mathbf{x})} \left(\nabla(\hat{\mathbf{\Omega}}^e)^{\mathrm{T}} \nabla(\hat{\mathbf{\Omega}}^e) - k^2 (\mathbf{\Omega}^e)^{\mathrm{T}} (\mathbf{\Omega}^e) \right) \, d\Omega \, , \tag{7.13b}$$

$$[\mathbf{A}_3^e] = \int_{\Gamma_r^e} \frac{1}{\rho(\mathbf{x})} (\bar{\mathbf{\Omega}}^e)^{\mathrm{T}} (\bar{\mathbf{\Omega}}^e) \, d\Gamma \tag{7.13c}$$

$$[\mathbf{A}_4^e] = \frac{1}{\rho(\mathbf{x})} c(\mathbf{x}) \hat{\mathbf{\Re}}^e(\mathbf{x}) + \sum_{i=1}^{n_e} \int_{\Gamma_r^e} \frac{1}{\rho(\mathbf{y})} \frac{\partial G}{\partial n} \hat{\mathbf{\Re}}^e(\mathbf{y}) d\Gamma, \quad \mathbf{x}, \mathbf{y} \in \Gamma_r \tag{7.13d}$$

$$[\mathbf{A}_5^e] = \sum_{i=1}^{n_e} \int_{\Gamma_r^e} \frac{1}{\rho(\mathbf{y})} G \hat{\mathbf{\Re}}^e(\mathbf{y}) d\Gamma, \quad \mathbf{x}, \mathbf{y} \in \Gamma_r \tag{7.13e}$$

$$[\mathbf{A}_6^e] = \frac{1}{\rho(\mathbf{x})} c(\mathbf{x}) \hat{\mathbf{\Re}}^e(\mathbf{x}) + \sum_{i=1}^{n_e} \int_{\Gamma_r^e} \frac{1}{\rho(\mathbf{y})} \frac{\partial G}{\partial n} \hat{\mathbf{\Re}}^e(\mathbf{y}) d\Gamma, \quad \mathbf{x} \in \Omega_f \cup \Omega_s, \mathbf{y} \in \Gamma_r \tag{7.13f}$$

$$[\mathbf{A}_7^e] = \frac{1}{\rho(\mathbf{x})} c(\mathbf{x}) \hat{\mathbf{\Re}}^e(\mathbf{x}) + \sum_{i=1}^{n_e} \int_{\Gamma_r^e} \frac{1}{\rho(\mathbf{y})} \frac{\partial G}{\partial n} \hat{\mathbf{\Re}}^e(\mathbf{y}) d\Gamma, \quad \mathbf{x} \in \Omega_f \cup \Omega_s, \mathbf{y} \in \Gamma_r \tag{7.13g}$$

Note that the global vector of unknown plane wave amplitudes corresponding to the pressure data has been divided into two vectors (see the column vector in (7.12)), namely, $\hat{\boldsymbol{\mathcal{A}}}_{\Omega_f \setminus \Gamma_r}$ and $\hat{\boldsymbol{\mathcal{A}}}_{\Omega_f \cap \Gamma_r}$.

As the subscript indices indicate, the vector $\hat{\boldsymbol{\mathcal{A}}}_{\Omega_f \setminus \Gamma_r}$ contains the unknown plane wave amplitudes of those nodes which lie in the computational domain Ω_f but not on the FE-BE coupling boundary Γ_r. Whereas, $\hat{\boldsymbol{\mathcal{A}}}_{\Omega_f \cap \Gamma_r}$ contains the plane wave amplitudes corresponding to the pressure data for only those nodes which lie on Γ_r. As shown in (7.12), the two block matrices $\mathbf{A}_1$ and $\mathbf{A}_2$, multiply with $\hat{\boldsymbol{\mathcal{A}}}_{\Omega_f \setminus \Gamma_r}$ and $\hat{\boldsymbol{\mathcal{A}}}_{\Omega_f \cap \Gamma_r}$ respectively. The blocks $\mathbf{A}_4$ and $\mathbf{A}_5$ are obtained by performing the boundary integrals related to BIE in (7.3) over the coupling boundary Γ_r following the same procedure used in Chapter 5 (see §5.6). Similarly, the blocks $\mathbf{A}_6$ and $\mathbf{A}_7$ are obtained by performing the boundary integrals related to the CHIEF integral equation (7.4) over Γ_r. The number of interior collocation points (n_c) for CHIEF is taken as 20% of $n_{\mathrm{FB}}M$. As can be seen, the right hand side vector is also split between vectors $\mathbf{b}_1$ and $\mathbf{b}_2$. The vector, $\mathbf{b}_1$ is obtained by collocation of the incident wave on the FE-BE coupling boundary Γ_r (see (7.3)), and the vector $\mathbf{b}_2$ is computed using the interior collocation of the incident wave in the CHIEF integral equation (see (7.4)). The precise dimensions of the block matrices can be determined as follows.

Let the total number of nodes in the computational domain be n_{tot} and n_{FB} be the total number of nodes on the FE-BE coupling boundary Γ_r. We assume, as before, a uniform enrichment i.e., each node is enriched with equal number of plane waves in the present implementation. If each node is enriched with a total of M plane waves[§], where

$$M = \sum_{l=1}^{L} m_l \tag{7.14}$$

The dimensions of the various block matrices in (7.12) are listed in Table 7.1, It can therefore

Matrix/Vector	Dimension
$\mathbf{A}_1$	$n_{\text{tot}}M$
$\mathbf{A}_2$	$n_{\text{FB}}M$
$\mathbf{A}_3$	$n_{\text{FB}}M$
$\mathbf{A}_4$	$n_{\text{FB}}M$
$\mathbf{A}_5$	$n_{\text{FB}}M$
$\mathbf{A}_6$	$n_c \times n_{\text{FB}}M$
$\mathbf{A}_7$	$n_c \times n_{\text{FB}}M$
$\hat{\boldsymbol{\mathcal{A}}}_{\Omega_f \setminus \Gamma_r}$	$(n_{\text{tot}} - n_{\text{FB}})M$
$\hat{\boldsymbol{\mathcal{A}}}_{\Omega_f \cap \Gamma_r}$	$n_{\text{FB}}M$
$\hat{\boldsymbol{\mathcal{B}}}_{\Gamma_r}$	$n_{\text{FB}}M$
$\mathbf{b}_1$	$n_{\text{FB}}M$
$\mathbf{b}_2$	n_c

Table 7.1: Dimensions of the block matrices and vectors in the coupled system (7.12), $n_c = 20\%(n_{\text{FB}}M)$.

be seen from Table 7.1, the size of the coupled PUFEM-PUBEM system matrix $[\mathbf{A}_c]$ will be

$$\text{nDof} = n_c + n_{\text{tot}}M + n_{\text{FB}}M \tag{7.15}$$

To understand how a PUFEM linear system visually compares with the coupled system in (7.12), see Figure 7.3. It can be observed that $[\mathbf{A}_c]$ is partly symmetric (due to presence of symmetric blocks $\mathbf{A}_1, \mathbf{A}_2$, and $\mathbf{A}_3$) and partly unsymmetric (due to presence of unsymmetric blocks $\mathbf{A}_4, \mathbf{A}_5, \mathbf{A}_6$ and $\mathbf{A}_7$) which renders use of a symmetric profile solver impossible. A matrix premultiplication such as $[\mathbf{A}_c]^{\text{T}}[\mathbf{A}_c]$ would make the resulting system symmetric but because both the PUFEM and PUBEM systems are ill-conditioned, such an approach may not be inefficient.

[§]Recall that L here is the total number of distinct density jumps.

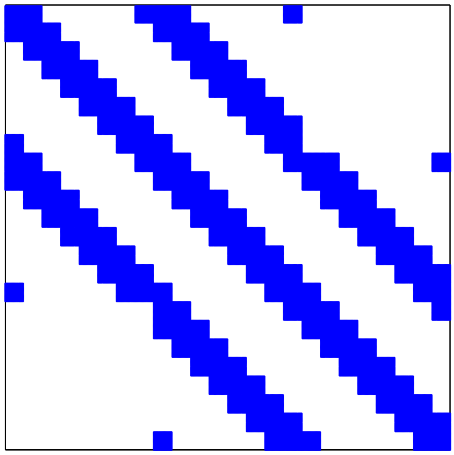

(a) PUFEM: nDof = 384, nnz = 43008

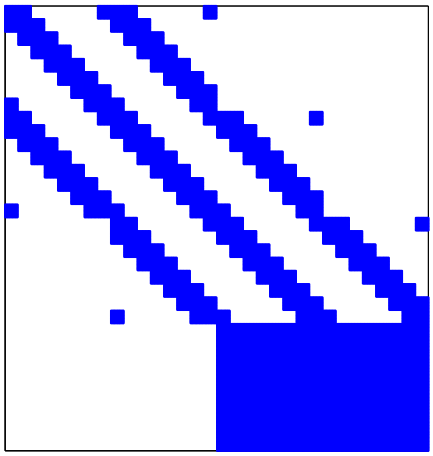

(b) Coupled PUFEM-PUBEM, nDof = 512, nnz = 88576

Figure 7.3: PUFEM vs Coupled PUFEM-PUBEM system comparison, nnz: number of non-zeros in the system matrix

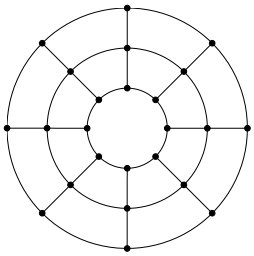

Figure 7.4: FE mesh for PUFEM and coupled PUFEM-PUBEM

7.4 Numerical examples

The PUFEM and coupled PUFEM-PUBEM approaches are compared in this section through various numerical examples arranged as follows. Firstly, the q and h convergence of the two methods are compared in §7.4.1 and §7.4.2 respectively. The q-convergence is achieved by increasing the total number of plane waves M at a finite element node, whereas the h-convergence is achieved by refining the FE mesh. This is followed by a comparison between PUFEM and coupled PUFEM-PUBEM for a fixed accuracy in computing the total acoustic field (§7.4.3). For all the results presented in §7.4.1, §7.4.2 and §7.4.3, the canonical problem of the plane wave scattering in annular layers (see Figure 6.1 in Chapter 6) will be used. PUFEM and coupled PUFEM-PUBEM are then compared with the polynomial FEM in §7.4.4 where the three methods are investigated for their accuracy for a given value of the parameter τ which represents the number of degrees of freedom per wavelength. Finally, the results for an example comparing the three methods where an analytical solution can not be obtained are shown. In the last case, a finite element solution with a very refined mesh (polynomial based FEM) is used as a reference solution to obtain a converged solution.

7.4.1 q-convergence:

To demonstrate the q-convergence of the coupled PUFEM-PUBEM approach and for comparison with PUFEM we consider the FE mesh with $n_\theta = 8$ and $n_r = 2$, where n_θ and n_r are the number of finite elements in the circumferential and the radial direction respectively (see Figure 7.4). It can be noted that the thickness of each fluid layer is contained within a single finite element. A numerical experiment is carried out by first setting $k_1 = \pi, k_0 = 2\pi$, and $\rho_0/\rho_1 = 1.2$. Therefore, the interior and exterior fluid layers will contain respectively 2 and 1 wavelengths each. These data are then reversed in the next test i.e., $k_1 = 2\pi, k_0 = \pi$, and $\rho_1/\rho_0 = 1.2$. It is evident from

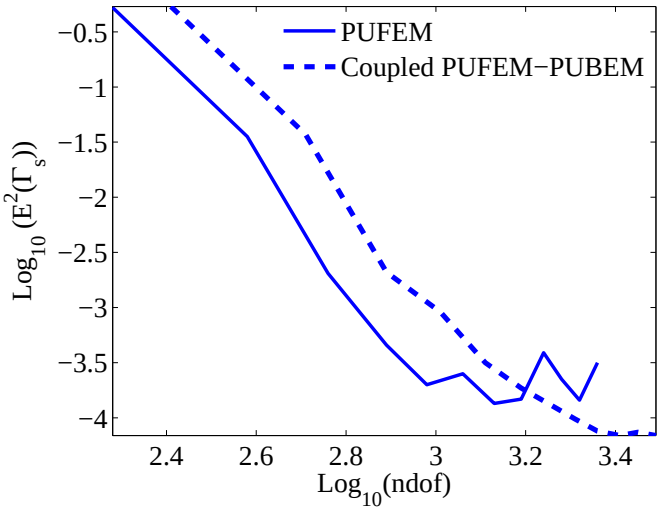

(a) $k_1 = \pi, k_0 = 2\pi$

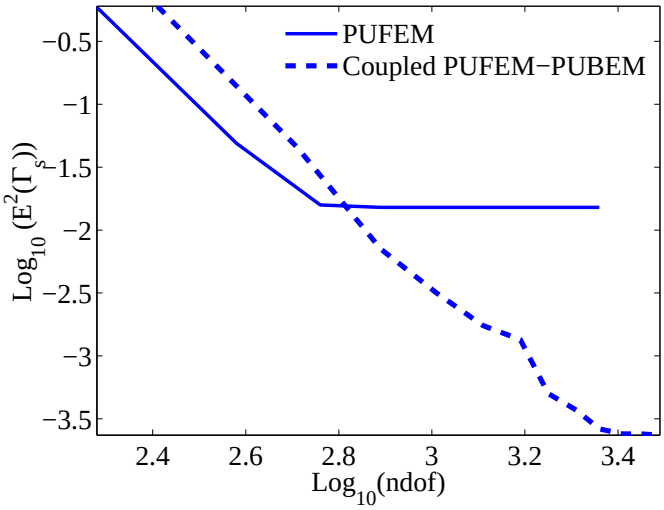

(b) $k_1 = 2\pi, k_0 = \pi$

Figure 7.5: L_2 error on Γ_s

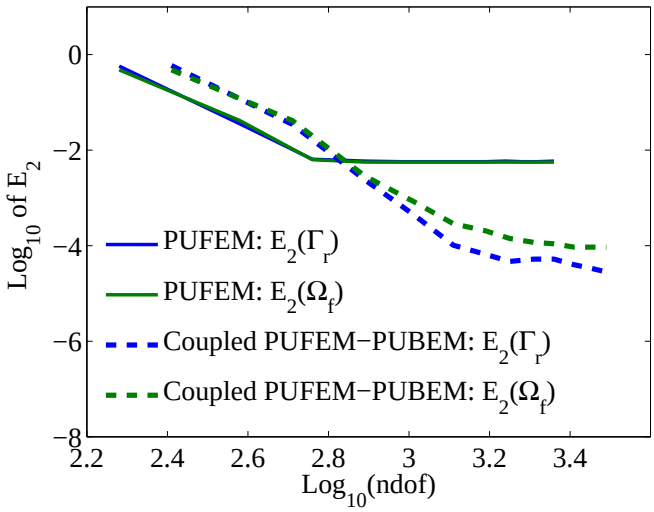

(a) $k_1 = \pi, k_0 = 2\pi$

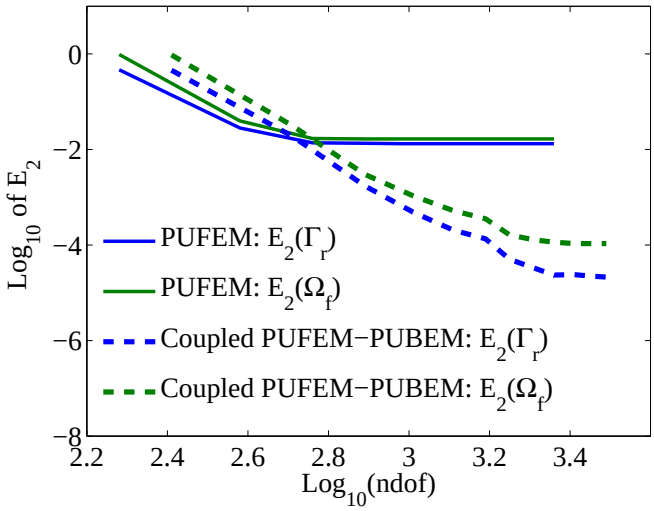

(b) $k_1 = 2\pi, k_0 = \pi$

Figure 7.6: L_2 error on Γ_r and in Ω_f

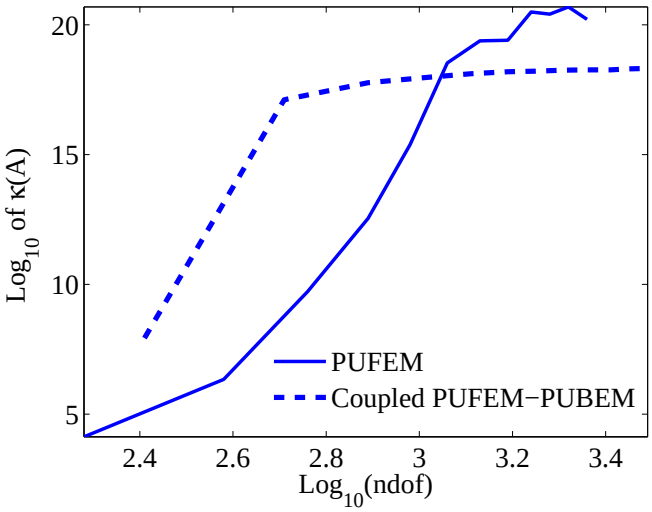

(a) $k_1 = \pi, k_0 = 2\pi$

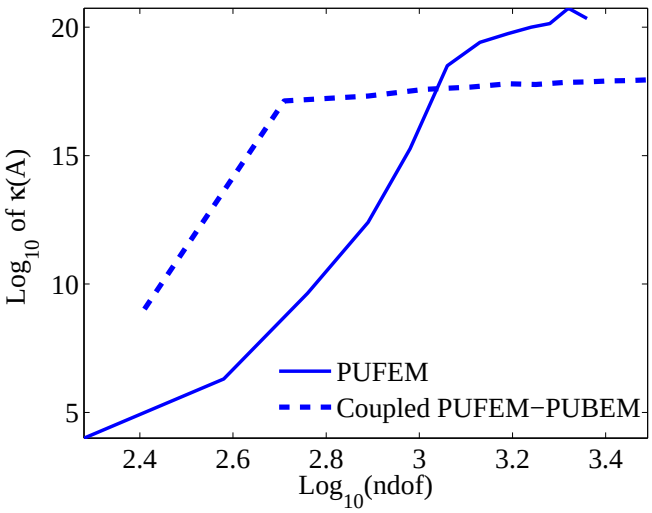

(b) $k_1 = 2\pi, k_0 = \pi$

Figure 7.7: Conditioning of the linear systems

the plots for the L_2 error on the scatterer in Figure 7.5a that the q-convergence performance on the scatterer surface, for both PUFEM and coupled PUFEM-PUBEM, is approximately the same below $\log_{10}(\text{nDof}) = 3.2$ and when $k_1 < k_0$. However, further addition of plane waves for the coupled PUFEM-PUBEM results in an improvement of approximately one order of magnitude in $E_2(\Gamma_s)$. The improvement achieved with the use of the coupled formulation is even more evident when the medium with longer wavelength (or smaller wavenumber) is placed in the exterior. Thus, when $k_0 < k_1$, the coupled PUFEM-PUBEM solution shows approximately 2 orders of magnitude improvement for the q-convergence for $E_2(\Gamma_s)$ (see Figure 7.5b). For the results on Γ_r and in Ω_f, the coupled PUFEM-PUBEM formulation again shows an improvement of close to 2 orders of magnitude for both $k_1 < k_0$ and $k_1 > k_0$ case (see Figure 7.6). Clearly, in the case of PUFEM, in order to effectively absorb an outgoing wave with longer wavelength, the boundary Γ_r needs to be placed further away from the scatterer. This would mean adding more layers of finite elements in the radial direction (i.e. increasing n_r) and therefore incurring an increased computational effort. It is known that both PUFEM and PUBEM result in ill-conditioned systems. The improvement in the accuracy in the case of the coupled PUFEM-PUBEM approach is accompanied with a corresponding rise in the condition number, $\kappa(\mathbf{A})$ ($\mathbf{A}$ is the given system matrix) (see Figure 7.7). However, the SVD solver used here, namely ZGELSS, is able to efficiently handle the ill-conditioning and yields an accurate solution.

For completeness, a comparison of the coupled PUFEM-PUBEM results with and without the use of the CHIEF method is shown in Figure 7.8. The L_2 error $E_2(\Omega_f)$ is plotted against the wavenumber k_0. For the results shown in Figure 7.8, the values of the wavenumber in the exterior (i.e. k_0) are chosen as the characteristic wavenumbers for the CBIE defined in eq. (7.3). At these wavenumbers, the CBIE in (7.3) fails to provide a unique solution, whether used individually or coupled with the weak form in (7.2). Note that the non-uniqueness of the CBIE is independent of the properties of the acoustic medium that lies in the interior or the density ratio ρ_1/ρ_0; see [119]. The wavenumbers on the x axis used in Figure 7.8 can be found by solving an interior Dirichlet problem on Γ_r, classically known as the Sturm-Liouville problem. The characteristic wavenumbers are then the square roots of these eigenvalues. The FE mesh used in this example is the same as used for q-convergence results and the number of plane waves per node is chosen such that $\tau_0 \approx 10$ is maintained. This value of τ_0 is chosen to ensure that

there are enough degrees of freedom to approximate the solution and any jump in the errors is not due to poor approximation of the solution. The wavenumber in the interior is taken as $k_0/2$ and ρ_0/ρ_1 as 1.2. As seen from Figure 7.8, the L^2 errors for the coupled PUFEM-PUBEM

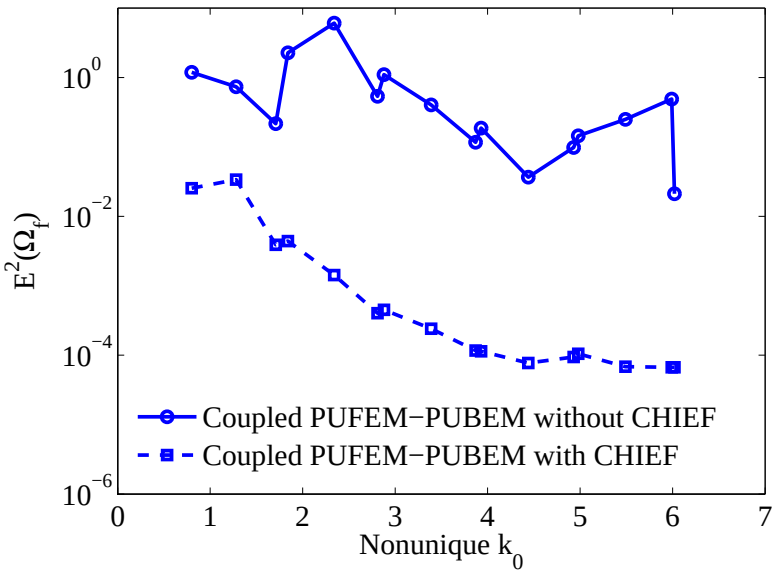

Figure 7.8: L^2 errors ($E^2(\Omega_f)$) for the coupled PUFEM-PUBEM: with and without CHIEF, all the values of k_0 are irregular wavenumbers

without the CHIEF method indicate that no correct solution is obtained. Whereas, using the interior collocation with the CHIEF method results in the solution with errors between 10^{-2} to 10^{-4} indicating that the non-uniqueness problem can be effectively overcome with the CHIEF method. For this case, the condition number comparison of the coupled system matrix $\mathbf{A}_c$ with and without the use of the CHIEF method is shown in Figure 7.9. It can be seen that with the use of the CHIEF method not only does the coupled system recover an accurate solution at characteristic wavenumbers, the method also shows some improvement in the condition number of the system matrix. As seen from Figure 7.8, close to two orders of magnitude improvement is achieved at characteristic wavenumbers with the use of the CHIEF method.

7.4.2 h-convergence:

Three different FE mesh configurations are considered (see Figure 7.10) for studying the h-convergence of PUFEM and coupled PUFEM-PUBEM approach. Tables 7.2-7.4 show a comparison between PUFEM and the coupled PUFEM-PUBEM for the various error norms given in (6.16)-(6.17). An additional error norm (see (7.16)) computed on the FE-BE coupling boundary Γ_r is also included which gives the accuracy of the given method to compute the pressure field

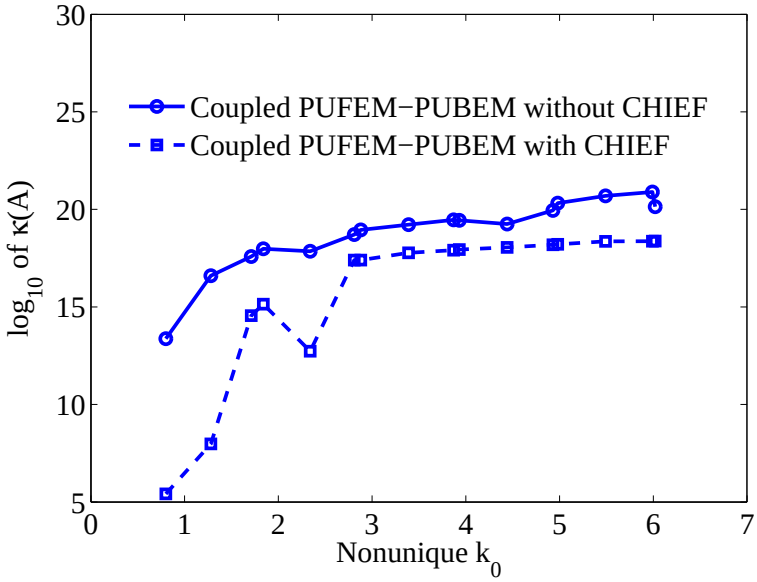

Figure 7.9: Condition number $\kappa(\mathbf{A}_c)$ for the coupled PUFEM-PUBEM approach: with and without CHIEF

	PUFEM				Coupled PUFEM-PUBEM			
Mesh	$E_2(\Gamma_s)$	$E_2(\Gamma_r)$	$E_2(\Omega_f)$	$\text{Log}_{10}(\kappa)$	$E_2(\Gamma_s)$	$E_2(\Gamma_r)$	$E_2(\Omega_f)$	$\text{Log}_{10}(\kappa)$
a	1.20E-02	1.10E-02	1.35E-02	7.83	1.01E-02	3.38E-03	5.47E-03	17.57
b	6.19E-03	1.00E-02	1.18E-02	13.91	1.69E-04	2.93E-05	8.40E-05	17.65
c	6.19E-03	1.00E-02	1.18E-02	19.57	1.23E-05	3.26E-05	1.96E-05	17.75

Table 7.2: h-convergence for $k_1 = 3\pi, k_0 = 2\pi, M_1 = 16, M_0 = 16$.

away from the scatterer.

$$E_2(\Gamma_r) = \frac{\|p - \tilde{p}\|_{L_2(\Gamma_r)}}{\|\tilde{p}\|_{L_2(\Gamma_r)}}, \tag{7.16}$$

The parameter κ listed in Tables 7.2-7.4 is the 2-norm condition number of the considered system matrix. It was found that a minimum of 16 plane waves per node for each wavenumber are needed (i.e., $M_1 = 16, M_0 = 16$) to achieve an accuracy of the order 10^{-2} for the cases considered in Tables 7.2 and 7.3. This requirement was found to be 32 plane waves per node for each wavenumber for the case in Table 7.4. It is seen that for the various cases of k_1 and k_0 considered, the coupled PUFEM-PUBEM formulation outperforms PUFEM. It is noteworthy that the improvement in the accuracy for PUFEM is accompanied by a steep rise (at least

	PUFEM				Coupled PUFEM-PUBEM			
Mesh	$E_2(\Gamma_s)$	$E_2(\Gamma_r)$	$E_2(\Omega_f)$	$\text{Log}_{10}(\kappa)$	$E_2(\Gamma_s)$	$E_2(\Gamma_r)$	$E_2(\Omega_f)$	$\text{Log}_{10}(\kappa)$
a	4.28E-02	4.28E-02	6.64E-02	5.82	4.84E-02	4.23E-02	7.90E-02	17.54
b	3.42E-03	8.73E-03	1.09E-02	10.75	6.05E-04	2.51E-04	3.43E-04	17.65
c	3.38E-03	8.73E-03	1.09E-02	17.86	1.60E-05	3.55E-05	2.02E-05	17.72

Table 7.3: h-convergence for $k_1 = 4\pi, k_0 = 3\pi, M_1 = 16, M_0 = 16$.

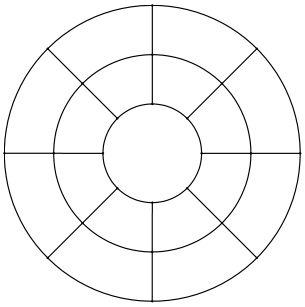

(a) Mesh a: $n_r = 2, n_\theta = 8$

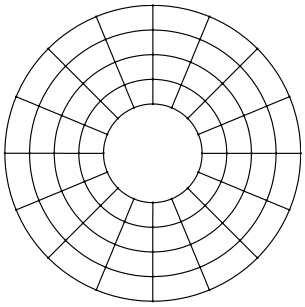

(b) Mesh b: $n_r = 4, n_\theta = 16$

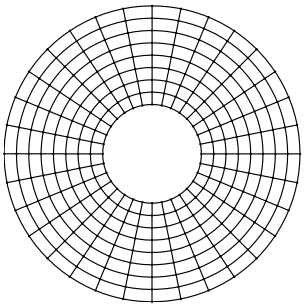

(c) Mesh c: $n_r = 8, n_\theta = 32$

Figure 7.10: FE meshes for h-convergence.

	PUFEM				Coupled PUFEM-PUBEM			
Mesh	$E_2(\Gamma_s)$	$E_2(\Gamma_r)$	$E_2(\Omega_f)$	$\text{Log}_{10}(\kappa)$	$E_2(\Gamma_s)$	$E_2(\Gamma_r)$	$E_2(\Omega_f)$	$\text{Log}_{10}(\kappa)$
a	4.03E-02	3.63E-02	8.55E-02	7.95	3.80E-02	2.20E-02	6.69E-02	17.99
b	1.72E-03	9.81E-03	1.09E-02	16.50	1.03E-04	2.57E-05	1.01E-04	18.03
c	1.72E-03	9.81E-03	1.09E-02	20.74	5.01E-05	3.47E-05	2.42E-05	18.67

Table 7.4: h-convergence for $k_1 = 6\pi, k_0 = 5\pi, M_1 = 32, M_0 = 32$.

10 orders of magnitude) in the condition number. In contrast, the condition numbers for the coupled PUFEM-PUBEM results remain within the same range as the accuracy of the solution improves with the mesh refinement.

7.4.3 PUFEM vs coupled PUFEM-PUBEM comparison for a fixed accuracy

Often engineers are interested in knowing the CPU time and the total degrees of freedom required to achieve a preset tolerance in the calculation of the solution variable. From the results in §7.4.1 or 7.4.2, it can be seen that it is difficult to obtain an accuracy of 1% (or $E^2(\Omega_f) \approx$1E$-$02) for PUFEM with the radius of the radiation boundary as $r(\Gamma_r) = 3m$. As mentioned earlier, the improvement in the PUFEM results can be obtained by placing the radiation boundary further away from the scatterer (i.e by increasing $r(\Gamma_r)$). We consider two cases for the fixed

	Interior wavenumber (k_1), $k_1/k_0 = 2$					Interior wavenumber (k_1), $k_1/k_0 = 3$				
	π	2π	3π	4π	5π	π	2π	3π	4π	5π
$\log_{10}$(nDof)(1)	2.95	3.13	3.35	3.43	3.55	2.95	3.13	3.25	3.43	3.65
$\log_{10}$(nDof)(2)	2.89	3.06	3.28	3.36	3.49	2.89	3.06	3.19	3.36	3.54
$\log_{10}$(nnz)(1)	5.87	6.22	6.67	6.83	7.08	5.87	6.22	6.47	6.83	7.27
$\log_{10}$(nnz)(2)	5.71	6.06	6.51	6.67	6.92	5.71	6.06	6.31	6.67	7.02
T_{intgn} (1)	0.71	5.01	29.9	80.69	243.23	0.71	4.99	19.95	81.25	342.52
T_{intgn} (2)	5.45	13.72	49.63	95.51	221.4	5.67	14.08	33.82	98.66	273.7
T_{solve} (1)	0.13	0.43	1.88	3.25	7.48	0.13	0.43	0.98	3.23	14.47
T_{solve} (2)	3.19	11.17	47.56	80.1	189.17	3.15	11.15	25.03	81.9	292.53

Table 7.5: Case (a): PUFEM vs coupled PUFEM-PUBEM for 1% accuracy,
(1): PUFEM, (2): coupled PUFEM-PUBEM

accuracy viz. (a) $E^2(\Omega_f) \approx 0.01$ and (b) $E^2(\Omega_f) \approx 0.005$. For both cases two ratios of k_1/k_0 are considered, viz. $k_1/k_0 = 2$ and $k_1/k_0 = 3$. Only for the PUFEM, we choose the radius of the radiation boundary as $r(\Gamma_r) = 4$ for case (a) and $r(\Gamma_r) = 5$ for case (b) to minimize the reflections at Γ_r. However, for the coupled PUFEM-PUBEM approach, the radius of the radiation boundary will not make a difference and therefore we use $r(\Gamma_r) = 3$, $n_r = 2$ for both the cases (a) and (b). For the case of PUFEM, we choose $n_r = 6$ for the case (a) and $n_r = 8$ for the case (b). For both PUFEM and the coupled PUFEM-PUBEM, we take $n_\theta = 16$. It may be noted that the tolerance limit in case (a) on $E^2(\Omega_f)$ is set to 0.01 (or 1%) which is generally regarded as the engineering accuracy. The total degrees of freedom for a particular case is increased by successively adding plane waves (increasing M) in the basis until the preset error tolerance is achieved.

Tables 7.5 and 7.6 compare various parameters obtained for 1% (case (a)) and 0.5% (case (b)) accuracies respectively. In total, five cases for k_1 are tested each for the ratios $k_1/k_0 = 2$ and $k_1/k_0 = 3$. For each case, PUFEM and coupled PUFEM-PUBEM are compared for the total dof (nDof), number of non-zero entries (nnz) in the system matrix, integration (T_{intgn}) and solution times (T_{solve}). Note that the integration time for the coupled PUFEM-PUBEM approach includes the time needed to integrate the weak form in (7.2) and the boundary integral equations in (7.3) and (7.4). In addition to the results in Tables 7.5 and 7.6, a graph is included showing the variation of the parameter τ_1 against the wavenumber k_1 for 1% and 0.5% accuracies for $k_1/k_0 = 2$ (Figure 7.11a) and $k_1/k_0 = 3$ (Figure 7.11b). The savings achieved in terms of the total degrees of freedom needed (nDof) and the amount of fill-in (nnz) are highlighted in Tables 7.7-7.8. As summarised in Tables 7.7-7.8, for an error tolerance of 1%, a significant amount of savings can be achieved in the total degrees of freedom needed ($\approx 12 - 15\%$) and in

	Interior wavenumber (k_1), $k_1/k_0 = 2$					Interior wavenumber (k_1), $k_1/k_0 = 3$				
	π	2π	3π	4π	5π	π	2π	3π	4π	5π
$\log_{10}$(nDof)(1)	3.06	3.36	3.54	3.61	3.71	3.06	3.36	3.46	3.54	3.80
$\log_{10}$(nDof)(2)	2.89	3.06	3.28	3.36	3.49	2.89	3.06	3.28	3.36	3.56
$\log_{10}$(nnz)(1)	6.1	6.7	7.05	7.19	7.4	6.10	6.70	6.89	7.05	7.58
$\log_{10}$(nnz)(2)	5.71	6.06	6.51	6.67	6.92	5.71	6.06	6.51	6.67	7.06
T_{intgn} (1)	1.46	18.56	94.43	218.91	563.65	1.44	18.64	62.11	164.79	840.00
T_{intgn} (2)	5.49	13.88	50.86	97.24	220.9	5.50	13.79	49.83	96.29	299.89
T_{solve} (1)	0.18	1.34	4.36	6.81	14.29	0.18	1.33	2.55	4.34	25.94
T_{solve} (2)	3.2	11.2	47.57	80.2	177.28	3.14	11.12	48.73	80.19	310.67

Table 7.6: Case (b): PUFEM vs coupled PUFEM-PUBEM for 0.5% accuracy, (1): PUFEM, (2): coupled PUFEM-PUBEM

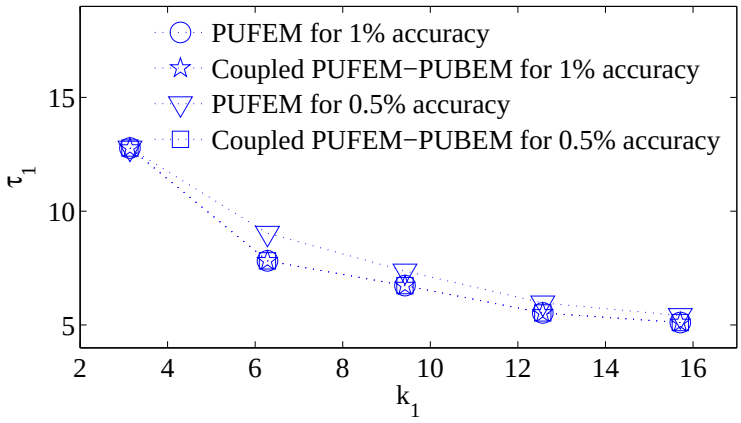

(a) $k_1/k_0 = 2$

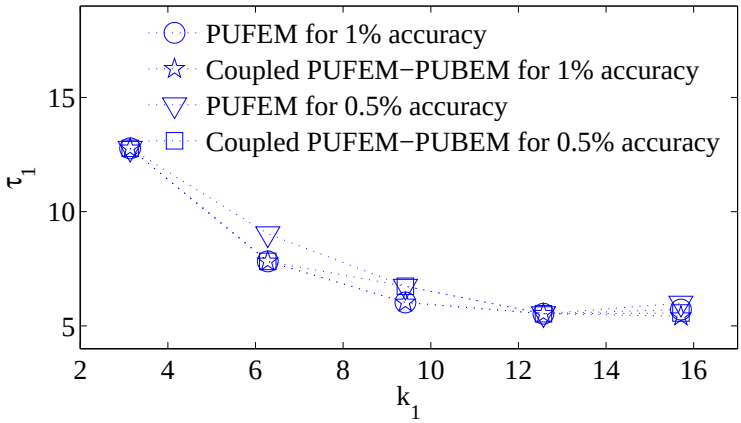

(b) $k_1/k_0 = 3$

Figure 7.11: Dependence of τ_1 on k_1

Interior wavenumber (k_1), $k_1/k_0 = 2$						
Accuracy		π	2π	3π	4π	5π
1%	% saving in nDof	12.90	14.89	14.89	14.89	12.90
	% saving in nnz	30.82	30.82	30.82	30.82	30.82
	% saving in T_{intgn}	-667.61	-173.85	-65.99	-18.37	8.98
0.5%	% saving in nDof	32.39	49.88	45.05	43.77	39.74
	% saving in nnz	59.26	77.09	71.16	69.80	66.89
	% saving in T_{intgn}	-276.03	25.22	46.14	55.58	60.81

Table 7.7: % saving achieved using coupled PUFEM-PUBEM approach for $k_1/k_0 = 2$

Interior wavenumber (k_1), $k_1/k_0 = 3$						
Accuracy		π	2π	3π	4π	5π
1%	% saving in nDof	12.90	14.89	12.90	14.89	22.38
	% saving in nnz	30.82	30.82	30.82	30.82	43.77
	% saving in T_{intgn}	-698.59	-182.16	-69.52	-21.43	20.09
0.5%	% saving in nDof	32.39	49.88	33.93	33.93	42.46
	% saving in nnz	59.26	77.09	58.31	58.31	69.80
	% saving in T_{intgn}	-281.94	26.02	19.77	41.57	64.30

Table 7.8: % saving achieved using coupled PUFEM-PUBEM approach for $k_1/k_0 = 3$

the amount of fill-in ($\approx 30\%$) if the coupled PUFEM-PUBEM approach is used. Of course, the integration time is higher for most cases of the coupled approach when 1% accuracy is sought. However, use of coupling PUFEM-PUBEM appears justifiable when higher accuracy of 0.5% is sought where we find an average 42% saving in the nDof and close to a 68% saving in the fill-in along with a significant reduction in the integration time. It can be observed from Figure 7.11 that the parameter τ_1 reduces as the wavenumber k_1 increases for both PUFEM and the coupled PUFEM-PUBEM and appears to approach a value close to 5.0.

7.4.3.1 Choice of M_1 and M_0

Intuitively, the mixed basis enrichment can be considered to be dependent upon the ratio of k_1 and k_0. The numerical tests, however, show that the best results can be obtained if the enrichment for k_1 and k_0 is nearly uniform[¶] i.e. by taking $M_1 \approx M_0$, where M_1 and M_0 are the number of plane waves at each node with k_1 and k_0 in the basis respectively. We consider again the canonical two layer problem defined in Figure 6.1 (Chapter 6). The finite element mesh used is seen in Figure 7.4. Four cases for the wavenumbers are considered (i) $k_1 = \pi, k_0 = 2\pi$, (ii) $k_1 = 2\pi, k_0 = \pi$, (iii) $k_1 = \pi, k_0 = 3\pi$ and (iv) $k_1 = 3\pi, k_0 = \pi$. Note that case (ii) is simply the data reversed in case (i) and case (iv) is the data reversed in case (iii). We take $M_1 + M_0 = 32$ for cases (i) and (ii) and $M_1 + M_0 = 40$ for cases (iii) and (iv). Figures 7.12 and 7.13 show the L_2 error in Ω_f ($E_2(\Omega_f)$) plotted against M_1. As seen from Figures 7.12 and 7.13, the L_2 errors are sensitive to the ratio of M_1 and M_0. Towards the left end of the plot, either in Figure 7.12 or 7.13, there will be too few plane waves with k_1 in the basis ($M_1 \ll M_0$) resulting in a poor modelling of the waves in the Ω_1 region. In contrast, towards the right end of the plots, $M_1 \gg M_0$ and there will be too few waves with k_0 in the basis causing poor modelling of the waves in the exterior Ω_2. From the results shown in Figures 7.12-7.13, a suitable combination

[¶]We observed similar behaviour in the results listed in Table 6.4 for PUFEM.

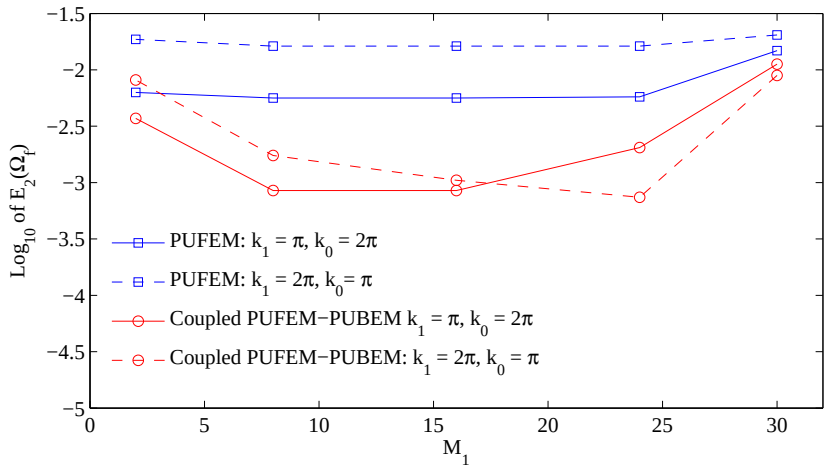

Figure 7.12: M_1 and M_0 combination, $k_1(k_0) = \pi, k_0(k_1) = 2\pi$, $M_1 + M_0 = 32$.

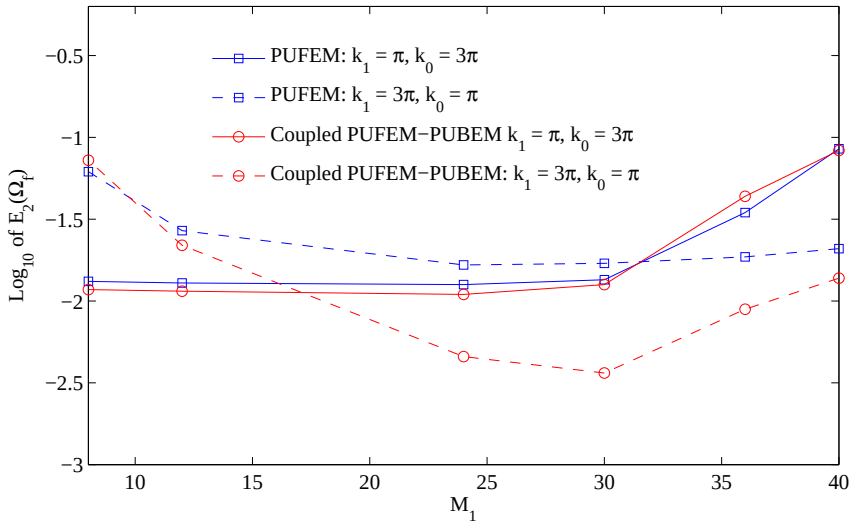

Figure 7.13: M_1 and M_0 combination, $k_1(k_0) = \pi, k_0(k_1) = 3\pi$, $M_1 + M_0 = 40$.

			$E^2(\Omega_f)$		
k_1	τ_1	τ_0	(a)	(b)	(c)
π	6.38	9.89	4.05E-01	6.76E-01	5.00E-01
2π	4.51	6.99	8.98E-01	5.37E-01	5.25E-01
3π	5.21	8.07	8.91E-01	3.35E-01	3.36E-01
4π	5.05	7.82	1.21E+00	3.30E-02	3.21E-02
5π	5.11	7.91	1.03E+00	1.37E-02	4.22E-03
6π	4.99	7.73	1.12E+00	1.11E-02	4.88E-03
7π	4.99	7.74	9.95E-01	9.78E-03	4.37E-03
8π	5.05	7.82	1.14E+00	1.79E-02	8.72E-03
9π	4.91	7.61	1.42E+00	3.42E-02	2.21E-02
10π	4.94	7.66	1.59E+00	1.11E-02	4.44E-03

Table 7.9: FEM (a) vs PUFEM (b) vs Coupled PUFEM-PUBEM (c) for a given τ_1, $k_0 = k_1/2$

appears to be $M_1 = M_0$ to achieve results with accuracy of 1% or better. We therefore choose $M_1 = M_0$ for all the numerical examples pertaining to the two layer problem.

7.4.4 Comparison with polynomial FEM for given τ_1

A comparison between the polynomial FEM, PUFEM and the coupled PUFEM-PUBEM is now presented. These three methods are compared for a given range of τ_1. It can be seen from (6.14a) (or (6.14b)) that using a fixed value of parameter τ_1 (or τ_0) can result in a non integer value for M. We therefore choose the parameter $\tau_1 \approx 5$ so that the total number of plane waves per node is an integer. Also, $\tau_1 \approx 5$ is chosen because the results in §7.4.3 indicate that τ_1 needs to be maintained close to 5 to achieve an accuracy of 1% (i.e. when $k_1 > k_0$). The FE mesh chosen for PUFEM and coupled PUFEM-PUBEM uses $n_\theta = 16$ and $n_r = 4$ and the radius of the radiation boundary is taken as $r(\Gamma_r) = 3m$. The number of plane waves per node M is then chosen such that (6.14a) results in a value for τ_1 that is close to 5. Also, the FE mesh for polynomial FEM is chosen such that the parameters τ_1 and τ_0 for PUFEM (or coupled PUFEM-PUBEM) match with the corresponding parameters for polynomial FEM. Table 7.9 gives $E^2(\Omega_f)$ for the three methods. The wavenumber k_1 varies between π to 10π and we take $k_0 = k_1/2$. As seen from Table 7.9, for lower wavenumbers ($k_1 \leq 3\pi$) all three methods perform poorly. This can also be observed from the PUFEM results published by Laghrouche *et al* (see Table 1 in ref. [106]) where higher values of τ are needed for an accuracy close to or better than 1% for wavenumbers below 4π. However, as the wavenumber k_1 is increased, both PUFEM and coupled PUFEM-PUBEM result in an accuracy between 1-3% for $\tau_1 \approx 5$. FEM results in an unacceptable solution with errors more than 100% for almost all the cases of $k_1 > 4\pi$. Table 7.9 again underlines that the plane wave enrichment can result in significant improvement in the accuracy over FEM for a given number of degrees of freedom.

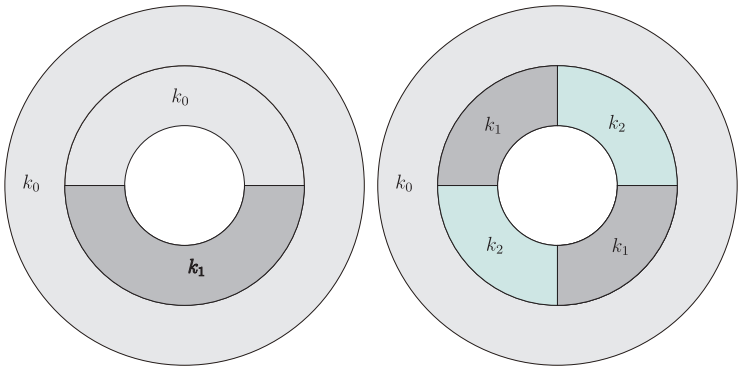

(a) problem 1 (b) problem 2

Figure 7.14: Split cylinder problems

Problem	k_1	k_2	k_0	ρ_1/ρ_0	ρ_2/ρ_0
Figure 7.14a	2π	-	π	1.2	-
Figure 7.14b	2π	1.5π	π	1.2	1.1

Table 7.10: Problem data for Figure 7.14

7.4.5 Split cylinder problem

For the two layer problem considered in §7.4.1, it was possible to construct an analytical solution. However, for a composite structure made up of a halfway split inner cylinder and each half with a different medium density (and hence different wavenumber), it will not be possible to obtain an analytical solution (see Figure 7.14a). A more complicated configuration is shown in Figure 7.14b where the inner cylinder is split into four equal sectors. The wavenumbers and density ratios used for this problem are listed in Table 7.10. As before, we consider the plane wave scattering (e^{ik_0x}) from the sound hard cylinder for the problems defined in Figures 7.14a-7.14b. Note that k_0 is the wavenumber of the homogeneous exterior medium. For both problems in Figure 7.14, the reference solution is obtained by a refined polynomial FEM with 164480 nodes in the mesh and with the radius of the circular radiation boundary Γ_r as 6m. The radius of Γ_r is taken as 6m in order to minimize the spurious reflections from the radiation boundary when obtaining the reference solution. Also, for both the problems in Figure 7.14, we use the same FE mesh as shown in Figure 7.4 for PUFEM and coupled PUFEM-PUBEM. The mixed basis discussed in the last chapter with $M_1 = M_0 = 8$ is used to solve the problem in Figure 7.14a, and $M_1 = M_2 = M_0 = 16$ for the problem in Figure 7.14b, for both PUFEM and coupled PUFEM-PUBEM. These values were chosen as they were found to result in a convergent solution. A polynomial FEM solution is also computed for comparison with the radius of the radiation

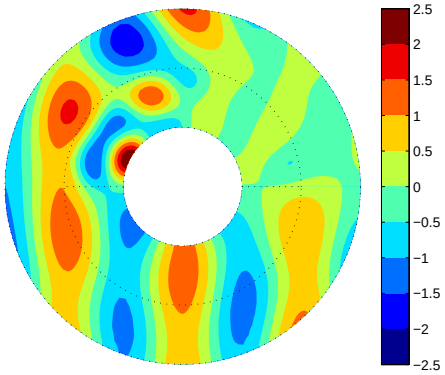

(a) Reference solution

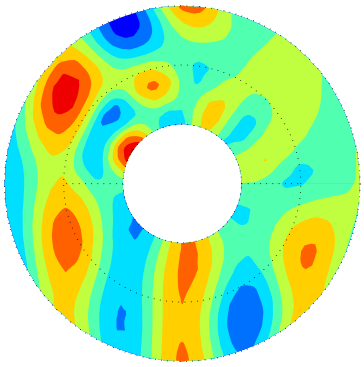

(b) Polynomial FEM

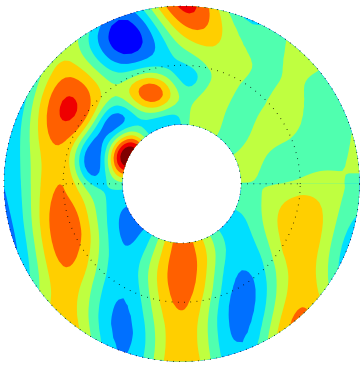

(c) PUFEM

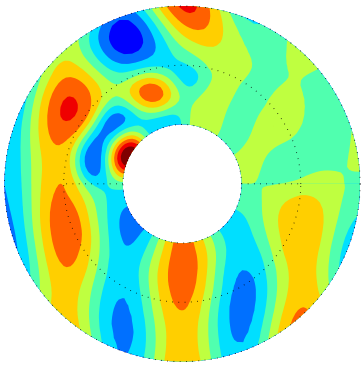

(d) Coupled PUFEM-PUBEM

Figure 7.15: $\Re(p)$ in Ω_f for split cylinder problem 1 in Figure 7.14a

boundary as 3. To demonstrate the advantage of using the mixed enrichment, the number of nodes used when polynomial FEM is used for comparison, are taken to be of the same order of magnitude as the total degrees of freedom used in the PUFEM or the coupled PUFEM-PUBEM approach. As can be seen from Figures 7.15 and 7.16, the wave scattering for the split cylinder problems is complicated at the interface of the two media. When the total degrees of freedom used is the same order for all methods, both PUFEM and coupled PUFEM-PUBEM show a clear advantage due to the use of the plane wave enrichment. The errors associated with PUFEM and coupled PUFEM-PUBEM are close to between 1-3% whereas the FEM results in an

	Figure 7.14a			Figure 7.14b		
	1	2	3	1	2	3
dof	520	384	512	1984	1152	1548
$E^2(\Omega_f)$ (%)	120	2.9	2.7	170	2.6	1.8

Table 7.11: 1: FEM, 2: PUFEM, 3: Coupled PUFEM-PUBEM, Reference solution is polynomial FEM with 164480 nodes

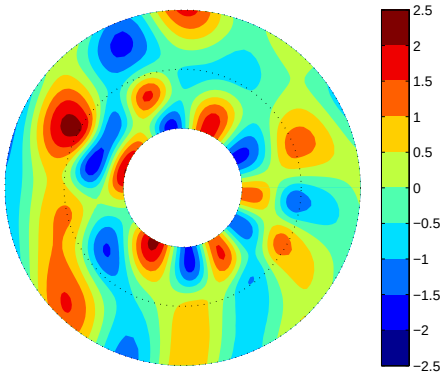

(a) Reference solution

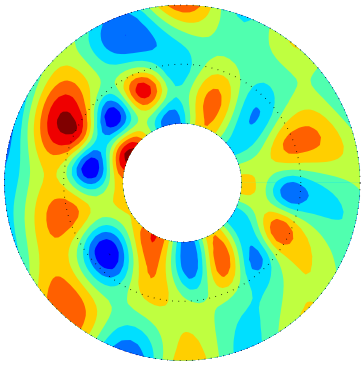

(b) Polynomial FEM

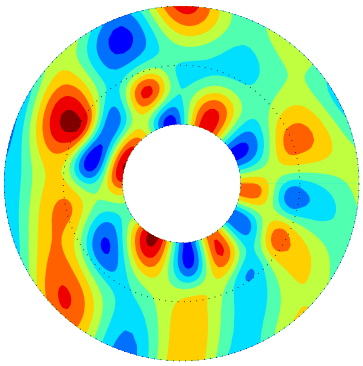

(c) PUFEM

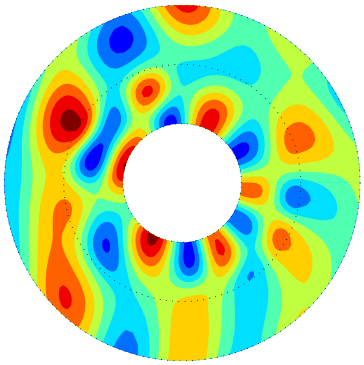

(d) Coupled PUFEM-PUBEM

Figure 7.16: $\Re(p)$ in Ω_f for split cylinder problem 2 in Figure 7.14b

unacceptable solution with an error of more than 100%. It should be noted that the errors given in Table 7.11 are only indicative as there is no analytical solution for the considered problem. Though the reference FE solution used here has 164480 nodes, it still is an approximate solution as it makes use of the BGT-2 NRBC on Γ_r.

7.5 Conclusions

In this chapter, the concept of mixed basis is shown to extend to the coupled PUFEM-PUBEM approach directly. The coupling of PUFEM and PUBEM is presented through detailed matrix equations. A comparison between FEM, PUFEM and coupled PUFEM-PUBEM for heterogeneous problems is presented. In general, it can be concluded that the plane wave based methods, both PUFEM and coupled PUFEM-PUBEM, outperform FEM. The error analyses presented, for both q and h refinement, indicates that close to two orders of magnitude improvement in the global error measure $E^2(\Omega_f)$ can be obtained with the coupled PUFEM-PUBEM algorithm in comparison with the PUFEM approach. Both FEM and PUFEM are limited in accuracy due to use of the approximate NRBC on Γ_r. A problem of a split cylinder is solved where an analytical solution can not be found and the mixed basis is shown to recover an accurate solution for this problem. It is also shown that FEM, when used with similar order for the total degrees of freedom results in unacceptable solutions.

Chapter 8

Conclusions

8.1 Concluding remarks

The main aim of this thesis was to present an algorithm to solve wave scattering problems in a heterogeneous medium in an unbounded domain. Coupling of PUFEM with PUBEM was motivated by the fact that PUFEM inherently needs an approximate boundary condition whereas PUBEM can accurately represent the scattered waves in the homogeneous domain. The use of a plane wave basis, both for FEM and BEM, was motivated by the fact these methods tend to become inefficient for high frequencies requiring 10 degrees of freedom per wavelength. Chapter 1 discussed these aspects and Chapter 2-4 further provided the background material on the theory of the acoustic waves, the weak formulation and the BIE (Chapter 2), element based discretization (Chapter 3) and the concept of plane wave basis (Chapter 4).

The motivation of the numerical studies carried out in Chapter 5 was to investigate an effective way to overcome the non-uniqueness problem in the BIE. Particularly, the effect of ill-conditioned systems and ability of CHIEF and Burton-Miller methods to accurately recover solutions at characteristic wavenumbers was of interest. It was demonstrated in Chapter 5 that scattering from smooth obstacles, when the exterior medium is homogeneous, can be effectively solved using the PUBEM approach. In general, L^2 errors of the order 10^{-6} could be achieved with the PUBEM using both the CHIEF and Burton-Miller approaches, although the CHIEF approach was found to always result in better accuracy. As demonstrated via results presented in Chapter 5, the number of degrees of freedom per wavelength (τ) needed for PUBEM is close to 3 for the examples considered and can go below 3 for higher wavenumbers. This is 3-4 times

smaller than that required in the polynomial based BEM where τ needs to be ≈ 10 to obtain solutions within the engineering accuracy of 1%. The results presented indicate that the CHIEF method is attractive is it involves simpler boundary integrals than those involved in the Burton-Miller approach, besides the ease of implementation of the former. Ill-conditioning of the linear systems still remains a problem, as also observed in previous works, but numerical results in Chapter 5 indicate that SVD is a reliable method to solve such systems.

Chapter 6 demonstrated the efficacy of PUFEM for solving wave scattering in heterogeneous media. The concept of mixed basis is shown to be effective in recovering the acoustic field for these problems. It was argued that the mixed basis is effective for problems where the number of distinct jumps (L) is small. The size of the PUFEM system can be seen to grow as a linear function of L (keeping the number of plane waves at each node constant). However, many practical applications such as composite structures where the interaction of waves (especially ultrasound) needs to be studied due to alternate layers which are themselves homogeneous, the approach of mixed basis presented in Chapter 6 can be effective.

Chapter 7 demonstrated the coupling of PUFEM with PUBEM. Since both methods are plane wave based, the coupling can be achieved by a simple matrix arrangement. From the results in §7.4.3, it can be concluded that the coupled PUFEM-PUBEM approach can be preferred over PUFEM when an accuracy close to or better than 1% is sought in view of savings achieved for the total degrees of freedom (nDof) (approx. 12-15%) and the fill-in (nnz) (approx. 30%). For the heterogeneous problems, for both PUFEM and coupled PUFEM-PUBEM, it is found that the parameter τ needed in the region with higher wavenumber is close to 5 to achieve accuracy between 1-3%. However, when similar values of τ in the higher wavenumber region are used for classical FEM, the results obtained are unacceptable with errors more than 100%. In general, the proposed method of coupling PUFEM and PUBEM is promising in view of the significant reductions achieved in the degrees of freedom required which motivates its extension in solving 3D heterogeneous wave problems. The disadvantage of using an unsymmetric coupling approach, such as the one used in this study, is clearly the high solution time needed. However, this can be justified given that the accuracy levels of $< 0.5\%$ cannot be achieved using PUFEM when $r(\Gamma_r)$ is small.

8.2 Recommendations for future work

8.2.1 Biomedical problems

In this thesis we assumed that the acoustic medium is lossless but very does rarely such a situation arise in real life. Of course, for practical purposes, many engineering computations can be safely carried out assuming no loss in the energy of the wave, other than the geometric spreading, as it propagates through the medium. One of the problems where PUFEM can become attractive is modelling ultrasound in an attenuating human tissue. To the author's knowledge, PUFEM has not been used to model high frequency sound waves in an attenuating media. If ultrasonic scattering from only a single tissue is sought and if the tissue properties can be considered as only weakly or slowly varying, the approach of spectral methods such as the k-space method or pseudospectral method, have been found to be effective [18, 123, 183]. However, a major shortcoming of the spectral methods remains that the heterogeneity that can be handled is only 'weak'. It is not clear, hitherto, as to how a scattering problem with severe impedance mismatch would be handled with the k-space approach. Such a problem could arise in the case of a tissue that is in close vicinity of a bone*. The concept of mixed basis discussed in Chapter 6 can be effective in such a case.

8.2.2 Coupling of PUFEM and plane wave based Galerkin BEM

The author acknowledges other methods of symmetric FE-BE coupling such as using Galerkin BEM and the Calderón projectors, which can result in a symmetric linear system resulting in a faster solution time. Perhaps the second most attractive feature of the Galerkin BEM, other than its symmetry, is its ability to handle the singularities of various orders (weak, strong and hyper) without the need for a special treatment for each singularity type. Various orders of singularities were discussed in Chapter 5 (see §5.3) and the need of $C^{1,\alpha}$ continuity for the hypersingular integrals†. With the use of Galerkin BEM it can be shown that one can use $C^{0,\alpha}$ continuity and the hypersingular integral still exists [19]. Although a comparison of (collocation based) PUBEM and plane wave based Galerkin BEM (PUGBEM) has not appeared in the literature to the author's knowledge, it is known that the Galerkin BEM is generally more accurate than

*Speed of an acoustic wave inside bone is $\approx$ 5000 m/s whereas the speed in a soft tissue is $\approx$ 1500 m/s and therefore a strong impedance mismatch.

†Recall that this is the reason we collocate away from element edges when using continuous elements.

collocation BEM. Coupling of PUFEM with PUGBEM is therefore a very attractive method and can be studied for its convergence properties.

8.2.3 Multiple scattering problems with non-circular boundaries

Consider a problem of multiple scattering as illustrated in Figure 8.1. The region between two scatterers gives rise to multiple reflections. More importantly, since the scattered waves

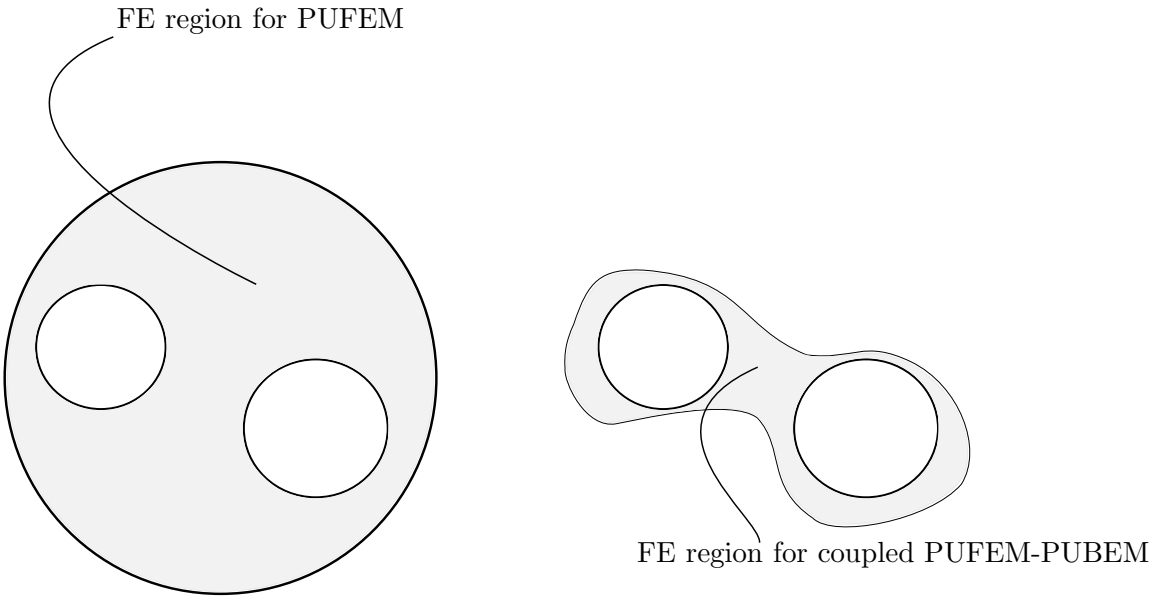

Figure 8.1: Multiple scattering problem

always have to be outgoing for the NRBC to be accurate, for multiple scattering problems, the truncation boundary Γ_r in the case of FEM or PUFEM always needs to be away from the region where multiple reflections are likely to occur. Traditional NRBCs can be extended to solve multiple scattering problems by enclosing each individual scatterer within a sphere and then deriving DtN maps between different spheres [64]. The limitation again is that of having to use canonical shapes like spheres for containing the scatterers. Although the examples solved here for demonstrating the convergence of the coupled PUFEM-PUBEM approach considered only a circular shape for Γ_r, PUBEM poses no restriction on the requirement of the shape of Γ_r. Theoretically, therefore, a problem where Γ_r is non-circular (see Figure 8.1) and where the normal vector to the boundary Γ_r can be uniquely defined, the coupled PUFEM-PUBEM approach can be shown to achieve a reduction in the total degrees of freedom needed. It should be remarked here from the conclusions drawn in Chapter 5 (§5.10) that the CHIEF method is stable for elongated geometries and no difficulty is encountered when solving scattering from such shapes. This indicates that not only the coupling of PUFEM-PUBEM is an attractive

alternative to the conventional NRBC based PUFEM, the stability of the CHIEF method to handle the non-uniqueness for an elongated geometry motivates its use in multiple scattering problems where the boundary Γ_r can be taken as line tracing the exterior of the scatterers.

References

[1] M. Abramowitz and I. A. Stegun. *Handbook of mathematical functions: with formulas, graphs, and mathematical tables*. Courier Dover Publications, 2012.

[2] S. Amini and P. Harris. A comparison between various boundary integral formulations of the exterior acoustic problem. *Computer Methods in Applied Mechanics and Engineering*, 84(1):59–75, 1990.

[3] E. Anderson, Z. Bai, C. Bischof, S. Blackford, J. Demmel, J. Dongarra, J. Du Croz, A. Greenbaum, S. Hammarling, A. McKenney, et al. *LAPACK Users' guide*, volume 9. Society for Industrial Mathematics, 1987.

[4] S. J. Anderson. Optimizing HF radar siting for surveillance and remote sensing in the strait of Malacca. *Geoscience and Remote Sensing, IEEE Transactions on*, 51(3):1805–1816, 2013.

[5] X. Antoine, C. Chniti, and K. Ramdani. On the numerical approximation of high-frequency acoustic multiple scattering problems by circular cylinders. *Journal of Computational Physics*, 227(3):1754–1771, 2008.

[6] O. Atak, B. Bergen, D. Huybrechs, B. Pluymers, and W. Desmet. Coupling of boundary element and wave based methods for the efficient solution of complex multiple scattering problems. *Journal of Computational Physics*, 258:165–184, 2014.

[7] N. Atalla and R. Bernhard. Review of numerical solutions for low-frequency structural-acoustic problems. *Applied Acoustics*, 43(3):271–294, 1994.

[8] F. Atkinson. LXI. On Sommerfeld's "radiation condition". *Philosophical Magazine*, 40(305):645–651, 1949.

[9] I. Babuška, F. Ihlenburg, T. Strouboulis, and S. Gangaraj. A posteriori error estimation for finite element solutions of Helmholtz equation. Part I: The quality of local indicators and estimators. *International Journal for Numerical Methods in Engineering*, 40(18):3443–3462, 1997.

[10] I. Babuška and S. Sauter. Is the Pollution Effect of the FEM Avoidable for the Helmholtz Equation Considering High Wave Numbers? *SIAM Review*, 42(3):451–484, 2000.

[11] L. Banjai and W. Hackbusch. Hierarchical matrix techniques for low-and high-frequency Helmholtz problems. *IMA journal of numerical analysis*, 28(1):46–79, 2008.

[12] D. E. Barrick, M. W. Evans, and B. L. Weber. Ocean surface currents mapped by Radar. *Science*, 198(4313):138–144, 1977.

[13] K.-J. Bathe. *Finite element procedures*. Klaus-Jurgen Bathe, 2006.

[14] A. Bayliss, M. Gunzburger, and E. Turkel. Boundary conditions for the numerical solution of elliptic equations in exterior regions. *SIAM Journal on Applied Mathematics*, 42(2):430–451, 1982.

[15] A. Bayliss and E. Turkel. Radiation boundary conditions for wave-like equations. *Communications on Pure and Applied Mathematics*, 33(6):707–725, 1980.

[16] P. Bettess. Waves. In O. Zienkiewicz, R. Taylor, and P. Nithiarasu, editors, *The Finite Element Method for Fluid Dynamics*, volume 3, chapter 8, pages 242–273. Elsevier Science, 5 edition, 2005.

[17] P. Bettess, J. Shirron, O. Laghrouche, B. Peseux, R. Sugimoto, and J. Trevelyan. A numerical integration scheme for special finite elements for the Helmholtz equation. *International Journal for Numerical Methods in Engineering*, 56(4):531–552, 2003.

[18] N. N. Bojarski. The k-space formulation of the scattering problem in the time domain. *The Journal of the Acoustical Society of America*, 72(2):570–584, 1982.

[19] M. Bonnet, G. Maier, and C. Polizzotto. Symmetric Galerkin boundary element methods. *Applied Mechanics Reviews*, 51(11):669–704, 1998.

[20] J. Bowman, T. Senior, and P. Uslenghi, editors. *Electromagnetic and Acoustic Scattering by Simple Shapes*. North-Holland Pub. Co., 1970.

[21] A. Brancati, M. Aliabadi, and I. Benedetti. Hierarchical adaptive cross approximation gmres technique for solution of acoustic problems using the boundary element method. *Computer Modeling in Engineering and Sciences (CMES)*, 43(2):149, 2009.

[22] A. Burton and G. Miller. The application of integral equation methods to the numerical solution of some exterior boundary-value problems. *Proceedings of the Royal Society of London. Series A, Mathematical and Physical Sciences*, 323(1553):201–210, 1971.

[23] M. Cerrolaza and E. Alarcon. A bi-cubic transformation for the numerical evaluation of the Cauchy principal value integrals in boundary methods. *International Journal for Numerical Methods in Engineering*, 28(5):987–999, 1989.

[24] O. Cessenat. *Application d'une nouvelle formulation variationnelle aux équations d'ondes harmoniques. Problèmes de Helmholtz 2D et de Maxwell 3D*. PhD Thesis, Université Paris IX, 1996.

[25] O. Cessenat and B. Despres. Application of an Ultra Weak Variational Formulation of Elliptic PDEs to the Two-Dimensional Helmholtz Problem. *SIAM J. Numer. Anal.*, 35(1):255–299, Feb. 1998.

[26] S. Chandler-Wilde and S. Langdon. A Galerkin boundary element method for high frequency scattering by convex polygons. *SIAM Journal on Numerical Analysis*, 45(2):610–640, 2007.

[27] S. N. Chandler-Wilde, S. Langdon, and M. Mokgolele. A High Frequency Boundary Element Method for Scattering by Convex Polygons with Impedance Boundary Conditions. *Communications in Computational Physics*, 11(2):573–593, 2011.

[28] S. N. Chandler-Wilde, S. Langdon, and L. Ritter. A high-wavenumber boundary-element method for an acoustic scattering problem. *Philosophical transactions. Series A, Mathematical, physical, and engineering sciences*, 362(1816):647–71, Mar. 2004.

[29] J. Chen, J. Lin, S. Kuo, and S. Chyuan. Boundary element analysis for the Helmholtz eigenvalue problems with a multiply connected domain. *Proceedings of the Royal Society*

of London. Series A: Mathematical, Physical and Engineering Sciences, 457(2014):2521–2546, 2001.

[30] K. Chen, J. Cheng, and P. J. Harris. A new study of the Burton and Miller method for the solution of a 3D Helmholtz problem. *IMA journal of applied mathematics*, 74(2):163–177, 2009.

[31] T. C. Chen. On bicubic transformation for the numerical evaluation of Cauchy principal value integrals. *Communications in numerical methods in engineering*, 9(4):307–311, 1993.

[32] H. Cheng, W. Y. Crutchfield, Z. Gimbutas, L. F. Greengard, J. F. Ethridge, J. Huang, V. Rokhlin, N. Yarvin, and J. Zhao. A wideband fast multipole method for the Helmholtz equation in three dimensions. *Journal of Computational Physics*, 216(1):300 – 325, 2006.

[33] C. C. Chien, H. Rajiyah, and S. N. Atluri. An effective method for solving the hyper-singular integral equations in 3-D acoustics. *The Journal of the Acoustical Society of America*, 88(2):918–937, 1990.

[34] R. D. Ciskowski and C. A. Brebbia. *Boundary element methods in acoustics*. Computational Mechanics Publications Southampton, Boston, 1991.

[35] R. W. Clough. The finite element method after twenty-five years: a personal view. *Computers & Structures*, 12(4):361–370, 1980.

[36] D. Colton and R. Kress. *Inverse acoustic and electromagnetic scattering theory*, volume 93. Springer, 2012.

[37] M. Costabel and E. Stephan. A direct boundary integral equation method for transmission problems. *Journal of Mathematical Analysis and Applications*, 106(2):367 – 413, 1985.

[38] A. Craggs. The use of simple three-dimensional acoustic finite elements for determining the natural modes and frequencies of complex shaped enclosures. *Journal of Sound and Vibration*, 23(3):331–339, 1972.

[39] M. J. Crocker et al. Prediction of transmission loss in mufflers by the finite- element method. *The Journal of the Acoustical Society of America*, 57(1):144–148, 1975.

[40] E. Darve. The fast multipole method: numerical implementation. *Journal of Computational Physics*, 160(1):195–240, 2000.

[41] Y. Decanini, A. Folacci, P. Gabrielli, and J. Rossi. Algebraic aspects of multiple scattering by two parallel cylinders: Classification and physical interpretation of scattering resonances. *Journal of Sound and Vibration*, 221(5):785–804, 1999.

[42] J. Donea and A. Huerta. *Finite element methods for flow problems*. John Wiley & Sons, 2003.

[43] M. El-Gebeily, W. M. Elleithy, and H. J. Al-Gahtani. Convergence of the domain decomposition finite element–boundary element coupling methods. *Computer Methods in Applied Mechanics and Engineering*, 191(43):4851–4867, 2002.

[44] B. Engquist and A. Majda. Absorbing boundary conditions for the numerical simulation of waves. *Mathematics of Computation*, 31(139):629–651, 1977.

[45] B. Engquist and A. Majda. Radiation boundary conditions for acoustic and elastic wave calculations. *Communications on Pure and Applied Mathematics*, 32(3):313–357, 1979.

[46] P. Etter. *Underwater Acoustic Modeling and Simulation*. Taylor & Francis, 4 edition, 2013.

[47] W. G. Facco, E. J. Silva, R. Adriano, A. S. Moura, and N. Z. Lima. Handling material discontinuities in a nonconforming generalized finite element method to solve wave propagation problems. *Microwave and Optical Technology Letters*, 54(12):2709–2716, 2012.

[48] C. Farhat, I. Harari, and L. P. Franca. The discontinuous enrichment method. *Computer Methods in Applied Mechanics and Engineering*, 190(48):6455 – 6479, 2001.

[49] C. Farhat, I. Harari, and U. Hetmaniuk. A discontinuous Galerkin method with lagrange multipliers for the solution of Helmholtz problems in the mid-frequency regime. *Computer Methods in Applied Mechanics and Engineering*, 192(11):1389–1419, 2003.

[50] C. Farhat, P. Wiedemann-Goiran, and R. Tezaur. A discontinuous Galerkin method with plane waves and Lagrange multipliers for the solution of short wave exterior Helmholtz problems on unstructured meshes. *Wave Motion*, 39(4):307 – 317, 2004. New computational methods for wave propagation.

[51] G. J. Fix and S. P. Marin. Variational methods for underwater acoustic problems. *Journal of Computational Physics*, 28(2):253–270, 1978.

[52] G. Gabard. Discontinuous Galerkin methods with plane waves for the displacement-based acoustic equation. *International Journal for Numerical Methods in Engineering*, 66(3):549–569, Apr. 2006.

[53] P. Gamallo and R. J. Astley. A comparison of two Trefftz-type methods: the ultraweak variational formulation and the least-squares method, for solving shortwave 2-D Helmholtz problems. *International Journal for Numerical Methods in Engineering*, 71(4):406–432, 2007.

[54] C. J. Gittelson, R. Hiptmair, and I. Perugia. Plane wave discontinuous Galerkin methods: Analysis of the h-version. *ESAIM: Mathematical Modelling and Numerical Analysis*, 43:297–331, 3 2009.

[55] D. Givoli. Non-reflecting boundary conditions. *Journal of Computational Physics*, 94(1):1–29, 1991.

[56] D. Givoli. *Numerical methods for problems in infinite domains*. Elsevier Amsterdam, 1992.

[57] D. Givoli. A spatially exact non-reflecting boundary condition for time dependent problems. *Computer Methods in Applied Mechanics and Engineering*, 95(1):97 – 113, 1992.

[58] D. Givoli. High-order local non-reflecting boundary conditions: a review. *Wave Motion*, 39(4):319–326, 2004.

[59] D. Givoli and J. B. Keller. A finite element method for large domains. *Computer Methods in Applied Mechanics and Engineering*, 76(1):41 – 66, 1989.

[60] G. Gladwell. A variational formulation of damped acousto structural vibration problems. *Journal of Sound and Vibration*, 4(2):172–186, 1966.

[61] C. I. Goldstein. A finite element method for solving Helmholtz type equations in waveguides and other unbounded domains. *Mathematics of Computation*, 39(160):309–324, 1982.

[62] G. Golub and W. Kahan. Calculating the singular values and pseudo-inverse of a matrix. *Journal of the Society for Industrial & Applied Mathematics, Series B: Numerical Analysis*, 2(2):205–224, 1965.

[63] M. J. Grote and J. B. Keller. Exact nonreflecting boundary conditions for the time dependent wave equation. *SIAM Journal on Applied Mathematics*, 55(2):280–297, 1995.

[64] M. J. Grote and C. Kirsch. Dirichlet-to-Neumann boundary conditions for multiple scattering problems. *Journal of Computational Physics*, 201(2):630–650, 2004.

[65] M. Guiggiani, G. Krishnasamy, T. Rudolphi, and F. Rizzo. A general algorithm for the numerical solution of hypersingular boundary integral equations. *ASME Journal of Applied Mechanics*, 59(3):604–614, 1992.

[66] B. Gustafsson and H.-O. Kreiss. Boundary conditions for time dependent problems with an artificial boundary. *Journal of Computational Physics*, 30(3):333 – 351, 1979.

[67] T. Hagstrom and H. Keller. Exact boundary conditions at an artificial boundary for partial differential equations in cylinders. *SIAM journal on mathematical analysis*, 17(2):322–341, 1986.

[68] T. Hagstrom and H. Keller. The numerical calculation of traveling wave solutions of nonlinear parabolic equations. *SIAM journal on scientific and statistical computing*, 7(3):978–988, 1986.

[69] L. Halpern and L. N. Trefethen. Wide-angle one-way wave equations. *The Journal of the Acoustical Society of America*, 84(4):1397–1404, 1988.

[70] P. C. Hansen. The L-Curve and its use in the numerical treatment of inverse problems. In *in Computational Inverse Problems in Electrocardiology, ed. P. Johnston, Advances in Computational Bioengineering*, volume 4, pages 119–142, 2000.

[71] I. Harari. A survey of finite element methods for time-harmonic acoustics. *Computer Methods in Applied Mechanics and Engineering*, 195(13-16):1594–1607, Feb. 2006.

[72] I. Harari and T. J. Hughes. Finite element methods for the Helmholtz equation in an exterior domain: model problems. *Computer Methods in Applied Mechanics and Engineering*, 87(1):59–96, 1991.

[73] I. Harari and T. J. Hughes. A cost comparison of boundary element and finite element methods for problems of time-harmonic acoustics. *Computer Methods in Applied Mechanics and Engineering*, 97(1):77–102, May 1992.

[74] I. Harari, I. Patlashenko, and D. Givoli. Dirichlet-to-Neumann maps for unbounded wave guides. *Journal of Computational Physics*, 143(1):200 – 223, 1998.

[75] B. Hariharan, S. Aluru, and B. Shanker. A scalable parallel fast multipole method for analysis of scattering from perfect electrically conducting surfaces. In *Supercomputing, ACM/IEEE 2002 Conference*, pages 42–42, 2002.

[76] O. Heaviside. *Electromagnetic Theory*, volume 3. Cosimo, Inc., 2008.

[77] D. Herrin, Z. Tao, F. Martinus, and A. Seybert. Predicting structural vibration and sound radiation from an engine cover. In *2004 IMAC-XXII: Conference and Exposition on Structural Dynamics*, 2004.

[78] T. J. Hughes. *The finite element method: linear static and dynamic finite element analysis*. Courier Dover Publications, 2012.

[79] T. Huttunen, J. Kaipio, and P. Monk. An ultra-weak method for acoustic fluid–solid interaction. *Journal of Computational and Applied Mathematics*, 213(1):166–185, 2008.

[80] T. Huttunen, P. Monk, F. Collino, and J. P. Kaipio. The ultra-weak variational formulation for elastic wave problems. *SIAM Journal on Scientific Computing*, 25(5):1717–1742, 2004.

[81] T. Huttunen, P. Monk, and J. P. Kaipio. Computational aspects of the ultra-weak variational formulation. *Journal of Computational Physics*, 182(1):27 – 46, 2002.

[82] W. S. Hwang. Hypersingular boundary integral equations for exterior acoustic problems. *The Journal of the Acoustical Society of America*, 101(6):3336–3342, 1997.

[83] F. Ihlenburg. *Finite Element Analysis of Acoustic Scattering*, volume 132. Springer, 1998.

[84] F. Ihlenburg and I. Babuška. Finite element solution of the Helmholtz equation with high wave number Part I: The h-version of the FEM. *Computers & Mathematics with Applications*, 30(9):9–37, 1995.

[85] M. Jensen and J. Freeze. A recursive Green's function method for boundary integral analysis of inhomogeneous domains. *Antennas and Propagation, IEEE Transactions on*, 46(12):1810–1816, Dec 1998.

[86] M. A. Jensen. A recursive Green's function technique for acoustic scattering from heterogeneous objects. *The Journal of the Acoustical Society of America*, 103(2):713–720, 1998.

[87] J. Jirousek and A. Wrblewski. Least-squares T-elments: Equivalent FE and BE forms of a substructure-oriented boundary solution approach. *Communications in Numerical Methods in Engineering*, 10(1):21–32, 1994.

[88] P. Johnston. Semi-sigmoidal transformations for evaluating weakly singular boundary element integrals. *International Journal for Numerical Methods in Engineering*, 47(10):1709–1730, 2000.

[89] P. R. Johnston and D. Elliott. A generalisation of Telles method for evaluating weakly singular boundary element integrals. *Journal of computational and applied mathematics*, 131(1):223–241, 2001.

[90] P. Juhl. A numerical study of the coefficient matrix of the boundary element method near characteristic frequencies. *Journal of sound and vibration*, 175(1):39–50, 1994.

[91] F. Kang. Finite element method and natural boundary reduction. In *Proceedings of the International Congress of Mathematicians*, pages 1439–1453, Warsaw, 1983.

[92] Y. J. Kang and J. S. Bolton. A finite element model for sound transmission through foam-lined double-panel structures. *The Journal of the Acoustical Society of America*, 99(5):2755–2765, 1996.

[93] J. B. Keller and D. Givoli. Exact non-reflecting boundary conditions. *Journal of Computational Physics*, 82(1):172–192, 1989.

[94] L. E. Kinsler, A. R. Frey, A. B. Coppens, and J. V. Sanders. Fundamentals of acoustics. *Fundamentals of Acoustics, 4th Edition, by Lawrence E. Kinsler, Austin R. Frey, Alan B. Coppens, James V. Sanders, pp. 560. ISBN 0-471-84789-5. Wiley-VCH, December 1999.*, 1, 1999.

[95] S. Kirkup. *The boundary element method in acoustics: a development in Fortran*. Number 1. Stephen Kirkup, 1998.

[96] R. Kittappa and R. Kleinman. Acoustic scattering by penetrable homogeneous objects. *Journal of Mathematical Physics*, 16(2):421–432, 2008.

[97] R. Kleinman and P. Martin. On single integral equations for the transmission problem of acoustics. *SIAM Journal on Applied Mathematics*, 48(2):307–325, 1988.

[98] G. Krishnasamy, F. Rizzo, and T. Rudolphi. Continuity requirements for density functions in the boundary integral equation method. *Computational Mechanics*, 9(4):267–284, 1992.

[99] G. Krishnasamy, L. Schmerr, T. Rudolphi, and F. Rizzo. Hypersingular boundary integral equations: some applications in acoustic and elastic wave scattering. *Journal of Applied Mechanics*, 57(2):404–414, 1990.

[100] O. Laghrouche and P. Bettess. 1o solving short wave problems using special finite elements-towards an adaptive approach. *The Mathematics of Finite Elements and Applications X (MAFELAP 1999)*, page 181, 2000.

[101] O. Laghrouche and P. BETTESS. Short wave modelling using special finite elements. *Journal of Computational Acoustics*, 8(01):189–210, 2000.

[102] O. Laghrouche, P. Bettess, and R. Astley. Modelling of short wave diffraction problems using approximating systems of plane waves. *International Journal for Numerical Methods in Engineering*, 54(10):1501–1533, 2002.

[103] O. Laghrouche, P. Bettess, and R. J. Astley. Modelling of short wave diffraction problems using approximating systems of plane waves. *International Journal for Numerical Methods in Engineering*, 54(10):1501–1533, 2002.

[104] O. Laghrouche, P. Bettess, and D. Le Houédec. Special finite elements for high frequency elastodynamic problems: first numerical experiments. In *Proceedings of the eighth international conference on The application of artificial intelligence to civil and structural engineering computing*, pages 181–182. Civil-Comp Press, 2001.

[105] O. Laghrouche, P. Bettess, E. Perrey-Debain, and J. Trevelyan. Plane wave basis finite-elements for wave scattering in three dimensions. *Communications in numerical methods in engineering*, 19(9):715–723, 2003.

[106] O. Laghrouche, P. Bettess, E. Perrey-Debain, and J. Trevelyan. Wave interpolation finite elements for Helmholtz problems with jumps in the wave speed. *Computer Methods in Applied Mechanics and Engineering*, 194(2):367–381, 2005.

[107] O. Laghrouche, A. El-Kacimi, and J. Trevelyan. A comparison of NRBCs for PUFEM in 2D Helmholtz problems at high wave numbers. *Journal of Computational and Applied Mathematics*, 234(6):1670–1677, 2010.

[108] O. Laghrouche and M. S. Mohamed. Locally enriched finite elements for the Helmholtz equation in two dimensions. *Computers and Structures*, 88(23-24):1469–1473, Dec. 2010.

[109] S. Li and Q. Huang. An improved form of the hypersingular boundary integral equation for exterior acoustic problems. *Engineering Analysis with Boundary Elements*, 34(3):189–195, 2010.

[110] S. Li and Q. Huang. A fast multipole boundary element method based on the improved Burton–Miller formulation for three-dimensional acoustic problems. *Engineering Analysis with Boundary Elements*, 35(5):719–728, 2011.

[111] S. Li and Q. Huang. A new fast multipole boundary element method for two dimensional acoustic problems. *Computer Methods in Applied Mechanics and Engineering*, 200(9):1333–1340, 2011.

[112] C. Linton and D. Evans. The interaction of waves with arrays of vertical circular cylinders. *Journal of Fluid Mechanics*, 215:549–569, 1990.

[113] Y. Liu and F. Rizzo. A weakly singular form of the hypersingular boundary integral equation applied to 3-D acoustic wave problems. *Computer Methods in Applied Mechanics and Engineering*, 96(2):271 – 287, 1992.

[114] Y. Liu and T. Rudolphi. Some identities for fundamental solutions and their applications to weakly-singular boundary element formulations. *Engineering Analysis with Boundary Elements*, 8(6):301–311, 1991.

[115] K. Manoj and S. Bhattacharyya. A family of second-order boundary dampers for finite element analysis of two and three-dimensional problems in transient exterior acoustics. *International Journal for Numerical Methods in Engineering*, 48(6):925–948, 2000.

[116] G. D. Manolis and R. P. Shaw. Green's function for the vector wave equation in a mildly heterogeneous continuum. *Wave Motion*, 24(1):59–83, Aug. 1996.

[117] S. Marburg and T. Wu. Treating the Phenomenon of Irregular Frequencies. In S. Marburg and B. Nolte, editors, *Computational Acoustics of Noise Propagation in Fluids-Finite and Boundary Element Methods*, chapter 15. Springer, 2008.

[118] S. Marin. Computing scattering amplitudes for arbitrary cylinders under incident plane waves. *Antennas and Propagation, IEEE Transactions on*, 30(6):1045–1049, Nov 1982.

[119] P. Martin. Identification of irregular frequencies in simple direct integral-equation methods for scattering by homogeneous inclusions. *Wave Motion*, 13:185–192, 1991.

[120] P. A. Martin. Integral-equation methods for multiple-scattering problems I. Acoustics. *The Quarterly Journal of Mechanics and Applied Mathematics*, 38(1):105–118, 1985.

[121] P. Massimi, R. Tezaur, and C. Farhat. A discontinuous enrichment method for three-dimensional multiscale harmonic wave propagation problems in multi-fluid and fluid-solid media. *International Journal for Numerical Methods in Engineering*, 76(3):400–425, 2008.

[122] P. Massimi, R. Tezaur, and C. Farhat. A discontinuous enrichment method for the efficient solution of plate vibration problems in the medium-frequency regime. *International Journal for Numerical Methods in Engineering*, 84(2):127–148, 2010.

[123] T. D. Mast, L. P. Souriau, D.-L. Liu, M. Tabei, A. I. Nachman, and R. C. Waag. A k-space method for large-scale models of wave propagation in tissue. *Ultrasonics, Ferroelectrics and Frequency Control, IEEE Transactions on*, 48(2):341–354, 2001.

[124] J. Melenk and I. Babuška. The partition of unity finite element method: basic theory and applications. *Computer Methods in Applied Mechanics and Engineering*, 139(1):289–314, 1996.

[125] J. Melenk and I. Babuška. Approximation with harmonic and generalized harmonic polynomials in the partition of unity method. *Computer Assisted Mechanics and Engineering Sciences*, 4:607–632, 1997.

[126] Y. Mi and M. Aliabadi. Dual boundary element method for three-dimensional fracture mechanics analysis. *Engineering Analysis with Boundary Elements*, 10(2):161 – 171, 1992.

[127] K. Michalski and J. Mosig. Multilayered media Green's functions in integral equation formulations. *Antennas and Propagation, IEEE Transactions on*, 45(3):508–519, Mar 1997.

[128] M. S. Mohamed. *Numerical Aspects of the PUFEM for Efficient Solution of Helmholtz Problems*. PhD thesis, Heriot-Watt University, April 2010.

[129] M. S. Mohamed, O. Laghrouche, and a. El-Kacimi. Some numerical aspects of the PUFEM for efficient solution of 2D Helmholtz problems. *Computers and Structures*, 88(23-24):1484–1491, Dec. 2010.

[130] G. Monegato and I. Sloan. Numerical solution of the generalized airfoil equation for an airfoil with a flap. *SIAM Journal on Numerical Analysis*, 34(6):2288–2305, 1997.

[131] P. Monk. *Finite element methods for Maxwell's equations*. Oxford University Press, 2003.

[132] P. Monk and D.-Q. Wang. A least-squares method for the Helmholtz equation. *Computer Methods in Applied Mechanics and Engineering*, 175(12):121 – 136, 1999.

[133] P. Morse. *Theoretical Acoustics*. Princeton University Press, 1986.

[134] H. Narain and H. Gupta. Koyna Earthquake. *Nature*, 217:1138–1139, 1968.

[135] D. Nefske, J. Wolf Jr, and L. Howell. Structural-acoustic finite element analysis of the automobile passenger compartment: a review of current practice. *Journal of Sound and Vibration*, 80(2):247–266, 1982.

[136] N. Nishimura. Fast multipole accelerated boundary integral equation methods. *Applied Mechanics Reviews*, 55(4):299–324, 2002.

[137] F. W. Olver. *NIST handbook of mathematical functions*. Cambridge University Press, 2010.

[138] P. Ortiz and E. Sanchez. An improved partition of unity finite element model for diffraction problems. *International Journal for Numerical Methods in Engineering*, 50(12):2727–2740, 2001.

[139] P. Pawliuk and M. Yedlin. Truncating cylindrical wave modes in two-dimensional multiple scattering. *Optics Letters*, 35(23):3997–3999, 2010.

[140] M. Peake, J. Trevelyan, and G. Coates. Extended isogeometric boundary element method (XIBEM) for two-dimensional Helmholtz problems. *Computer Methods in Applied Mechanics and Engineering*, 259:93–102, 2013.

[141] M. Peake, J. Trevelyan, and G. Coates. Novel basis functions for the partition of unity boundary element method for Helmholtz problems. *International Journal for Numerical Methods in Engineering*, 93(9):905–918, 2013.

[142] E. Perrey-Debain, O. Laghrouche, P. Bettess, and J. Trevelyan. Plane-wave basis finite elements and boundary elements for three-dimensional wave scattering. *Philosophical Transactions of the Royal Society of London. Series A: Mathematical, Physical and Engineering Sciences*, 362(1816):561–577, 2004.

[143] E. Perrey-Debain, J. Trevelyan, and P. Bettess. New special wave boundary elements for short wave problems. *Communications in Numerical Methods in Engineering*, 18(4):259–268, 2002.

[144] E. Perrey-Debain, J. Trevelyan, and P. Bettess. P-wave and S-wave decomposition in boundary integral equation for plane elastodynamic problems. *Communications in Numerical Methods in Engineering*, 19(12):945–958, 2003.

[145] E. Perrey-Debain, J. Trevelyan, and P. Bettess. Plane wave interpolation in direct collocation boundary element method for radiation and wave scattering: numerical aspects and applications. *Journal of Sound and Vibration*, 261(5):839 – 858, 2003.

[146] E. Perrey-Debain, J. Trevelyan, and P. Bettess. Use of wave boundary elements for acoustic computations. *Journal of Computational Acoustics*, 11(02):305–321, 2003.

[147] E. Perrey-Debain, J. Trevelyan, and P. Bettess. Wave boundary elements: a theoretical overview presenting applications in scattering of short waves. *Engineering Analysis with Boundary Elements*, 28(2):131–141, 2004.

[148] P. Pinsky and N. Abboud. Transient finite element analysis of the exterior structural acoustics problem. *Journal of Vibration and Acoustics*, 112(2):245–256, 1990.

[149] P. M. Pinsky and N. N. Abboud. Finite element solution of the transient exterior structural acoustics problem based on the use of radially asymptotic boundary operators. *Computer Methods in Applied Mechanics and Engineering*, 85(3):311 – 348, 1991.

[150] V. C. Protopappas, I. C. Kourtis, L. C. Kourtis, K. N. Malizos, C. V. Massalas, and D. I. Fotiadis. Three-dimensional finite element modeling of guided ultrasound wave propagation in intact and healing long bones. *The Journal of the Acoustical Society of America*, 121(6):3907–3921, 2007.

[151] S. Quek and G. Liu. *Finite Element Method: A Practical Course: A Practical Course*. Butterworth-Heinemann, 2003.

[152] J. N. Reddy and D. K. Gartling. *The finite element method in heat transfer and fluid dynamics*. CRC press, 2010.

[153] P. Roux, W. Kuperman, N. Group, et al. Extracting coherent wave fronts from acoustic ambient noise in the ocean. *The Journal of the Acoustical Society of America*, 116(4):1995–2003, 2004.

[154] P. Roux, K. G. Sabra, W. Kuperman, and A. Roux. Ambient noise cross correlation in free space: Theoretical approach. *The Journal of the Acoustical Society of America*, 117(1):79–84, 2005.

[155] H. A. Schenck. Improved integral formulation for acoustic radiation problems. *Journal of the Acoustical Society of America*, 44(1):41–58, 1968.

[156] B. Shanker, A. Ergin, K. Aygun, and E. Michielssen. Analysis of transient electromagnetic scattering from closed surfaces using a combined field integral equation. *Antennas and Propagation, IEEE Transactions on*, 48(7):1064–1074, Jul 2000.

[157] N. M. Shapiro and M. Campillo. Emergence of broadband Rayleigh waves from correlations of the ambient seismic noise. *Geophysical Research Letters*, 31(7), 2004.

[158] R. P. Shaw and N. Makris. Green's functions for Helmholtz and Laplace equations in heterogeneous media. *Engineering Analysis with Boundary Elements*, 10(2):179 – 183, 1992.

[159] L. Shen and Y. Liu. An adaptive fast multipole boundary element method for three-dimensional acoustic wave problems based on the burtonmiller formulation. *Computational Mechanics*, 40(3):461–472, 2007.

[160] J. J. Shirron. *Solution of exterior Helmholtz problems using finite and infinite elements*. PhD thesis, University of Maryland, College Park, 1995.

[161] J. J. Shirron and I. Babuka. A comparison of approximate boundary conditions and infinite element methods for exterior Helmholtz problems. *Computer Methods in Applied Mechanics and Engineering*, 164(12):121 – 139, 1998. Exterior Problems of Wave Propagation.

[162] J. R. Silva, H. Power, and L. Wrobel. A hypersingular integral equation formulation for Stokes' flow in ducts. *Engineering Analysis with Boundary Elements*, 12(3):185 – 193, 1993.

[163] R. Simpson and J. Trevelyan. A partition of unity enriched dual boundary element method for accurate computations in fracture mechanics. *Computer Methods in Applied Mechanics and Engineering*, 200(1):1–10, 2011.

[164] K. M. Singh and M. Tanaka. On non-linear transformations for accurate numerical evaluation of weakly singular boundary integrals. *International Journal for Numerical Methods in Engineering*, 50(8):2007–2030, 2001.

[165] V. Sladek and J. Sládek. *Singular integrals in boundary element methods*. Computational Mechanics Publications Southampton, 1998.

[166] R. Snieder. Extracting the Green's function from the correlation of coda waves: A derivation based on stationary phase. *Physical Review E*, 69(4):046610, 2004.

[167] D. Soares Jr, O. Von Estorff, and W. Mansur. Iterative coupling of BEM and FEM for nonlinear dynamic analyses. *Computational Mechanics*, 34(1):67–73, 2004.

[168] A. Sommerfeld. *Partial differential equations in physics*, volume 1. Academic press, 1949.

[169] M. Stojek. Least-squares Trefftz-type elements for the Helmholtz equation. *International Journal for Numerical Methods in Engineering*, 41(5):831–849, 1998.

[170] J. A. Stratton. *Electromagnetic theory*, volume 33. John Wiley & Sons, 2007.

[171] R. Sugimoto, P. Bettess, and J. Trevelyan. A numerical integration scheme for special quadrilateral finite elements for the Helmholtz equation. *Communications in numerical methods in engineering*, 19(3):233–245, 2003.

[172] S. Sung and D. Nefske. A coupled structural-acoustic finite element model for vehicle interior noise analysis. *Journal of Vibration, Acoustics Stress and Reliability in Design*, 106(2):314–318, 1984.

[173] J. Telles. A self-adaptive co-ordinate transformation for efficient numerical evaluation of general boundary element integrals. *International Journal for Numerical Methods in Engineering*, 24(5):959–973, 1987.

[174] R. Tezaur, I. Kalashnikova, and C. Farhat. The discontinuous enrichment method for medium-frequency Helmholtz problems with a spatially variable wavenumber. *Computer Methods in Applied Mechanics and Engineering*, 268(0):126 – 140, 2014.

[175] L. L. Thompson. A review of finite-element methods for time-harmonic acoustics. *The Journal of the Acoustical Society of America*, 119(3):1315, 2006.

[176] L. Ting and M. J. Miksis. Exact boundary conditions for scattering problems. *The Journal of the Acoustical Society of America*, 80(6):1825–1827, 1986.

[177] M. Turley, R. Gardiner-Garden, and D. Holdsworth. High-resolution wide area remote sensing for hf radar track registration. In *Radar (Radar), 2013 International Conference on*, pages 128–133, Sept 2013.

[178] A. Villarreal and J. A. Scales. Distributed three-dimensional finite-difference modeling of wave propagation in acoustic media. *Computers in Physics*, 11(4):388–399, 1997.

[179] L. Wagatha. On boundary conditions for the numerical simulation of wave propagation. *Applied Numerical Mathematics*, 1(4):309 – 314, 1985.

[180] K. Wapenaar, E. Slob, and R. Snieder. Unified Green's Function Retrieval by Cross Correlation. *Physical Review Letters*, 97(23):234301, Dec. 2006.

[181] R. L. Weaver and O. I. Lobkis. Ultrasonics without a source: Thermal fluctuation correlations at MHz frequencies. *Physical Review Letters*, 87(13):134301, 2001.

[182] C. H. Wilcox. An expansion theorem for electromagnetic fields. *Comm. Pure Appl. Math*, pages 115–1334, 1956.

[183] G. Wojcik, B. Fomberg, R. Waag, L. Carcione, J. Mould, L. Nikodym, and T. Driscoll. Pseudospectral methods for large-scale bioacoustic models. In *Ultrasonics Symposium, 1997. Proceedings., 1997 IEEE*, volume 2, pages 1501–1506. IEEE, 1997.

[184] H. Wu, Y. Liu, and W. Jiang. A fast multipole boundary element method for 3D multi-domain acoustic scattering problems based on the Burton–Miller formulation. *Engineering Analysis with Boundary Elements*, 36(5):779–788, 2012.

[185] H. Wu, Y. Liu, and W. Jiang. A low-frequency fast multipole boundary element method based on analytical integration of the hypersingular integral for 3D acoustic problems. *Engineering analysis with boundary elements*, 37(2):309–318, 2013.

[186] T. Wu. *Boundary element acoustics: Fundamentals and computer codes*, volume 7. WIT Press/ Computational Mechanics, 2000.

[187] T. Wu and A. Seybert. A weighted residual formulation for the CHIEF method in acoustics. *The Journal of the Acoustical Society of America*, 90:1608, 1991.

[188] J. Young and J. Bertrand. Multiple scattering by two cylinders. *The Journal of the Acoustical Society of America*, 58:1190, 1975.

[189] L. Zhang, R. Tezaur, and C. Farhat. The discontinuous enrichment method for elastic wave propagation in the medium-frequency regime. *International journal for numerical methods in engineering*, 66(13):2086–2114, 2006.

[190] O. C. Zienkiewicz and P. Morice. *The finite element method in engineering science*, volume 1977. McGraw-Hill London, 1971.

Appendices

Appendix A

Fundamental solutions and their derivatives

In Chapter 5 (see §5.4.1), we are required to evaluate the fundamental solutions G, G_0 and their derivatives. We have

$$G = \frac{i}{4}H_0(kr) = \frac{i}{4}(J_0(kr) + iY_0(kr)) \tag{A.1}$$

$$G_0 = \frac{1}{2\pi}\ln\frac{1}{r} = -\frac{1}{2\pi}\ln r \tag{A.2}$$

The first derivatives of these fundamental solutions are as follows:

$$\frac{\partial G}{\partial n_{\mathbf{x}}} = \frac{k}{4}(Y_1(kr) - iJ_1(kr))\frac{\partial r}{\partial n_{\mathbf{x}}} \tag{A.3}$$

$$\frac{\partial G}{\partial n_{\mathbf{y}}} = \frac{k}{4}(Y_1(kr) - iJ_1(kr))\frac{\partial r}{\partial n_{\mathbf{y}}} \tag{A.4}$$

$$\frac{\partial G_0}{\partial n_{\mathbf{x}}} = -\frac{1}{2\pi r}\frac{\partial r}{\partial n_{\mathbf{x}}} \tag{A.5}$$

$$\frac{\partial G_0}{\partial n_{\mathbf{y}}} = -\frac{1}{2\pi r}\frac{\partial r}{\partial n_{\mathbf{y}}} \tag{A.6}$$

and in which we can use the derivatives

$$\frac{\partial r}{\partial n_{\mathbf{x}}} = \frac{-\mathbf{r}\cdot\mathbf{n}(\mathbf{x})}{r}, \frac{\partial r}{\partial n_{\mathbf{y}}} = \frac{\mathbf{r}\cdot\mathbf{n}(\mathbf{y})}{r} \tag{A.7}$$

The second derivatives of the fundamental solutions are as follows:

$$\frac{\partial^2 G}{\partial n_{\mathbf{x}} \partial n_{\mathbf{y}}} = \frac{k}{4} \left[Y_1(kr) - iJ_1(kr) \right] \frac{\partial^2 r}{\partial \mathbf{n_x} \partial \mathbf{n_y}} + \frac{1}{4} \left[\left(kY_0(kr) - \frac{Y_1(kr)}{r} \right) - i \left(kJ_0(kr) - \frac{J_1(kr)}{r} \right) \right] \frac{\partial r}{\partial n_{\mathbf{x}}} \frac{\partial r}{\partial n_{\mathbf{y}}} \tag{A.8}$$

$$\frac{\partial^2 G_0}{\partial n_{\mathbf{x}} \partial n_{\mathbf{y}}} = \frac{1}{2\pi r^2} \frac{\partial r}{\partial n_{\mathbf{x}}} \frac{\partial r}{\partial n_{\mathbf{y}}} - \frac{1}{2\pi r} \frac{\partial^2 r}{\partial \mathbf{n_x} \partial \mathbf{n_y}} \tag{A.9}$$

in which we can use the derivative

$$\frac{\partial^2 r}{\partial \mathbf{n_x} \partial \mathbf{n_y}} = \frac{-1}{r} \left(\mathbf{n_x} \cdot \mathbf{n_y} + \frac{\partial r}{\partial \mathbf{n_x}} \frac{\partial r}{\partial \mathbf{n_y}} \right) \tag{A.10}$$

Appendix B

Analytical solution for two layer problem

The analytical solution given here is for a two layer problem but the procedure can also be generalised for a multi-layered problem. Consider the geometry in Figure 6.1. It is convenient to consider the polar coordinate (r, θ) system for specifying any point in $(\Omega_0 \cup \Omega_1)$. The pressure at a point (r, θ) in Ω_0 due to the incident wave in the exterior region (Ω_0) with wavenumber $k_0 = \omega/c_0$ is given as [133]

$$\begin{aligned} p_{0i} &= e^{ik_0 r\cos(\theta)} \\ &= \sum_{n=0}^{\infty} \epsilon_n i^n J_n(k_0 r)\cos(n(\theta - \theta^I)) \end{aligned} \tag{B.1}$$

where,

$$\epsilon_n = \begin{cases} 1, & \text{if } n = 0 \\ 2, & \text{otherwise,} \end{cases} \tag{B.2}$$

where, i is the imaginary unit and $J_0(\cdot)$ is the Bessel function of first kind. The total pressure in Ω_0 is

$$p_0 = p_{0i} + p_{0s} \tag{B.3}$$

where p_{0s} is the scattered pressure in the exterior region and can be expressed as

$$p_{0s} = \sum_{n=0}^{\infty} C_n H_n^{(1)}(k_0 r)\cos(n\theta). \tag{B.4}$$

where $H_n^{(1)}(\cdot)$ is the Hankel function of the first kind. The total pressure in the inner region (Ω_1) can be given as

$$p_1 = \sum_{n=0}^{\infty} \Big(A_n H_n^{(1)}(k_1 r) + B_n H_n^{(2)}(k_1 r) \Big) \cos(n\theta). \tag{B.5}$$

where, $H_n^{(2)}(\cdot)$ is the Hankel function of the second kind.

B.1 Boundary conditions

In order to obtain explicit expressions for the interface coefficients viz. A_n, B_n and C_n we need three boundary conditions. The natural boundary condition for a sound hard cylinder surface is,

$$\frac{\partial p_1}{\partial r} = 0 \quad \text{on} \quad \Gamma_s \tag{B.6}$$

Using eq. (B.5) and setting $r = a$ in eq. (B.6) where a is the radius of the cylinder centred at origin,

$$\frac{\partial}{\partial r} \left(\sum_{n=0}^{\infty} \Big(A_n H_n^{(1)}(k_1 a) + B_n H_n^{(2)}(k_1 a) \Big) \cos(n\theta) \right) = 0. \tag{B.7}$$

Rearranging the above equation,

$$A_n H_n^{(1)'}(k_1 a) + B_n H_n^{(2)'}(k_1 a) = 0, \tag{B.8}$$

or,

$$A_n C_1 = -B_n C_2. \tag{B.9}$$

where $C_1 = H_n^{(1)'}(k_1 a)$ and $C_2 = H_n^{(2)'}(k_1 a)$ and the primes indicate the derivative with respect to the argument. The second boundary condition is the continuity of acoustic pressure on Γ_i, Let the radius of the circular interface Γ_i between Ω_1 and Ω_0 be denoted as r_i. Then the boundary condition specifying the continuity of acoustic pressure on Γ_i at $r = r_i$ is

$$p_{0i} + p_{0s} = p_1 \tag{B.10}$$

Using (B.1), (B.4) and (B.5) and setting $r = r_i$, we get,

$$C_3 A_n + C_4 B_n = C_6 + C_5 C_n. \tag{B.11}$$

$C_3 = H_n^{(1)}(k_1 r_i)$, $C_4 = H_n^{(2)}(k_1 r_i)$, $C_5 = H_n^{(1)}(k_0 r_i)$ and $C_6 = \epsilon_n i^n J_n(k_0 r_i)$.

Continuity of radial component of particle velocity on Γ_1:

The continuity of radial component of velocity is given by

$$\frac{1}{\rho_0}\frac{\partial}{\partial r}\left(p_{0i} + p_{0s}\right) = \frac{1}{\rho_1}\frac{\partial p_1}{\partial r} \tag{B.12}$$

Using (B.1), (B.4) and (B.5) and setting $r = r_i$, we get,

$$C_7 A_n + C_8 B_n = C_9 C_n + C_{10}, \tag{B.13}$$

where, $C_7 = qH_n^{(1)'}(k_1 r_i)$, $C_8 = qH_n^{(2)'}(k_1 r_i)$, $C_9 = H_n^{(1)'}(k_0 r_i)$, $C_{10} = \epsilon_n i^n J_n'(k_0 r_i)$ and $q = \rho_0/\rho_1$.

B.2 Coefficients:

(B.9) gives

$$A_n = -\frac{C_2}{C_1} B_n \tag{B.14}$$

(B.11) gives

$$-C_3\frac{C_2}{C_1}B_n + C_4 B_n = C_5 C_n + C_6 \qquad \rightarrow \left(C_4 - \frac{C_2 C_3}{C_1}\right) B_n = C_5 C_n + C_6 \tag{B.15}$$

(B.13) with (B.14) gives

$$-C_7\frac{C_2}{C_1}B_n + C_8 B_n = C_9 C_n + C_{10} \tag{B.16}$$

(B.15) gives

$$B_n = \left(\frac{C_5 C_1}{C_1 C_4 - C_2 C_3}\right) C_n + \frac{C_6 C_1}{C_1 C_4 - C_2 C_3} \tag{B.17}$$

Use (B.17) in (B.16), thus,

$$\left(C_8 - \frac{C_7 C_2}{C_1}\right)\left(\frac{C_5 C_1}{C_1 C_4 - C_2 C_3} C_n + \frac{C_6 C_1}{C_1 C_4 - C_2 C_3}\right) = C_9 C_n + C_{10} \tag{B.18}$$

Simplifying,

$$C_n = \frac{C_{12} - C_{10}}{C_9 - C11} \tag{B.19}$$

where,

$$C_{11} = \left(\frac{C_1 C_8 - C_2 C_7}{C_1 C_4 - C_2 C_3} \right) C_5 \tag{B.20}$$

$$C_{12} = \left(\frac{C_1 C_8 - C_2 C_7}{C_1 C_4 - C_2 C_3} \right) C_6 \tag{B.21}$$

Coefficients C_n (eq. B.19), B_n (eq. B.17) and A_n (eq. B.14) can now be used to compute the total wave at any point in the entire domain i.e. $\Omega_1 \cup \Omega_0$.

Appendix C

Sturm-Liouville problem

As discussed in Chapter 6 and 7, the boundary Γ_r, is always taken as a perfect circle enclosing the heterogeneous fluid domain (Ω_f) to be modelled. It is therefore clear that when using a plane wave enriched coupled FE-BE algorithm, we are only concerned with the eigenvalues of the interior Dirichlet problem that is defined with a circular boundary. This amounts to finding the eigenvalues of an idealized membrane in $\mathbb{R}^2$ classically known as the 'Sturm-Liouville problem'.

C.1 The Sturm-Liouville problem

Consider a circular membrane of radius R^*. It is immediately clear that the most convenient form of describing a transverse motion of a point on the membrane surface is writing the Helmholtz equation in cylindrical coordinates, i.e.,

$$\frac{\partial^2 u}{\partial r^2} + \frac{1}{r}\frac{\partial u}{\partial r} + \frac{1}{r^2}\frac{\partial^2 u}{\partial \theta^2} + k^2 u = 0, \tag{C.1}$$

where $u(r, \theta)$ is the transverse displacement of a point given by the polar coordinates (r, θ) and k is the wavenumber. Let,

$$u = \mathcal{R}(r)\Theta(\theta), \tag{C.2}$$

and let the membrane be subject to a homogeneous Dirichlet boundary condition at $r = R$, i.e.,

$$\mathcal{R}(R) = 0. \tag{C.3}$$

*Only on this occasion, we denote the radius of FE-BE coupling boundary Γ_r to be R.

Using equation (C.2) into equation (C.1) gives,

$$\Theta\frac{d^2\mathcal{R}}{dr^2}+\frac{\Theta}{r}\frac{d\mathcal{R}}{dr}+\frac{\mathcal{R}}{r^2}\frac{d^2\Theta}{d\theta^2}+k^2\mathcal{R}\Theta=0. \tag{C.4}$$

Multiplying equation (C.4) by $r^2/\Theta\mathcal{R}$ and rearranging,

$$\frac{r^2}{\mathcal{R}}\left(\frac{d^{\mathcal{R}}}{dr^2}+\frac{1}{r}\frac{d\mathcal{R}}{dr}\right)+k^2r^2=-\frac{1}{\Theta}\frac{d^2\Theta}{d\theta^2}. \tag{C.5}$$

It is evident that the left hand side of equation (C.5) is a function of radial coordinate r alone and the right hand side of equation (C.5) is a function of θ alone. It therefore transpires that both the sides of equation (C.5) must be equal to the same constant. Let this number be denoted as m^2. Thus the right hand side of equation (C.5) now becomes,

$$\begin{aligned}-\frac{1}{\Theta}\frac{d^2\Theta}{d\theta^2}&=m^2,\quad\text{or,}\\ \frac{d^2\Theta}{d\theta^2}&=-m^2\Theta\end{aligned} \tag{C.6}$$

Using equation (C.6) in equation (C.5)

$$\frac{d^2\mathcal{R}}{dr^2}+\frac{1}{r}\frac{d\mathcal{R}}{dr}+\left(k^2-\frac{m^2}{r^2}\right)\mathcal{R}=0 \tag{C.7}$$

Equation (C.7) is known as the 'Bessel's equation' and its solution can be given in the form,

$$\mathcal{R}(r)=\mathbf{A}J_m(kr)+\mathbf{B}Y_m(kr). \tag{C.8}$$

Note that $Y_m(kr)$ is singular at $r=0$ and therefore in order to have a finite displacement at $r=0$ (i.e., at the origin), we must have $\mathbf{B}=0$. Therefore,

$$\mathcal{R}(r)=\mathbf{A}J_m(kr). \tag{C.9}$$

In view of the Dirichelt boundary condition in equation (C.3), to have a nontrivial solution (i.e. $\mathbf{A}\neq 0$), we must have

$$J_m(kR)=0 \tag{C.10}$$

Therefore, if j_{mn} denotes the argument for which equation (C.10) holds, then the wavenumber k assumes discrete values $k_{mn} = j_{mn}/R$.

C.2 Characteristic wavenumbers

Recall now the classical two layer acoustic scattering problem defined earlier in Chapter 6, (see Figure 6.1) and is reproduced here for convenience (see Figure C.1). Let the radius of the

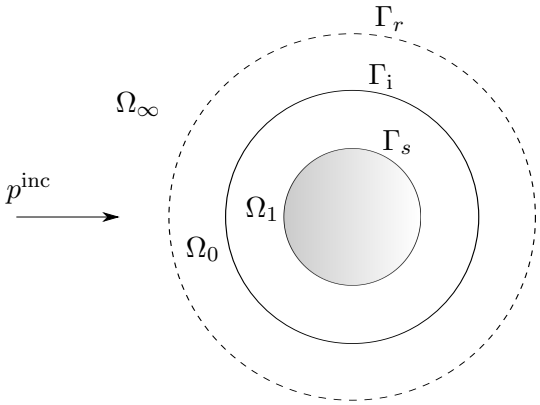

Figure C.1: Wave scattering in medium with a jump in wavenumber.

truncation boundary be $r(\Gamma_r) = 3$. Figure C.2 shows the Bessel functions of first kind (J_m) with their zero crossings marked. Only the Bessel functions up to the 2nd order (i.e., from J_0 to J_2) are plotted for a wavenumber ranging from 0.1 to 10. The marked zeros crossings are also listed in Table C.1.

m \ n	1	2	3	4	5
0	0.8016	1.8400	2.8846	3.9305	4.9770
1	1.2772	2.3385	3.3912	4.4412	5.4902
2	1.7119	2.8057	3.8733	4.9320	5.9866

Table C.1: Characteristic wavenumbers of interior Dirichlet problem.

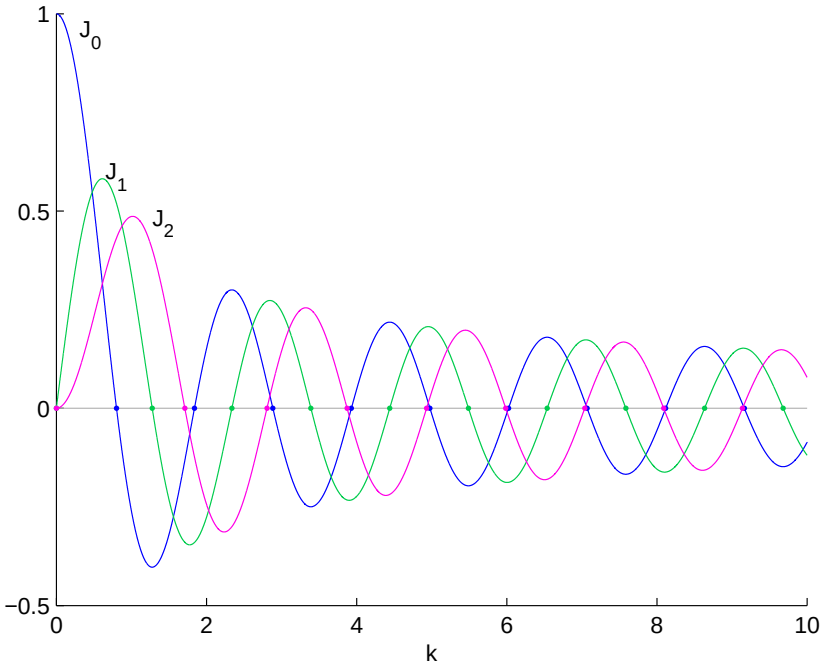

Figure C.2: Bessel functions with zero crossings

As we know that non-uniqueness is independent of the interior wavenumber k_1 or the density ratio ρ_1/ρ_0, we can set interior wavenumber $k_1 = 0.8k_0$, with no loss of generality. The density ratio is $\rho_1/\rho_0 = 1.2$ if $k_1 > k_0$ and $\rho_0/\rho_1 = 1.2$ if $k_0 > k_1$. We use the coupled FE-BE formulation with the polynomial basis alone for this exercise. For all the computations, we use $n_\theta = 48$ and $n_r = 20$, unless otherwise mentioned. The principal reason behind using a polynomial basis is that the linear system will not suffer from the ill-conditioning due to the plane wave basis. The ill-conditioning, if any, should arise only on account of the non-uniqueness. Figure C.3 shows the L_2 errors on the scatterer when one of the wavenumbers (either k_1 or k_0) is set to the wavenumbers listed in Table C.1. The blue lines correspond to the results when the wavenumber in the exterior is the non-unique k listed in Table C.1 and the red lines correspond to the results when the wavenumber in the interior is set to the non-unique k. The exercise of

setting the interior k to the non-unique k is performed purely to show that the non-uniqueness is independent of the wavenumber in the interior. Note that the dof are fixed for this exercise which is the reason behind an increasing L_2 error with the increase in the wavenumber. It can be noted from Figure C.4 that the condition number for the case when the non-unique k is in the exterior is slightly higher compared to the case when it is in the interior.

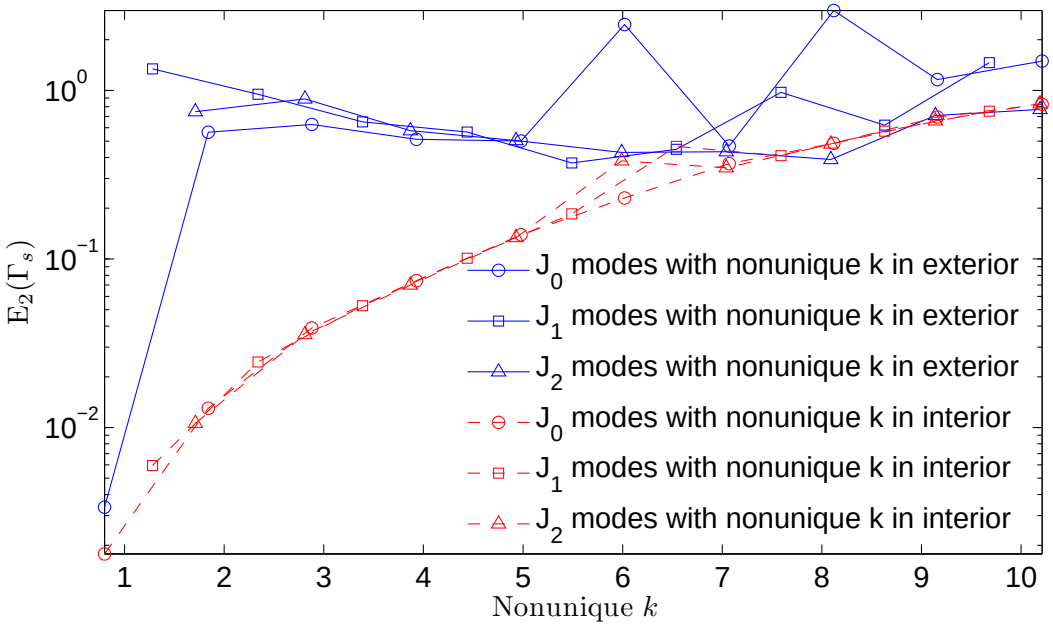

Figure C.3: L_2 errors on the scatterer: coupled polynomial FEM-BEM

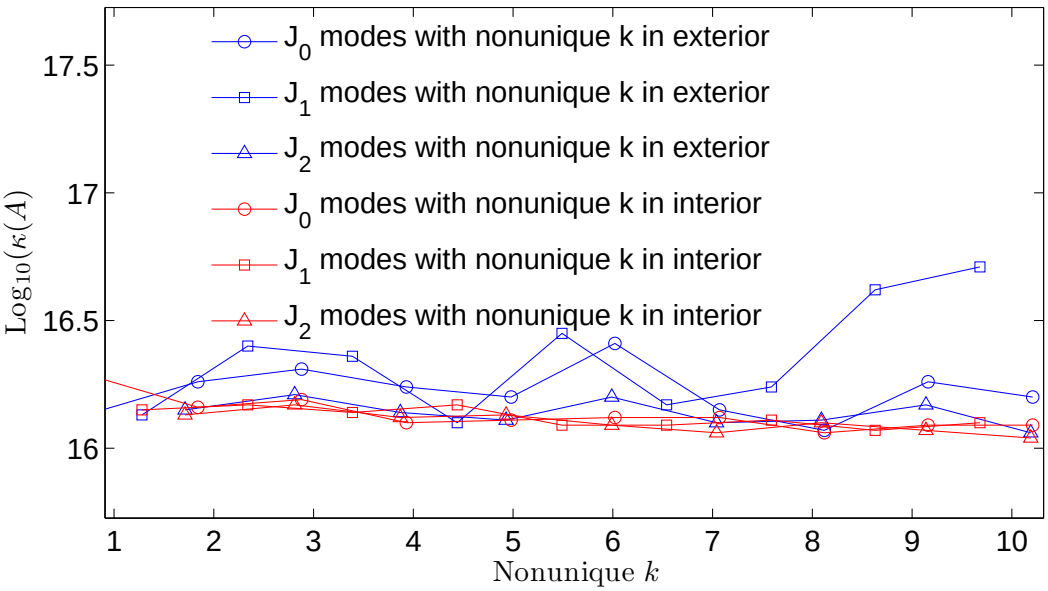

Figure C.4: Condition number of the system matrix: coupled polynomial FEM-BEM

For the sake of completeness, a L_2 error plot comparing the results when CHIEF method is used is shown in Figure C.5. The comparison is shown only for the modes corresponding to J_0 when used as the wavenumber in the exterior. The advantage due to CHIEF method is evident from figures C.5-C.6.

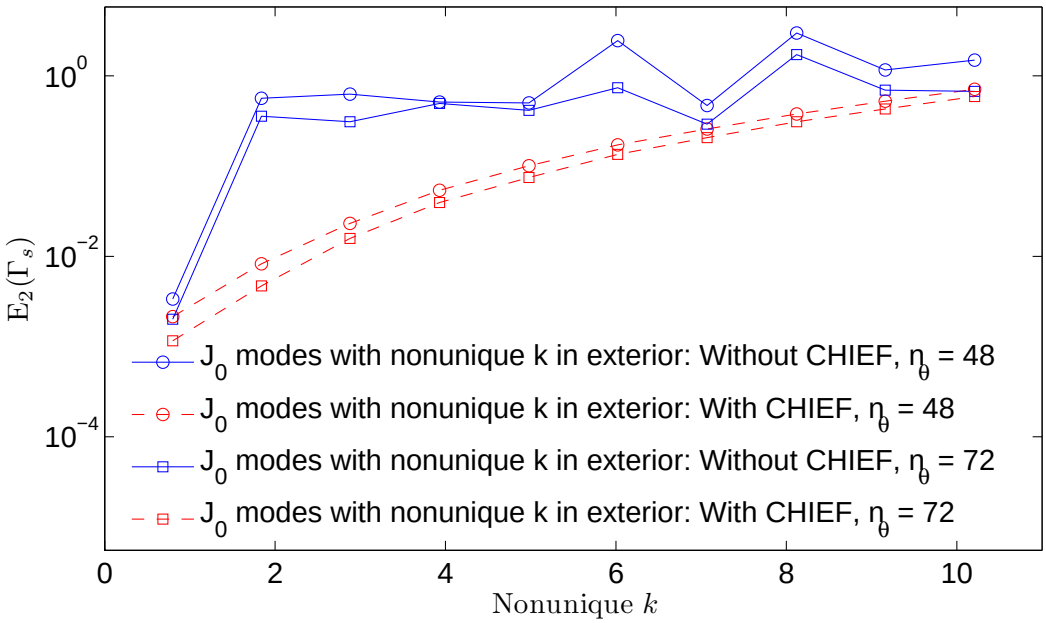

Figure C.5: $E^2(\Gamma_s)$ for coupled polynomial FEM-BEM: with and without CHIEF method

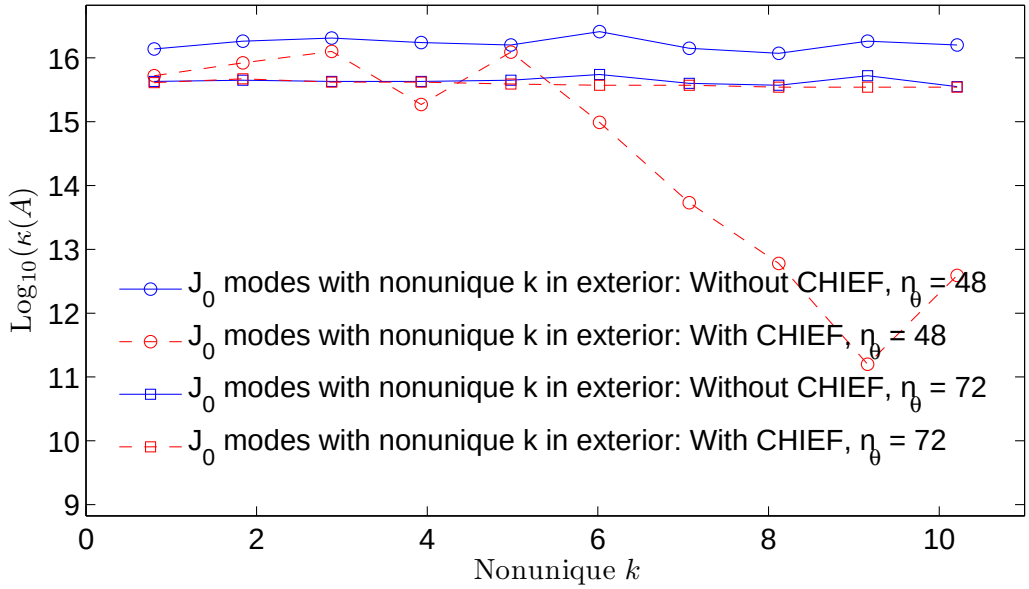

Figure C.6: Condition number of the system matrix for coupled polynomial FEM-BEM: with and without CHIEF method